

Supramolecular charge transfer systems

Citation for published version (APA):

Rösch, A. T. (2021). *Supramolecular charge transfer systems*. [Phd Thesis 1 (Research TU/e / Graduation TU/e), Chemical Engineering and Chemistry]. Eindhoven University of Technology.

Document status and date:

Published: 21/06/2021

Document Version:

Publisher's PDF, also known as Version of Record (includes final page, issue and volume numbers)

Please check the document version of this publication:

- A submitted manuscript is the version of the article upon submission and before peer-review. There can be important differences between the submitted version and the official published version of record. People interested in the research are advised to contact the author for the final version of the publication, or visit the DOI to the publisher's website.
- The final author version and the galley proof are versions of the publication after peer review.
- The final published version features the final layout of the paper including the volume, issue and page numbers.

[Link to publication](#)

General rights

Copyright and moral rights for the publications made accessible in the public portal are retained by the authors and/or other copyright owners and it is a condition of accessing publications that users recognise and abide by the legal requirements associated with these rights.

- Users may download and print one copy of any publication from the public portal for the purpose of private study or research.
- You may not further distribute the material or use it for any profit-making activity or commercial gain
- You may freely distribute the URL identifying the publication in the public portal.

If the publication is distributed under the terms of Article 25fa of the Dutch Copyright Act, indicated by the "Taverne" license above, please follow below link for the End User Agreement:

www.tue.nl/taverne

Take down policy

If you believe that this document breaches copyright please contact us at:

openaccess@tue.nl

providing details and we will investigate your claim.

Supramolecular charge transfer systems

PROEFSCHRIFT

ter verkrijging van de graad van doctor aan de Technische Universiteit Eindhoven,
op gezag van de rector magnificus prof.dr.ir. F.P.T. Baaijens,
voor een commissie aangewezen door het College voor Promoties,
in het openbaar te verdedigen op maandag 21 juni 2021 om 16:00 uur

door

Andreas Thomas Rösch

geboren te Wertheim, Duitsland

Dit proefschrift is goedgekeurd door de promotoren en de samenstelling van de promotiecommissie is als volgt:

voorzitter: prof.dr. F. Gallucci
1^e promotor: prof.dr. E.W. Meijer
copromotor: prof.dr.ir. A.R.A. Palmans
leden: prof.dr. S. De Feyter (KU Leuven)
prof.dr. H.-W. Schmidt (University of Bayreuth)
prof.dr. Ž. Tomović
dr. S.C.J. Meskers
adviseur: dr. G.M.E. Vantomme

Het onderzoek of onderwerp dat in dit proefschrift wordt beschreven is uitgevoerd in overeenstemming met de TU/e Gedragscode voor Wetenschapsbeoefening.

Cover design: Andreas Rösch

Printed on recycled paper by: Gildeprint – the Netherlands

A catalogue record is available from the Eindhoven University of Technology Library

ISBN: 978-90-386-5287-0

This work has been supported financially by the Dutch Ministry of Education, Culture and Science (Gravity program 024.001.035).

Table of contents

Chapter 1

Intra- and intermolecular charge transfer in organic materials

1.1 Introduction	2
1.2 Intramolecular charge transfer	3
1.2.1 General remarks on organic dyes and color theory	3
1.2.2 Photophysical processes in (photo-)excited D- π -A dyes	4
1.2.3 Twisted ICT (TICT) and planar ICT (PICT)	6
1.2.4 Impact of the solvent polarity on the fluorescence properties of D- π -A dyes	7
1.2.5 Enhanced reactivity in the excited-state	8
1.2.6 Aggregation-induced emission	8
1.2.7 Design principles of D- π -A systems for sensing applications and organic electronics	10
1.2.7.1 Fluorescent probes based on D- π -A dyes	10
1.2.7.2 Sensors for chemical species based on D- π -A dyes	11
1.2.7.3 Dye-sensitized solar cells	12
1.2.7.4 Bulk heterojunction solar cells	13
1.2.7.5 Organic light emitting diodes	14
1.2.7.6 Spintronic applications	14
1.3 Intermolecular charge transfer complexation between electron donor and electron acceptor chromophores	15
1.3.1 Milestones in research on CT complexes	15
1.3.2 CT complex formation in solution	16
1.3.3 Liquid crystalline CT complexes	18
1.3.4 Crystalline CT complex between pyrene and NDI chromophores	19
1.4 Surface patterning using electron donor-electron acceptor systems	20
1.4.1 Imaging D and A moieties on HOPG surface using scanning tunneling microscopy	21
1.4.2 Co-assembly of hexabenzocoronenes and perylene diimide in plane	22
1.4.3 Co-adsorption of alkoxy-pyrene on top of NDI lamellae	24
1.5 Aim and outline of the thesis	25
1.6 References	26

Chapter 2

Synthesis and characterization of novel chiral squaraine dyes

2.1 Introduction	34
2.2 Synthesis and characterization of novel squaraine dyes	38
2.2.1 Nucleophilic reagents as a prerequisite for squaraine dye formation	38

2.2.2 Synthesis and characterization of <i>para-N,N</i> -dimethylamino substituted squaraine dyes a-SQ-1 , S-SQ-1 and u-SQ-1	39
2.2.3 Rotational isomerism of squaraine dye a-SQ-1	43
2.2.4 Synthesis and characterization of <i>para</i> -hydroxy substituted squaraine dyes a-SQ-2 and S-SQ-2	48
2.2.5 Chemical stability of <i>p</i> -hydroxy substituted squaraine dyes a-SQ-2 and S-SQ-2 ...	51
2.2.6 Synthesis and characterization of oDMS-functionalized <i>para-N,N</i> -dimethylamino substituted squaraine dyes	52
2.3 Conclusions	55
2.4 Experimental Section	56
2.4.1 Materials and Methods	56
2.4.2 Synthetic procedures.....	56
2.4.3 Calculation of the activation energy barriers according to Shanani-Atidi.....	65
2.4.4 Density function theory.....	66
2.5 References	67

Chapter 3

Helicity control in the aggregation of achiral squaraine dyes in solution and thin films

3.1 Introduction	72
3.1.1 Mesomerism and pH dependent optical properties	72
3.1.2 Formation of H- and J-type aggregates	73
3.1.3 Emission of fluorescence in the molecularly dissolved and aggregated state	74
3.1.4 Chiral squaraine dyes	75
3.2 Photophysical properties in the molecularly dissolved state	77
3.3 Formation of CD active aggregates of a-SQ-1 and S-SQ-1 in aqueous solution	83
3.4 Formation of CD active aggregates of a-SQ-1 and S-SQ-1 in thin film.....	86
3.5 Aggregation of the siloxane-appended squaraine dyes	92
3.6 Cyclic voltammetry (CV).....	93
3.7 Organic field effect transistors (OFET).....	95
3.8 Investigation of spin-filtering properties by magnetic-conductive atomic force microscopy.....	96
3.9 Conclusions.....	98
3.10 Experimental Section	99
3.10.1 Optical measurements	99
3.10.2 Investigation of thin film morphology and spin-filtering properties.....	100
3.10.3 Determination of the Huang-Rhys parameter <i>S</i>	100
3.10.4 Cyclic voltammetry	101
3.10.5 Organic field effect transistors	101
3.11 References	101

Chapter 4

Towards novel graphitic carbon nitrides: a supramolecular approach

4.1 Introduction	106
4.2 Synthesis of supramolecular building blocks containing the <i>s</i> -heptazine motif.....	107
4.2.1 Synthesis of <i>s</i> -heptazine tribenzoic acid 5	107
4.2.2 Synthesis of amide functionalized <i>s</i> -heptazines.....	108
4.3 Characterization in the solid state	109
4.3.1 Fourier-transform infrared spectroscopy.....	109
4.3.2 Thermal properties of amide functionalized <i>s</i> -heptazines AHA and UAHA	110
4.4 Assessing the formation of CD active aggregates by AHA and UAHA in solution and in thin film.....	111
4.5 Investigating the thermal stability of the morphologies of thin films and the impact of heating on optical properties	114
4.6 Conclusions and outlook.....	117
4.7 Experimental Section	118
4.7.1 Materials and Methods	118
4.7.2 Synthetic procedures.....	118
4.8 References	121

Chapter 5

Tuning the pitch of *N,N'*-bis(*n*-alkyl)-naphthalenediimide double lamellae in 2D and 3D

5.1 Introduction	126
5.2 Synthesis and characterization of <i>N,N'</i> -bis(<i>n</i> -alkyl)-naphthalene-diimides.....	129
5.3 Optical properties of the NDIs	130
5.4 Physisorbed self-assembled monolayers formed at the solution/HOPG interface	132
5.4.1 Structural details of the monolayers formed within the series of homologues ..	132
5.4.2 Structural details at the boundaries of the domains.....	136
5.4.3 Transformation of the collinear to the non-collinear regime	137
5.4.4 Formation of very large domains by flow-deposition	138
5.5 Thermal properties of all NDIs.....	138
5.6 Morphologies observed by X-ray scattering in bulk	142
5.7 Comparison of the morphologies formed on surface and in bulk.....	146
5.8 Conclusions	148
5.9 Experimental Section	149
5.9.1 Materials and Methods	149
5.9.2 Synthetic procedures.....	150
5.10 References	152

Chapter 6

Stepwise formation of charge transfer complexes at the 1-phenyloctane/HOPG interface	
6.1 Introduction	156
6.2 Synthesis and characterization of pyrene and naphthalene-based compounds.....	158
6.3 Physisorbed self-assembled monolayers formed by double pyrenes at the solution/HOPG interface	159
6.4 Physisorbed self-assembled monolayers formed in D-A mixtures of double pyrene and double NDIs at the solution/HOPG interface	160
6.4.1 New surface structures formed by D-A co-adsorption.....	162
6.4.2 Structural details of laterally co-adsorbed PyO-C6-OPy and NDI-C8-NDI	164
6.4.3 Structural details of vertically co-adsorbed PyO-C9-OPy and NDI-C5-NDI.....	165
6.4.4 Discussion on the new surface morphologies formed by D-A co-adsorption	166
6.5 Co-assembly of pyrene-NDI mixtures in bulk material	168
6.5.1 Optical properties of pyrene-NDI mixtures	168
6.5.2 X-Ray scattering profiles of pyrene-NDI mixtures	169
6.6 Conclusions	173
6.7 Experimental Section	174
6.7.1 Materials and Methods	174
6.7.2 Synthetic procedures.....	174
6.8 References	179
Summary	181
Some general conclusions and future perspectives	183
Curriculum Vitae	184
List of Publications	185
Acknowledgements	186

Chapter 1

Intra- and intermolecular charge transfer in organic materials

Abstract:

Colorful organic materials have fascinated scientists already for more than 200 years. The intense colors stem from an optical transition that induces the transfer of electronic charge from an electron-rich donor moiety (D) to an electron-poor acceptor moiety (A). Charge-transfer (CT) can occur either intramolecularly (ICT) when D and A are connected covalently by a π -conjugated bridge or intermolecularly when an adduct between D and A moieties, the so-called CT complex, is formed. Whereas research on ICT systems has produced a plethora of functional dyes for various (opto-)electronic applications, the formation of CT complexes has been used for the preparation of many supramolecular systems in the solution or the bulk phase which have been proposed for a variety of applications, too. However, the directed formation of CT complexes on surfaces remains a pressing research question in the field of nanotechnology and its achievement is expected to innovate microelectronics. This introductory chapter summarizes the progress of research on both intra- and intermolecular CT systems and presents the reported structure-property relationships to spark research on developing the next generation of CT materials for surface applications.

1.1 Introduction

Humankind has been using paints for already more than 40000 years to convey messages and to preserve cultural heritage. Whereas the dyes that were used initially were natural products, technological advances provided access to synthetic colorants such as the azo dyes^[1-4] which revolutionized the use of colors in everyday life. Today, the color of a dye molecule can be characterized by ultraviolet-visible (UV/Vis) spectroscopy. In combination with the determination of the chemical structure and quantum chemical theory, structure-property relationships of organic colorants have been investigated quantitatively.^[5]

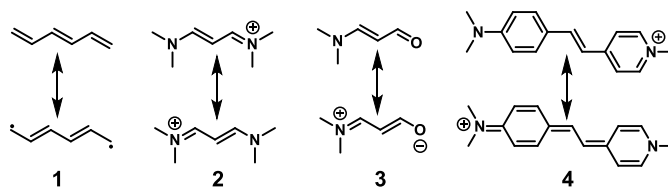
An important class of colorants is given by organic materials that exhibit charge transfer (CT).^[5-11] Prominent examples for compounds that exhibit intramolecular CT (ICT) are push-pull dyes.^[12-18] Owing to their synthetic accessibility, tunable photophysical properties and their high extinction coefficients, a variety of these organic dyes has already been in commercial use for more than a century.^[19] Today, the molecular design principles for the synthesis of organic compounds that exhibit ICT are well-known and were used for the preparation of a plethora of functional dyes with a large variety of (opto-)electronic applications.^[20-31] Intermolecular CT occurs when D and A moieties of two different molecules form an adduct, the co-called CT complex. Since CT complex formation is accompanied by the formation of an intense color,^[32] the process has already been reported more than 200 years ago.^[8,33,34] The corresponding study described the formation of an intense blue color after the addition of iodine to an aqueous solution of starch. However, an explanation of the observed phenomenon was possible only much later.^[8,33,34] Once the structural requirements for forming a CT complex were better understood, research on CT complexes resulted in the development of organic materials that were electrically conducting, too.^[35,36] As a result, the development of modern CT materials with applications in organic electronics was initiated.^[37,38] In contrast to the preparation of functional dyes that exhibit ICT and solution or bulk systems which contain CT complexes, the preparation of structured surfaces containing a regular arrangement of CT complexes is just at its beginning.^[39,40]

In the introductory chapter of this thesis, the photophysical processes of ICT species are presented and the corresponding structure-property relationships as well as optoelectronic applications are discussed. Next, examples for systems that involve the formation of CT complexes in solutions, in the liquid crystalline state and in the solid state are shown. Finally, D-A systems are highlighted which have been used in literature to generate patterned surfaces with alternating D and A moieties.

1.2 Intramolecular charge transfer

1.2.1 General remarks on organic dyes and color theory

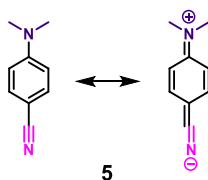
The first report on the relationship between the color and the molecular structure of a chemical compound was submitted by Graebe and Liebermann^[41] already in 1868. The scientists found that the color of an organic molecule is related to the presence of unsaturated bonds. Hereafter, Witt^[42] developed the “classical theory of color” which ascribed the color of an organic molecule to the presence of functional groups that he termed “chromophores”. The original theory suggested that the chromophores were constituted by N=O, N=N, C=C and C=O groups and typically required the presence of a so-called “auxochromic group” such as the -NH₂ or -OH group to develop a color that was observable by eye. The theory was later refined by other researchers who suggested to label the functional groups with a color brightening effect such as the N=O and C=O groups as “anti-auxochromic groups”.^[43,44] Finally, the consensus shifted and the visible color of an organic molecule was not assigned to the presence of individual chromophores anymore but considered to emerge from the presence of a larger conjugated system.^[45,46] König^[47] reported on molecules containing an odd number of methine or heteroanalogous groups (“mesochrome”) and terminal groups (“perichromes”). He assigned the color of these linear molecules, the so-called polymethine chromophores to the formation of a “chromostate” which described a conjugated state that is marked by a high degree of bond equalization and charge alternation.^[5] As already suggested by Witt,^[42] C=C group containing molecules do not necessarily exhibit intense colors when no auxochromic groups are present. The formation of the intense colors after the addition of the auxochromic groups is due to the stabilization of the resonance structure with the opposing both length alternation. As noticed in Scheme 1.1, this second mesomeric form is unfavored for a polyene such as **1** that does not contain auxochromic groups since this second mesomeric form contains two terminal radical species. The second type of mesomeric structure becomes energetically favorable when auxochromic groups are added as exemplarily shown for cyanine **2**, merocyanine **3** or hemicyanine dyes **4** since no radical species are formed.^[15–17]



Scheme 1.1: Mesomeric forms for hexatriene **1**, cyanine **2**, merocyanine **3** or hemicyanine dyes **4**.^[15–17]

1.2.2 Photophysical processes in (photo-)excited D- π -A dyes

Whereas the above-mentioned studies clearly identified the necessity of a π -conjugated system to develop visible colors in organic materials, only quantum chemistry could attribute the color formation to the absorption of light of a particular wavelength. Furthermore, the intensity of the observed color could be ascribed to the transition probability and the shapes of the absorption bands to molecular vibrations.^[5] One class of dyes that is particularly interesting owing to typically strong adsorption of light in the visible region and the possibility to emit two individual bands of fluorescence are D- π -A dyes.^[48–52] The first D- π -A dye that has been described to exhibit “dual emission” after photoexcitation is 4-(dimethylamino)benzonitrile **5** (“normal” and quinoid mesomeric forms of the compounds are shown in Scheme 1.2).^[48]



Scheme 1.2: Molecular structure and mesomerism of 4-(dimethylamino)benzonitrile **5**.^[48] The D moiety is highlighted in purple, the A moiety in magenta.

Photoexcitation of a D- π -A dye is accompanied by the redistribution of electronic charge. Thereby an alternation of the molecule’s dipole moment is induced which has already been anticipated by Förster^[49,53] in 1939. His study described the structures of a polar compound in the ground state by the wavefunction Ψ_g and in the excited state by the wavefunction Ψ_e . These wavefunctions were obtained by the superposition of the wavefunction of the “normal” structure Ψ_N and the quinoid structure Ψ_Q .^[49]

$$\Psi_g = c_N \Psi_N + c_Q \Psi_Q \text{ and } \Psi_e = c_Q \Psi_N - c_N \Psi_Q \quad (\text{a})$$

When investigating the photophysical properties of D- π -A dye **5** experimentally, it was found that the emission band noticed at the blue end of the emission spectrum occurred predominately in apolar solvents. The band at the red end that was noticed in polar solvents was indicative of the formation of two species with different dipole moments. To explain the photophysical processes in D- π -A dyes in more detail, the potential energy surfaces of the ground and excited states are depicted schematically in Figure 1.1. Photoexcitation from the ground state S_0 to the second excited state S_2 is followed by relaxation via internal conversion to the equilibrated S_1 locally excited (LE) state. By overcoming the reaction barrier E_a , charge can be transferred intramolecularly and the energetically more favorable ICT state is reached. As suggested by experimental evidence and theoretical calculations, the electronic and geometrical structure of the ICT state is often described as twisted with respect to the ground state (when the rigidity of the molecular skeleton is not too high).^[54,55] The emission of fluorescence can occur both from the LE and the ICT states and is

accompanied by the relaxation to the corresponding Franck-Condon states $E(\text{FC}, \text{LE})$ and $E(\text{FC}, \text{ICT})$ located in the ground state S_0 . Since the wavelength of the emitted light depends on the energy differences between the LE or the ICT state and each corresponding Franck-Condon state, the emission of light with two different wavelengths is noticed.^[56] We note that besides the photo-induced emission of fluorescence, also electrochemically generated chemiluminescence has been described for D- π -A dyes.^[57,58]

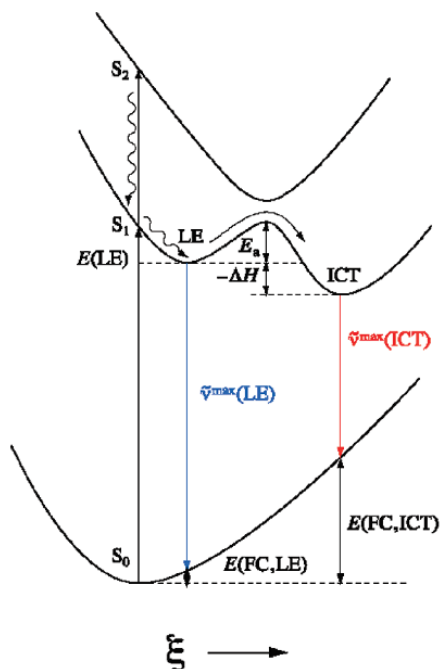


Figure 1.1: Potential energy surfaces for the ground state S_0 and the excited states S_1 , S_2 including the LE and ICT states. The vertical coordinate represents the energy and the horizontal coordinate ξ describes the changes in molecular geometry such as bond length and binding angles during the photophysical processes. Figure reproduced with permission from reference [56] (copyright 2010 American Chemical Society).

1.2.3 Twisted ICT (TICT) and planar ICT (PICT)

The electronic and the geometrical structures of the ICT state result from the competition of the LE state and the electron transfer (ET) state in the first excited state of the molecule (the ET state describes the full transfer of the charge from D to A).^[59] Both states are distinguished by the electronic structures of their highest occupied molecular orbitals (HOMOs) and lowest unoccupied molecular orbitals (LUMOs).^[60] The geometrical structures of these two states are still an important point of discussion in the literature.

According to one hypothesis, a twisted ICT (TICT) state is formed. The LE state is represented by the co-planar arrangement of D and A moieties which results in mesomeric interactions between the two π -subsystems (ψ_1 and ψ_2). As a result, the HOMO level is increased in energy and the LUMO level is decreased which makes the orbital overlap overall energetically favorable (Figure 1.2a top). In contrast, the ET state is energetically more favorable in the absence of frontier orbital interactions (Figure 1.2a bottom) which is achieved for a perpendicular orientation of the π -subsystems.^[49] Without frontier orbital overlap, the relative energy level of the ET state can be approximated as the difference between the electron affinity (EA) of A and the ionization potential (IP) of D. As a result, the ET state is stabilized best by strong D and strong A moieties.^[60] The energy landscape of the ICT state is obtained by mixing LE and ET states (Figure 1.2b).

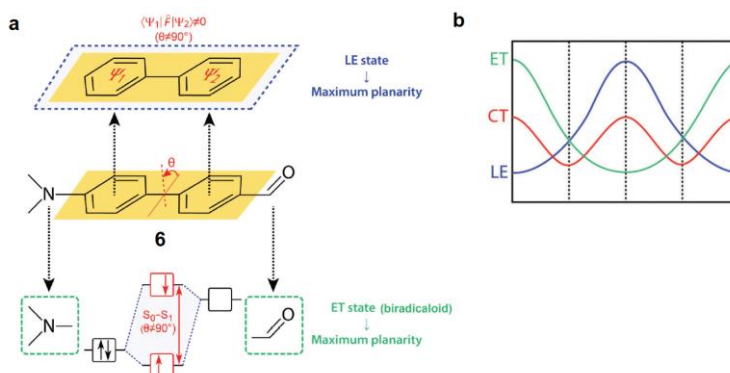


Figure 1.2: (a) Photoexcitation of 4'-(dimethylamino)-[1,1'-biphenyl]-4-carbaldehyde **6**: top: The co-planar LE state is stabilized by mesomeric interactions of the π -subsystems (ψ_1 and ψ_2). bottom: The ET state favors zero overlap between the frontier orbitals which is achieved by the perpendicular orientation of the D and A moieties. (b) Schematic representation of the energy landscape of the ICT state as obtained by mixing LE and ET states. Images adapted with permission from reference [60] (copyright 2016 Royal Society of Chemistry).

The most important observation that led to postulating TICT was that steric effects typically have a strong impact on the emissive properties of D- π -A dyes. For example, fixing the free electron pair of the amino group of 4-(dimethylamino)benzonitrile chemically in plane (compound **7** in Figure 1.3) resulted in observing the emission band at the shorter wavelength only. In contrast, a hindered rotation (compound **8** in Figure 1.3) or fixation of the free electron pair perpendicular to the phenyl ring (compound **9** in Figure 1.3) resulted in emitting exclusively the fluorescence band with the longer wavelength.^[61,62]

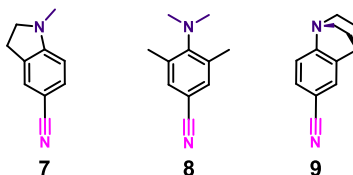


Figure 1.3: Derivatives of 4-(dimethylamino)benzonitrile investigated upon steric effects on the fluorescence properties in D- π -A dyes. **7**: D and A moieties are structurally fixed in a nearly coplanar orientation; **8**: Hindered rotation; **9**: Fixation in a nearly perpendicular orientation.^[61,62]

Since the expected conformations of these compounds were however not determined experimentally, also planar ICT (PICT) was proposed which suggested that the formation of the ICT state does not require a twisted molecular backbone, but depends solely on the energy landscape of the first excited state.^[63] PICT was also confirmed by X-ray diffraction which could show that a 4-(dimethylamino)benzonitrile derivative was able to form an equilibrated ICT state without adopting a twisted conformation. The recorded X-ray data showed that the twisting angle between amino group and benzene ring was even decreased from 14° to 10° upon the formation of the ICT state.^[64] Further arguments for PICT are given by the fluorescence properties of *meta*-substituted (dimethylamino)benzonitriles which have considerably higher twisting angles than their *para*-substituted counterparts but nevertheless favor the emission from the LE state.^[65]

1.2.4 Impact of the solvent polarity on the fluorescence properties of D- π -A dyes

In the absence of steric effects, the relative proportions of the intensities of the two emission bands of D- π -A dyes and λ_{\max} of the emission band of the ICT state depend strongly on the polarity of the solvent. When the polarity of the solvent is increased, the fluorescence intensity of the ICT state is typically increased, too and its λ_{\max} undergoes a red-shift. Spectroscopic studies showed that for many D- π -A dyes, λ_{\max} of the emission band of the ICT state depends approximately linearly on the solvent polarity. Consequently, the effect of the solvent polarity on the emissive properties is typically non-specific.^[66,67] The fluorosolvatochromism of D- π -A dyes was assigned to the difference of the dipole moments in the S_1 and S_0 state. Typically, the ICT state is more polar than the ground state and becomes more stabilized when the polarity of the solvent is increased. As a result, the energy difference between the ICT state and the corresponding Frank-Condon ground state

becomes smaller when the polarity of the solvent is increased and a red-shift of λ_{\max} of the emission band of the ICT state is observed. To quantify the effect of the solvent polarity on the fluorescence spectra and to calculate the dipole moment of the excited state, the Lippert-Mataga equation^[52,68] was developed which was later followed by the Bakhshiev,^[69] Bilot-Kawski^[70] and Chamma-Viallet models.^[71,72] In case of some dyes, a non-linear relationship between solvent polarity and λ_{\max} of the emission band of the ICT state was found. These exceptions typically occurred when the dyes formed hydrogen bonds to strongly hydrogen-bonding protic solvents such as alcohols or water and indicated a specific interaction with the solvent.^[73,74] Calculating the dipole moments of derivatives of 4-(dimethylamino)benzonitrile in the excited state by using the data obtained via optical measurements^[74–76] resulted in similar values as determined by other techniques such as electrooptical emission measurements,^[77] thermochromism^[78] or time-resolved microwave-conductivity.^[49,79] Also in agreement with theoretical calculations, a full separation of the charges was suggested for the ICT state. Since the determined dipole moments did not depend on the polarity of the solvent, it was concluded that polarizability effects do commonly not play an important role for the electronic structure of the ICT state.^[49]

1.2.5 Enhanced reactivity in the excited-state

Owing to the redistribution of electronic charge during photoexcitation, properties such as acidity and basicity are changed, too. As a result, molecules are typically more reactive towards reducing and oxidizing agents in their electronically excited states than in their ground state (schematically shown in Figure 1.4) since these type of reactions are typically very fast and compete with the relaxation processes.^[49]

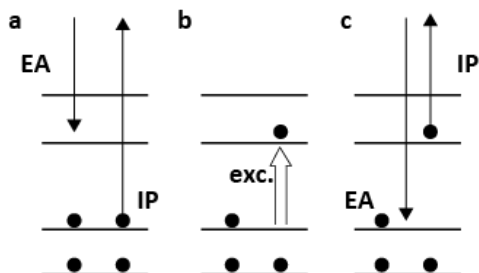


Figure 1.4: Schematic illustration of the electron affinity (EA) and the ionization potential (IP) of a molecule before and after photoexcitation (exc.). (a) ground state, (b) photoexcitation, (c) excited state. Figure adapted with permission from reference [49] (copyright 2003 American Chemical Society).

1.2.6 Aggregation-induced emission

Since intramolecular motions are the key factor for the fluorescence properties of many D- π -A dyes, this class of compounds has also been used to develop aggregation-induced emission (AIE) luminogens.^[9,80–82] AIE luminogens are typically only weakly fluorescent in

the molecularly dissolved state.^[83] Upon aggregation in a poor solvent or in the solid state, intramolecular motions are restricted and the compounds become highly fluorescent.^[83–85] Molecular structures of D- π -A-based AIE luminogens are shown in Figure 1.5.

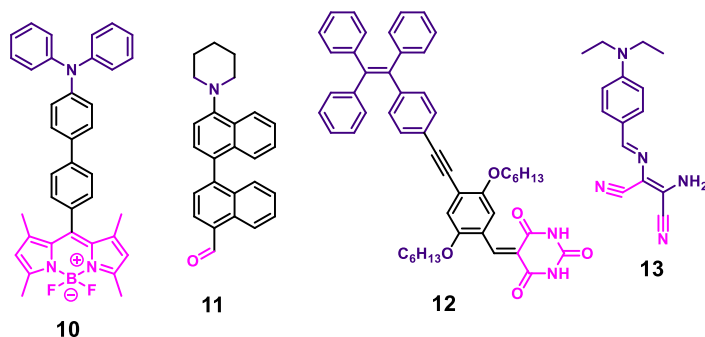


Figure 1.5: Molecular structures of AIE luminogens based on the BODIPY **10**^[80] and binaphthyl **11** structures^[81] as well as the barbituric acid functionalized tetraphenyl-ethene **12**^[82] and the diamino-maleonitrile functionalized Schiff base **13**.^[9]

Several AIE luminogens that contain strong D and A moieties have been described to change their fluorescence properties upon applying an external stimulus.^[9,86] **13** exhibited fluorosolvatochromism in the molecular dissolved state which indicated the pronounced formation of a twisted ICT state upon increasing the polarity of the solvent. The formation of fluorescent aggregates in solution was induced by the addition of water as poor solvent. Interestingly, the fluorescence intensity of the aggregates decreased when the volume fraction of water was higher than 80%. A time-dependent experiment showed that the large volume fraction of water in the solvent mixture resulted in the formation of larger crystals. A combined spectroscopic and electron microscopic study showed that the fluorescence intensity emitted by the crystals depended on their size which in turn suggested that the emission occurred predominately at surface defects. The hypothesis was confirmed by noticing an increased fluorescence after etching large crystals with acetone (Figure 1.6a-c). Owing to this structure-property relationship, the crystals of the compound could also be used as mechanofluorochromic material (Figure 1.6d-f) for detecting shear-forces. The corresponding detection limit was 1 N.^[9]

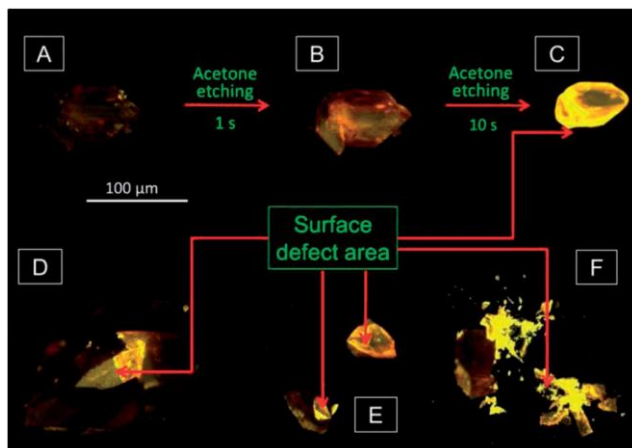


Figure 1.6: Emission of fluorescence by differently treated crystals of **13**. (a) untreated, (b) etched with acetone for 1 s, (c) etched with acetone for 10 s, (d and e) pressed with spatula and (f) crushed by mechanical force. Figure reproduced with permission from reference [9] (copyright 2013 Royal Society of Chemistry).

1.2.7 Design principles of D- π -A systems for sensing applications and organic electronics

Today, D- π -A dyes are widely applied as fluorescent probes,^[6,12,87–98] in dye-sensitized solar cells (DSSCs),^[99–103] bulk heterojunction solar cells (BHJ-OSCs),^[104–115] organic light emitting devices (OLEDs)^[26,116–125] and nonlinear optical materials.^[29,30] The functionality of the compounds stems from photophysical properties such as the absorption of light and the emissive behavior which both can be tuned by chemical modification of the molecular structure.^[13,126]

1.2.7.1 Fluorescent probes based on D- π -A dyes

The relationship between the emission properties of one specific D- π -A dye and the polarity of the solvent depends on the chemical structure of the dye. Sunahara *et al.*^[6] exploited this relationship to prepare a library of boron-dipyrromethene (BODIPY)-based compounds **14** and **15** (Figure 1.7) with application as polarity sensors. When a certain threshold of the environmental polarity was reached, the fluorescent LE states of the dyes were converted into non-emissive ICT states. Using the library of compounds, the polarity of the surface of bovine serum albumin (BSA) and the internal membranes of HeLa cells could be estimated.^[6]

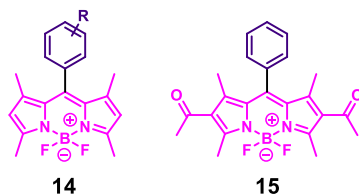


Figure 1.7: Molecular structures of the BODIPYs **14** and **15** described by Sunahara et al.^[6] The chosen residues *R* attached to the aromatic unit (which were naphthalene or anthracene units for several derivatives) were methyl, methoxy, phenyl or amino groups. The type of donor moiety influenced the relationship between the emission of fluorescence and the polarity of the solvent.^[6]

In addition to its polarity, the viscosity of the medium has an influence on the emissive properties of certain D- π -A dyes, too. This type of structure-property relationship has been used to perform fluorescence imaging of the microenvironmental viscosity. The used class of D- π -A fluorophores is called “molecular rotors” since their fluorescence intensity is enhanced in sterically restricted environments such as viscous media which prevent the twisting of the molecule and the formation of the ICT state.^[91,92] Examples for this type of fluorophores is depicted in Figure 1.8. Derivatives of 9-(2-carboxy-2-cyanovinyl)julolidine **16** have been used to image amyloid deposition^[93] as well as to investigate the relaxation of polymer glasses at interfaces,^[94] contact mechanics,^[95] and fluid dynamics.^[96] Thioflavin-T7 **17** has been used in drug discovery assays to study amyloid-related neurodegenerative diseases.^[97]

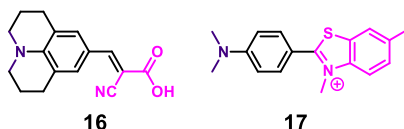
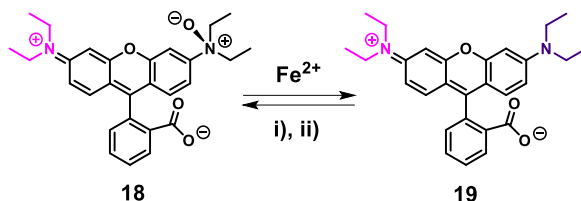


Figure 1.8: Chemical structures of 9-(2-carboxy-2-cyanovinyl)julolidine **16** and thioflavin-T7 **17** applied as fluorophores with viscosity-dependent emission properties.^[97]

1.2.7.2 Sensors for chemical species based on D- π -A dyes

Besides the mentioned applications as polarity probes, D- π -A dyes have also been used to detect chemical species. RhoNox-1 **18** (Scheme 1.3) prefers a twisted conformation that favors the only weakly fluorescent ICT state over the strongly fluorescent LE state.^[98] In the presence of Fe²⁺-ions, the *N*-oxide moiety is selectively reduced and highly fluorescent Rhodamine B **19** is formed in situ.^[98] Other examples for such fluorescent sensors include D- π -A based dyes for the detection of cyanide,^[87] hydrazine^[88,89] or alkaline-earth-metal ions.^[90,127]



Scheme 1.3: Weakly fluorescent RhoNox-1 **18** is transformed to highly fluorescent Rhodamine B **19** in the presence of Fe²⁺-ions. **18** is regenerated by i) neutralizing **19** with NaOH and ii) subsequent the oxygenation using meta-chloroperbenzoic acid.^[98]

1.2.7.3 Dye-sensitized solar cells

The generation of electrical current in a Dye-sensitized solar cell (DSSC) is initiated by the absorption of light by a dye that is adsorbed on the TiO₂-photoanode.^[99,100,128] The excited electron is injected into the conduction band of the TiO₂ and transported to the back contact. This electron transfer oxidizes the dye. The dye is subsequently reduced by a redox mediator, typically I⁻.^[129] The regeneration of the redox mediator by electrochemical reduction at the counter electrode results in the generation of voltage and electrical current.^[99,100,128,129] Owing to the strong absorption of light in the visible region and the typically reversible oxidation and reduction, D- π -A dyes are an excellent choice as sensitizers for DSSCs.^[18,28,101–103] A recent study by Zhu *et al.*^[102] highlighted how the chemical structure of a D- π -A dye is responsible for photophysical properties and its optimization can be used to improve the efficiency of a DSSC. The molecular structures of the reported dyes both contained the electron-rich indoline and the electron-poor 2-cyano-2-propenoic acid moiety but differentiated in the type of π -conjugated bridge (Figure 1.9). **20** contained a bithiophene as π -conjugated bridge. For the synthesis of **21**, an additional benzothiadiazole (BT) unit was implemented. The presence of the BT unit resulted in a red-shift of λ_{\max} in the absorption spectrum. Although this red-shift indicated a decreased optical band gap, a higher photo-voltage and increased efficiency of the DSSC was measured when using **21** as sensitizer. This observation was particularly intriguing since a decreased optical band gap typically decreases the photo-voltage in DSSCs. The increased device efficiency was ascribed to an increased potential of the conduction band and a suppressed charge recombination.^[102]

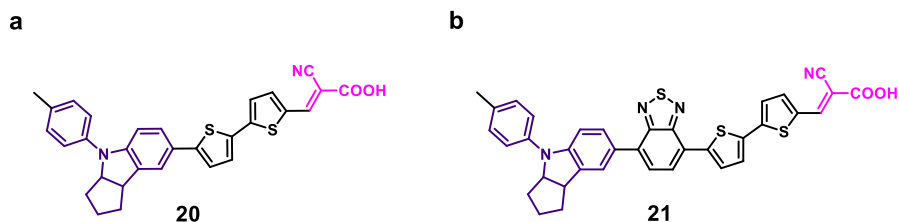


Figure 1.9: Dithiophene-bridged indoline—2-cyano-2-propenoic acid-based dyes **20** and **21** reported by Zhu *et al.*^[102] The D moiety of the D- π -A dye is highlighted in purple, the A moiety in magenta.

1.2.7.4 Bulk heterojunction solar cells

Besides optimizing the chemical structures of small molecules that are based on the D- π -A architecture, a plethora of studies investigated the consequences of increasing the number of D and A moieties in the π -conjugated system to prepare π -conjugated polymers.^[130–133] One particularly famous class of π -conjugated D-A polymers that absorb light with wavelengths longer than 620 nm (optical band gap $E_g^{\text{opt}} < 2$ eV) are the so-called low band gap polymers.^[104–106,108–115,134,135] The realization of such low band gaps was achieved by establishing an alternating sequence of electron-rich D and electron-poor A units in the polymer backbone.^[133] Since the solar spectrum has a high photon flux in the near infrared regime,^[109,136] semiconducting low band gap polymers are suitable for application in organic bulk heterojunction solar cells.^[105,108,109,137] In contrast to silicon-based photovoltaic devices that contain a p - n junction, the absorption of light in the organic semiconductor does not directly generate holes and electrons. Due to the rather low dielectric constants of organic materials, closely-bound electron-hole pairs, the so-called excitons, are formed instead.^[107] To improve the dissociation of the excitons into holes and electrons, modern metal-free organic solar cells are typically a composite material of a low band gap polymer and an additional electron acceptor such as fullerenes or perylene bisimides.^[107,138] Owing to differences in the electronic structures of both materials, the generated excitons migrate to the interface where the dissociation into holes and electrons is facilitated. Whereas the hole remains within the low band gap polymer and is transported to one electrode, the electron is transferred into the electron accepting compound and transported to the opposite electrode. The generation of electrical current by converting visible light makes these compounds fascinating examples for charge transfer materials.^[105,108,109,137]

1.2.7.5 Organic light emitting diodes

In contrast to photovoltaic applications, organic light emitting diodes (OLEDs) applied in display technology require organic semiconductors with reasonably large band gaps to emit light in the visible regime.^[26] Owing to the chemical modifiability of D- π -A systems,^[139] also a wide range of small molecules and conjugated polymers suitable for application in OLEDs has been reported.^[116,118–120,140–144] At this point, we want to highlight the D- π -A-polymers **22** and **c-22** (Figure 1.10) that are based on the dialkylfluorene-*alt*-benzothiadiazole repeating unit since these compounds are well-known for their application in illuminating devices^[145,146] which can also be used for the emission of circularly polarized light (CPL) with preferred handedness.^[121–123] In the reported studies, the emission of CPL with preferred handedness was achieved by creating chiral order by either blending **22** with chiral dopants^[116] or implementing the chiral side chains to obtain **c-22**.^[118] The fabrication of illuminating devices that exhibit CPL is of high interest for the display industry since it improves the contrast of the images that are shown on the screen. Currently, commercially used displays already enhance the contrast by CPL. However, CPL is achieved by circularly polarizing filters that completely block circularly polarized light of one handedness. As a result, half of the generated light is trapped inside the display and not used for illumination. Since the generation of CPL during the emission is suggested to make the polarizing filters obsolete, an improvement of the energy efficiency in CPL contrast-enhanced OLED displays is envisioned.^[116,118]

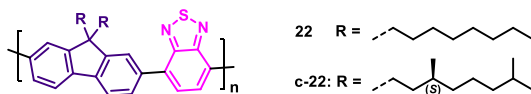


Figure 1.10: Molecular structure of **22** and **c-22**. CPL emitting devices were prepared by blending the achiral **22** with chiral dopants,^[116] or by using homochiral **c-22**.^[118] The fluorene D moiety is highlighted in purple, the benzothiadiazole A moiety in magenta.

1.2.7.6 Spintronic applications

Another prospective application for chiral D- π -A systems are organic spintronics.^[147] Research on organic spintronics focusses on an improved fundamental understanding of the role of chirality and the electron spin or electromagnetic fields in both chemical^[148,149] and biological systems.^[150–152] One of the first examples for organic spintronics is the use of a highly ordered chiral layer of double stranded deoxyribonucleic acid (ds-DNA) as a spin filter.^[153] The reported study showed that electrons that have a random orientation of the electron spin can be spin-polarized by the transmission through the highly ordered chiral layer of ds-DNA.^[153] The term spin-polarized means that the populations of spin-up and spin-down aligned electrons are not equal after the transmission through the chiral layer as illustrated schematically in Figure 1.11. The type of spin alignment that is favored is correlated with the handedness of the helicity of the layer. This type of electron spin manipulation has also been called chiral-induced spin selectivity (CISS) effect.^[154] Although

the spin polarization that has been measured in CISS based systems so far has never been absolute,^[155] various applications such as water-splitting in electrochemical cells similar to DSSCs,^[148,156–158] enantio-separation of racemates^[159,160] and enantioselective reactions^[161] have been realized.

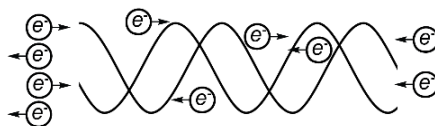


Figure 1.11: Schematic illustration of the CISS effect. Electrons with one type of spin alignment are transported preferably through a chiral helical environment. The spin-selective electron transport results in measuring a spin polarization of the electrons after the transmission. Figure adapted with permission from reference ^[154] (copyright 2012 American Chemical Society).

1.3 Intermolecular charge transfer complexation between electron donor and electron acceptor chromophores

Another important class of organic CT materials is given by CT complexes that are adducts between individual molecules. In contrast to ICT systems, the transfer of electronic charge in the CT complex occurs between the D moiety of one molecule to the A moiety of another molecule.^[162] Owing to the electronic properties which arise from the CT complex, CT materials often exhibit intense colors.^[32]

1.3.1 Milestones in research on CT complexes

One of the very early reports on CT complex formation dates back to the beginning of the 19th century and describes the development of an intense blue color when adding iodine to starch.^[8,33,34] Based on this finding, the use of starch as an indicator for iodine was established and the so-called starch-iodine test became a standard experiment in chemical education.^[163] Interestingly, the structure of the CT complex formed between the two components is a clathrate of polyiodide and amylose which was proposed only much later^[8] and still remains to be characterized fully.^[34] Very important findings of research on CT complexes were the development of the electrically conducting perylene–bromine^[35] and tetrathiafulvalene–7,7,8-tetracyano-quinodimethane^[36] (TTF–TCNQ) complexes of which the latter was found to behave like a metal over a wide temperature range. These findings have triggered a plethora of investigations that resulted in today's variety of supramolecular CT systems with potential applications in artificial photosystems,^[164] rotaxanes and catenanes,^[165] synthetic ion channels,^[166] liquid crystals,^[167] foldamers,^[168] polymers,^[169] nanoparticles,^[170] organo-^[171] and hydrogels^[172] of which we will present several examples in the following.

1.3.2 CT complex formation in solution

The association constants of CT complexes formed in solution have been determined experimentally by UV/Vis and NMR spectroscopy and in some cases by isothermal titration calorimetry.^[173–175] Since the association constants of CT complexes are usually low,^[176] CT complexes that are formed in solution often need to be stabilized by the formation of additional attractive forces such as hydrogen bonds,^[171,177,178] solvophobic forces^[179,180] or metal-ligand coordination.^[181] An exemplary system for the stabilization of CT complexes by hydrogen-bond formation is the co-assembly of the amide functionalized dialkoxynaphthalene (DAN) and *N,N'*-bis(*n*-alkyl)-naphthalenediimide (NDI) derivatives depicted in Figure 1.12.^[171,177,178] Studying compounds that contain the NDI motif are of particular interest owing to the combination of the NDI's strong tendency to form π -stacked aggregates and its *n*-type semiconductivity.^[182,183] DAN-NDI pairs with an equal distance between the two amide groups ($L_1 \approx L_2$) showed the formation of alternating D-A stacks that contained CT complexes.^[171,178] In the absence of the amide groups or in case of a mismatch of the distance between them ($L_1 \neq L_2$), no CT complex formation was observed.^[177] Interestingly, even equal distances between the amide groups in the D-A pair did not exclude the formation of self-sorted aggregates for some D-A combinations. The self-sorting was more pronounced after aging which corroborated the weak association constants of CT complexes (highest association constants reported for this system: 342 M^{-1} and 1300 M^{-1} in the solvent 1,1,2,2-tetrachloroethane).^[171,178]

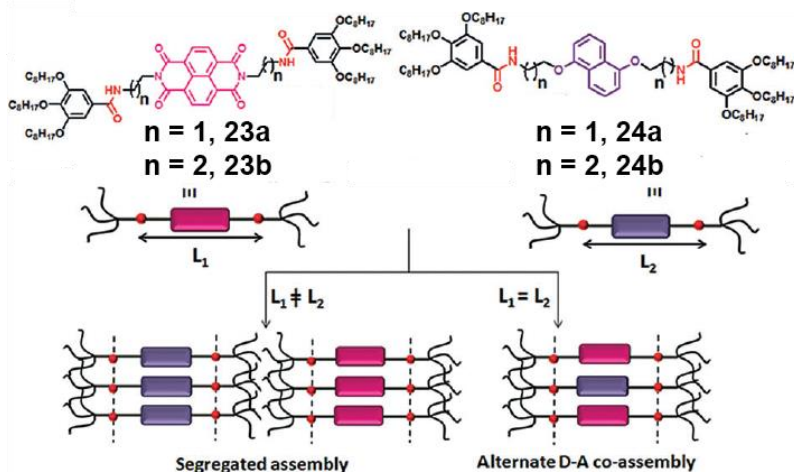


Figure 1.12: Supramolecular architectures based on co-assembled electron-poor NDI derivatives **23a** and **23b** and electron-rich dialkoxy-naphthalenes (DAN) **24a** and **24b**. The CT complexes formed in organic solvent were stabilized in solution by hydrogen bond formation.^[171,177,178] Image reproduced with permission from reference^[176] (copyright 2014 John Wiley & Sons, Inc.).

The system presented in Figure 1.13 is an example for aiding the formation of CT complexes in aqueous medium by solvophobic forces.^[179,180] Individually, the viologen functionalized DAN and NDI derivatives formed aggregates whose structures were dictated by the hydrophilicity of the charged head groups and the hydrophobicity of the molecules' centers. In aqueous medium, these structures had fibrillar and spherical micellar morphologies. In equimolar D-A mixtures, the formation of CT complexes and aggregate structures with fibrillar or sheet-like morphologies were observed. The change of the microstructure upon co-assembly was ascribed to the interplay of the attachment positions of the viologen substituents in both types of molecules and the rotational angle between D and A chromophores in the supramolecular stack.^[179,180]

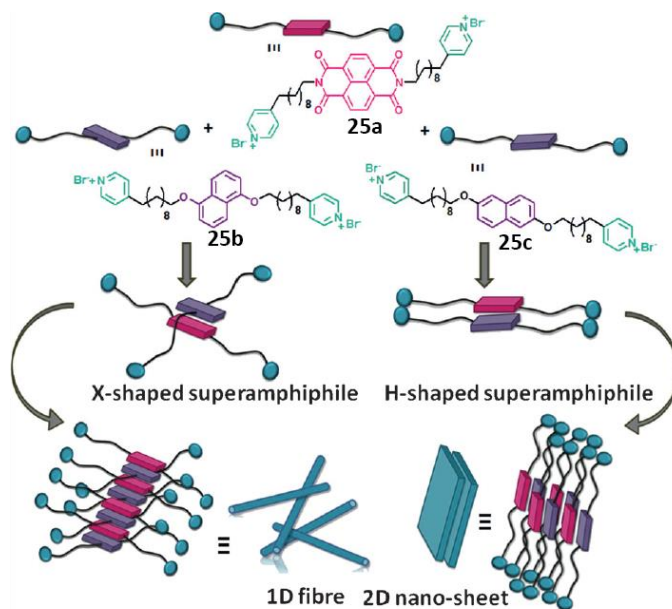


Figure 1.13: Supramolecular architectures based on co-assembled electron-poor NDI derivatives **25a** and electron-rich DAN **25b** and **25c**. The CT complexes were stabilized by an amphiphilic architecture.^[179,180] Image reproduced with permission from reference ^[176] (copyright 2014 John Wiley & Sons, Inc.).

In addition to the systems that predominantly exhibit an alternating arrangement of D and A chromophores, the formation of block-like supramolecular polymeric architectures has been reported, too.^[184] The co-assembly of π -conjugated *O*-bridged triphenylborane and triphenylamines (molecular structures in Figure 1.14) was already noticed by eye under UV-illumination since the D-A mixture emitted light of a different color than the individual compounds did. However, a detailed spectroscopic and theoretical study was required to develop a molecular picture of the prepared supramolecular copolymers. The spectral changes in the fluorescence spectrum suggested the formation of excited state complexes

(exciplexes) between the electron-rich and electron-poor compounds. The formation of the hetero-adducts was corroborated by emission lifetime measurements. Since the absorption and CD spectra of the supramolecular copolymer resembled the linear combination of the spectra recorded for the individual species, a block-like microstructure was suggested. Theoretical calculations and the transfer of helicity from the chiral *O*-bridged triphenylborane **S-26** to the achiral triphenylamine **a-28** corroborated the hypothesized blocky microstructure.^[184]

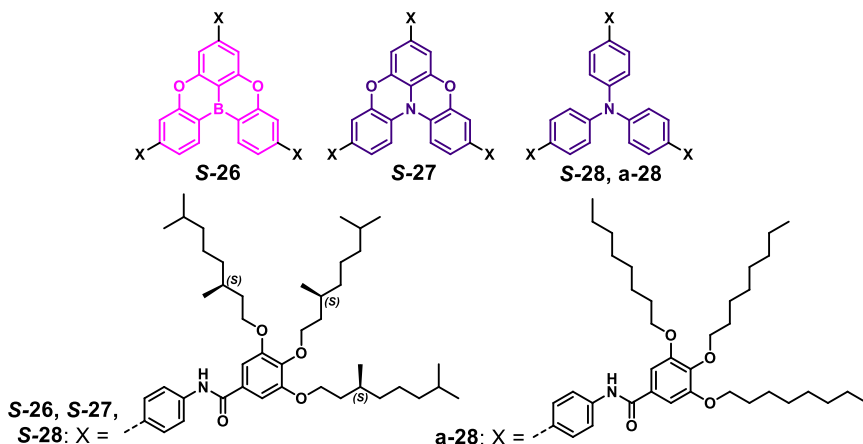


Figure 1.14: Molecular structures of *O*-bridged triphenylborane **S-26** and triphenylamines **S-27**, **S-28** and **a-28** used to prepare supramolecular polymers with a blocky microstructure.^[184]

1.3.3 Liquid crystalline CT complexes

Lee et al.^[185] prepared liquid crystalline dyad and triad molecules **29** and **30** that contained the electron-rich triphenylene and electron-poor perylene-3,9,10,10-tetracarboxylic diimide (PDI) moieties (Figure 1.15). Supramolecular organization of the compounds in thin films resulted in the formation of liquid crystalline materials. The dyad formed a hexagonal liquid crystalline mesophase and the triad a columnar oblique liquid crystalline mesophase. The compounds were coated on top of multilayered photonic metamaterials that consisted of alternating Ag and Al₂O₃ layers with 10 nm thickness. Measuring the charge recombination in time-dependent experiments showed that an increasing number of Ag and Al₂O₃ layers in the metamaterial decelerated the charge recombination in the CT material. The observation was ascribed to the metamaterial influencing the dielectric permittivity of the adjacent D-A material and thereby modulating the barrier height that needs to be overcome to recombine the charges. These results indicated that CT dynamics can be tuned even without the chemical modification of the involved molecules.^[185]

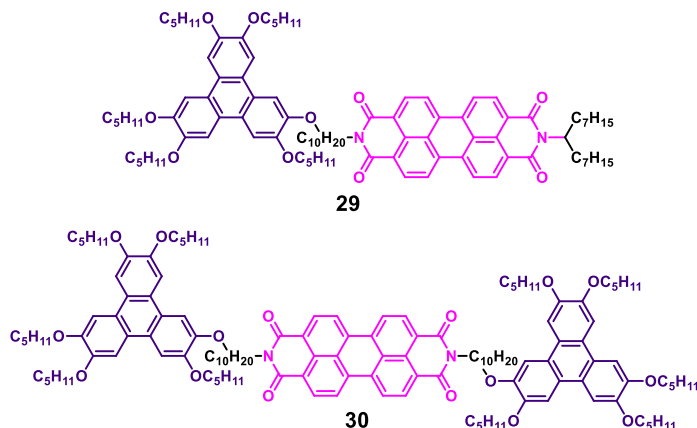


Figure 1.15: Molecular structures of the liquid crystalline dyad and triad molecules reported by Lee *et al.*^[185] The electron-rich triphenylene moieties are highlighted in purple and the electron-poor perylene-3,4,9,10-tetracarboxylic diimide (PDI) moieties in magenta.

1.3.4 Crystalline CT complex between pyrene and NDI chromophores

Another well-studied CT complex involving the NDI motif is formed by co-assembly with the electron-rich pyrene chromophore.^[186] Depending on the chemical structure of pyrene and NDI, CT complexes have been formed in various media such as the crystalline state,^[187] in a polymer blend^[188] or in solution.^[189] Yeh *et al.*^[190] investigated the CT interaction between the pyrene and NDI chromophores in detail by density-functional theory (DFT). In accordance with structural information that was obtained by X-ray scattering in a previous study, a parallel sandwich configuration with a rotational angle of 53° between the chromophores was found (Figure 1.16).^[187] The parallel face-to-face packing of the aromatic compounds maximized the dispersion forces between the molecules in this sandwich configuration, which has also been described for other large polycyclic systems.^[191] The rotational angle that was found between the NDI and pyrene chromophores in the cocrystal was ascribed to the overlap of the wavefunctions of LUMO_{NDI} and the HOMO_{pyrene}. As a result of this overlap, angles above 50° were suggested to result in attractive forces.^[190]

Since the CT complex formation between NDI and pyrene chromophores is so well-understood and the chemical modification of the two compounds is straightforward, the preparation of CT complexes based on this D-A couple has been used to develop various applications such as organogels,^[192] healable polymer networks^[193–197] and as a fluorescent supramolecular mechanophore.^[198]

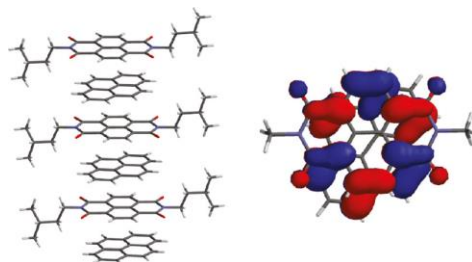


Figure 1.16: Crystal structure of the CT complex formed between NDI and pyrene derivatives as reported by Gujrati et al.^[187] The co-crystal consists of alternating, π -stacked NDI and pyrene chromophores. The rotational angle between NDI and pyrene chromophores of 53° preserves in-phase interactions of $HOMO_{pyrene}$ — $LUMO_{NDI}$ as highlighted by the red and blue colors. Figure reproduced with permission from reference ^[187] (copyright 2011 American Chemical Society).

1.4 Surface patterning using electron donor-electron acceptor systems

Whereas the formation of CT complexes is well-described for various liquid and solid bulk systems, research on the CT complex formation at interfaces is relatively underexplored.^[39] Until now, the purposeful design of multicomponent systems for surface patterning remains challenging in general since surface structures are governed by the complex interplay of substrate-adsorbate, adsorbate-adsorbate and adsorbate-solvent interactions.^[199,200] Nevertheless, several literature studies on the preparation of multicomponent systems on surfaces do exist. Depending on the molecular structures, co-adsorption on surface was observed and ascribed to the formation of the combination of van der Waals interactions and geometrical restrictions,^[201–203] hydrogen bonding^[204–207] and/or fluorophilicity.^[208] The reported studies typically investigated the formed morphologies with scanning tunneling microscopy (STM)^[209] to determine the structural details of the monolayers with a (sub-)molecular resolution.^[210] Inspired by these reports on the preparation of multicomponent systems on surfaces, research on the co-adsorption of D-A systems which aims for realizing functional multicomponent system is starting to attract increased scientific attention.^[211]

1.4.1 Imaging D and A moieties on HOPG surface using scanning tunneling microscopy

Before we present the literature examples for surface structures that were generated by multicomponent D-A systems, we first highlight the versatility of STM when imaging surfaces that are decorated with chemical species that locally differ in electron density. A very nice example to highlight the advantages of using STM is the study reported by Miura et al.^[212] which described the formation of self-assembled monolayers by the oligo *p*-phenylene vinylene (OPV) functionalized PDI **31** (Figure 1.17) on graphite surface.

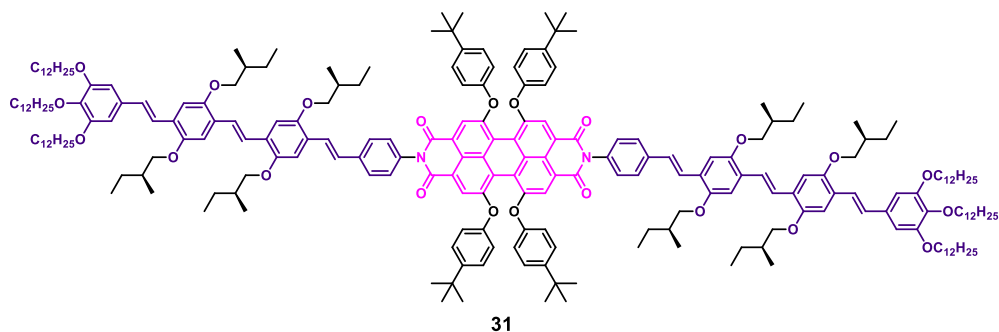


Figure 1.17: Molecular structure of the oligo *p*-phenylene vinylene (OPV) functionalized PDI **31** reported by Miura et al.^[212]

On graphite surface, the **31** formed self-assembled monolayers that exhibited a lamellar structure (Figure 1.18a,b). Since the tunnelling current measured by STM depends on the electronic properties of the adsorbates,^[213] potential-dependent imaging could be used to distinguish the electron-rich OPV from the electron-poor PDI moieties and the insulating alkyl chains. The STM images depicted in Figure 1.18c show that a strongly negative bias of the applied voltage (−1.19 V to −1.06 V) resulted in the OPV parts being noticed as the brightest elements. When the bias voltage was changed stepwise from −0.77 V to +1 V, the OPVs moieties became gradually darker and PDI moieties became brighter instead. At strongly negative potentials (−1.19 V and −1.06 V), tunneling occurred preferably via the HOMO of the OPV and made these D moieties appear very bright. In contrast, positive potentials preferred tunneling via the LUMO of the PDI and made these A moieties appear brighter.^[212]

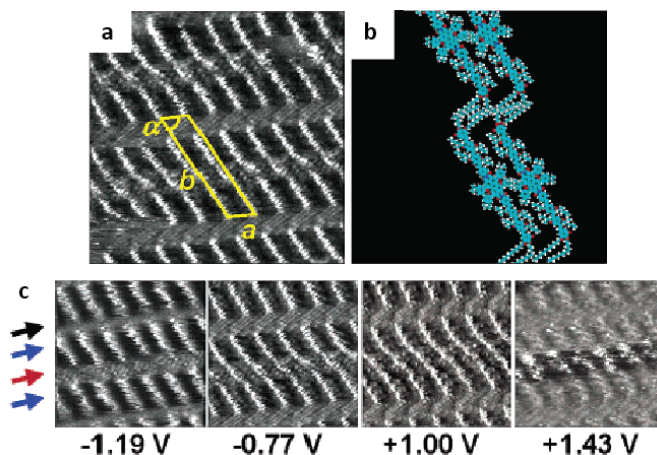


Figure 1.18: (a) STM image of the monolayer formed by **31** on graphite surface. (b) Molecular model of the surface structure. (c) Bias-dependent STM images: Varying the applied sample bias (values are given below corresponding images) changed the contrast of the STM images. The arrows indicate the position of different parts of the molecule. Black: alkyl chains; blue: OPV; red: PDI. Image adapted with permission from reference ^[212] (copyright 2003 American Chemical Society).

1.4.2 Co-assembly of hexabenzocoronenes and perylene diimide in plane

Velpula *et al.*^[40] reported on the co-adsorption of D-A mixtures in a 2D monolayer. The co-assembly of hexabenzocoronene (HBC) **32** and **33** and perylene diimide (PDI) **34** based building blocks (Figure 1.19a) was induced by the combination of the molecules' geometry and the formation of intermolecular hydrogen bonds as additional directional interactions. As noticed in the STM micrographs in Figure 1.19b and c and the corresponding molecular models in Figure 1.19d and e, the geometries of the molecules resulted in an arrangement that separated the D and A chromophores spatially. This spatial separation suggested the absence of CT complexes in the monolayer containing co-adsorbed D and A molecules.^[40]

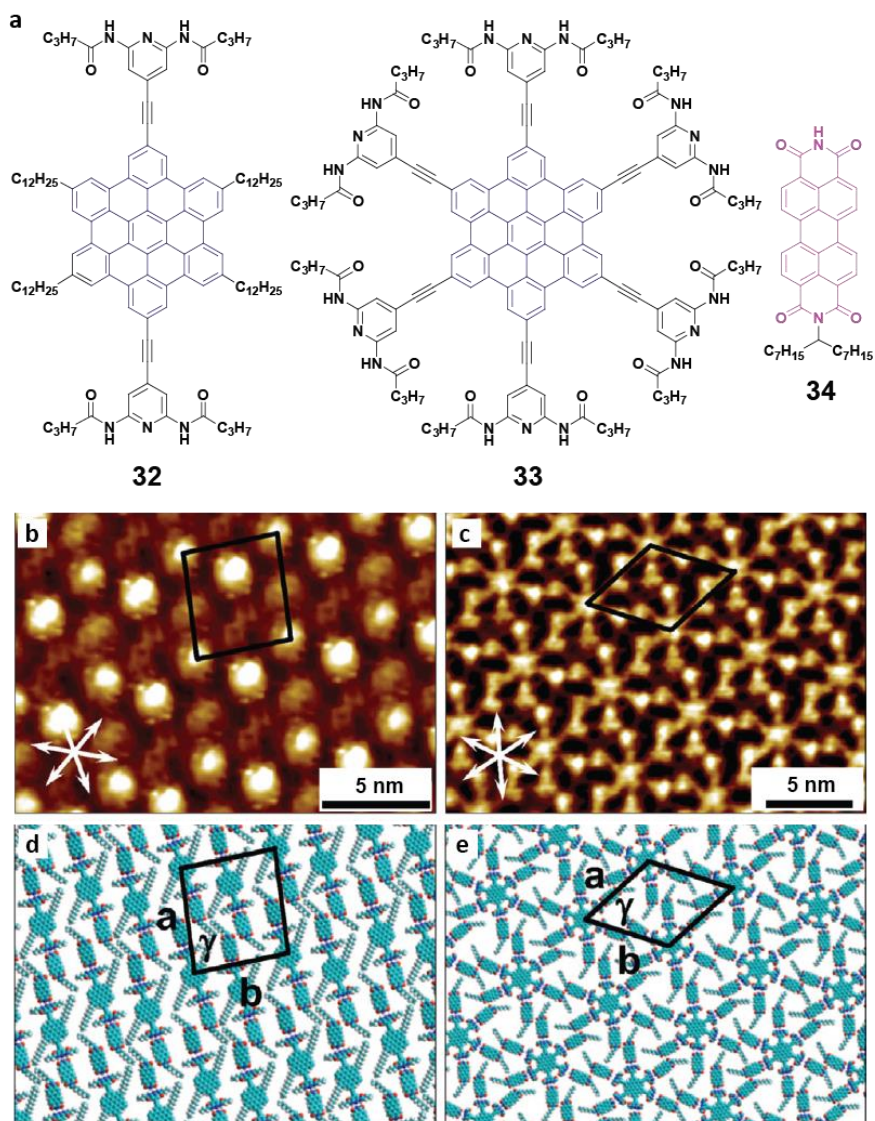


Figure 1.19: (a) Molecular structures of hexabenzocoronene (**32** and **33**) and the PDI **34** used for the formation of self-assembled monolayers on HOPG surface. STM indicated the formation of co-adsorbed monolayers containing (b) **32** and **34** and (c) **33** and **34**. Molecular models (d,e) indicated that the co-adsorption in the monolayers was induced by the formation of intermolecular hydrogen bonds and matching molecular geometries. Due to the spatial separation between HBC and PDI cores, the formation of CT complexes was absent in the monolayers. Image adapted with permission from reference [40] (copyright 2018 John Wiley & Sons, Inc.).

1.4.3 Co-adsorption of alkoxy-pyrene on top of NDI lamellae

To induce the formation of CT complexes on surface, a stacked system similar to the structures obtained by metal-ligand coordination^[214–217] is highly desirable. A recent study by Heideman *et al.*^[39] reported on the stepwise functionalization of HOPG surface with stacked architectures that were formed by the co-adsorption of electron-rich pyrenes **35**, **36** and **37** (Figure 1.20a) on top of a monolayer of electron-poor NDI **38**. STM images showed that the pyrene chromophores were however not adsorbed on top but next to the NDI cores (Figure 1.20b and c). Molecular modelling suggested that the periodic adsorption of the pyrene derivatives occurred on top of the unsaturated bonds of the 11-tritriacontenyl side chains (Figure 1.20d). Due to the spatial off-set between D and A chromophores, the formation of CT complexes remained elusive.^[39]

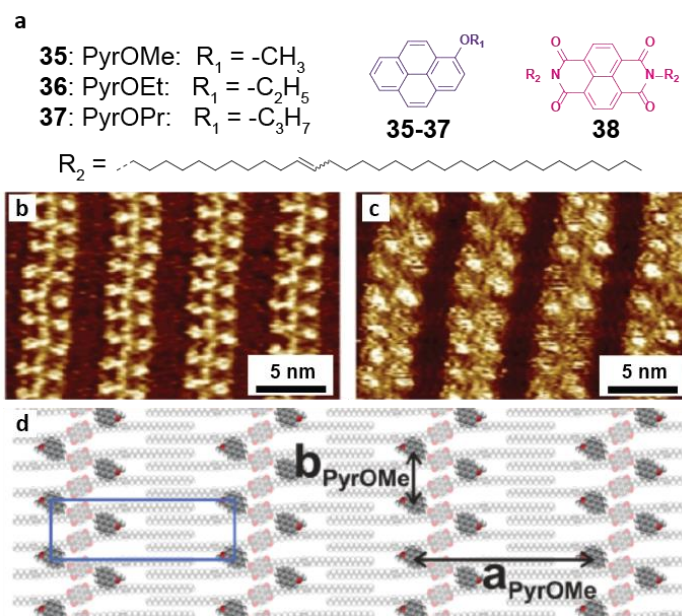


Figure 1.20: (a) Molecular structures of alkoxy pyrenes **35-37** the 11-tritriacontenyl functionalized NDI **38** which were investigated upon co-adsorption. (b-c) STM micrographs indicating the adsorption of **35** on top of the NDI-monolayer. (d) Molecular model suggesting the adsorption on top of the unsaturated bonds of the 11-tritriacontenyl side chains. Image adapted with permission from reference [39] (copyright 2021 John Wiley & Sons, Inc.).

1.5 Aim and outline of the thesis

Owing to the cultural and economic relevance of colors, scientists have been investigating dyes and pigments in great detail. With the advent of organic chemistry, research on organic CT systems resulted in the development of a plethora of colorful materials. Today's artificial systems are ranging from functional dyes to supramolecular materials and enable many more applications than the usage as colorants only. Whereas photovoltaic devices based on organic CT systems are already well-described in the literature, the development of organic spintronics based on chiral materials is just at the beginning. Since we showed in the previous section that D- π -A compounds are an excellent choice for electron transporting materials and their chemical structures can be modified extensively which also allows for the implementation of chirality, we aim for the preparation of novel organic CT materials that can be used as spin-filters, i.e. to manipulate the spin orientation of transmitted electrons. Another paucity in the field of CT materials is the formation of CT complexes on surfaces which currently still remains a pressing research question in the field of nanotechnology. In the second part of this thesis, we aim for the design of novel supramolecular building blocks to develop a novel system for the formation of CT complexes on highly oriented pyrolytic graphite (HOPG) surface.

In Chapter 2, we begin our study with the design, synthesis and characterization of novel chiral and achiral squaraine dyes that contain the D- π -A- π -D architecture since this class of compounds has recently been highlighted for exhibiting a very strong optical activity. We prepare two types of colorful squaraine dyes in chiral and achiral form and investigate the rotational isomerism of one squaraine dye in detail. Finally, we develop a synthetic strategy to implement the squaraine core in a soft siloxane matrix.

In Chapter 3, the chiroptical properties, aggregation behavior and (opto-)electronic applications of the prepared squaraine dyes are explored. We show that the optical properties of the dyes are pH responsive and change upon aggregation. Spin-coated thin films prepared by co-assembling chiral and achiral derivatives of one set of dyes show the highest optical activity for a 1:3 feed ratio. Magnetic-conducting atomic force microscopy shows that this feed ratio induces the highest spin polarization of the transmitted electrons.

In Chapter 4, we apply our gained knowledge on the design of spin-filtering materials to prepare two novel chiral supramolecular building blocks based on the nitrogen-rich *s*-heptazine motif intended for the fabrication of catalytically active electrode coatings. Both compounds are aggregated in solution and in thin film. Whereas the thin film formed by one compound is optically active, the nitrogen content of the thin film formed by the other can be increased by the thermally induced cleavage of the catalytically inactive side chains.

In Chapter 5, we present a series of novel double *N,N'*-bis(*n*-alkyl)-naphthalenediimides (NDIs) for the functionalization of HOPG surfaces with electron-poor double lamellar structures. The pitch of the NDI lamellae is precisely tuned by the length of the alkyl chain that covalently connects two NDI cores. An investigation of the bulk morphologies by X-ray

scattering indicates that also in bulk, lamellar structures are formed which have comparable structural repeating units as the surface structures. Nevertheless, the lamellae formed in bulk and on surfaces exhibit subtle differences that are noticed when investigating the structural details.

In Chapter 6, the stepwise functionalization of surfaces with CT complexes is explored. Electron-rich pyrenes are added on top of the NDI double lamellae described in Chapter 5. Depending on the molecular structures of the NDIs and the pyrenes, different morphologies are formed during the co-adsorption step. Whereas the STM images of most pyrene-NDI combinations show lateral or vertical phase separation, we also find the formation of co-adsorbed structures. The close proximity of D and A chromophores in the stacked systems is indicative of the desired CT complex formation.

1.6 References

- [1] A. Burawoy, *J. Chem. Soc.* **1937**, 1865.
- [2] J. W. Franck, Heinz-Gerhard Stadelhofer, *Industrielle Aromatenchemie: Rohstoffe · Verfahren · Produkte*, Springer Science, Berlin, Germany, **2013**.
- [3] G. Irick, G. Pacifici, *Text. Res. J.* **1972**, *42*, 391.
- [4] C. Nançoz, G. Licari, J. S. Beckwith, M. Soederberg, B. Dereka, A. Rosspeintner, O. Yushchenko, R. Letrun, S. Richert, B. Lang, E. Vauthey, *Phys. Chem. Chem. Phys.* **2018**, *20*, 7254.
- [5] J. Fabian, H. Hartmann, *Light Absorption of Organic Colorants*, Springer, Berlin, Germany, **1980**.
- [6] H. Sunahara, Y. Urano, H. Kojima, T. Nagano, *J. Am. Chem. Soc.* **2007**, *129*, 5597.
- [7] R. F. Kubin, A. N. Fletcher, *J. Lumin.* **1982**, *27*, 445.
- [8] W. Saenger, *Naturwissenschaften* **1984**, *71*, 31.
- [9] T. Han, Y. Hong, N. Xie, S. Chen, N. Zhao, E. Zhao, J. W. Y. Lam, H. H. Y. Sung, Y. Dong, B. Tong, B. Z. Tang, *J. Mater. Chem. C* **2013**, *1*, 7314.
- [10] P. M. Alvey, J. J. Reczek, V. Lynch, B. L. Iverson, *J. Org. Chem.* **2010**, *75*, 7682.
- [11] J. Wojtyk, A. McKerrow, P. Kazmaier, E. Buncel, *Can. J. Chem.* **1999**, *77*, 903.
- [12] X. Niu, P. Gautam, Z. Kuang, C. P. Yu, Y. Guo, H. Song, Q. Guo, J. M. W. Chan, A. Xia, *Phys. Chem. Chem. Phys.* **2019**, *21*, 17323.
- [13] F. Ricci, F. Elisei, P. Foggi, A. Marrocchi, A. Spalletti, B. Carlotti, *J. Phys. Chem. C* **2016**, *120*, 23726.
- [14] B. A. Reinhardt, L. L. Brott, S. J. Clarson, A. G. Dillard, J. C. Bhatt, R. Kannan, L. Yuan, G. S. He, P. N. Prasad, *Chem. Mater.* **1998**, *10*, 1863.
- [15] S. S. Malhotra, W. M. C., *J. Chem. Soc.* **1960**, 34.
- [16] L. A. Ernst, R. K. Gupta, R. B. Mujumdar, A. S. Waggoner, *Cytometry* **1989**, *10*, 3.
- [17] X. Cao, R. W. Tolbert, J. L. McHale, W. D. Edwards, *J. Phys. Chem. A* **1998**, *102*, 2739.
- [18] Y. S. Yen, H. H. Chou, Y. C. Chen, C. Y. Hsu, J. T. Lin, *J. Mater. Chem.* **2012**, *22*, 8734.
- [19] R. Christie, *Colour Chemistry*, The Royal Society Of Chemistry, **2001**.
- [20] G. Sedghi, K. Sawada, L. J. Esdaile, M. Hoffmann, H. L. Anderson, D. Bethell, W. Haiss, S. J. Higgins, R. J. Nichols, *J. Am. Chem. Soc.* **2008**, *130*, 8582.
- [21] K. V. Mikkelsen, M. A. Ratner, *Chem. Rev.* **1987**, *87*, 113.
- [22] H. Sirringhaus, T. Kawase, R. H. Friend, T. Shimoda, M. Inbasekaran, W. Wu, E. P. Woo, *Science* **2000**, *290*, 2123.
- [23] M. Gsänger, D. Bialas, L. Huang, M. Stolte, F. Würthner, *Ad. Mater.* **2016**, *28*, 3615.
- [24] J. L. Brédas, J. P. Calbert, D. A. Da Silva Filho, J. Cornil, *Proc. Natl. Acad. Sci.* **2002**, *99*, 5804.
- [25] Y.-J. Cheng, S.-H. Yang, C.-S. Hsu, *Chem. Rev.* **2009**, *109*, 5868.
- [26] K. T. Kamtekar, A. P. Monkman, M. R. Bryce, *Adv. Mater.* **2010**, *22*, 572.
- [27] G. J. Zhao, J. Y. Liu, L. C. Zhou, K. L. Han, *J. Phys. Chem. B* **2007**, *111*, 8940.
- [28] A. Yella, R. Humphry-Baker, B. F. E. Curchod, N. Ashari Astani, J. Teuscher, L. E. Polander, S. Mathew, J. E. Moser, I. Tavernelli, U. Rothlisberger, M. Grätzel, M. K. Nazeeruddin, J. Frey, *Chem. Mater.* **2013**, *25*, 2733.

- [29] M. Torrent-Sucarrat, S. Navarro, E. Marcos, J. M. Anglada, J. M. Luis, *J. Phys. Chem. C* **2017**, *121*, 19348.
- [30] A. J. T. Lou, E. F. C. Dreyer, S. C. Rand, T. J. Marks, *J. Phys. Chem. C* **2017**, *121*, 16491.
- [31] Z. He, L. Zhao, Q. Zhang, M. Chang, C. Li, H. Zhang, Y. Lu, Y. Chen, *Adv. Funct. Mater.* **2020**, *30*, 1910301.
- [32] D. Sharada, A. Saha, B. K. Saha, *New J. Chem.* **2019**, *43*, 7562.
- [33] J. J. Colin, H. G. de Claubry, *Ann. Chim.* **1814**, *90*, 87.
- [34] S. Madhu, H. A. Evans, V. V. T. Doan-Nguyen, J. G. Labram, G. Wu, M. L. Chabiny, R. Seshadri, F. Wudl, *Angew. Chem. Int. Ed.* **2016**, *55*, 8032.
- [35] H. Akamatu, H. Inokuchi, Y. Matsunaga, *Nature* **1954**, *173*, 168.
- [36] J. Ferraris, D. O. Cowan, V. Walatka, J. H. Perlstein, *J. Am. Chem. Soc.* **1973**, *95*, 948.
- [37] Y. Takahashi, J. Hasegawa, Y. Abe, Y. Tokura, K. Nishimura, G. Saito, *Appl. Phys. Lett.* **2005**, *86*, 1.
- [38] K. P. Goetz, D. Vermeulen, M. E. Payne, C. Kloc, L. E. McNeil, O. D. Jurchescu, *J. Mater. Chem. C* **2014**, *2*, 3065.
- [39] G. H. Heideman, J. A. Berrocal, E. W. Meijer, B. L. Feringa, *Chem. Eur. J.* **2020**, DOI 10.1002/chem.202004008.
- [40] G. Velpula, M. Li, Y. Hu, Y. Zagranyski, W. Pisula, K. Müllen, K. S. Mali, S. De Feyter, *Chem. Eur. J.* **2018**, *24*, 12071.
- [41] C. Graebe, K. Liebermann, *Ber. Dtsch. Chem. Ges.* **1868**, *1*, 106.
- [42] O. N. Witt, *Ber. Dtsch. Chem. Ges.* **1876**, *9*, 522.
- [43] W. Dilthey, *J. Prakt. Chem.* **1925**, *109*, 273.
- [44] R. Wizinger, *Organische Farbstoffe*, Dümmler, Berlin, Germany, **1933**.
- [45] R. Nietzky, *Chemie Der Organischen Farbstoffe*, Springer, Berlin, Germany, **1889**.
- [46] H. Armstrong, *Proc. Chem. Soc.* **1888**, *4*, 21.
- [47] W. König, *J. Prakt. Chemie* **1926**, *112*, 1.
- [48] E. Lippert, W. Lüder, F. Moll, W. Nägele, H. Boos, H. Prigge, I. Seibold-Blakenstein, *Angew. Chem.* **1961**, *73*, 695.
- [49] Z. R. Grabowski, K. Rotkiewicz, W. Rettig, *Chem. Rev.* **2003**, *103*, 3899.
- [50] C. A. Hoelzel, H. Hu, C. H. Wolstenholme, B. A. Karim, K. T. Munson, K. H. Jung, H. Zhang, Y. Liu, H. P. Yennawar, J. B. Asbury, X. Li, X. Zhang, *Angew. Chem. Int. Ed.* **2020**, *59*, 4785.
- [51] R. A. Marcus, *Annu. Rev. Phys. Chem.* **1964**, *15*, 155.
- [52] E. Lippert, *Z. Naturforsch.* **1955**, *10*, 541.
- [53] T. Förster, *Z. Elektrochem. Angew. Phys. Chem.* **1939**, *45*, 571.
- [54] Z. R. Grabowski, K. Rotkiewicz, A. Siemiarz, *J. Lumin.* **1979**, *18–19*, 420.
- [55] A. Siemiarz, Z. R. Grabowski, A. Krówczyński, M. Asher, M. Ottolenghi, *Chem. Phys. Lett.* **1977**, *51*, 315.
- [56] S. I. Druzhinin, P. Mayer, D. Stalke, R. Von Bülow, M. Noltemeyer, K. A. Zachariasse, *J. Am. Chem. Soc.* **2010**, *132*, 7730.
- [57] M. Itaya, S. Toshima, *Chem. Phys. Lett.* **1977**, *51*, 447.
- [58] M. Kawai, K. Itaya, S. Toshima, *J. Phys. Chem.* **1980**, *84*, 2368.
- [59] G. L. Closs, J. R. Miller, *Science* **1988**, *240*, 440.
- [60] S. Sasaki, G. P. C. Drummen, G. I. Konishi, *J. Mater. Chem. C* **2016**, *4*, 2731.
- [61] K. Rotkiewicz, W. Rubaszewska, *Chem. Phys. Lett.* **1980**, *70*, 444.
- [62] T. Okada, M. Uesugi, G. Köhler, K. Rechthaler, K. Rotkiewicz, W. Rettig, G. Grabner, *Chem. Phys.* **1999**, *241*, 327.
- [63] K. A. Zachariasse, S. I. Druzhinin, W. Bosch, R. Machinek, *J. Am. Chem. Soc.* **2004**, *126*, 1705.
- [64] S. Techert, K. A. Zachariasse, *J. Am. Chem. Soc.* **2004**, *126*, 5593.
- [65] S. I. Druzhinin, V. A. Galievsky, A. Demeter, S. A. Kovalenko, T. Senyushkina, S. R. Dubbaka, P. Knochel, P. Mayer, C. Grosse, D. Stalke, K. A. Zachariasse, *J. Phys. Chem. A* **2015**, *119*, 11820.
- [66] P. Suppan, *Chem. Phys. Lett.* **1986**, *128*, 160.
- [67] W. Rettig, *J. Mol. Struct.* **1982**, *84*, 303.
- [68] N. Mataga, Y. Kaifu, M. Koizumi, *Bull. Chem. Soc. Jpn.* **1956**, *29*, 465.
- [69] G. V. Bakhshiev, Nikolay G.; Knyazhanski, M. I.; Minkin, Vladimir I.; Osipov, O. A.; Saidov, *Rus. Chem. Rev.* **1969**, *38*, 740.
- [70] A. Kowski, P. Bojarski, *Spectrochim. Acta - Part A Mol. Biomol. Spectrosc.* **2011**, *82*, 527.
- [71] V. M. Divac, D. Šakić, T. Weitner, M. Gabričević, *Spectrochim. Acta - Part A Mol. Biomol. Spectrosc.* **2019**, *212*, 356.
- [72] A. C. P. Viallet, *Acad. Sci. Paris Ser C* **1970**, 1901.

- [73] E. M. Kosower, H. Dodiuk, *J. Am. Chem. Soc.* **1976**, *98*, 924.
- [74] W. Baumann, H. Bischof, J. C. Fröhling, C. Brittinger, W. Rettig, K. Rotkiewicz, *J. Photochem. Photobiol. A Chem.* **1992**, *64*, 49.
- [75] C. Brittinger, A. K. Maiti, W. Baumann, N. Detzer, *Z. Naturforsch.* **1990**, *45a*, 883.
- [76] W. Rettig, F. Marschner, *Nouv. J. Chim.* **1990**, *14*, 819.
- [77] W. Baumann, H. Bischof, *J. Mol. Struct.* **1982**, *84*, 181.
- [78] P. Suppan, C. Tsiamis, *J. Chem. Soc. Faraday Trans. 2 Mol. Chem. Phys.* **1981**, *77*, 1553.
- [79] M. P. De Haas, J. M. Warman, *Chem. Phys.* **1982**, *73*, 35.
- [80] R. Hu, E. Lager, A. Aguilar-Aguilar, J. Liu, J. W. Y. Lam, H. H. Y. Sung, I. D. Williams, Y. Zhong, K. S. Wong, E. Peña-Cabrera, B. Z. Tang, *J. Phys. Chem. C* **2009**, *113*, 15845.
- [81] S. Sasaki, Y. Niko, K. Igawa, G. I. Konishi, *RSC Adv.* **2014**, *4*, 33474.
- [82] E. Wang, J. W. Y. Lam, R. Hu, C. Zhang, Y. S. Zhao, B. Z. Tang, *J. Mater. Chem. C* **2014**, *2*, 1801.
- [83] W. Frank, *Angew. Chem. Int. Ed.* **2020**, *59*, 14192.
- [84] Y. Hong, J. W. Y. Lam, B. Z. Tang, *Chem. Soc. Rev.* **2011**, *40*, 5361.
- [85] R. T. K. Kwok, C. W. T. Leung, J. W. Y. Lam, B. Z. Tang, *Chem. Soc. Rev.* **2015**, *44*, 4228.
- [86] N. Zhao, Z. Yang, J. W. Y. Lam, H. H. Y. Sung, N. Xie, S. Chen, H. Su, M. Gao, I. D. Williams, K. Sing Wong, B. Zhong Tang, *Chem. Commun.* **2012**, *48*, 8637.
- [87] B. Chen, Y. Ding, X. Li, W. Zhu, J. P. Hill, K. Ariga, Y. Xie, *Chem. Commun.* **2013**, *49*, 10136.
- [88] B. Chen, X. Sun, X. Li, H. Ågren, Y. Xie, *Sensors Actuators, B Chem.* **2014**, *199*, 93.
- [89] D. Zhou, Y. Wang, J. Jia, W. Yu, B. Qu, X. Li, X. Sun, *Chem. Commun.* **2015**, *51*, 10656.
- [90] T. Morozumi, T. Anada, H. Nakamura, *J. Phys. Chem. B* **2001**, *105*, 2923.
- [91] M. A. Haidekker, E. A. Theodorakis, *Org. Biomol. Chem.* **2007**, *5*, 1669.
- [92] B. Daly, J. Ling, A. P. De Silva, *Chem. Soc. Rev.* **2015**, *44*, 4203.
- [93] K. Cao, M. Farahi, M. Dakanali, W. M. Chang, C. J. Sigurdson, E. A. Theodorakis, J. Yang, *J. Am. Chem. Soc.* **2012**, *134*, 17338.
- [94] R. D. Priestley, C. J. Ellison, L. J. Broadbelt, J. M. Torkelson, *Science* **2005**, *309*, 456.
- [95] T. Suhina, B. Weber, C. E. Carpentier, K. Lorincz, P. Schall, D. Bonn, A. M. Brouwer, *Angew. Chem. Int. Ed.* **2015**, *54*, 3688.
- [96] A. Mustafic, H. M. Huang, E. A. Theodorakis, M. A. Haidekker, *J. Fluoresc.* **2010**, *20*, 1087.
- [97] N. Amdursky, Y. Erez, D. Huppert, *Acc. Chem. Res.* **2012**, *45*, 1548.
- [98] T. Hirayama, K. Okuda, H. Nagasawa, *Chem. Sci.* **2013**, *4*, 1250.
- [99] A. Hagfeldt, G. Boschloo, L. Sun, L. Klöö, H. Pettersson, *Chem. Rev.* **2010**, *110*, 6595.
- [100] J. M. Cole, G. Pepe, O. K. Al Bahri, C. B. Cooper, *Chem. Rev.* **2019**, *119*, 7279.
- [101] K. Gräf, M. A. Rahim, S. Das, M. Thelakkt, *Dye. Pigment.* **2013**, *99*, 1101.
- [102] H. Zhu, W. Li, Y. Wu, B. Liu, S. Zhu, X. Li, H. Ågren, W. Zhu, *ACS Sustain. Chem. Eng.* **2014**, *2*, 1026.
- [103] S. G. Bairu, E. Mghanga, J. Hasan, S. Kola, V. J. Rao, K. Bhanuprakash, L. Giribabu, G. P. Wiederrecht, R. Da Silva, L. G. C. Rego, G. Ramakrishna, *J. Phys. Chem. C* **2013**, *117*, 4824.
- [104] D. Mühlbacher, M. Scharber, M. Morana, Z. Zhu, D. Waller, R. Gaudiana, C. Brabec, *Adv. Mater.* **2006**, *18*, 2884.
- [105] G. Li, W. H. Chang, Y. Yang, *Nat. Rev. Mater.* **2017**, *2*, 1.
- [106] Y. Liang, Z. Xu, J. Xia, S. T. Tsai, Y. Wu, G. Li, C. Ray, L. Yu, *Adv. Mater.* **2010**, *22*, 135.
- [107] L. Lu, T. Zheng, Q. Wu, A. M. Schneider, D. Zhao, L. Yu, *Chem. Rev.* **2015**, *115*, 12666.
- [108] T. Xu, L. Yu, *Mater. Today* **2014**, *17*, 11.
- [109] E. Bundgaard, F. C. Krebs, *Sol. Energy Mater. Sol. Cells* **2007**, *91*, 954.
- [110] D. Gendron, P. O. Morin, P. Berrouard, N. Allard, B. R. Aich, C. N. Garon, Y. Tao, M. Leclerc, *Macromolecules* **2011**, *44*, 7188.
- [111] L. Dou, C. C. Chen, K. Yoshimura, K. Ohya, W. H. Chang, J. Gao, Y. Liu, E. Richard, Y. Yang, *Macromolecules* **2013**, *46*, 3384.
- [112] Y. Liu, J. Zhao, Z. Li, C. Mu, W. Ma, H. Hu, K. Jiang, H. Lin, H. Ade, H. Yan, *Nat. Commun.* **2014**, *5*, DOI 10.1038/ncomms6293.
- [113] J. C. Bijleveld, A. P. Zoombelt, S. G. J. Mathijssen, M. M. Wienk, M. Turbiez, D. M. De Leeuw, R. A. J. Janssen, *J. Am. Chem. Soc.* **2009**, *131*, 16616.
- [114] T. Y. Chu, J. Lu, S. Beaupré, Y. Zhang, J. R. Pouliot, S. Wakim, J. Zhou, M. Leclerc, Z. Li, J. Ding, Y. Tao, *J. Am. Chem. Soc.* **2011**, *133*, 4250.
- [115] R. S. Ashraf, I. Meager, M. Nikolka, M. Kirkus, M. Planells, B. C. Schroeder, S. Holliday, M. Hurhangee, C. B. Nielsen, H. Sirringhaus, I. McCulloch, *J. Am. Chem. Soc.* **2015**, *137*, 1314.

- [116] D. M. Lee, J. W. Song, Y. J. Lee, C. J. Yu, J. H. Kim, *Adv. Mater.* **2017**, *29*, 6.
- [117] K. C. Pan, S. W. Li, Y. Y. Ho, Y. J. Shiu, W. L. Tsai, M. Jiao, W. K. Lee, C. C. Wu, C. L. Chung, T. Chatterjee, Y. S. Li, K. T. Wong, H. C. Hu, C. C. Chen, M. T. Lee, *Adv. Funct. Mater.* **2016**, *26*, 7560.
- [118] D. Di Nuzzo, C. Kulkarni, B. Zhao, E. Smolinsky, F. Tassinari, S. C. J. Meskers, R. Naaman, E. W. Meijer, R. H. Friend, *ACS Nano* **2017**, *11*, 12713.
- [119] M. Held, Y. Zakharko, M. Wang, F. Jakubka, F. Gannott, J. W. Rumer, R. S. Ashraf, I. McCulloch, J. Zaumseil, *Org. Electron.* **2016**, *32*, 220.
- [120] B. C. Thompson, L. G. Madrigal, M. R. Pinto, T. S. Kang, K. S. Schanze, J. R. Reynolds, *J. Polym. Sci. Pol. Chem.* **2005**, *43*, 1417.
- [121] D. Kabra, L. P. Lu, M. H. Song, H. J. Snaith, R. H. Friend, *Adv. Mater.* **2010**, *22*, 3194.
- [122] K. Morii, M. Ishida, T. Takashima, T. Shimoda, Q. Wang, M. K. Nazeeruddin, M. Grätzel, *Appl. Phys. Lett.* **2006**, *89*, 1.
- [123] G. Bernardo, Q. Ferreira, G. Brotas, R. E. Di Paolo, A. Charas, J. Morgado, *J. Appl. Phys.* **2010**, *108*, DOI 10.1063/1.3456997.
- [124] E. Ravindran, N. Somanathan, *J. Mater. Chem. C* **2017**, *5*, 4763.
- [125] T. Liu, L. Zhu, C. Zhong, G. Xie, S. Gong, J. Fang, D. Ma, C. Yang, *Adv. Funct. Mater.* **2017**, *27*, DOI 10.1002/adfm.201606384.
- [126] Y. Zhao, X. Li, Z. Wang, W. Yang, K. Chen, J. Zhao, G. G. Gurzadyan, *J. Phys. Chem. C* **2018**, *122*, 3756.
- [127] J. Kim, T. Morozumi, H. Hiraga, H. Nakamura, *Anal. Sci.* **2009**, *25*, 1319.
- [128] B. O'Regan, M. Grätzel, *Nature* **1991**, *353*, 737.
- [129] J. Wu, Z. Lan, J. Lin, M. Huang, Y. Huang, L. Fan, G. Luo, *Chem. Rev.* **2015**, *115*, 2136.
- [130] H. A. M. Mullekom, J. A. J. M. Vekemans, E. E. Havinga, E. W. Meijer, *Mater. Sci. Eng.* **2001**, *32*, 1.
- [131] J. A. J. M. Vekemans, L. Groenendaal, A. R. A. Palmans, D. A. P. Delnoye, H. A. M. van Mullekom, E. W. Meijer, *Bull. la Soc. Chim. Belgique* **1996**, *105*, 659.
- [132] H. A. M. Van Mullekom, J. A. J. M. Vekemans, E. W. Meijer, *Chem. Eur. J.* **1998**, *4*, 1235.
- [133] K. Müllen, W. Pisula, *J. Am. Chem. Soc.* **2015**, *137*, 9503.
- [134] J. Hou, H. Y. Chen, S. Zhang, G. Li, Y. Yang, *J. Am. Chem. Soc.* **2008**, *130*, 16144.
- [135] Z. Chen, Y. Zheng, H. Yan, A. Facchetti, *J. Am. Chem. Soc.* **2009**, *131*, 8.
- [136] "National Renewable Energy Laboratory (NREL), MS ExcelTM spreadsheet," can be found under <http://rredc.nrel.gov/solar/%0Aspectra/am1.5/>, **2020**.
- [137] R. N. Marks, J. J. M. Halls, D. D. C. Bradley, R. H. Friend, A. B. Holmes, *J. Phys. Condens. Matter* **1994**, *6*, 1379.
- [138] B. A. Gregg, *J. Phys. Chem. B* **2003**, *107*, 4688.
- [139] T. Marszalek, M. Li, W. Pisula, *Chem. Commun.* **2016**, *52*, 10938.
- [140] Y. Olivier, M. Moral, L. Muccioli, J. C. Sancho-García, *J. Mater. Chem. C* **2017**, *5*, 5718.
- [141] Y. Liu, C. Li, Z. Ren, S. Yan, M. R. Bryce, *Nat. Rev. Mater.* **2018**, *3*, DOI 10.1038/natrevmats.2018.20.
- [142] S. Izumi, H. F. Higginbotham, A. Nyga, P. Stachelek, N. Tohnai, P. De Silva, P. Data, Y. Takeda, S. Minakata, *J. Am. Chem. Soc.* **2020**, *142*, 1482.
- [143] Y. Li, J. Y. Liu, Y. Di Zhao, Y. C. Cao, *Mater. Today* **2017**, *20*, 258.
- [144] Y. Wang, Y. Zhu, X. Lin, Y. Yang, B. Zhang, H. Zhan, Z. Xie, Y. Cheng, *J. Mater. Chem. C* **2018**, *6*, 568.
- [145] Y. Geng, A. C. A. Chen, J. J. Ou, S. H. Chen, K. Klubek, K. M. Vaeth, C. W. Tang, *Chem. Mater.* **2003**, *15*, 4352.
- [146] K. M. Omer, S. Y. Ku, K. T. Wong, A. J. Bard, *J. Am. Chem. Soc.* **2009**, *131*, 10733.
- [147] V. Varade, T. Z. Markus, K. Vankayala, N. Friedman, M. Sheves, D. H. Waldeck, R. Naaman, *Phys. Chem. Chem. Phys.* **2017**, DOI 10.1039/C7CP06771B.
- [148] W. Mtangi, V. Kiran, C. Fontanesi, R. Naaman, *J. Phys. Chem. Lett.* **2015**, *6*, 4916.
- [149] F. A. Garcés-Pineda, M. Blasco-Ahicart, D. Nieto-Castro, N. López, J. R. Galán-Mascarós, *Nat. Energy* **2019**, *4*, 519.
- [150] P. J. Hore, *Proc. Natl. Acad. Sci.* **2012**, *109*, 1357.
- [151] D. Mishra, T. Z. Markus, R. Naaman, M. Kettner, B. Gohler, H. Zacharias, N. Friedman, M. Sheves, C. Fontanesi, *Proc. Natl. Acad. Sci.* **2013**, *110*, 14872.
- [152] K. Michaeli, N. Kantor-Uriel, R. Naaman, D. H. Waldeck, *Chem. Soc. Rev.* **2016**, *45*, 6478.
- [153] B. Göhler, V. Hamelbeck, T. Z. Markus, M. Kettner, G. F. Hanne, Z. Vager, R. Naaman, H. Zacharias, *Science* **2011**, *331*, 894.
- [154] R. Naaman, D. H. Waldeck, *J. Phys. Chem. Lett.* **2012**, *3*, 2178.
- [155] C. Kulkarni, A. K. Mondal, T. K. Das, G. Grinbom, F. Tassinari, M. F. J. Mabesoone, E. W. Meijer, R. Naaman,

- Adv. Mater.* **2020**, *32*, 1.
- [156] W. Mtangi, F. Tassinari, K. Vankayala, A. Vargas Jentsch, B. Adelizzi, A. R. A. Palmans, C. Fontanesi, E. W. Meijer, R. Naaman, *J. Am. Chem. Soc.* **2017**, *139*, 2794.
- [157] F. Tassinari, K. Banerjee-Ghosh, F. Parenti, V. Kiran, A. Mucci, R. Naaman, *J. Phys. Chem. C* **2017**, *121*, 15777.
- [158] B. Adelizzi, A. T. Rösch, D. J. van Rijen, R. S. Martire, S. Esiner, M. Lutz, A. R. A. Palmans, E. W. Meijer, *Helv. Chim. Acta* **2019**, e201900065.
- [159] F. Tassinari, J. Steidel, S. Paltiel, C. Fontanesi, M. Lahav, Y. Paltiel, R. Naaman, *Chem. Sci.* **2019**, *10*, 5246.
- [160] K. Banerjee-Ghosh, O. Ben Dor, F. Tassinari, E. Capua, S. Yochelis, A. Capua, S. H. Yang, S. S. P. P. Parkin, S. Sarkar, L. L. Kronik, L. T. Baczewski, R. Naaman, Y. Paltiel, *Science* **2018**, *360*, 1331.
- [161] T. S. Metzger, S. Mishra, B. P. Bloom, N. Goren, A. Neubauer, G. Shmul, J. Wei, S. Yochelis, F. Tassinari, C. Fontanesi, D. H. Waldeck, Y. Paltiel, R. Naaman, *Angew. Chem. Int. Ed.* **2020**, *59*, 1653.
- [162] R. Foster, C. A. Fyfe, *Prog. Nucl. Magn. Reson. Spectrosc.* **1969**, *4*, 1.
- [163] B. Naiman, *J. Chem. Educ.* **1937**, 138.
- [164] R. Bhosale, J. Mišek, N. Sakai, S. Matile, *Chem. Soc. Rev.* **2010**, *39*, 138.
- [165] H. Y. Au-Yeung, G. D. Pantoş, J. K. M. Sanders, *Proc. Natl. Acad. Sci.* **2009**, *106*, 10466.
- [166] P. Talukdar, G. Bollot, J. Mareda, N. Sakai, S. Matile, *J. Am. Chem. Soc.* **2005**, *127*, 6528.
- [167] W. Pisula, M. Kastler, D. Wasserfallen, J. W. F. Robertson, F. Nolde, C. Kohl, K. Müllen, *Angew. Chem. Int. Ed.* **2006**, *45*, 819.
- [168] V. J. Bradford, B. L. Iverson, *J. Am. Chem. Soc.* **2008**, *130*, 1517.
- [169] S. De, S. Ramakrishnan, *Macromolecules* **2009**, *42*, 8599.
- [170] J. Li, L. Guo, L. Zhang, C. Yu, L. Yu, P. Jiang, C. Wei, F. Qin, J. Shi, *Dalt. Trans.* **2009**, 823.
- [171] A. Das, M. R. Molla, A. Banerjee, A. Paul, S. Ghosh, *Chem. Eur. J.* **2011**, *17*, 6061.
- [172] K. V. Rao, K. Jayaramulu, T. K. Maji, S. J. George, *Angew. Chem. Int. Ed.* **2010**, *49*, 4218.
- [173] D. González-Rodríguez, A. P. H. J. Schenning, *Chem. Mater.* **2011**, *23*, 310.
- [174] G. Briegleb, *Elektronen-Donator-Acceptor-Komplexe*, Springer, Berlin, Germany, **1961**.
- [175] M. B. Nielsen, J. O. Jeppesen, J. Laut, C. Lomholt, D. Damgaard, J. P. Jacobsen, J. Becher, J. F. Stoddart, *J. Org. Chem.* **2001**, *66*, 3559.
- [176] A. Das, S. Ghosh, *Angew. Chem. Int. Ed.* **2014**, *53*, 2038.
- [177] M. R. Molla, A. Das, S. Ghosh, *Chem. Eur. J.* **2010**, *16*, 10084.
- [178] A. Das, M. R. Molla, B. Maity, D. Koley, S. Ghosh, *Chem. Eur. J.* **2012**, *18*, 9849.
- [179] K. Liu, Y. Yao, Y. Liu, C. Wang, Z. Li, X. Zhang, *Langmuir* **2012**, *28*, 10697.
- [180] K. Liu, C. Wang, Z. Li, X. Zhang, *Angew. Chem. Int. Ed.* **2011**, *50*, 4952.
- [181] S. Ghosh, S. Ramakrishnan, *Angew. Chem.* **2004**, *116*, 3326.
- [182] J. Hak, S. Sabin-Lucian, W. Y. Lee, M. Könemann, H. W. Höffken, C. Röger, R. Schmidt, Y. Chung, W. C. Chen, F. Würthner, Z. Bao, *Adv. Funct. Mater.* **2010**, *20*, 2148.
- [183] A. Dey, A. Kalita, P. K. Iyer, *ACS Appl. Mater. Interfaces* **2014**, *6*, 12295.
- [184] B. Adelizzi, P. Chidchob, N. Tanaka, B. A. G. Lamers, S. C. J. Meskers, S. Ogi, A. R. A. Palmans, S. Yamaguchi, E. W. Meijer, *J. Am. Chem. Soc.* **2020**, *142*, 16681.
- [185] K. J. Lee, Y. Xiao, E. S. Kim, F. Mathevet, L. Mager, O. Cregut, Frédéric Fages, J. C. Ribierre, J. W. Wu, A. D'Aléo, *ACS Photonics* **2019**, *6*, 2649.
- [186] N. S. S. Kumar, M. D. Gujrati, J. N. Wilson, *Chem. Commun.* **2010**, *46*, 5464.
- [187] M. D. Gujrati, N. S. S. Kumar, A. S. Brown, B. Captain, J. N. Wilson, *Langmuir* **2011**, *27*, 6554.
- [188] S. Burattini, H. M. Colquhoun, J. D. Fox, D. Friedmann, B. W. Greenland, P. J. F. Harris, W. Hayes, M. E. MacKay, S. J. Rowan, *Chem. Commun.* **2009**, 6717.
- [189] P. Rajdev, M. R. Molla, S. Ghosh, *Langmuir* **2014**, *30*, 1969.
- [190] M. Y. Yeh, H. C. Lin, *Phys. Chem. Chem. Phys.* **2014**, *16*, 24216.
- [191] S. M. Ryno, C. Risko, J. L. Brédas, *J. Am. Chem. Soc.* **2014**, *136*, 6421.
- [192] S. Bartocci, J. A. Berrocal, P. Guarracino, M. Grillaud, L. Franco, M. Mba, *Chem. Eur. J.* **2018**, *24*, 2920.
- [193] L. R. Hart, J. H. Hunter, N. A. Nguyen, J. L. Harries, B. W. Greenland, M. E. Mackay, H. M. Colquhoun, W. Hayes, *Polym. Chem.* **2014**, *5*, 3680.
- [194] S. Burattini, H. M. Colquhoun, J. D. Fox, D. Friedmann, B. W. Greenland, P. J. F. Harris, W. Hayes, M. E. Mackay, S. J. Rowan, *Chem. Commun.* **2009**, 6717.
- [195] W. X. Xiao, D. Liu, C. J. Fan, Y. Xiao, K. K. Yang, Y. Z. Wang, *Polymer* **2020**, *190*, 122228.
- [196] J. Qin, F. Lin, D. Hubble, Y. Wang, Y. Li, I. A. Murphy, S. H. Jang, J. Yang, A. K. Y. Jen, *J. Mater. Chem. A* **2019**, *7*, 6773.

- [197] S. Chakraborty, D. Ray, V. K. Aswal, S. Ghosh, *Chem. Eur. J.* **2018**, *24*, 16379.
- [198] K. Imato, R. Yamanaka, H. Nakajima, N. Takeda, *Chem. Commun.* **2020**, *56*, 7937.
- [199] J. A. Berrocal, G. H. Heideman, B. F. M. de Waal, E. W. Meijer, B. L. Feringa, *ACS Nano* **2020**, DOI 10.1021/acsnano.0c06274.
- [200] B. Ilan, G. M. Florio, M. S. Hybertsen, B. J. Berne, G. W. Flynn, *Nano Lett.* **2008**, *8*, 3160.
- [201] Y. T. Shen, K. Deng, X. M. Zhang, D. Lei, Y. Xia, Q. D. Zeng, C. Wang, *J. Phys. Chem. C* **2011**, *115*, 19696.
- [202] E. Mena-Osteritz, P. Bäuerle, *Adv. Mater.* **2006**, *18*, 447.
- [203] G. Velpula, T. Takeda, J. Adisojoso, K. Inukai, K. Tahara, K. S. Mali, Y. Tobe, S. De Feyter, *Chem. Commun.* **2017**, *53*, 1108.
- [204] J. A. Theobald, N. S. Oxtoby, M. A. Phillips, N. R. Champness, P. H. Beton, *Nature* **2003**, *424*, 1029.
- [205] M. O. Blunt, J. C. Russell, M. D. C. Gimenez-Lopez, N. Taleb, X. Lin, M. Schröder, N. R. Champness, P. H. Beton, *Nat. Chem.* **2011**, *3*, 74.
- [206] J. Teyssandier, S. De Feyter, K. S. Mali, *Chem. Commun.* **2016**, *52*, 11465.
- [207] M. T. Räisänen, A. G. Slater, N. R. Champness, M. Buck, *Chem. Sci.* **2012**, *3*, 84.
- [208] K. Tahara, K. Kaneko, K. Katayama, S. Itano, C. H. Nguyen, D. D. Amorim, S. De Feyter, Y. Tobe, *Langmuir* **2015**, *31*, 7032.
- [209] G. Binnig, H. Rohrer, *IBM J. Res. Dev.* **1986**, *30*, 355.
- [210] A. M. Sweetman, S. P. Jarvis, H. Sang, I. Lekkass, P. Rahe, Y. Wang, J. Wang, N. R. Champness, L. Kantorovich, P. Moriarty, *Nat. Commun.* **2014**, *5*, DOI 10.1038/ncomms4931.
- [211] S. Casalini, C. A. Bortolotti, F. Leonardi, F. Biscarini, *Chem. Soc. Rev.* **2017**, *46*, 40.
- [212] A. Miura, Z. Chen, H. Uji-I, S. De Feyter, M. Zdanowska, P. Jonkheijm, A. P. H. J. Schenning, E. W. Meijer, F. Würthner, F. C. De Schryver, *J. Am. Chem. Soc.* **2003**, *125*, 14968.
- [213] P. Bäuerle, T. Fischer, B. Bidlingmeier, A. Stabel, and J. P. Rabe, *Angew. Chem. Int. Ed.* **1995**, *34*, 303.
- [214] R. Hahn, F. Bohle, S. Kotte, T. J. Keller, S. S. Jester, A. Hansen, S. Grimme, B. Esser, *Chem. Sci.* **2018**, *9*, 3477.
- [215] J. Visser, N. Katsonis, J. Vicario, B. L. Feringa, *Langmuir* **2009**, *25*, 5980.
- [216] J. V. Barth, *Surf. Sci.* **2009**, *603*, 1533.
- [217] S. Haq, B. Wit, H. Sang, A. Floris, Y. Wang, J. Wang, L. Pérez-García, L. Kantorovitch, D. B. Amabilino, R. Raval, *Angew. Chem. Int. Ed.* **2015**, *54*, 7101.

Chapter 2

Synthesis and characterization of novel chiral squaraine dyes

Abstract:

Colorful squaraine dyes are commonly prepared by the condensation of squaric acid with nucleophilic reagents. We show that *N*-(3-(dialkylamino)phenyl)amides and *N*-(3,5-dihydroxyphenyl)amides are suitable for the preparation of both chiral and achiral squaraine dyes. The synthesized dyes based on *N*-(3-(dialkylamino)phenyl)amide show intramolecular hydrogen-bond formation that results in rotational isomerism in chlorinated solvents. We find that the interconversion of the rotamers is accelerated by the addition of trifluoroacetic acid. In contrast, the dyes based on *N*-(3,5-dihydroxyphenyl)amide do not exhibit observable rotational isomerism. Owing to the better chemical stability of *N*-(3-(dialkylamino)-phenyl)amide based squaraine dyes, one derivative is functionalized with oligomeric siloxane side chains of three discrete lengths. X-Ray scattering indicates that the green soft materials exhibit a cylindrically ordered morphology with dimensions on the nanoscale that is of potential interest for neuromorphic computing applications.

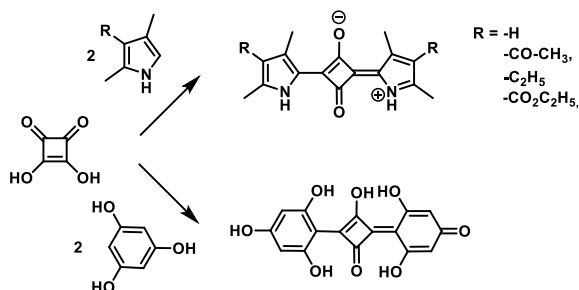
Part of his work has been published:

A.T. Rösch, Q. Zhu, J. Robben, F. Tassinari, S.C.J. Meskers, R. Naaman, A.R.A. Palmans, and E.W. Meijer, *Chem. Eur. J.* **2021**, 27, 298.

A.T. Rösch, S.H.M. Söntjens, J. Robben, A.R.A. Palmans, and T. Schnitzer - *Submitted*

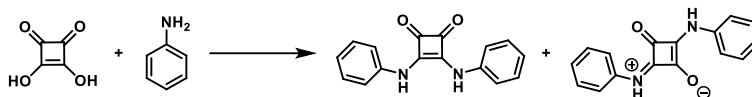
2.1 Introduction

Squaraine dyes are well-known for their strong absorption of visible light which makes them promising materials for various (opto-)electronic applications.^[1,2] Today, squaraine dyes are successfully applied in (bio-)labelling,^[3–5] photodynamic therapy,^[6] dye-sensitized^[7–10] and organic bulk heterojunction solar cells.^[11] The preparation of the first squaraine dyes has been reported by Treibs and Jacob in 1965.^[12] The colorful materials were obtained by the condensation of squaric acid with two equivalents of pyrrole or phloroglucinol in boiling ethanol. The reported condensation reactions and proposed molecular structures of the dyes are depicted Scheme 2.1.^[12]



Scheme 2.1: Synthetic approach for the preparation of squaraine dyes reported by Treibs and Jacob in 1965.^[12]

The spectroscopic data suggested that the dyes contained a highly conjugated π -system which was assigned to the formation of 1,3-regioisomers as reaction products. Shortly after this initial report, Sprenger and Ziegenbein suggested to improve the synthesis by removing the water generated by the condensation reaction and proposed that certain reagents induce the formation of 1,2-regioisomers as main products.^[13] Since spectroscopic proofs of the proposed 1,2-regioisomers remained elusive, Neuse and Green^[14] aimed for determining the regioselectivity of the condensation reaction and investigated the reaction of squaric acid with aniline. Interestingly, the condensation reaction did not yield the *para*-amino substituted squaraine dye. Instead, aniline's amino group reacted as nucleophile and underwent condensation with squaric acid. As a result, instead of forming a C-C bond to yield the squaraine dye, a C-N bond was formed and a squaramide was obtained.^[15–17] The analysis of the reaction mixture indicated the formation of two different constitutional isomers of the squaramide (Scheme 2.2). A mechanistic study of the reaction suggested that increasing the acidity of the medium promoted the formation of the 1,2-condensation product over the 1,3-product.^[14]



Scheme 2.2: Molecular structures of the two different constitutional isomers obtained by the twofold condensation of squaric acid with aniline as reported by Neuse and Green.^[14]

Since the study suggested that regioselectivity can be an issue in condensation reactions that involve squaric acid, the regioselectivity during the squaraine dye synthesis was further investigated by Law and Bailey.^[18] The chemical structures of the investigated *N,N*-dimethylamino based squaraine dyes are depicted in Figure 2.1.^[18] The conducted study confirmed that the correct structure of a squaraine dye is the 1,3-regioisomer that was also initially proposed by Treibs and Jacob.^[12] Law and Bailey reported further that the formation of the 1,2-regioisomer can be induced, too. However, 1,2-regioisomers were formed only when the synthesis of the squaraine dye was performed in two steps. In the report, the 1,2-substituted byproducts were obtained during the synthesis of asymmetrical squaraine dyes (Figure 2.1b) and found to be chemically unstable and inclined to polymerization.^[18]

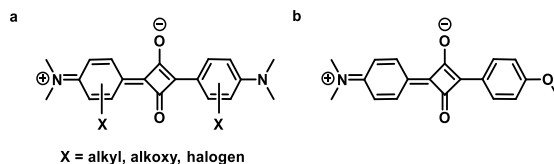
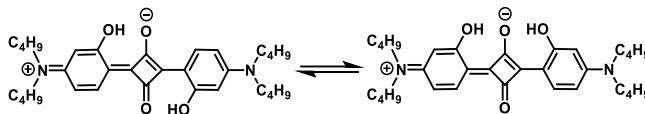


Figure 2.1: Chemical structure of symmetrical (a) and unsymmetrical (b) *N,N*-dimethylamino based squaraine dyes.^[18]

Besides the formation of different regioisomers, squaraine dyes are also known for the formation of rotational isomers.^[19,20] A study by Kazmaier *et al.*^[19] reported on the ¹H NMR spectra of *N,N*-dimethylamino substituted squaraine dyes that contained hydroxy groups in the ortho positions to the quadratic core as additional functional groups. The NMR spectra of the dyes showed the presence of two spin systems which were ascribed to rotational isomerism. The proposed chemical structures of both rotamers are depicted in Scheme 2.3. The observation of rotational isomerism suggested a hindered rotation about the covalent C-C-bond that connected the quadratic core with the phenyl substituent. The hinderance in rotation was ascribed to the formation of intramolecular hydrogen bonds between the protons of the hydroxy groups and the oxygen atoms that were attached to the quadratic core. Although a proof of the chemical structures and the assignment of the major and the minor form to one spin system each remained elusive, the study suggested a difference of 3.0 kJ/mol between the free energy of the conformations of both rotamers.^[19]



Scheme 2.3: Rotational isomerism of squaraine dyes reported by Kazmaier et al.^[19]

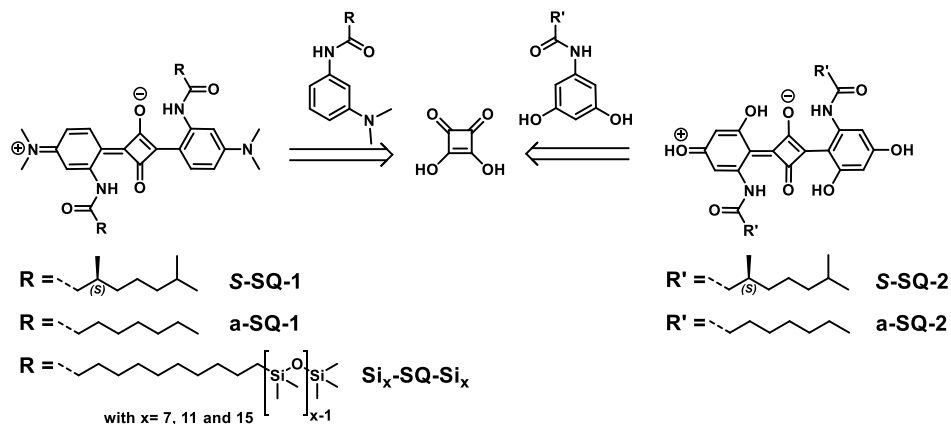
In the subsequent years, the scope of substrates and the synthetic procedures to modify squaric acid were expanded quickly.^[21] In the emerging field of squaric acid based compounds, squaraine dyes remained the most important subsection which they owe to their excellent absorption properties. Today, the chemical structures of most squaraine dyes contain *N*-alkyl nitrogen-based heterocycles^[3,13,22–24] or *N,N*-dimethylamino substituents.^[1,15,18,25–32] The popularity of these two structural elements is due to the necessity of electron donating groups in the chemical structure of the reagent to undergo condensation with squaric acid.^[33]

In addition to reports on the optical properties of squaraine dyes in solution, many studies investigated the fundamentals of dye aggregation^[22,25,28,34,35] and found that this class of compounds has a pronounced tendency to form H- and J-type aggregates.^[32,36,37] Since most of these studies focused on achiral squaraine dyes, research on chiral squaraine dyes is currently still at the beginning and only a few studies report on the application of chiral squaraine dyes as materials for organic electronic applications such as photodiodes for the detection of circularly polarized light.^[38–40]

Inspired by a recent study on the giant intrinsic circular dichroism of chiral prolinol-derived squaraine dyes in thin film,^[35] we aim for the preparation of a supramolecular squaraine dye aggregate that exhibits a very high circular dichroism effect. A well-known molecular design which has often been used to prepare well-defined supramolecular architectures is the combination of a planar and rigid molecular core and side chains capable of hydrogen bond formation.^[41–43] In the supramolecular systems based on benzene-1,3,5-tricarboxamide (BTA),^[44–48] porphyrin^[49–51] or naphthalene diimide (NDI),^[52,53] the supramolecular aggregation resulted from the combination of dipolar interactions^[54] and intermolecular hydrogen bond formation. This molecular design has also been applied to prepare an acyl hydrazone functionalized squaraine dye used for the formation of a supramolecular polymer.^[55] Supramolecular systems based on the combination of a planar core and amide functionalized side chains that form intramolecular hydrogen bonds are also reported in the literature, but not yet for squaraine dyes. Prominent examples for the reported systems are based on acylated 2,2'-bipyridine-3,3'-diamines^[56] or hexacarboxamidohexaazatriphenylenes.^[57] and have been used for the preparation of lyotropic^[58] or thermotropic^[59] liquid crystals as well as the formation of supramolecular polymers in solution.^[57,60]

The molecular structures of the squaraine dyes designed by us are depicted in Scheme 2.4. One set of dyes was based on the well-known *para-N,N*-dimethylamino substitution

motif. The other was based on the *para*-hydroxy motif which has already been reported by Treibs and Jacob in 1965^[12] but received less attention in the past decades^[33,61–63] which was presumably due to the sensitivity of this type of compounds to oxidation that has been suggested by another literature report.^[64] All presented structures combined the squaraine motif with amide functionalized side chains for the formation of hydrogen bonds. Owing to the *ortho*-position of the amide to the quadratic core, the compounds were expected to form intramolecular hydrogen bonds which were in turn suggested to result in rotational isomerism.^[19]



Scheme 2.4: Para-N,N-dimethylamino substituted squaraine dyes and para-hydroxy substituted squaraine dyes as obtained by the condensation reaction of squaric acid with electron-rich arenes.

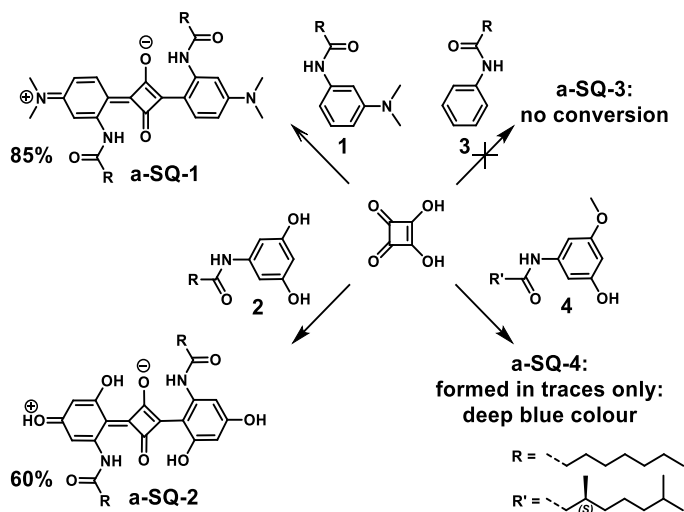
This chapter focuses on the synthesis and characterization of the novel amide substituted squaraine dyes. In an initial screening experiment, we tested four different types of amide functionalized substrates upon the formation of squaraine dyes via the condensation with squaric acid. We identified two suitable reagents and prepared two sets of squaraine dyes (Scheme 2.4). We fully characterized the compounds by nuclear magnetic resonance (NMR), Fourier-transform infrared (FT-IR) spectroscopy and matrix-assisted laser ionization time of flight mass spectrometry (MALDI-TOF-MS). The *N*-(3-(dialkylamino)phenyl)-amide based dyes were highly stable and exhibited observable rotational isomerism in chloroform and 1,1,2,2-tetrachloroethane. Subsequently, we functionalized the *N*-(3-(dialkylamino)phenyl)-amide based dye that contained terminal double bonds with oligo(dimethylsiloxanes) (oDMS) of three discrete lengths. The bulk properties of the materials such as thermal transitions and bulk ordering were investigated by a combination of X-ray scattering, differential scanning calorimetry (DSC) and polarized optical microscopy (POM). The optical properties of all described compounds will be discussed in Chapter 3.

2.2 Synthesis and characterization of novel squaraine dyes

2.2.1 Nucleophilic reagents as a prerequisite for squaraine dye formation

We started our study by a screening experiment to probe the formation of squaraine dyes between squaric acid and the four different amide substituted reagents **1-4** (Scheme 2.5) that distinguish in the number and type of additional substituents of the phenyl ring. Reacting **1** with squaric acid resulted in the formation of the green squaraine dye **a-SQ-1**, which was obtained in high yield (85%) and high purity. Since the reaction was very efficient, we moved on to reagent **2**. Instead of the *N,N*-dimethylamino group, **2** contained two hydroxy groups that were located in the meta positions to the amide. Gratifyingly, the reaction of **2** with squaric acid resulted in the formation of the blue squaraine dye **a-SQ-2** which was obtained in moderate yield (60%). We found that attempting the condensation of squaric acid with **3** did not result in the formation of an intense color. The absence of conversion was confirmed by ¹H NMR spectroscopy. We conclude – in agreement with a report by Griffiths *et al.*^[33] – that reagents lacking highly electron-rich substituents cannot be used to synthesize squaraine dyes. Finally, the synthesis of squaraine dye **a-SQ-4** was attempted. Similar to the observation from **a-SQ-2**, the formation of a deep blue color was noticed after heating the reaction mixture to 125 °C. ¹H NMR spectroscopy indicated that the conversion was very low (unreacted **4** was still present after 24 hours reaction time) and accompanied by the formation of an undesired byproduct which prevented the isolation of **a-SQ-4**.

The screening experiment indicated that the formation of amide functionalized squaraine dyes can be performed by the condensation of squaric acid with *N,N*-dimethylamino and dihydroxy substituted amidobenzenes. In the absence of electron donating groups, no conversion was achieved and in case of the slight modification to hydroxy methoxy substituted amidobenzenes only a chemically very unstable compound was formed. The details of the synthetic procedures and the molecular characterization will be explained in the following subchapters.



Scheme 2.5: The reagents **1**, **2**, **3** and **4** were tested upon reaction with squaric acid. Reagents **1** and **2** were used to prepare the squaraine dyes **a-SQ-1** and **a-SQ-2**. The attempted reaction of **3** with squaric acid did not show conversion even after a prolonged period of time. Using **4** resulted in the formation of a deep blue color but only traces of **a-SQ-4**.

2.2.2 Synthesis and characterization of *para*-*N,N*-dimethylamino substituted squaraine dyes **a-SQ-1**, **S-SQ-1** and **u-SQ-1**

Para-*N,N*-dimethylamino substituted squaraine dyes were prepared both in achiral (**a-SQ-1**) and chiral (**S-SQ-1**) form. Additionally, a third derivative that contained side chains with terminal double bonds (**u-SQ-1**) was prepared. The molecular structures of these synthesized dyes are given in Figure 2.2.

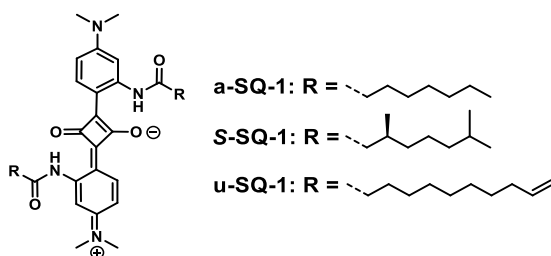
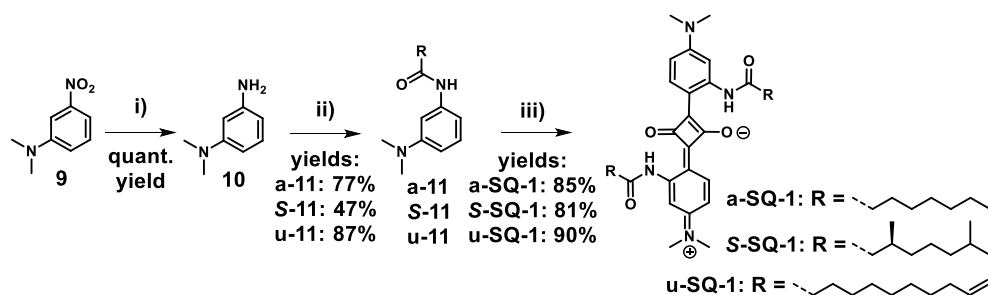


Figure 2.2: Molecular structures of the synthesized squaraine dyes **a-SQ-1**, **S-SQ-1** and **u-SQ-1**.

To enable the synthesis of the chiral **S-SQ-1** derivative with high enantiopurity, we selected commercially available (*S*)-(-)- β -citronellol (obtained from Takasago International Corporation) as an affordable commercially accessible starting material with high enantiomeric excess (98.4% ee).^[65] From this, (*S*)-3,7-dimethyloctanoyl chloride **8** was

prepared according to the procedure by Nieuwenhuizen *et al.* in an overall yield of 74% and in high purity.^[66] As depicted in Scheme 2.6, the synthesis of the squaraine dyes was started by the reduction of the nitro group in **9** in a hydrogen atmosphere using Pd/C as catalyst. The aromatic amine **10** was obtained in quantitative yield. Reaction of **10** with the chiral acid chloride **8** in dry dichloromethane (DCM) yielded chiral **5-11**. The same reaction conditions were also used to react **10** with the commercially available octanoyl chloride or undec-10-enoyl chloride, respectively. Compounds **a-11**, **S-11** and **u-11** were obtained in moderate to high yields (47-87%). In a final step, squaraine dyes **a-SQ-1**, **S-SQ-1** and **u-SQ-1** were prepared by the twofold condensation of squaric acid with the respective amide substituted reagent under constant water removal using a Dean-Stark trap. The successful dye formation was indicated by the development of an intense green color. After purification by recrystallization from acetonitrile, the dyes were obtained as green solids in high (81-90%) yields.



Scheme 2.6: Synthesis of para-N,N-dimethylamino substituted squaraine dyes a-SQ-1, S-SQ-1 and u-SQ-1. Reagents and conditions: i) Pd/C, H₂, EtOAc, R.T., 32 h, ii) aliphatic acid chloride, triethylamine, DCM, 0 °C - R.T., 16 h, iii) squaric acid, n-propanol, 100 °C - R.T., 20 h.

All three dyes were fully characterized by NMR and FT-IR spectroscopy and MALDI-TOF mass spectrometry. The results showed that the final compounds were obtained in high purity. The MALDI-TOF-MS spectrum depicted in Figure 2.3a shows only one peak at 602.42 Da which corresponds with the exact mass of **a-SQ-1**. The FT-IR spectrum in Figure 2.3b indicated the presence of the conjugated π -system which exhibits vibrations at 3096 cm^{-1} ($\nu_{\text{aryl-C-H}}$), 1706 cm^{-1} ($\nu_{\text{aryl-C-H}}$, overtone) and 1609 cm^{-1} ($\nu_{\text{C=C}}$, stretching). The amide's $\nu_{\text{C=O}}$ stretching vibration was superimposed by the vibrations of the aryl system. N-H bending $\nu_{\text{N-H}}$ was noticed at 1578 cm^{-1} . Weak absorption bands at 3140 cm^{-1} and 3100 cm^{-1} were assigned to N-H stretching of protons that are involved in hydrogen bonds.^[67] These bands were also observed when the spectrum is recorded in a 4 mM solution in the good solvent chloroform (red line in Figure 2.3b and c) which suggested that the hydrogen bonds are formed intramolecularly.

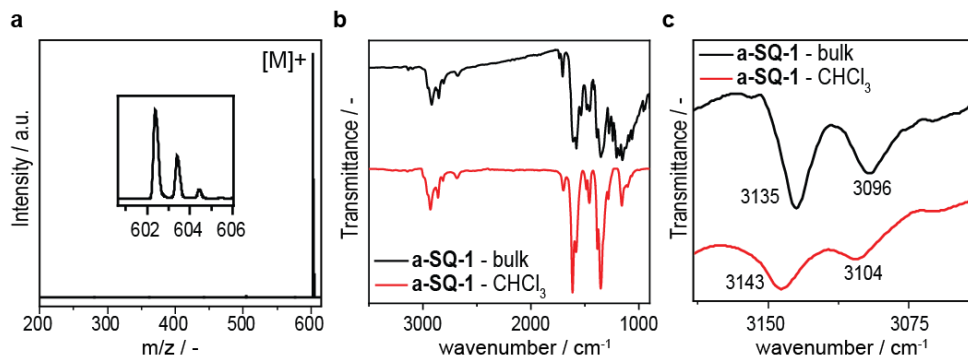


Figure 2.3: (a) MALDI-TOF-MS and (b) FT-IR spectra of **a-SQ-1**. (c) zoom-in of (b).

The ¹H NMR and ¹³C spectra recorded for **a-SQ-1** showed two spin systems that were indicative of the formation of two different isomers (Figure 2.4). According to the integration of the ¹H NMR spectrum, the ratio of the two isomers was 1.00:0.64 (in-set in Figure 2.4a). The formation of both 1,2- and 1,3-regioisomers was excluded as possible explanation for the two spin systems since our reaction conditions have been reported to result in the formation of 1,3-products exclusively^[18] and thin layer chromatography showed the presence of only one compound. Another possible explanation of the two spin systems which has already been reported in the literature of squaraine dyes is rotational isomerism.^[19] Kazmaier *et al.*^[19] proposed a hindered rotation in the squaraine backbone by the formation of intramolecular hydrogen bonds from the *ortho*-hydroxyl substituents to the oxygen atoms attached to the quadratic core. Since FT-IR spectroscopy indicated the formation of intramolecular hydrogen bonds in **a-SQ-1** in chloroform solution which is also the solvent used for the NMR experiments, we assumed that the *ortho*-amide substituents were capable of the formation of similar hydrogen bonds as the *ortho*-hydroxyl substituents of the literature system. As depicted in Scheme 2.7, the proposed intramolecular hydrogen bonds resulted in a hindered the rotation about the C(2)–C(3)-bond which induced the two spin systems in the NMR spectra.

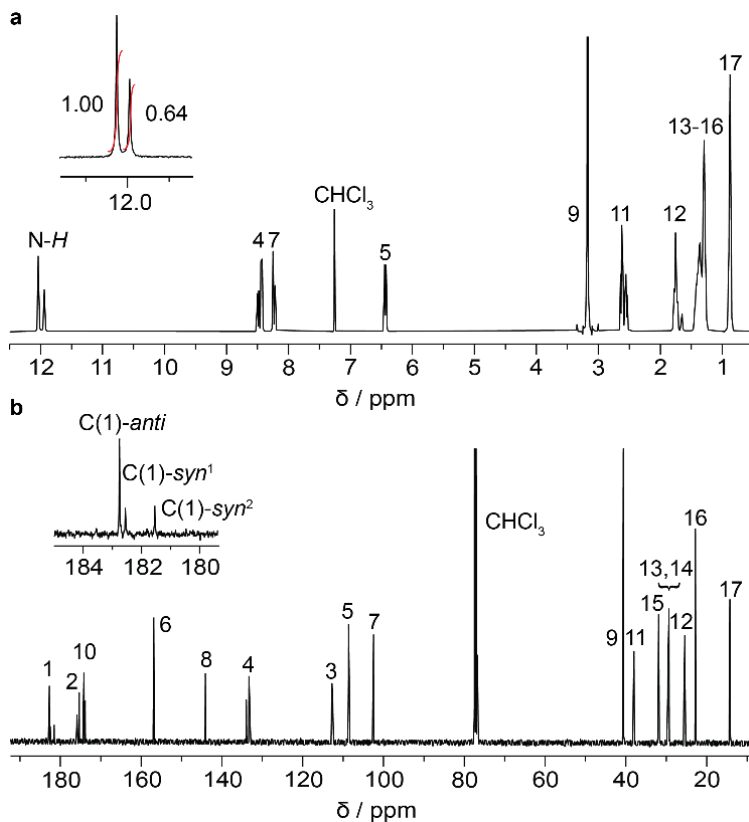
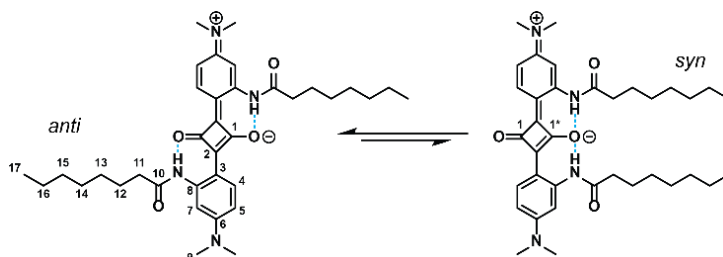


Figure 2.4: (a) ^1H NMR spectrum recorded for $\alpha\text{-SQ-1}$ in chloroform- d_1 (400 MHz) set-in: integration of the signals of the N-H protons; (b) ^{13}C NMR spectrum recorded for $\alpha\text{-SQ-1}$ in chloroform- d_1 (100 MHz).



Scheme 2.7: Molecular structures of the proposed rotational isomers of $\alpha\text{-SQ-1}$.

We performed 2D NMR experiments (heteronuclear single quantum coherence spectroscopy and heteronuclear multiple bond correlation) to assign the recorded signals to their corresponding nuclei in the chemical structure. In the low-field region of the ^1H NMR spectrum, four groups of signals were visible. The singlets at 12.0 and 11.9 (N-H) ppm

originated from the protons attached to the amides. For these two signals, the presence of the two spin systems was most apparent. The doublets at 8.55 and 8.49 (H-4) ppm ($J = 9.2$ Hz), 8.31 and 8.30 (H-7) ppm ($J = 2.4$ Hz) as well as 6.48 (H-5) ppm (dd, $J_1 = 9.2$ Hz, $J_2 = 2.4$ Hz) originated from the protons which were attached to the phenyl rings. The singlet at 3.18 (H-9) ppm originated from the protons of the methyl groups of the aromatic amine. The signals below 2.63 ppm (two multiplets of N-CH₂ of the two spin systems) (H-11) belonged to protons in the aliphatic side chains (H-12 – H-16). The characteristic triplet for the terminal methyl groups was present at 0.88 (H-17) ppm ($J = 6.0$ Hz). The ¹³C spectra revealed peaks of sp²-hybridized carbons from the central squaric unit (C(1) and C(2)), the amide (C(10)) and the phenyl rings (C(3) – C(8)) in the low-field region. Similar to the ¹H spectrum, two spin systems were apparent in the ¹³C NMR spectrum. High-field signals were caused by the resonance of the aliphatic carbon atoms of the *N,N*-dimethylamino groups (C(9)) and the linear side chain (C(11) – C(16)). The terminal methyl groups (C(17)) posed the most high-field signals with chemical shifts δ of 14.53 ppm.

In order to differentiate between the *syn*- and *anti*-rotamers, we focused on the NMR signals of the carbon atoms of the quadratic core that were labelled C(1). The in-set in the ¹³C spectrum (Figure 2.4) showed one signal for C(1) in the major form. In contrast, two signals were noticed for C(1) in the minor form. The major form was assigned to the *anti*-rotamer, since it had C_{2h} point symmetry that resulted in magnetic equivalence of carbon atoms C(1). As a consequence of the magnetic equivalence, only one signal was recorded for both nuclei in ¹³C spectrum. The minor form was assigned to the *syn*-rotamer that had C_{2v} symmetry, which resulted in magnetic inequivalence of the two carbon atoms C(1) and the signal splitting in the ¹³C spectrum.

2.2.3 Rotational isomerism of squaraine dye a-SQ-1

We continued our study with the investigation of the rotational isomerization of squaraine dye **a-SQ-1** using computational analysis to confirm the proposed molecular structures of the rotamers. In order to increase the calculation speed, we simplified the chemical structure of **a-SQ-1** by replacing the octyl chains by methyl groups. We studied the conformation of **a-SQ-1*** using a conformational search using the program Macromodel^[68] with OPLS3 force field^[69] and a solvent model for chloroform.^[70,71] The DFT calculations were performed by Tobias Schnitzer. The geometries of the obtained low energy structures were optimized by density functional theory calculations on a B3LYP-D3/6-31G** level.^[72–75] The calculations yielded two planar low energy structures (Figure 2.5) that suggested the complete conjugation of the π -system (which is in good agreement with the absorption properties of **a-SQ-1** which will be discussed in detail in Chapter 3).^[1] The amide groups of both structures form intramolecular hydrogen bonds to the oxo-substituents of the squaraine core which was in agreement with the findings from FT-IR spectroscopy. Similar to the molecular structure of the rotamers proposed by Kazmaier *et al.*,^[19] the structures differed in the orientation of the amide substituents. In the lowest energy structure, each amide group was hydrogen bonded to a different oxygen atom ("*anti*-conformer"). In

contrast, both amide substituents of the second conformer were bonded to the same oxygen substituent (“*syn*-conformer”). Our calculation suggested that the *syn*-conformer is 2.9 kJ/mol higher in energy compared to the *anti*-conformer. The increased stability of the *anti*-conformer was in agreement with the findings from ^{13}C NMR spectroscopy and the energy difference was in good agreement with the report by Kazmaier *et. al.*^[19]

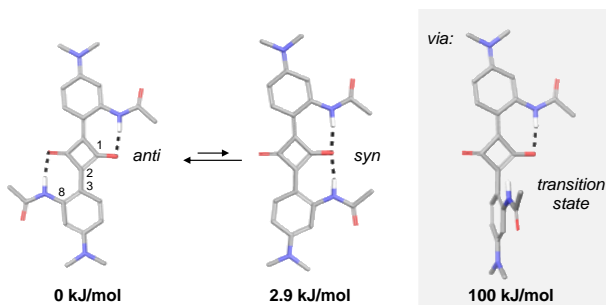


Figure 2.5: Computational analysis of *anti*- and *syn*-rotamer and the transition state of the isomerization of **a-SQ-1***.

Next, we studied the transition state between the two conformers to determine the activation energy for the rotation about the $\text{C}(\text{sp}^2)\text{--C}(\text{sp}^2)$ bond. Using the transition state locator of the program Jaguar, a transition state with a torsion angle of -93° ($\text{C}(1)\text{--C}(2)\text{--C}(3)\text{--C}(8)$) was identified. This conformer was 100 kJ/mol higher in energy compared to the *anti*-conformer which corroborated that both conformers were observed in the NMR spectra recorded at room temperature.

We aimed for also investigating the activation energy barriers for the interconversion of the two rotamers of **a-SQ-1** from our spectroscopic data. We followed the chemical shifts of the protons in a variable temperature (VT) experiment. The signals that were assigned to N-H, H(4) and H(5) of the two conformers were fully separated at room temperature and started to partially overlap when the sample was heated to 50°C . Yet, no coalescence was observed below 61°C , which was the boiling point of the solvent chloroform- d_1 . We reasoned that the rotation about the $\text{C}(2)\text{--C}(3)$ bond was still hindered noticeably at the elevated temperature because of the intramolecular hydrogen bond formation. We replaced the solvent chloroform- d_1 by 1,1,2,2-tetrachloroethane- d_2 (TCE- d_2) as a comparable chlorinated solvent with higher boiling point and continued our VT-NMR study. The solvent replacement resulted observing the signal of the minor rotamer with a higher chemical shift than the signal of the major rotamer (Figure 2.6a). We performed ^{13}C NMR spectroscopy to investigate the origin of the spectral changes. For a comparison, the low field regions of the ^{13}C NMR spectra recorded in chloroform- d_1 , TCE- d_2 and in the 50:50 mixture of both solvents are depicted in Figure 2.6c. Using the geometrical considerations previously used to analyze the ^{13}C NMR spectra recorded in chloroform, the signals indicated that not the *anti*- but the *syn*-rotamer was the preferred form in TCE- d_2 . Hence,

the spectral changes in the ^1H NMR spectrum were ascribed to the changed ratio of *anti*- and *syn*-form from 1.00:0.64 in chloroform- d_1 to 0.70:1.00 in TCE- d_2 . In the 50:50 mixture of both solvents, the ratio was 1.00:0.93 (Figure 2.6b). We ascribed the changed ratios to small enthalpic or entropic changes when replacing the solvent. Such solvent-dependent changes in the conformer ratio have been observed for other systems as well.^[76,77]

In TCE- d_2 , the coalescence of the two spin systems was observed at 64 °C. In general, the spectral changes that are observed during the transition from two spin systems into one depend on spin-spin and spin-lattice relaxation.^[78] The exact analysis of the observed line broadening can be derived from the Bloch equations.^[79] An approximated analysis that is more straightforward and commonly used for determining the free energy of activation for the interconversion of the rotamers is given by Eyring's equations as modified by Shanani-Atidi.^[80,81] The set of equations is particularly useful for a system that contains two unequally populated rotamers. According to the calculations (stated in the experimental part), the coalescence temperature T_c of 64 °C corresponded with the activation energy barrier ΔG^\ddagger_{anti} between the *anti*-conformation and the transition state of 73 ± 1 kJ/mol. Analogously, ΔG^\ddagger_{syn} was 75 ± 1 kJ/mol. The experimentally determined activation energy barrier was lower than expected from the DFT calculations. The difference of both values was ascribed to the solvent which is accounted for only implicitly and the absence of the octadecyl chains in the molecular model structure used for the DFT calculations.

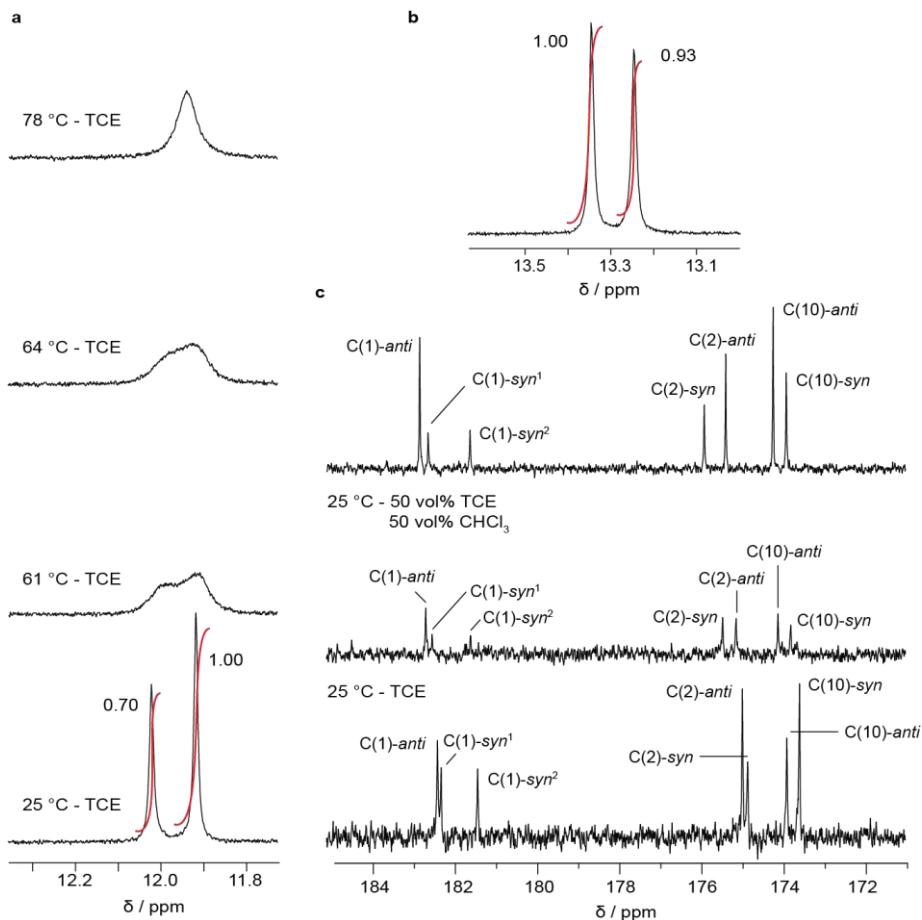


Figure 2.6 (a) ^1H NMR spectra of α -SQ-1 recorded during the VT-NMR study in the solvent 1,1,2,2-tetrachloroethane- d_2 (TCE- d_2) solution (400 MHz). Concentration: 6.6 mM. (b) ^1H NMR spectrum of α -SQ-1 recorded in a 50:50 mixture of TCE- d_2 and chloroform- d_1 at room temperature (400 MHz). (c) ^{13}C NMR spectra recorded in chloroform- d_1 (top) and TCE- d_2 (bottom) and a 50:50 mixture of both solvents (middle) at room temperature (100 MHz).

We assumed that the addition of trifluoroacetic acid (TFA) which is known to break hydrogen bonds, should accelerate the isomerization and induce coalescence of the spin systems also in the low-boiling solvent chloroform- d_1 in which the *anti*-rotamer is more stable. In order to probe our hypothesis, we recorded ^1H NMR spectra at room temperature using 0.01, 0.05, 0.07 and 0.10 vol% TFA- d_1 as a cosolvent (Figure 2.7). The spectrum that was recorded for the concentration of 0.01 vol% cosolvent TFA- d_1 showed a slight spectral broadening of the signals of the two spin systems. The spectral broadening suggested that the addition of TFA- d_1 indeed facilitated the interconversion of the rotamers. For the TFA- d_1 fractions of 0.05 vol% or 0.07 vol%, respectively, the spectral broadening was even more

pronounced and a distinct overlap of the signals of the two spin systems was noticed. Finally, at a concentration of 0.10 vol% TFA- d_1 , only one spin-system was observed which suggested that T_c was reduced to or even below room temperature.

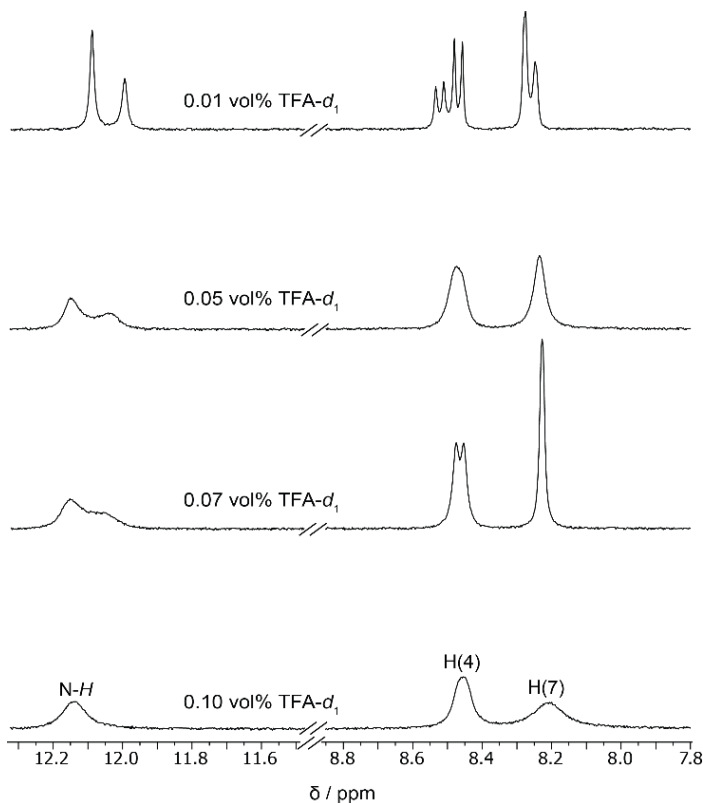


Figure 2.7: ^1H NMR spectrum of **a-SQ-1** (concentration: 6.6 mM) recorded at room temperature in chloroform- d_1 using 0.01-0.1 vol% TFA- d_1 as cosolvent (400 MHz).

The samples containing the cosolvent were subsequently investigated by VT- ^1H NMR spectroscopy. For the cosolvent fraction of 0.01 vol% TFA- d_1 , T_c was still above 50 °C. For the samples that contained 0.05 vol% or 0.07 vol% TFA- d_1 , T_c was determined at 45 °C and 35 °C, respectively. According to calculations using Eyring's equations, activation energy barriers ΔG_{syn}^\ddagger and ΔG_{anti}^\ddagger of the two rotamers of **a-SQ-1** are 69 ± 1 kJ/mol and 72 ± 1 kJ/mol when 0.05 vol% TFA- d_1 were present as cosolvent. When the concentration of the cosolvent was increased to 0.07 vol%, the activation energy barriers ΔG_{syn}^\ddagger and ΔG_{anti}^\ddagger were reduced to 67 ± 1 kJ/mol and 69 ± 1 kJ/mol. The decrease of T_c with an increasing fraction of TFA- d_1 corroborated the accelerating effect of the cosolvent on the interconversion of the rotamers.

Since the *para-N,N*-dimethylamino substituted squaraine dyes were synthetically easily accessible and also showed the expected rotational isomerism, we moved on to the investigation of *p*-hydroxy substituted squaraine dyes. Owing to the chemical structure of the used reagents, these dyes did not only contain amide substituents as hydrogen bond donors in the ortho position of the quadratic core but also hydroxy groups. The compounds were hence expected to exhibit an even stronger hindered rotation about the squaraine backbone.

2.2.4 Synthesis and characterization of *para*-hydroxy substituted squaraine dyes **a-SQ-2** and **S-SQ-2**

Para-hydroxy substituted squaraine dyes were prepared both in achiral (**a-SQ-2**) and chiral (**S-SQ-2**) form. The molecular structures of the synthesized dyes are given in Figure 2.8 and the synthetic approach is depicted in Scheme 2.8.

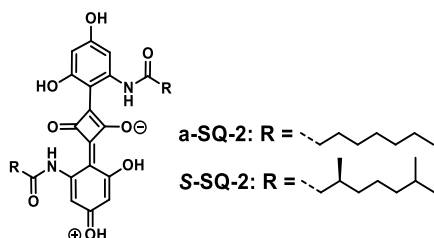
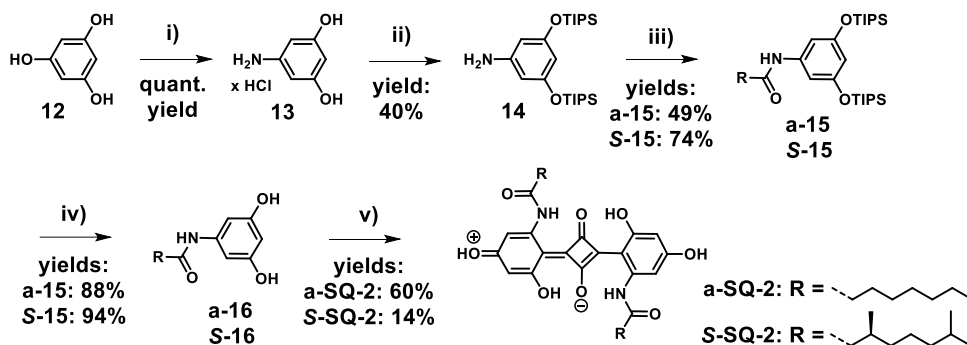


Figure 2.8: Molecular structures of the synthesized squaraine dyes **a-SQ-2** and **S-SQ-2**.

The chosen synthetic route was inspired by reports on *p*-hydroxy substituted squaraine dyes^[33,64] and studies on the amidization of phloroglucinol.^[82–84] The synthesis was started with the amination of phloroglucinol **12** in aqueous ammonia solution. Acidification after the amination yielded the hydrochloride **13**. The hydroxy groups of **13** were protected with triisopropylsilane (TIPS) groups to increase the solubility and enable the purification of the aromatic amine by column chromatography. The colorless oil **14** was reacted with two different aliphatic acid chlorides to prepare a chiral and an achiral amide derivative. Reaction of **14** with the chiral (*S*)-3,7-dimethyloctanoyl chloride **8** in dry DCM yielded chiral **S-15**. The same reaction conditions were also used to react **14** with the commercially available octanoyl chloride to synthesize the achiral counterpart **a-15**. Removal of the TIPS protection groups using tetra-*n*-butylammonium fluoride (TBAF) yielded the desired reagents **S-16** and **a-16**.

The condensation of the reagents **S-16** and **a-16** with squaric acid was performed using the same conditions as previously used for the synthesis of the *para-N,N*-dimethylamino substituted squaraine dyes. The successful dye formation was indicated by the development of an intense blue color. Purification was performed by the dispersion of the product in a water / EtOAc mixture and subsequent filtration. The purification was

accompanied by a substantial loss of product when the reaction was performed on smaller scale (used for **S-SQ-2**).



Scheme 2.8: Synthesis of *para*-hydroxy substituted squaraine dyes **a-SQ-2** and **S-SQ-2**. Reagents and conditions: i) 1. $\text{NH}_3(\text{aq.})$, water, R.T., 16 h, 2. $\text{HCl}(\text{aq.})$ R.T. - 40 °C, 20 mbar, ii) TIPSCl, imidazole, THF, 0 °C - R.T., 16 h., iii) aliphatic acid chloride, triethylamine, DCM, 0 °C - R.T., 16 h, iv) TBAF, THF, 0 °C - R.T., 1 h., v) squaric acid, *n*-propanol, 100°C - R.T., 20 h.

The dyes **a-SQ-2** and **S-SQ-2** were fully characterized by ^1H NMR, FT-IR, MALDI-TOF-MS and elemental analysis. The solubility of both compounds was found to be very low in all common organic solvents, which prevented characterization by ^{13}C NMR spectroscopy. Exemplary for both squaraine dyes, the ^1H NMR, FT-IR and MALDI-TOF-MS spectra recorded for **S-SQ-2** are shown in Figure 2.9. The MALDI-TOF-MS spectrum of **S-SQ-2** showed one peak at 659 Da which corresponded well with the exact mass of the [**S-SQ-2-Na** $^+$] adduct. The spectrum contained a high background noise which was ascribed to an impaired preparation of the MALDI-TOF-MS sample stemming from the very low solubility of **S-SQ-2** in all organic solvents with low boiling point. The purity of the compound was further assessed by elemental analysis which indicated the correct ratio of C, H, N and O atoms. The ^1H NMR spectrum showed only one spin system that indicated the formation of only one regioisomer. In the low-field region of the ^1H NMR spectrum, four groups of signals were visible. The strongest deshielding is observed for the singlets at 12.41 (H-1/2) and 11.25 (H-1/2) ppm which indicates the close vicinity of the respective protons to the electron-poor quadratic core of the dye. The singlets at 7.58 (H-3/4) and 5.97 (H-3/4) ppm were deshielded less and assigned to the protons which are attached to the aromatic ring structure. The signals below 2.41 ppm (multiplets of N- CH_2) (H-5) belonged to protons in the aliphatic side chains. The characteristic doublets for the methyl groups were present at 0.92 ppm ($J = 6.7$ Hz, H-9) and 0.83 ppm ($J = 6.6$ Hz, H-10). The signals of the protons of the hydroxy groups in *para* positions to the quadratic core were not noticed in the NMR spectrum. The absence of these signals was ascribed to a rapid exchange which was induced by their high acidity that has also been mentioned in a literature report on *para*-hydroxy substituted squaraine

dyes.^[33] The FT-IR spectrum recorded in the solid state, showed a broad vibration band with wavenumbers around 3100 cm^{-1} which corroborated acidity of these. The conjugated π -system exhibited vibrations at 1610 cm^{-1} ($\nu_{\text{C=C}}$, stretching). The shift of these vibrations to smaller wavenumbers was due to the close vicinity of the electron-poor central quadratic unit. The very low intensity of the C=O stretching at wavenumbers around 1680 cm^{-1} was in accordance with literature reports on squaraine dyes that suggested that the C-O bonds of the squaric core have very low double bond character and the electrons are fully localized in the central squaric unit.^[18] The amides N-H bending $\nu_{\text{N-H}}$ was found at 1583 cm^{-1} . Due to the low solubility of **S-SQ-2** in all tested solvents, the formation of intramolecular hydrogen bonds in solution could not be investigated.

The proposed chemical structure of **S-SQ-2** contained the amide substituents in the *ortho*-position of the quadratic core. The absence of a *para*-amido substituted dye was assigned to the mesomerism of the amide since this type of mesomerism results in a positive charge on the nitrogen atom and this is unsuitable due to the mesomeric forms of squaraine dyes. Although the similarity of the molecular structure of **S-SQ-2** with the *para*-*N,N*-dimethylamino substituted squaraine dyes suggested the presence of rotational isomerism, only one spin system was noticed. Since the chemical characterization had proven the chemical structure of **S-SQ-2**, we assumed that rotational isomerism was probably still present, but not noticed in the NMR spectra. The absence of the second spin system likely stemmed from one of the two following scenarios. One of the rotamers was energetically much more favorable than the other. As a result, the second rotamer was not distinguishable from the noise in the NMR spectrum. Otherwise, the fourfold intramolecular hydrogen bond formation resulted in magnetically very similar environments for the nuclei in *syn*- and *anti*-form which in turn resulted in chemical shifts that were indistinguishable in the recorded NMR spectrum.^[20]

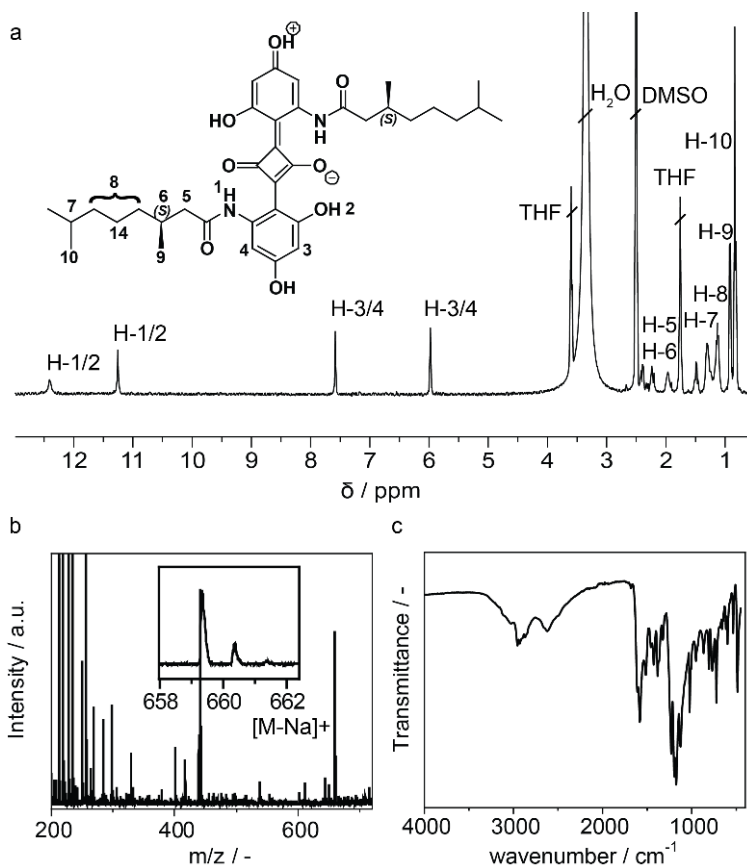


Figure 2.9: (a) ^1H NMR spectrum recorded for **S-SQ-2** in $\text{DMSO-}d_6$ (400 MHz); (b) MALDI-TOF-MS and (c) FT-IR spectra of **S-SQ-2**.

2.2.5 Chemical stability of *p*-hydroxy substituted squaraine dyes **a-SQ-2** and **S-SQ-2**

Since **a-SQ-2** and **S-SQ-2** are structurally related to bis(2,4,6-tri-hydroxyphenyl) squaraine which is a compound that has been described as extremely sensitive to oxidation,^[64] we assessed the chemical stability of **a-SQ-2** and **S-SQ-2**. Figure 2.10 shows the ^1H NMR spectrum that was recorded for the solution of **S-SQ-2** in $\text{DMSO-}d_6$ after sonication for 30 minutes in a sonication bath. When comparing the spectrum with the spectrum shown in Figure 2.9, additional signals with chemical shifts close to the protons H-3/4 are noticed. Furthermore, the ratio of the alkyl protons to the aryl protons was doubled. The difference in integration indicated a decomposition of 50% of the dye within 30 minutes of sonicating. As a result, we conclude that **a-SQ-2** and **S-SQ-2** have a similarly limited chemical stability as bis(2,4,6-tri-hydroxyphenyl)squaraine and must be handled with care during the investigation of their photophysical properties.

Since *p*-hydroxy substituted squaraine dyes exhibited a low solubility and impaired chemical stability, we continued our study with embedding our *para*-*N,N*-dimethylamino substituted squaraine dyes into a siloxane matrix to fabricate squaraine dye based soft materials.

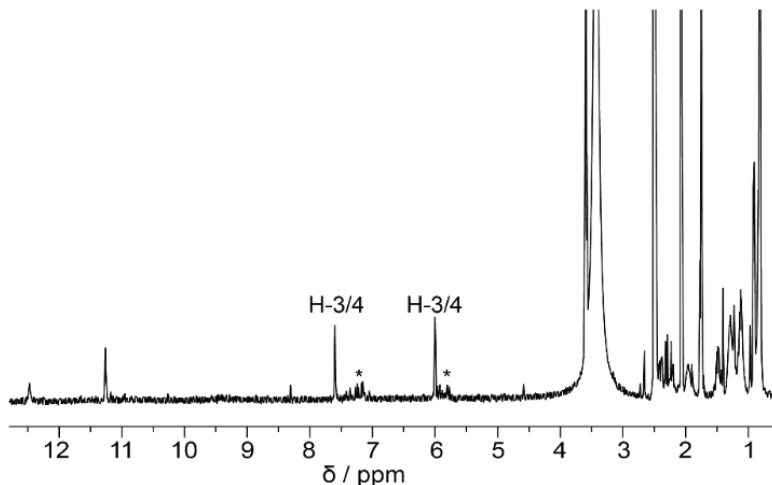


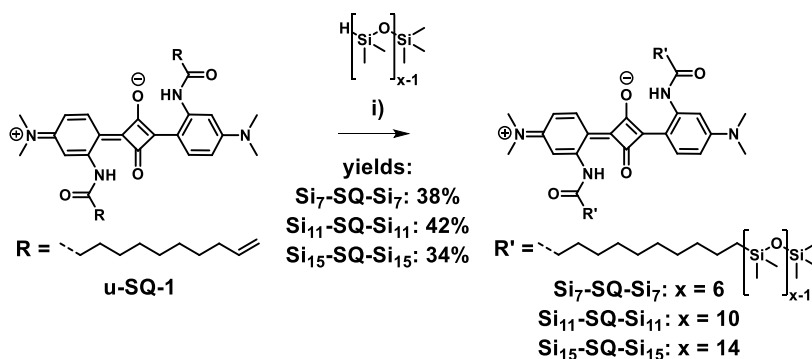
Figure 2.10: ^1H NMR spectrum recorded for **S-SQ-2** in $\text{DMSO-}d_6$ (400 MHz) after the sample had been stored in a sonication bath for 30 min.

2.2.6 Synthesis and characterization of oDMS-functionalized *para*-*N,N*-dimethylamino substituted squaraine dyes

Liquid crystals (LCs) and block copolymers (BCPs) are well-known for the formation of precise lamellar, cylindrical, bicontinuous cubic and spherical phases with molecular dimensions.^[85] In the LC systems, the order is established by the combination of directionality of the mesogen and the mobility of the side chain(s). In case of BCPs, order results from the microphase separation of the immiscible blocks that are incorporated in the molecular structure. Several examples for these types of nanomaterials have been suggested for various applications in organic electronics, optics or membranes.^[86–88] Embedding the squaraine motif that has already been reported for a broad range of optoelectronic applications^[10,11,89] in a soft siloxane matrix is possibly useful for application in neuromorphic computing which aims for the targeted creation of conducting paths in materials with tunable conductivity.^[90,91] Additionally, the materials are also potentially useful for the fabrication of organic photodetectors based on the bulk photovoltaic effect. In such systems that have already been described in the literature, ordered materials with permanent dipole moment (e.g. columns of stacked amides) generate a photocurrent by the absorption of visible light.^[92]

The synthesis of oligo(dimethylsiloxane) (oDMS) functionalized *para*-*N,N*-dimethylamino substituted squaraine dyes was achieved by the twofold hydrosilylation of

u-SQ-1 (synthesis has been described in subchapter 2.2.2). We selected three different oDMS with discrete chain lengths (seven, eleven or fourteen silicon atoms) to study the consequences of oDMS-functionalization on material properties such thermal phase-transition temperatures and bulk morphologies. The hydrosilylation was performed using Karstedt's catalyst. The corresponding reaction scheme for the hydrosilylation is depicted in Scheme 2.9. During the hydrosilylation reaction a partial isomerization of the terminal double bonds was observed. The isomerization is a common side reaction and transforms the terminal olefin bond into an internal olefin which causes its deactivation for the hydrosilylation.^[93] The desired double oDMS functionalized products were isolated in moderate yields (34-42%) using recycle gel permeation chromatography (rGPC). The compounds showed a deep green color and had a paste-like appearance.



Scheme 2.9: Synthesis of oDMS-functionalized para-N,N-dimethylamino substituted squaraine dyes. Reagents and conditions: i) oDMS-H, Karstedt's catalyst, DCM, R.T., 3 h.

¹H and ¹³C NMR indicated the successful reaction of **u-SQ-1** with the discrete oDMS by the disappearance of the signals from the C=C bonds. We note that the rotational isomerism of **u-SQ-1** with the ratio of 1.00:0.64 for major and minor forms is observed in chloroform solutions for the oDMS functionalized compounds, too. FT-IR spectra recorded after the functionalization show vibrations at 1258-1257 cm⁻¹, 1020-1015 cm⁻¹ and 792-790 cm⁻¹. The bands are assigned to the ν_{Si-C} and ν_{Si-O} stretching and match well with the values reported for this functional group in the literature.^[94] Depending on the length of the oDMS chain, the recorded MALDI-TOF-MS spectra show signals that appear exclusively at 1720.87 Da, 2313.98 Da or 2907.12 Da, respectively. The values matched perfectly with the calculated m/z ratios for the singly charged oDMS-functionalized *para*-N,N-dimethylamino substituted squaraine dyes and indicated the high purity of the compounds.

The thermal properties of the materials were investigated by dynamic scanning calorimetry (DSC) and polarized optical microscopy (POM). As depicted in the POM images in Figure 2.11a, all three soft materials showed birefringent textures at room temperature that were indicative of anisotropic materials. DSC indicated a thermal phase transition at 150 °C (Figure 2.11b). Since birefringent structures disappeared above this temperature it

was assigned to the isotropization temperature. Interestingly, another phase transition was observed around 125 °C in the DSC traces for all materials. This transition was not accompanied by changes of the birefringent texture.

The isotropization temperature of **u-SQ-1** which does not contain oDMS chains was reached at 230 °C. The decrease of the isotropization temperature after functionalization indicated that the attachment of oDMS had a plasticizing effect on the material. We note that none of our squaraine dyes were chemically stable in the isotropically melted state. Thermogravimetry indicated that **u-SQ-1** decomposed in the melt and ¹H NMR spectroscopy indicated that oDMS attached squaraine dyes decomposed after annealing the materials for several minutes in the isotropic melt. Hence, the rather broad temperature windows of the thermal transitions noticed in the DSC traces were assigned to a partial thermal decomposition that had already occurred during annealing in the first heating cycle.

Finally, the bulk morphologies of **Si₇-SQ-Si₇**, **Si₁₁-SQ-Si₁₁** and **Si₁₅-SQ-Si₁₅** were investigated by two-dimensional (2D) transmission X-ray scattering. The X-Ray scattering study was performed in collaboration with Brigitte Lamers. The data were acquired in medium- and wide-angle modes (MAXS and WAXS, $0.1 < q < 30 \text{ nm}^{-1}$). All three materials showed multiple scattering peaks which indicated the presence of well-defined hexagonally packed cylinders as bulk morphologies (Figure 2.11c). **Si₇-SQ-Si₇** had a domain spacing of 5.2 nm. For **Si₁₁-SQ-Si₁₁** and **Si₁₅-SQ-Si₁₅** these values were 5.7 nm and 6.3 nm, respectively. We note that **Si₇-SQ-Si₇** and **Si₁₁-SQ-Si₁₁** contained not only one but two types of hexagonally packed cylinders. In contrast, **Si₁₅-SQ-Si₁₅** that had the longest oDMS chains in the series showed the formation of only one type of hexagonally packed cylinders.

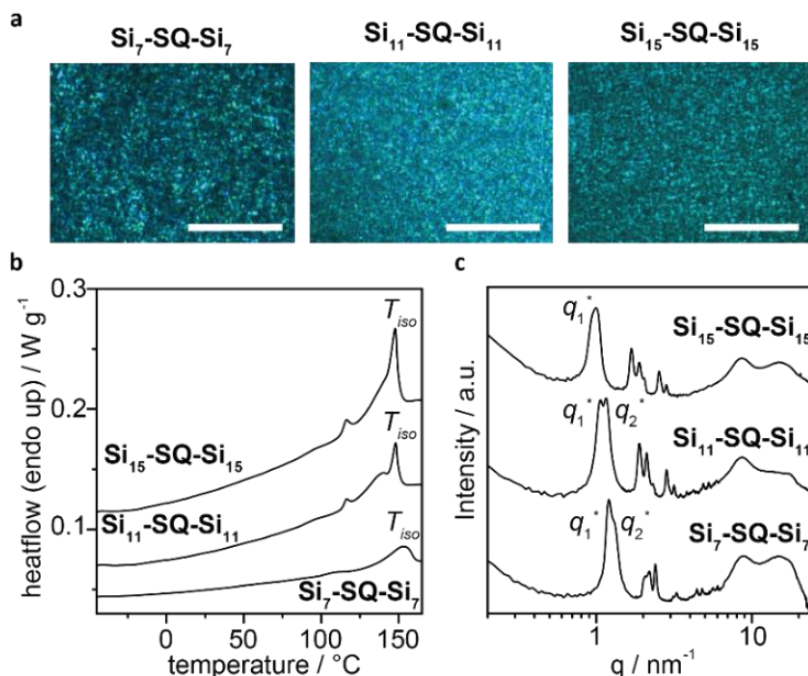


Figure 2.11: (a) POM micrographs of $\text{Si}_7\text{-SQ-Si}_7$, $\text{Si}_{11}\text{-SQ-Si}_{11}$ and $\text{Si}_{15}\text{-SQ-Si}_{15}$ which were recorded at room temperature after heating and cooling cycle. White bar: 100 μm . (b) DSC heating traces (second cycle, heating rate 2 K min^{-1}). (c) 1D Transmission X-ray SAXS data indicates hexagonal packed cylinders as primary lattice for all materials. In case of $\text{Si}_7\text{-SQ-Si}_7$, $\text{Si}_{11}\text{-SQ-Si}_{11}$, reflections which are indicative of a second hexagonally packed lattice were found, too.

2.3 Conclusions

The formation of squaraine dyes is commonly achieved by the twofold condensation of squaric acid with highly electron-rich reagents such as *N,N*-dialkylanilines. We investigated the reactivity of squaric acid towards four chemically different reagents and found that amide substituted dihydroxy-benzenes are another suitable class of substrates for the preparation of squaraine dyes. We used both *N,N*-dialkylanilines and dihydroxy-benzenes that were functionalized with amide substituents to prepare two sets of novel squaraine dyes. Each set comprised a chiral and an achiral derivative. In contrast to the dihydroxy-benzene based dyes, we observed rotational isomers for the *N,N*-dialkylanilines substituted dyes in chloroform- d_1 and TCE- d_2 solutions. Experimental data and DFT calculations suggested that for both rotamers, the squaraine backbone was in a fully planar conformation. The hydrogen atoms of the amide substituents formed intramolecular hydrogen bonds to the oxygen atoms that were attached to the quadratic core. Whereas the amide substituents were located on opposite sides of the molecule in the *anti*-form, they were on the same side in the *syn*-form. We found that TCE- d_2 favored the formation

of the *syn*-rotamer and chloroform- d_1 the formation of the *anti*-rotamer. The rate of the interconversion between both rotamers was increased by the addition of TFA- d_1 as a cosolvent which was breaking the intramolecular hydrogen bonds. We showed that a derivative of the chemically stable *N,N*-dimethylamino amide substituted squaraine dyes could be functionalized with terminal olefinic bonds and reacted with discrete oligomeric siloxanes using the Karstedt-catalyzed hydrosilylation. The obtained soft materials showed ordering on the nanoscopic scale with dimensions that depended on the length of the discrete oligomeric siloxane side chain. The ordering of the semiconducting cores in the cylindrical morphology is expected to generate semi conducting pathways through the insulating siloxane matrix with potential application in organic electronics. The optical properties and optoelectronic applications of all prepared squaraine dyes will be investigated in the following chapter.

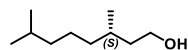
2.4 Experimental Section

2.4.1 Materials and Methods

All chemicals were purchased from commercial sources and used without further purification. Dry solvents were obtained with an MBRAUN Solvent Purification System (MB-SPS). Reactions were followed by thin-layer chromatography (TLC) using 60-F254 silica gel plates from Merck and visualized by UV light at 254 nm. Silica column purifications were performed on a Grace Reveleris X2 automated column machine with Reveleris Silica Flash Cartridges and on a Biotage Isolera 1 with Biotage SNAP KP-SIL columns. Recycle gel permeation chromatography was performed on a SHIMADZU LC 10AD VP liquid chromatograph coupled with a SHIMADZU SPD 10AV VP UV/Vis detector. ^1H - and ^{13}C -NMR spectra were recorded with a Varian Mercury Vx 400 MHz. Deuterated solvents were purchased from Cambridge Isotope Laboratories and are indicated for each measurement. Chemical shifts (δ) are expressed in ppm and are referred to the residual peak of the solvent. Peak multiplicity is abbreviated as s: singlet; d: doublet, q: quartet; p: pentet; m: multiplet; dd: double doublet; dt: double triplet; dq: double quartet. MALDI-TOF spectra were recorded with Bruker Autoflex Speed using α -cyano-4-hydroxycinnamic acid (CHCA) or trans-2-[3-(4-tert-butylphenyl)-2-methyl-2-propenyl-iden]-malononitrile (DCBT) as matrix. FT-IR spectra were recorded on a PerkinElmer Spectrum One spectrometer. Polarized optical microscopy (POM) was performed on an optical microscope from Jenaval. Images were recorded using an Infinity1 camera provided by Lumenera. DSC was performed on a Q2000 from TA Instruments. Bulk small angle X-ray scattering (SAXS) was performed on an instrument from Ganesha Lab. The flight tube and sample holder are all under vacuum in a single housing, with a GeniX-Cu ultra low divergence X-ray generator. The source produces X-rays with a wavelength (λ) of 0.154 nm and a flux of 1×10^8 ph s $^{-1}$. Scattered X-rays were captured on a 2D Pilatus 300K detector with 487×619 pixel resolution. The sample-to-detector distance was 0.084 m (WAXS mode) or 0.48 m (MAXS mode). The instrument was calibrated with diffraction patterns from silver behenate.

2.4.2 Synthetic procedures

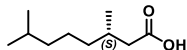
Synthesis of (S)-3,7-dimethyloctan-1-ol (6)^[66]



(S)-Citronellol (20.0 g, 0.13 mol) was dissolved in 150 mL ethyl acetate. Argon was bubbled through the solution for 15 minutes before Pd/C (0.25 g, 10%) was added. The vessel was inserted into a Parr hydration apparatus and the hydrogen pressure was adjusted to 70 psi. The reaction was started by shaking the vessel and a decreasing hydrogen pressure was noticed. During the following three hours of shaking, the hydrogen pressure had to be readjusted repeatedly. Having shaken the vessel at room temperature in the hydrogen atmosphere for 6 h in total, the catalyst was removed by filtration through diatomaceous earth. The filter was washed with ethyl acetate. Having removed the solvent by reduced pressure, the pure product was obtained as a clear oil. (S)-3,7-

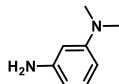
Dimethyloctan-1-ol was obtained in quantitative yield (20.6 g, 0.13 mol). $^1\text{H NMR}$ (400 MHz, Chloroform- d_1): δ [ppm] = 3.75 – 3.64 (m, 2H), 1.69 – 1.07 (m, 10H), 0.90 (d, J = 6.6 Hz, 3H), 0.87 (d, J = 6.7 Hz, 6H).

Synthesis of (S)-3,7-dimethyloctanoic acid (7)^[66]



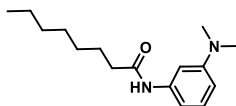
Periodic acid (15.85 g, 69.5 mmol, 2.2 eq.) was dissolved in 250 mL acetonitrile and cooled with an ice bath. Then, (S)-3,7-dimethyloctan-1-ol (5 g, 31.6 mmol, 1 eq.) was dissolved in 40 mL acetonitrile and added dropwise to the cooled solution of periodic acid. After pyridinium chlorochromate (136 mg, 0.6 mmol, 0.02 eq.) had been added, the reaction mixture turned yellow. Stirring was continued for 15 min at 0 °C and subsequently for 16 h at room temperature. The solution was concentrated, diluted in 500 mL ethyl acetate and extracted with 250 mL of a water/brine solution (v/v = 1/1), 250 mL saturated aqueous NaHSO_3 solution and 250 mL brine. The organic layer was dried with MgSO_4 , filtered and the filter cake was washed with ethyl acetate. The organic phase was concentrated by reduced pressure. The crude product was purified by Kugelrohr distillation (1 mbar, 120 °C). (S)-3,7-dimethyloctanoic acid was obtained in 74% yield (4.01 g, 23.3 mmol). $^1\text{H NMR}$ (400 MHz, Chloroform- d_1): δ [ppm] = 2.35 (dd, J = 15.0, 5.9 Hz, 1H), 2.15 (dd, J = 14.9, 8.2 Hz, 1H), 2.02 – 1.91 (m, 1H), 1.57 – 1.47 (m, 1H), 1.39 – 1.11 (m, 6H), 0.97 (d, J = 6.7 Hz, 3H), 0.87 (d, J = 6.6 Hz, 6H).

Synthesis of *N,N*-dimethylbenzene-1,3-diamine (10)



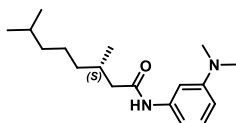
N,N-Dimethyl-3-nitroaniline (2.56 g, 15 mmol) was dissolved in 100 mL of ethyl acetate. The orange solution was bubbled through with argon for 15 minutes. Then Pd/C (30.2 mg, 10%) was added to the solution. The reaction mixture flask was pressurized with hydrogen gas (5 bar) for 32 hours. The colorless reaction mixture was filtered through diatomaceous earth. The filtrate's solvent was removed by rotary evaporation to afford an orange liquid. The obtained *N,N*-dimethylbenzene-1,3-diamine (2.04 g, 15 mmol, 100%) was used for the following reaction without further purification. $^1\text{H NMR}$ (400 MHz, Chloroform- d_1): δ [ppm] = 7.03 (t, J = 8.0 Hz, 1H), 6.20 (dd, J = 8.5, 2.1 Hz, 1H), 6.13 – 6.06 (m, 2H), 3.58 (br, 2H), 2.91 (s, 6H).

Synthesis of *N*-(3-(dimethylamino)phenyl)octanamide (a-11)



N,N-Dimethylbenzene-1,3-diamine (2.00 g, 15 mmol) and triethylamine (2.66 mL, 19 mmol) were added to 50 mL dry dichloromethane under argon atmosphere. After the solution was cooled to 0°C, octanoyl chloride (2.67 g, 16 mmol) was added. A precipitate formed upon the addition. The reaction mixture was allowed to warm up to room temperature and was further stirred for 16 hours. The reaction mixture was extracted three times with 25 mL water, four times with 25 mL of an one molar aqueous solution of sodium hydroxide solution and finally twice 25 mL with brine. The organic phase was dried with MgSO_4 , filtered and the solvent was removed by rotary evaporation to obtain *N*-(3-(Dimethylamino)phenyl)octanamide in 77% yield (3.29 g, 12.5 mmol). $^1\text{H NMR}$ (400 MHz, Chloroform- d_1): δ [ppm] = δ 7.17 – 7.13 (m, 2H), 7.08 (br, 1H), 6.69 (d, J = 7.9 Hz, 1H), 6.49 – 6.46 (m, 1H), 2.94 (s, 6H), 2.33 (t, J = 7.6 Hz, 2H), 1.72 (q, J = 7.4 Hz, 2H), 1.34 – 1.28 (m, 8H), 0.87 (t, J = 6.8 Hz, 3H).

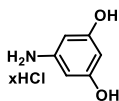
Synthesis of (S)-*N*-(3-(dimethylamino)phenyl)-3,7-dimethyloctanamide (S-11)



(S)-3,7-Dimethyloctanoic acid (2.83 g, 16.7 mmol) was dissolved in dry dichloromethane (40 mL) in dried glassware under argon. After the solution was cooled to 0°C, oxalyl chloride (2.91 g, 23 mmol) and *N,N*-dimethylformamide

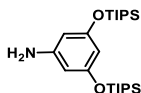
(0.2 mL, cat.) were added to the solution. The reaction mixture was then allowed to warm up to room temperature and reacted for 1.5 hours. The reaction mixture was distilled at 65°C under 1 atm. The residue was redissolved in dry dichloromethane and added dropwise to a cooled solution of *N,N*-dimethyl-3-nitroaniline (2.09 g, 15 mmol) and triethylamine (2.35 mL, 17 mmol) in dry dichloromethane (40 mL) under argon. After 60 hours, the reaction mixture was extracted three times with brine and twice with water. The organic phase was dried with MgSO₄, filtered and the solvent was removed by rotary evaporation to afford 4.34 g of black crude product. The crude product was purified on a silica column (heptane - ethyl acetate, 0-50%) to afford (*S*)-*N*-(3-(Dimethylamino)phenyl)-3,7-dimethyloctanamide as viscous beige oil in 47% yield (2.09 g, 7.1 mmol). ¹H NMR (400 MHz, Chloroform-*d*₁): δ [ppm] = 7.15 (t, J = 8.1 Hz, 2H), 7.02 (br, 1H), 6.69 (d, J = 7.2 Hz, 1H), 6.48 (dd, J = 8.3, 2.0 Hz, 1H), 2.95 (s, 6H), 2.37 – 2.32 (m, 1H), 2.12 – 2.07 (m, 2H), 1.51 (sept, J = 6.6 Hz, 1H), 1.37 – 1.15 (m, 6H), 0.99 (d, J = 6.2 Hz, 3H), 0.86 (d, J = 7.6 Hz, 6H).

Synthesis of 5-aminobenzene-1,3-diol hydrochloride (13)



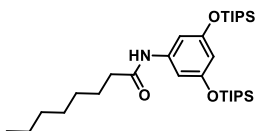
Argon gas was bubbled through 40 mL aqueous ammonia solution for 15 min. The solution was cooled to 0 °C before phloroglucinol dihydrate (8 g, 49 mmol, 1.0 eq.) was added. The mixture was allowed to warm up to room temperature and was stirred for 16 h under argon atmosphere. The turbid solution was concentrated by distillation under reduced pressure until ca. 20 mL water had been removed. 20 mL 3 N HCl_(aq) (63 mmol, 1.3 eq.) was added and the dispersion was concentrated until dryness. 5-Aminobenzene-1,3-diol hydrochloride (7.8 g, 48.3 mmol) was obtained as a yellowish solid (99% yield) and used without purification in the following reaction. ¹H NMR (400 MHz, DMSO-*d*₆): δ [ppm] = 10.02 (s, 3H), 7.47 – 7.09 (m, 1H), 6.28 – 6.22 (m, 2H).

Synthesis of 3,5-bis((triisopropylsilyl)oxy)aniline (14)



The reaction was carried out under inert conditions in dried glassware under argon. 5-Aminobenzene-1,3-diol hydrochloride (3.72 g, 23 mmol, 1 eq.) and imidazole (6.0 g, 88 mmol, 3.8 eq.) were dissolved in 25 mL dry *N,N*-dimethylformamide. The mixture was cooled to 0 °C and triisopropylsilyl chloride (12.3 mL, 58 mmol, 2.5 eq.) was added. The reaction mixture was allowed to warm up to room temperature and stirring was continued for 16 h. The reaction was stopped by addition of an aqueous saturated NH₄Cl solution (20 mL). The mixture was extracted twice with 50 mL ethyl acetate. The combined organic layers were washed with 50 mL water and 50 mL brine and finally dried with MgSO₄. The yellowish solution was filtrated, and the filter cake was washed with ethyl acetate. Concentration by rotary evaporation yielded crude product which was purified by silica column chromatography with chloroform (20-50%) in heptane as eluent. Pure 3,5-bis((triisopropylsilyl)oxy)aniline was obtained as yellow oil in 40% yield (4.0 g, 9.2 mmol). ¹H NMR (400 MHz, Chloroform-*d*₁): δ [ppm] = 5.87 (s, 3H), 3.52 (s, 2H), 1.26 – 1.19 (m, 6H), 1.09 (d, J = 7.2 Hz, 36H).

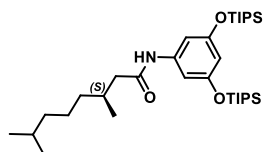
Synthesis of *N*-(3,5-bis((triisopropylsilyl)oxy)phenyl)octanamide (a-15)



The reaction was carried out under inert conditions in dried glassware under argon. Caprylic acid (2.16 g, 15 mmol, 1 eq.) were dissolved in 30 mL dry dichloromethane. The solution was cooled to 0 °C and 0.96 mL oxalyl chloride (16.5 mmol, 1.1 eq.) and 57 μL *N,N*-dimethylformamide (0.75 mmol, 0.05 eq.) were added. The reaction mixture was allowed to warm up to room temperature again and stirred for two hours before the solvent was removed by distillation under reduced pressure. The crude product was dissolved in 15 mL dry dichloromethane and added dropwise to a cool solution of 3,5-bis((triisopropylsilyl)oxy)aniline (6.2 g, 15 mmol, 1.0 eq.) and triethylamine

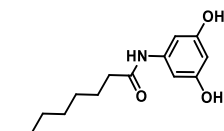
(2.17 mL, 16.5 mmol, 1.1 eq.) in dry dichloromethane. The reaction mixture was allowed to warm up to room temperature again and stirred for 16 h. The reaction mixture was extracted with 25 mL brine, 25 mL water and dried with MgSO₄. The mixture was filtered, and the filter cake was washed with dichloromethane. Subsequently, the obtained solution was concentrated. Purification was performed by silica column chromatography with chloroform (0-100%) in heptane as eluent. The pure product was obtained as white solid in 49% yield (49%, 7.25 mmol). ¹H NMR (400 MHz, Chloroform-*d*₁): δ [ppm] = 6.91 (s, 1H), 6.74 (s, 2H), 6.18 (s, 1H), 2.30 (t, J = 7.6 Hz, 2H), 1.74 – 1.67 (s, 2H), 1.37 – 1.08 (m, 42H), 0.88 (t, J = 6.8 Hz, 3H).

Synthesis of *N*-(3,5-bis((triisopropylsilyl)oxy)phenyl)octanamide (S-15)

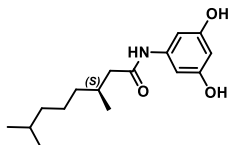


The reaction was carried out under inert conditions in dried glassware under argon. (*S*)-3,7-Dimethyloctanoic acid (1.59 g, 9.2 mmol, 1 eq.) was dissolved in 20 mL dry dichloromethane. The solution was cooled to 0 °C and oxalyl chloride (0.87 mL, 10.1 mmol, 1.1 eq.) as well as *N,N*-dimethylformamide (35 μL, 0.46 mmol, 0.05 eq.) were added. The reaction mixture was allowed to warm up to room temperature again and stirred for two hours before the solvent was removed by distillation under reduced pressure. The crude product was dissolved in 10 mL dry dichloromethane and added dropwise to a cool solution of 3,5-bis((triisopropylsilyl)oxy)aniline (4 g, 9.1 mmol, 1.0 eq.) and triethylamine (1.42 mL, 10.2 mmol, 1.1 eq.) in 20 mL of dry dichloromethane. The reaction mixture was allowed to warm up to room temperature again and stirred for 16 h. The reaction mixture was extracted with 25 mL brine and 25 mL water. The organic phase was dried with MgSO₄. The mixture was filtered and the filter cake was washed with dichloromethane. Subsequently, the obtained solution was concentrated to yield crude (*S*)-*N*-(3,5-bis((triisopropylsilyl)oxy)phenyl)-3,7-dimethyloctanamide. Purification was performed by silica column chromatography with dichloromethane (20-60%) in heptane as eluent. The pure product was obtained as white solid in 74% yield (3.98 g, 6.7 mmol). ¹H NMR (400 MHz, Chloroform-*d*₁): δ [ppm] = 6.90 (s, 1H), 6.74 (s, 2H), 6.18 (s, 1H), 2.32 (q, J = 9.4 Hz, 1H), 2.06 (q, J = 7.9 Hz, 2H), 1.52 – 1.46 (m, 1H), 1.35 – 1.08 (m, 46H), 0.98 (d, J = 5.9 Hz, 2H), 0.90 – 0.85 (m, J = 19.4 Hz, 9H).

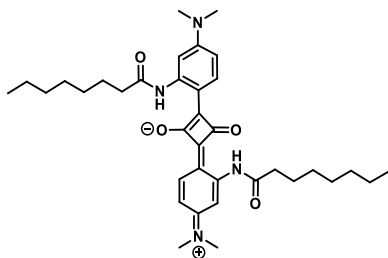
Synthesis of *N*-(3,5-dihydroxyphenyl)octanamide (a-16)



The reaction was carried out under inert conditions in dried glassware under argon. *N*-(3,5-bis((triisopropylsilyl)oxy)phenyl)octanamide (4.04 g, 7.1 mmol, 1 eq.) were dissolved in 50 mL dry tetrahydrofuran. The solution was cooled to 0 °C before 22 mL tetra-*n*-butylammoniumfluoride (1M in tetrahydrofuran, 22 mmol, 3 eq.) were added. The reaction mixture was allowed to warm up to room temperature again and stirred for three hours. The obtained solution was diluted with 50 mL ethyl acetate and extracted with 20 mL saturated aqueous NH₄Cl solution, 20 mL brine and 20 mL water. The organic phase was dried with MgSO₄, filtered and the filter cake was washed with ethyl acetate. Subsequently, the obtained solution was concentrated to yield crude product. Purification was performed by silica column chromatography with methanol (0-10%) in dichloromethane as eluent. The pure product was obtained as white solid in 88% yield (1.57 g, 6.2 mmol). ¹H NMR (400 MHz, DMSO-*d*₆): δ [ppm] = 9.53 (s, 1H), 9.10 (s, 2H), 6.55 (d, J = 2.1 Hz, 2H), 5.87 (t, J = 2.2 Hz, 1H), 2.23 (t, J = 7.4 Hz, 2H), 1.58 – 1.525 (m, 2H), 1.32 – 1.20 (m, 8H), 0.85 (t, J = 7.0 Hz 3H).

Synthesis of (*S*)-*N*-(3,5-dihydroxyphenyl)-3,7-dimethyloctanamide (*S*-16)


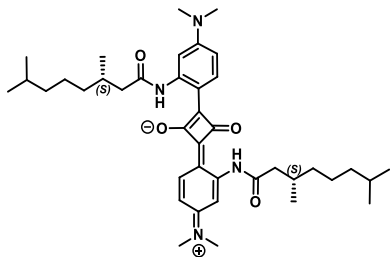
The reaction was carried out under inert conditions in dried glassware under argon. (*S*)-*N*-(3,5-Bis((triisopropylsilyloxy)phenyl)-3,7-dimethyloctanamide (1.02 g, 1.73 mmol, 1 eq.) was dissolved in 20 mL dry tetrahydrofuran. The solution was cooled to 0 °C before tetra-*n*-butylammoniumfluoride (1 M in tetrahydrofuran, 5.2 mL, 5.19 mmol, 3 eq.) was added. The reaction mixture was allowed to warm up to room temperature again and stirred for three hours. The obtained solution was diluted with 25 mL ethyl acetate and extracted with 10 mL saturated aqueous NH₄Cl solution, 10 mL brine and 10 mL water. The organic phase was dried with MgSO₄, filtered and the filter cake was washed with ethyl acetate. Subsequently, the obtained solution was concentrated to yield crude (*S*)-*N*-(3,5-bis((triisopropylsilyloxy)phenyl)-3,7-dimethyloctanamide. Purification was performed by silica column chromatography with methanol (0-20%) in chloroform as eluent. The pure product was obtained as white solid in 94% yield (455 mg, 1.6 mmol). ¹H NMR (400 MHz, Acetone-*d*₆): δ [ppm] = 8.86 (s, 1H), 8.13 (s, 1H), 6.76 (d, J = 2.1 Hz, 2H), 6.06 (t, J = 2.2 Hz, 1H), 2.30 (dd, J = 13.8, 6.0 Hz, 1H), 2.13 – 2.08 (m, 1H), 2.00 – 1.98 (m, 1H), 1.58 – 1.48 (m, 1H), 1.40 – 1.1 (m, 6H), 0.94 (d, J = 6.6 Hz, 3H), 0.86 (d, J = 6.6 Hz, 6H).

Synthesis of a-SQ-1


A flask filled with 80 mL of 50/50 *n*-propanol/toluene was fitted with a Dean-Stark trap and cooler and heated to 110 °C. After the trap was fully filled with solvent and manually emptied once, squaric acid (218 mg, 1.9 mmol, 1 eq.) was added. Heating and stirring were continued for 15 minutes before *N*-(3-(dimethylamino)phenyl)octanamide (1.0 g, 3.8 mmol, 2 eq.) was added. The solution turned dark green and heating and stirring were continued. After 20 hours of reaction, the mixture had a deep turquoise color. The reaction mixture was cooled down and the solvent was removed by rotary evaporation to afford a green crude product (1.08 g, 1.79 mmol, 89%). The crude product was recrystallized from acetonitrile to afford pure **a-SQ-1** in high yield (0.97 g, 1.61 mmol, 85%). ¹H NMR (400 MHz, Chloroform-*d*₁): δ [ppm] = 12.04 and 11.94 (s, 2H),¹ 8.49 and 8.43 (d, J = 9.2 Hz, 2H), 8.25 and 8.22 (d, J = 2.4 Hz, 2H), 6.45 – 6.42 (m, 2H), 3.18 (s, 12H), 2.62 and 2.56 (t, J = 7.2 Hz, 4H), 1.76 (quin, J = 7.2 Hz, 4H), 1.46 – 1.29 (m, 16H), 0.876 (t, J = 6.0 Hz, 6H). ¹³C NMR (101 MHz, Chloroform-*d*₁): δ [ppm] = 182.74, 182.53 and 181.52 (2C), 175.86 and 175.33 (2C), 174.19 and 173.87 (2C), 156.88 (2C), 144.09 (2C), 133.95 and 133.30 (2C), 112.76 and 112.55 (2C), 108.64 (2C), 102.48 (2C), 40.63 (4C), 38.18 and 38.01 (2C), 31.93 and 31.89 (2C), 29.62, 29.40, 29.36 and 29.33 (4C), 25.42 and 25.42 (2C), 22.87 (2C), 14.53 (2C). MALDI-TOF found 602.42 m/z (calculated 602.38). FT-IR (cm⁻¹): 3135 (w), 3096 (w), 2953 (w), 2918 (m), 2872 (w), 2852 (m), 2808 (w), 2676 (w), 1706 (m), 1609 (s), 1578 (s), 1535 (m), 1483 (m), 1458 (m), 1389 (s), 1352 (s), 1278 (s), 1242 (s), 1207 (s), 1179 (s), 1154 (s), 1125 (s), 1090 (s), 1063 (s), 958 (m), 944 (m), 891 (s), 853 (s), 821 (s) 804 (m), 781 (s), 725 (m), 707 (m), 684 (m), 663 (m), 641 (m), 593 (w), 565 (w), 524 (s) 500 (s), 461 (s).

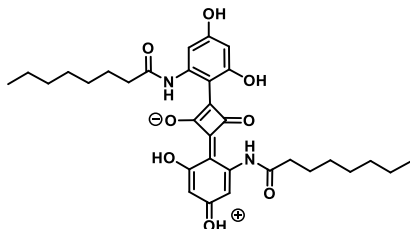
¹ See subchapter "Temperature dependent NMR **a-SQ-1**" for the explanation of the splitting

Synthesis of **S-SQ-1**



A flask filled with 100 mL of 50/50 *n*-propanol/toluene was fitted with a Dean-Stark trap and cooler and heated to 110 °C. After the trap was fully filled and manually emptied twice, squaric acid (99.7 mg, 0.86 mmol, 1 eq.) was added. After 30 minutes, (S)-*N*-(3-(dimethylamino)phenyl)-3,7-dimethyloctanamide (0.51 g, 1.7 mmol, 2 eq.) was added to the solution which turned dark green upon addition. After 20 hours of reaction the mixture had a deep turquoise color. The reaction mixture was cooled down and the solvent was removed by rotary evaporation to afford a green crude product (507 mg, 0.77 mmol, 45%). The crude product was recrystallized from acetonitrile to afford pure **S-SQ-1** in high yield (456 mg, 0.69 mmol, 81%). ¹H NMR (400 MHz, Chloroform-*d*₁): δ [ppm] = 12.08 and 11.94 (s, 2H), 8.55 and 8.49 (d, 9.2 Hz, 2H), 8.31 and 8.30 (d, 2.4 Hz, 2H), 6.48 (dd, *J* = 9.2 Hz, *J* = 2.4 Hz, 2H), 3.22 (s, 12H), 2.66 – 2.53 (m, 2H), 2.45 – 2.37 (m, 2H), 2.14 (br, 2H), 1.59 – 1.47 (m, 2H), 1.45 – 1.14 (m, 12H), 1.03 (d, *J* = 6.6 Hz, 6H), 0.88 – 0.84 (m, 12H). ¹³C NMR (101 MHz, Chloroform-*d*₁): δ [ppm] = 182.74 and 181.68 (2C), 176.03 and 175.57 (2C), 173.85 and 173.47 (2C), 156.95 (2C), 144.09 and 143.98 (2C), 134.00 and 133.38 (2C), 112.80 and 112.59 (2C), 108.73 (2C), 102.60 (2C), 45.91 and 45.65 (2C), 40.67 (4C), 39.23, 37.37 and 37.23 (4C), 30.86 and 30.83 (2C), 28.15 (2C), 25.08 and 25.01 (2C), 22.87, 22.85, 22.75 and 22.71 (4C), 20.07 and 19.96 (2C). MALDI-TOF found 658.47 *m/z* (calculated 658.45). FT-IR (cm⁻¹): 3133 (w), 2953 (m), 2925 (m), 2868 (m), 2681 (w), 1710 (w), 1607 (s), 1574 (s), 1532 (m), 1484 (w), 1455 (m), 1412 (w), 1382 (m), 1354 (s), 1325 (s), 1277 (s), 1241 (s), 1195 (s), 1139 (s), 1124 (s), 1063 (s), 902 (s), 879 (s), 862 (s), 812 (s), 781 (s), 725 (s), 681 (m), 664 (m), 649 (m), 556 (w), 520 (s), 498 (s), 463 (m).

Synthesis of **a-SQ-2**

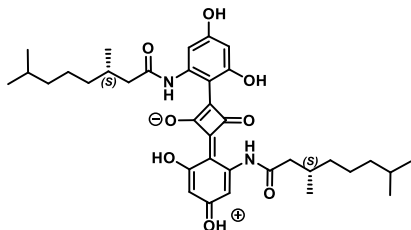


A flask filled with 50 mL of 50/50 *n*-propanol/toluene was fitted with a Dean-Stark trap and cooler and heated to 110 °C. Squaric acid (114 mg, 1.0 mmol, 1 eq.) was added and heating was continued for three hours. *N*-(3,5-Dihydroxyphenyl)octanamide (510 mg, 2.0 mmol, 2 eq.) was added. The mixture was heated and stirred for 20 h. The reaction mixture formed a deep blue color, was cooled down and concentrated until dryness. The dark blue residue was dispersed in 30 mL ethyl acetate by sonication. After extraction with 20 mL 0.5 M aqueous hydrochloric acid solution a dark blue solid was filtered off the organic layer. The obtained product was dried in vacuum and characterized without further purification. **a-SQ-2** was obtained in 60% yield (350 mg, 0.6 mmol). ¹H NMR (400 MHz, DMSO-*d*₆): δ [ppm] = 12.46 (br, 2H), 11.26 (s, 2H), 7.58 (s, 2H), 6.00 (s, 2H), 2.40 (t, *J* = 7.4 Hz, 4H), 1.65 – 1.55 (m, 4H), 1.29 – 1.25 (m, 16H), 0.86 – 0.83 (m, 6H). MALDI-TOF found 580.30 *m/z* (calculated 580.28). FT-IR (cm⁻¹): 2954 (m), 2922 (m), 2854 (m), 2625 (m), 1681 (w), 1583 (s), 1516 (m), 1455 (m), 1427 (m), 1383 (m), 1322 (m), 1226 (m), 1191 (s), 1174 (s), 1135 (s), 1123 (s), 1099 (m), 1024 (s), 948 (m), 866 (m), 801 (s), 760 (s), 723

Synthesis and characterization of novel chiral squaraine dyes

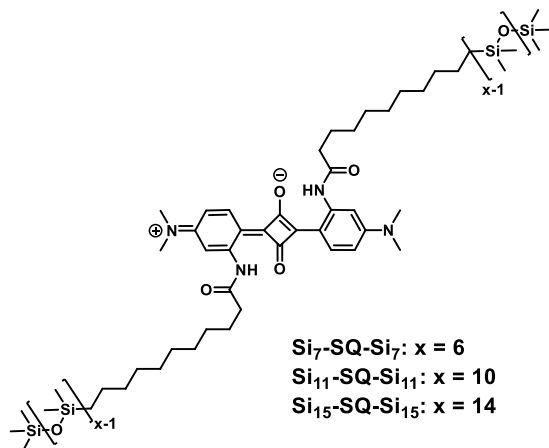
(s), 659 (m), 619 (m), 598 (m), 538 (m), 486 (s). Elemental analysis: found 66.10% C, 6.91% H, 4.81% N, 21.84% O (calculated: 66.19% C, 6.94% H, 4.82% N, 22.04% O).²

Synthesis of (3*S*,3'*S*)-*N,N'*-((2,4-dioxocyclobutane-1,3-diyl)bis(3,5-dihydroxy-2,1-phenylene))bis(3,7-dimethyloctanamide) **5-SQ-2**



A flask filled with 50 mL of 50/50 *n*-propanol/toluene was fitted with a Dean-Stark trap and cooler and heated to 110 °C. Squaric acid (19 mg, 0.17 mmol, 1 eq.) was added and heating was continued for three hours. (*S*)-*N*-(3,5-dihydroxyphenyl)-3,7-dimethyloctanamide (100 mg, 0.36 mmol, 2.1 eq.) was added. The mixture was heated and stirred for 20 h. The reaction mixture formed a deep blue color, was cooled down and concentrated until dryness. The dark blue residue was dispersed in 40 mL ethyl acetate by sonication. After extraction with 20 mL 0.5 M aqueous hydrochloric acid solution a dark blue solid was filtered off the organic layer. The obtained product was dried in vacuum and characterized without further purification. **5-SQ-2** was obtained in 11% yield (12 mg, 0.02 mmol). The low yield was caused by the small scale of the reaction. ¹H NMR (400 MHz, DMSO-*d*₆): δ [ppm] = 12.41 (br, 2H), 11.26 (s, 2H), 7.58 (s, 2H), 5.97 (s, 2H), 2.41 (dd, *J* = 14.2, 6.4 Hz, 2H), 2.23 (dd, *J* = 14.3, 7.6 Hz, 2H), 1.98 (br, 2H), 1.54 – 1.44 (m, 2H), 1.35 – 1.09 (m, 12H), 0.92 (d, *J* = 6.7 Hz, 6H), 0.83 (d, *J* = 6.6 Hz, 12H). MALDI-TOF found 659.34 *m/z* (calculated [M]⁺+Na⁺ 659.33). FT-IR (cm⁻¹): 2955 (m), 2928 (m), 2868 (m), 2620 (br), 1682 (w), 1610 (m), 1583 (s), 1517 (m), 1458 (w), 1426 (m), 1383 (m), 1325 (w), 1229 (s), 1196 (s), 1174 (s), 1125 (s), 1024 (s), 953 (m), 866 (m), 806 (m), 770 (m), 723 (s), 659 (w), 616 (m), 598 (m), 535 (m), 486 (m). Elemental analysis: found 66.91% C, 7.47% H, 4.29% N, 19.84% O (calculated: 67.90% C, 7.60% H, 4.40% N, 20.10% O).

Synthesis of **Si₇-SQ-Si₇**, **Si₁₁-SQ-Si₁₁** and **Si₁₅-SQ-Si₁₅**



The reaction was carried out under inert conditions in dried glassware under argon. **u-SQ-1** and 2.5 eq. discrete siloxane (C₁₅H₄₆O₆Si₇, C₂₃H₇₀O₁₀Si₁₁ or C₃₁H₉₄O₁₄Si₁₅) were dissolved in dry DCM. The exact amounts of substance and reaction temperatures are given in Table 2.1.

² The elemental analysis showed the presence of 0.34 wt% contamination of other elements than C, H, N and O. The material is most likely salt accumulated during the purification.

Table 2.1: Synthesis of **Si₇-SQ-Si₇**, **Si₁₁-SQ-Si₁₁** and **Si₁₅-SQ-Si₁₅** – amounts of used substances and reaction temperature.

entry	siloxane	u-SQ-1	DCM	Temp.
1	95 mg, 0.18 mmol C ₁₅ H ₄₆ O ₆ Si ₇	50 mg, 0.07 mmol	25 mL	R.T.
2	149 mg, 0.18 mmol C ₂₃ H ₇₀ O ₁₀ Si ₁₁	50 mg, 0.07 mmol	5 mL	35 °C
3	203 mg, 0.18 mmol C ₃₁ H ₉₄ O ₁₄ Si ₁₅	50 mg, 0.07 mmol	50 mL	R.T.

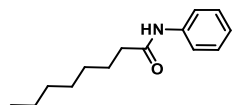
One droplet of Karstedt catalyst was added and stirring was continued. After 30 minutes, conversion was investigated by ¹H NMR spectroscopy and another droplet of Karstedt catalyst was added. Investigation of conversion and addition of an additional droplet of catalyst was continued until complete conversion of **u-SQ-1** was reached. Purification was performed in two steps. Step one was silica column chromatography with methanol (0-10%) and isopropylamine (0-2%) in chloroform as eluent. The second step was a recycle gel permeation chromatography GPC) performed on 100 mg crude using chloroform as eluent.

Si₇-SQ-Si₇ was obtained in 38% yield (49 mg, 28.5 μmol). ¹H NMR (399 MHz, Chloroform-*d*₁): δ [ppm] = 12.07 and 11.98 (s, 2H), 8.54 – 8.47 (m, 2H), 8.29 – 8.25 (m, 2H), 6.46 (s, 2H), 3.22 (s, 12H), 2.60 (dt, *J* = 27.1, 7.2 Hz, 4H), 1.76 (p, *J* = 7.5, 7.1 Hz, 4H), 1.46 – 1.22 (m, 28H), 0.52 (s, 4H), 0.12 – -0.03 (m, 92H). ¹³C NMR (101 MHz, Chloroform-*d*₁): δ [ppm] = 182.87, 175.41, 175.03, 174.27, 156.99, 144.19, 134.03, 133.36, 108.72, 102.60, 40.68, 38.24, 38.07, 33.68, 29.87, 29.82, 29.77, 29.74, 29.68, 29.61, 29.46, 25.66, 25.44, 23.40, 18.43, 1.94, 1.33, 1.30, 1.22, 0.34. MALDI-TOF found 1720.87 m/z in negative mode (calculated 1718.78). FT-IR (cm⁻¹): 2961 (m), 2922 (m), 2853 (w), 1709 (w), 1610 (m), 1581 (m), 1535 (w), 1488 (w), 1454 (w), 1384 (w), 1324 (m), 1257 (s), 1200 (m), 1141 (m), 1020 (s), 891 (m), 839 (m), 790 (s), 704 (m), 685 (m), 666 (m), 643 (m), 522 (m).

Si₁₁-SQ-Si₁₁ was obtained in 42% yield (71.8 mg, 30.7 μmol). ¹H NMR (399 MHz, Chloroform-*d*₁): δ [ppm] = 12.00 and 11.92 (s, 2H), 8.74 – 8.40 (m, 2H), 8.22 – 8.19 (d, *J* = 14.7 Hz, 2H), 6.42 – 6.40 (d, *J* = 8.9 Hz, 2H), 3.21 (s, 12H), 2.60 (dt, *J* = 26.4, 7.0 Hz, 4H), 1.76 (p, *J* = 7.3 Hz, 4H), 1.35 (d, *J* = 60.1 Hz, 28H), 0.52 (s, 4H), 0.17 – -0.12 (m, 140H). ¹³C NMR (101 MHz, Chloroform-*d*₁): δ [ppm] = 182.87, 175.43, 157.00, 144.20, 133.39, 112.76, 108.72, 102.59, 40.67, 38.24, 38.06, 33.68, 30.59, 29.88, 29.83, 29.77, 29.74, 29.68, 29.61, 29.46, 25.67, 25.45, 23.40, 18.43, 1.93, 1.32, 1.29, 1.20, 0.33. MALDI-TOF found 2313.98 m/z in positive mode (calculated 2313.98). FT-IR (cm⁻¹): 2962 (m), 2923 (m), 2854 (w), 1709 (w), 1612 (m), 1581 (m), 1534 (w), 1455 (w), 1385 (w), 1331 (m), 1257 (s), 1202 (m), 1145 (m), 1016 (s), 891 (m), 840 (m), 791 (s), 704 (m), 685 (m), 666 (m), 523 (m).

Si₁₅-SQ-Si₁₅ was obtained in 34% yield (31.5 mg, 10.8 μmol). ¹H NMR (399 MHz, Chloroform-*d*₁): δ [ppm] = 12.00 and 11.92 (s, 2H), 8.46 and 8.41 (d, *J* = 9.1 Hz, 2H), 8.22 and 8.18 (d, *J* = 2.1 Hz, 2H), 6.42 and 6.40 (d, *J* = 2.4 Hz, 2H), 3.14 (s, 12H), 2.53 (dt, *J* = 27.1, 7.6 Hz, 4H), 1.69 (p, *J* = 7.5 Hz, 4H), 1.40 – 1.14 (m, 28H), 0.45 (s, 4H), 0.04 – -0.05 (m, 188H). ¹³C NMR (101 MHz, Chloroform-*d*₁): δ [ppm] = 181.69, 174.22, 173.06, 155.81, 141.53, 132.86, 107.53, 101.40, 39.48, 36.85, 32.48, 28.63, 28.57, 28.54, 28.42, 28.26, 28.01, 24.25, 22.21, 17.23, 0.73, 0.12, 0.09, -0.00, -0.87. MALDI-TOF found 2907.12 m/z in negative mode (calculated 2903.08). FT-IR (cm⁻¹): 2962 (m), 2923 (w), 2854 (w), 1708 (w), 1614 (m), 1582 (m), 1534 (w), 1454 (w), 1387 (w), 1353 (m), 1258 (s), 1209 (m), 1179 (w), 1153 (m), 1015 (s), 892 (m), 841 (m), 792 (s), 685 (m), 665 (m), 524 (m).

Synthesis of *N*-phenyloctanamide (3)



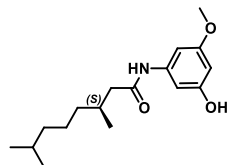
The reaction was carried out under inert conditions in dried glassware under argon. Octanoyl chloride (3.9 mL, 23 mmol, 1.0 eq.) was dissolved in 20 mL dry dichloromethane and added dropwise to a cool solution of aniline hydrochloride (3.0 g, 23 mmol, 1.0 eq.) and triethylamine (6.7 mL, 48 mmol, 2.1 eq.) in dry dichloromethane. The reaction mixture was allowed to warm up to room temperature again and stirred for 16 h. The reaction mixture was extracted once with an aqueous solution of hydrochloric acid (pH = 0) mL and twice with 25 mL water. The organic phase was dried with MgSO₄. The mixture was filtered and the filter cake was washed with dichloromethane. Subsequently, the obtained solution was concentrated. The pure product was obtained in 85%

yield (4.3 g, 19 mmol). $^1\text{H NMR}$ (400 MHz, DMSO- d_6): δ [ppm] = 9.83 (s, 1H), 7.58 (d, J = 7.9 Hz, 2H), 7.27 (t, J = 7.8 Hz, 2H), 7.01 (t, J = 7.3 Hz, 1H), 2.28 (t, J = 7.4 Hz, 2H), 1.63 – 1.53 (m, 2H), 1.30 – 1.24 (m, 8H), 0.86 (t, J = 6.7 Hz, 3H).

Synthesis attempt of a-SQ-3

A flask filled with 50 mL of 50/50 *n*-propanol/toluene was fitted with a Dean-Stark trap and cooler and heated to 110 °C. Squaric acid (520 mg, 4.6 mmol, 1 eq.) was added and heating was continued for three hours. *N*-phenyloctanamide (2 g, 10 mmol, 2.2 eq.) was added. The mixture was heated and stirred for 20 h. The reaction mixture did not form a deep blue color and NMR spectroscopy proved the absence of product formation.

Synthesis of (*S*)-*N*-(3-hydroxy-5-methoxyphenyl)-3,7-dimethyloctan-amide (4)



The synthesis of (**4**) was started from *N*-(3,5-bis((triisopropylsilyloxy)phenyl)octanamide and performed in three steps (**S-15**).

The first reaction was carried out under inert conditions in dried glassware under argon. (*S*)-*N*-(3,5-Bis((triisopropylsilyloxy)phenyl)-3,7-dimethyloctanamide (2.05 g, 3.4 mmol, 2 eq.) was dissolved in 50 mL dry tetrahydrofuran. The solution was cooled to 0 °C before tetra-*n*-butylammoniumfluoride (1 M in tetrahydrofuran, 1.75 mL, 1.75 mmol, 1 eq.) was added. The reaction mixture was allowed to warm up to room temperature again and stirred for three hours. The obtained solution was diluted with 25 mL ethyl acetate and extracted with 20 mL saturated aqueous NH_4Cl solution, 20 mL brine and 20 mL water. The organic phase was dried with MgSO_4 , filtered and the filter cake was washed with ethyl acetate. Subsequently, the obtained solution was concentrated to yield crude (*S*)-*N*-(3-hydroxy-5-((triisopropylsilyloxy)phenyl)-3,7-dimethyloctan-amide. Purification was performed by silica column chromatography with EtOAc (0-20%) in heptane as eluent. Still double protected starting material was isolated, too. After two deprotection cycles and purification, the pure product was obtained as white oil in 56% yield (840 mg, 1.9 mmol). $^1\text{H NMR}$ (400 MHz, Chloroform- d_1): δ [ppm] = 7.10 (s, 1H), 6.96 (s, 1H), 6.40 (s, 1H), 6.17 (s, 1H), 5.67 (s, 1H), 2.34 (q, 1H), 2.13 – 2.03 (m, 2H), 1.59 – 1.45 (m, 1H), 1.38 – 1.13 (m, 9H), 1.10 (d, J = 7.3 Hz, 18H), 0.98 (d, J = 6.2 Hz, 3H), 0.86 (dd, J = 6.6, 1.2 Hz, 6H).

In the second step, (*S*)-*N*-(3-hydroxy-5-((triisopropylsilyloxy)phenyl)-3,7-dimethyloctanamide (0.63 g, 1.4 mmol) was dissolved in 40 mL acetone. K_2CO_3 (1.01 g, 7.3 mmol) and MeI (0.38 mL, 6.1 mmol) were added to the solution. The reaction mixture was stirred for 40 hours at 45°C. The reaction mixture was diluted with 40 mL EtOAc and extracted with 25 mL water. The water phase was extracted with 20 mL EtOAc. The combined organic phases were washed with 30 mL aqueous saturated K_2CO_3 solution. The organic phase was then dried with MgSO_4 and filtered. The filter was washed with 10 mL EtOAc and solvent was removed by rotary evaporation to afford a crude (0.62 g). The crude was purified on a silica column (heptane-EtOAc, 0-20%) to afford pure (*S*)-*N*-(3-methoxy-5-((triisopropylsilyloxy)phenyl)-3,7-dimethyloctanamide in 73% yield (300 mg, 0.7 mmol). $^1\text{H NMR}$ (400 MHz, Chloroform- d_1): δ [ppm] = 6.95 (s, 1H), 6.86 (s, 1H), 6.66 (s, 1H), 6.21 (s, 1H), 3.76 (s, 3H), 2.32 (q, 1H), 2.08 (t, J = 9.0 Hz, 2H), 1.56 – 1.45 (m, 1H), 1.40 – 1.13 (m, 9H), 1.10 (d, J = 7.3 Hz, 18H), 0.99 (d, J = 6.1 Hz, 3H), 0.86 (dd, J = 6.7, 1.1 Hz, 6H).

The third reaction was carried out under inert conditions in dried glassware under argon. (*S*)-*N*-(3-methoxy-5-((triisopropylsilyloxy)phenyl)-3,7-dimethyloctanamide (0.485 g, 1.1 mmol, 1 eq.) was dissolved in 20 mL dry tetrahydrofuran. The solution was cooled to 0 °C before tetra-*n*-butylammoniumfluoride (1 M in tetrahydrofuran, 1.6 mL, 1.6 mmol, 1.5 eq.) was added. The reaction mixture was allowed to warm up to room temperature again and stirred for three hours. The obtained solution was diluted with 25 mL ethyl acetate and extracted with 10 mL saturated aqueous NH_4Cl solution, 10 mL brine and 10 mL water. The organic phase was dried with MgSO_4 , filtered and the filter cake was washed with ethyl acetate. Subsequently, the obtained solution was concentrated to yield crude (*S*)-*N*-(3-hydroxy-5-methoxyphenyl)-3,7-dimethyloctanamide. Purification was performed by silica column chromatography with EtOAc (0-100%) in heptane as eluent. The pure product was obtained as white solid in 89% yield (280 mg, 1.0 mmol). $^1\text{H NMR}$ (400 MHz, Chloroform- d_1): δ [ppm] = 7.16 (s, 1H), 7.04 (s, 1H), 6.41 (t, J = 2.0 Hz,

1H), 6.29 (s, 1H), 6.21 (t, J = 2.2 Hz, 1H), 3.77 (s, 3H), 2.36 (dd, J = 13.5, 5.5 Hz, 1H), 2.19 – 1.97 (m, 2H), 1.52 (s, 1H), 1.41 – 1.11 (m, 6H), 0.99 (d, J = 6.3 Hz, 3H), 0.86 (dd, J = 6.6, 1.2 Hz, 6H).

Synthesis attempt of a-SQ-4

A flask filled with 50 mL of 50/50 *n*-propanol/toluene was fitted with a Dean-Stark trap and cooler and heated to 110 °C. Squaric acid (49 mg, 0.43 mmol, 1 eq.) was added and heating was continued for three hours. *N*-phenyloctanamide (0.28 g, 1.0 mmol, 2.2 eq.) was added. The mixture was heated and stirred at 50 °C for 20 h. The reaction mixture formed a deep blue color. NMR spectroscopy indicated a small conversion. Prolonged reaction time and increased temperature did not result in improving the amount of product in the reaction mixture but increased the amount of an insoluble greenish byproduct.

2.4.3 Calculation of the activation energy barriers according to Shanan-Atidi

The free energies of activation $\Delta G_{major}^{\ddagger}$ and $\Delta G_{minor}^{\ddagger}$ between one rotamer and the transition state are defined as:^[80,81]

$$\Delta G_{major}^{\ddagger} = 4.57 \cdot T_c \left\{ 10.62 + \ln \left[\frac{X}{2\pi(1-\Delta P)} \right] + \ln (T_c/\Delta\nu) \right\} \quad (a)$$

$$\Delta G_{minor}^{\ddagger} = 4.57 \cdot T_c \left\{ 10.62 + \ln \left[\frac{X}{2\pi(1+\Delta P)} \right] + \ln (T_c/\Delta\nu) \right\} \quad (b)$$

T_c is the coalescence temperature that is determined by VT-NMR spectroscopy. As seen in Figure 2.6, the signals of the two rotamers of **a-SQ-1** coalesce at 64 °C (336 K) in the solvent 1,1,2,2-tetrachloroethane-*d*₂. $\Delta\nu$ is the frequency difference between the signals of protons of the amides of both rotamers. The spectrum recorded at room temperature (Figure 2.6) shows that $\Delta\nu$ is 42 Hz. ΔP is the difference between the populations of the major and minor form is defined as:

$$\Delta P = \frac{P_{major} - P_{minor}}{P_{major} + P_{minor}} \text{ with } P_{major} > P_{minor} \quad (c)$$

The required parameters P_{major} and P_{minor} for solving equation (c) were obtained by the integration of the signals for the N-*H* protons of each rotamer in the ¹H NMR spectrum that was recorded at room temperature. P_{major} was 1.00 and P_{minor} 0.70. Solving equation c yields ΔP with 0.18. The last required parameter for solving equations (a) and (b) is X . X is defined as $X = 2\pi\tau\Delta\nu$ and derived from the mean lifetime τ and the chemical shift difference $\Delta\nu$ between the conformers. X can also be calculated from ΔP after transposing equation (d):

$$\Delta P = \left[\frac{X^2 - 2}{3} \right]^{\frac{3}{2}} \cdot \frac{1}{X} \quad (d)$$

Using the known ΔP , X was calculated³ as 1.86. With the determination of all required parameters which are summarized in Table 2.2, the energy of activation for the interconversion between both rotamers were determined using equations (a) and (b):

$$\Delta G_{major}^{\ddagger} = \Delta G_{syn}^{\ddagger} = 17993 \frac{\text{cal}}{\text{mol}} \cong 75 \text{ kJ/mol}$$

$$\Delta G_{minor}^{\ddagger} = \Delta G_{anti}^{\ddagger} = 17433 \frac{\text{cal}}{\text{mol}} \cong 73 \text{ kJ/mol}$$

The parameters used for the calculation of the activation energy barriers in CHCl₃-*d*₁ are given in Table 2.2, too. Analogous calculation as described above result in the activation energy barriers stated in the subchapter on the rotational isomerism of **a-SQ-1**.

³ calculated using <https://www.wolframalpha.com/>.

Table 2.2: Parameters ΔP , X and Δv required for the calculation of the activation energy barriers in TCE- d_2 and CHCl_3 - d_1 .

solvent	ratio major/minor	ΔP	X	Δv
TCE- d_2	1.00:0.70	0.18	1.86	42 Hz
CHCl_3 - d_1	1.00:0.64	0.22	1.92	39 Hz

The error of the calculated activation energy barriers was performed using the propagation of uncertainty. The propagation of uncertainty is commonly expressed as:

$$s_f = \text{sqrt} \left(\left(\frac{\partial f}{\partial x} \right)^2 * s_x^2 + \left(\frac{\partial f}{\partial y} \right)^2 * s_y^2 + \left(\frac{\partial f}{\partial z} \right)^2 * s_z^2 + \dots \right) \quad (\text{e})$$

s_f is the error of the value that is calculated using equation f and the measured parameters x, y, z, \dots that have the errors s_x, s_y, s_z, \dots which are experimentally caused.

Using equation (e), the following expression was obtained for the calculation of $s_{G^\ddagger}^{\text{minor}}$ (error of $\Delta G^\ddagger_{\text{minor}}$):

$$s_{G^\ddagger}^{\text{minor}} = \text{sqrt} \left(\left(53.1034 + 4.57 * \ln(T_c/\Delta v) + 4.57 * \ln(-0.159155 * \Delta X)/(-1 + \Delta P) \right)^2 * (s_{T_c})^2 + \left((4.57 * T_c)/\Delta X \right)^2 * (s_{\Delta X})^2 + \left(-4.57 * T_c/(-1 + \Delta P) \right)^2 * (s_{\Delta P})^2 + \left(-4.57 * T_c/\Delta v \right)^2 * (s_{\Delta v})^2 \right) \quad (\text{f})$$

The error s_{T_c} of T_c was estimated as 3 K based on the calibration of the temperature unit of the NMR machine and the noise of the spectra. The error $s_{\Delta v}$ of Δv was estimated as 0.5 Hz K based on noise of the spectra. The ratio of the rotamers was determined by integration of the NMR spectra. Based on the noise of the baseline, the error of the integration was estimated to be 0.02 assuming an integral of the major form of 1.00. As a result of the error in integration, the errors $s_{\Delta X}$ and $s_{\Delta P}$ were estimated as 0.0255 and 0.15 respectively.

Using equation (f) and the data presented in Table 2.2 as well as the estimated experimental errors, $s_{G^\ddagger}^{\text{minor}}$ is 332 cal/mol = 1 kJ/mol. When the propagation of uncertainty is used for determining $s_{G^\ddagger}^{\text{major}}$ (the error of $\Delta G^\ddagger_{\text{major}}$) the value of 1 kJ/mol was obtained, too. We conclude that the errors of the calculated activation energy barriers were 1 kJ/mol in our experiment series.

2.4.4 Density function theory

A derivative of **a-SQ-1** with two acetamide substituents **a-SQ-1*** was used for the calculations to reduce calculation time. Conformational searches (5.000 steps) were performed using MacroModel 11.0^[68] with the OPLS3 force field^[69] in CDCl_3 ^[70,71] and a cutoff of 21 kJ/mol. The search provided two conformers (*syn* and *anti*). Geometry optimization using Jaguar at the B3-LYP-D3/6-31G** level of theory.^[72-75] Solvation corrections were performed on gas-phase geometries using a PBF implicit solvent model for CHCl_3 . The population of the structures was calculated according to the Boltzman distribution. The transition state was located using the transition state search module of Jaguar using both conformers (*syn* and *anti*) as reference points for a search along the lowest hessian eigenvector at the B3-LYP-D3/6-31G** level of theory in CHCl_3 . The results are listed in Table 2.3.

Table 2.3: Results from the DFT calculations.

	Solution Phase Energy (au)	Relative Energy (kJ/mol)	Population (%)
<i>Syn</i> -Conformer	-1450.263470	2.9	23
<i>Anti</i> -Conformer	-1450.264596	0.0	77
Transition State	-1450.226296	100.4	-

2.5 References

- [1] K. Y. Law, *Chem. Rev.* **1993**, *93*, 449.
- [2] S. Sreejith, P. Carol, P. Chithra, A. Ajayaghosh, *J. Mater. Chem.* **2008**, *18*, 264.
- [3] V. Grande, C.-A. A. Shen, M. Deiana, M. Dudek, J. Olesiak-Banska, K. Matczyszyn, F. Würthner, *Chem. Sci.* **2018**, *9*, 8375.
- [4] S. K. Shaw, W. Liu, C. F. A. Gómez Durán, C. L. Schreiber, M. de L. Betancourt Mendiola, C. Zhai, F. M. Roland, S. J. Padanilam, B. D. Smith, *Chem. Eur. J.* **2018**, *24*, 13821.
- [5] D. S. Philips, S. Ghosh, K. V. Sudheesh, C. H. Suresh, A. Ajayaghosh, *Chem. Eur. J.* **2017**, *23*, 17973.
- [6] P. S. S. Babu, P. M. Manu, T. J. Dhanya, P. Tapas, R. N. Meera, *Sci. Rep.* **2017**, *7*, 42126.
- [7] J. H. Cheon, S. A. Kim, K. S. Ahn, M. S. Kang, J. H. Kim, *Electrochim. Acta* **2012**, *68*, 240.
- [8] W. S. M. Klein, R. Pankiewicz, M. Zalas, *Sci. Rep.* **2016**, *6*, 30077.
- [9] M. Matsui, Y. Haishima, Y. Kubota, K. Funabiki, J. Jin, T. H. Kim, K. Manseki, *Dye. Pigment.* **2017**, *141*, 457.
- [10] K. Gräf, M. A. Rahim, S. Das, M. Thelakkat, *Dye. Pigment.* **2013**, *99*, 1101.
- [11] P. C. R. Varma, M. A. G. Namboothiry, *Phys. Chem. Chem. Phys.* **2016**, *18*, 3438.
- [12] A. Treibs, K. Jacob, *Angew. Chem. Int. Ed.* **1965**, *4*, 694.
- [13] H. E. Sprenger, W. Ziegenbein, *Angew. Chem. Int. Ed.* **1967**, *6*, 553.
- [14] E. W. Neuse, B. R. Green, *J. Org. Chem.* **1974**, *39*, 3881.
- [15] G. Xia, H. Wang, *J. Photochem. Photobiol. C Photochem. Rev.* **2017**, *31*, 84.
- [16] R. P. Sijbesma, E. W. Meijer, *Chem. Commun.* **2003**, 5.
- [17] G. Maahs, P. Hegenberg, *Angew. Chem. Int. Ed.* **1966**, *5*, 888.
- [18] K. K. Law, F. C. Bailey, *J. Org. Chem.* **1992**, 3278.
- [19] P. M. Kazmaier, G. K. Hamer, R. A. Burt, *Can. J. Chem.* **1990**, *68*, 530.
- [20] L. Yang, Y. Zhu, Y. Jiao, D. Yang, Y. Chen, J. Wu, Z. Lu, S. Zhao, X. Pu, Y. Huang, *Dye. Pigment.* **2017**, *145*, 222.
- [21] A. H. Schmidt, *Synthesis* **1980**, *12*, 961.
- [22] K. Jyothish, M. Hariharan, D. Ramaiah, *Chem. Eur. J.* **2007**, *13*, 5944.
- [23] M. H. Schreck, M. I. S. Röhr, T. Clark, V. Stepanenko, F. Würthner, C. Lambert, *Chem. Eur. J.* **2019**, *25*, 2831.
- [24] A.-J. Payne, G. C. Welch, *Org. Biomol. Chem.* **2017**, *15*, 3310.
- [25] H. Chen, M. S. Farahat, K. Y. Law, D. G. Whitten, *J. Am. Chem. Soc.* **1996**, *118*, 2584.
- [26] G. J. Ashwell, *J. Mater. Chem.* **1998**, *8*, 373.
- [27] C. W. Dirk, W. C. Herndon, F. C. Henry, S. Martinez, P. Kalamegham, A. Tan, G. Campos, M. Velez, J. Zyss, I. Ledoux, L. Cheng, *J. Am. Chem. Soc.* **1995**, *117*, 2214.
- [28] H. Chen, K.-Y. Law, J. Perlstein, D. G. Whitten, *J. Am. Chem. Soc.* **1995**, *117*, 7257.
- [29] K. T. Arun, D. T. Jayaram, R. R. Avirah, D. Ramaiah, *J. Phys. Chem. B* **2011**, *115*, 7122.
- [30] S. Das, K. J. G. Thomas, K. J. G. Thomas, P. V. Kamat, M. V. George, *J. Phys. Chem.* **1994**, *98*, 9291.
- [31] K. Y. Law, *J. Phys. Chem.* **1987**, *91*, 5184.
- [32] K. Liang, M. S. Farahat, J. Perlstein, K. Y. Law, D. G. Whitten, *J. Am. Chem. Soc.* **1997**, *119*, 830.
- [33] J. Griffiths, J. Mama, *Dye. Pigment.* **2000**, *44*, 9.
- [34] R. S. Stoll, N. Severin, J. P. Rabe, S. Hecht, *Adv. Mater.* **2006**, *18*, 1271.
- [35] M. Schulz, J. Zablocki, O. S. Abdullaeva, S. Brück, F. Balzer, A. Lützen, O. Arteaga, M. Schiek, *Nat. Commun.* **2018**, *9*, 2413.
- [36] M. Tristani-Kendra, C. J. Eckhardt, *J. Chem. Phys.* **1984**, *81*, 1160.
- [37] E. Buncel, A. J. McKerron, P. M. Kazmaier, *J. Chem. Soc. Chem. Commun.* **1992**, 1242.
- [38] S. Brück, C. Krause, R. Turrisi, L. Beverina, S. Wilken, W. Saak, A. Lützen, H. Borchert, M. Schiek, J. Parisi, *Phys. Chem. Chem. Phys.* **2014**, *16*, 1067.
- [39] M. Schulz, M. Mack, O. Kollege, A. Lützen, M. Schiek, *Phys. Chem. Chem. Phys.* **2017**, *19*, 6996.
- [40] M. Schulz, F. Balzer, D. Scheunemann, O. Arteaga, A. Lützen, S. C. J. Meskers, M. Schiek, *Adv. Funct. Mater.* **2019**, *29*, 1900684.
- [41] T. F. A. A. De Greef, M. M. J. J. Smulders, M. Wolfs, A. P. H. J. H. J. Schenning, R. P. Sijbesma, E. W. Meijer, *Chem. Rev.* **2009**, *109*, 5687.
- [42] L. N. J. De Windt, C. Kulkarni, H. M. M. Ten Eikelder, A. J. Markvoort, E. W. Meijer, A. R. A. Palmans, *Macromolecules* **2019**, *52*, 7430.
- [43] T. Aida, E. W. Meijer, *Isr. J. Chem.* **2020**, *60*, 33.
- [44] M. P. Lightfoot, F. S. Mair, R. G. Pritchard, J. E. Warren, *Chem. Commun.* **1999**, 1945.

- [45] R. Q. Albuquerque, A. Timme, R. Kress, J. Senker, H. W. Schmidt, *Chem. Eur. J.* **2013**, *19*, 1647.
- [46] S. Cantekin, T. F. A. A. De Greef, A. R. A. A. Palmans, *Chem. Soc. Rev.* **2012**, *41*, 6125.
- [47] K. Sakamoto, M. Hatano, *Bull. Chem. Soc. Jpn.* **1980**, *53*, 339.
- [48] P. J. M. M. Stals, J. C. Everts, R. De Bruijn, I. A. W. W. Filot, M. M. J. J. Smulders, R. Martín-Rapún, E. A. Pidko, T. F. A. A. De Greef, A. R. A. A. Palmans, E. W. Meijer, *Chem. Eur. J.* **2010**, *16*, 810.
- [49] M. Shirakawa, N. Fujita, S. Shinkai, *J. Am. Chem. Soc.* **2005**, *127*, 4164.
- [50] T. Hirose, F. Helmich, E. W. Meijer, *Angew. Chem. Int. Ed.* **2013**, *52*, 304.
- [51] M. F. J. Mabesoone, A. J. Markvoort, M. Banno, T. Yamaguchi, F. Helmich, Y. Naito, E. Yashima, A. R. A. Palmans, E. W. Meijer, *J. Am. Chem. Soc.* **2018**, *140*, 7810.
- [52] M. R. Molla, A. Das, S. Ghosh, *Chem. Eur. J.* **2010**, *16*, 10084.
- [53] A. Das, S. Ghosh, *Angew. Chem. Int. Ed.* **2014**, *53*, 2038.
- [54] C. R. Martinez, B. L. Iverson, *Chem. Sci.* **2012**, *3*, 2191.
- [55] U. Mayerhöffer, F. Würthner, *Chem. Sci.* **2012**, *3*, 1215.
- [56] A. R. A. Palmans, J. A. J. M. Vekemans, E. W. Meijer, *Recl. des Trav. Chim. des Pays-Bas* **1995**, *114*, 277.
- [57] M. Palma, J. Levin, O. Debever, Y. Geerts, M. Lehmann, P. Samori, *Soft Matter* **2008**, *4*, 303.
- [58] A. R. A. Palmans, J. A. J. M. Vekemans, R. A. Hikmet, H. Fischer, E. W. Meijer, *Adv. Mater.* **1998**, *10*, 873.
- [59] A. R. A. Palmans, J. A. J. M. Vekemans, H. Fischer, R. A. Hikmet, E. W. Meijer, *Chem. Eur. J.* **1997**, *3*, 300.
- [60] A. R. A. Palmans, J. A. J. M. Vekemans, E. E. Havinga, E. W. Meijer, *Angew. Chem. Int. Ed.* **1997**, *36*, 2648.
- [61] S. Sreejith, X. Ma, Y. Zhao, *J. Am. Chem. Soc.* **2012**, *134*, 17346.
- [62] K. L. Diehl, J. L. Bachman, E. V. Anslyn, *Dye. Pigment.* **2017**, *141*, 316.
- [63] D. T. Jayaram, B. H. Shankar, D. Ramaiah, *Chem. Asian J.* **2015**, *10*, 2689.
- [64] S. Das, K. G. Thomas, M. V. George, *J. Chem. Soc., Faraday Trans.* **1992**, *88*, 3419.
- [65] P. J. M. Stals, M. M. J. Smulders, R. Martín-Rapún, A. R. A. Palmans, E. W. Meijer, *Chem. Eur. J.* **2009**, *15*, 2071.
- [66] M. M. L. Nieuwenhuizen, T. F. A. De Greef, R. L. J. Van Der Bruggen, J. M. J. Paulusse, W. P. J. Appel, M. M. J. Smulders, R. P. Sijbesma, E. W. Meijer, *Chem. Eur. J.* **2010**, *16*, 1601.
- [67] A. Timme, R. Kress, R. Q. Albuquerque, H. W. Schmidt, *Chem. Eur. J.* **2012**, *18*, 8329.
- [68] *MarcoModel, Version 11.4, Schrödinger, LLC, Schrödinger Release 2017-4. New York, NY, 2017., n.d.*
- [69] E. Harder, W. Damm, J. Maple, C. Wu, M. Reboul, J. Y. Xiang, L. Wang, D. Lupyan, M. K. Dahlgren, J. L. Knight, J. W. Kaus, D. S. Cerutti, G. Krilov, W. L. Jorgensen, R. Abel, R. A. Friesner, *J. Chem. TheoryComput.* **2016**, *12*, 281.
- [70] W. C. Still, A. Tempczyk, R. C. Hawley, T. Hendrickson, *J. Am. Chem. Soc.* **1990**, *112*, 6127.
- [71] D. Qiu, P. S. Shenkin, F. P. Hollinger, W. C. Still, *J. Phys. Chem. A* **1997**, *101*, 3005.
- [72] A. D. Bochevarov, E. Harder, T. F. Hughes, J. R. Greenwood, D. A. Braden, D. M. Philipp, D. Rinaldo, M. D. Halls, J. Zhang, R. A. Friesner, *Int. J. Quantum Chem.* **2013**, *113*, 2110.
- [73] C. Lee, W. Yang, R. G. Parr, *Phys. Rev. B* **1988**, *37*, 785.
- [74] B. Miehlisch, A. Savin, H. Stoll, H. Preuss, *Chem. Phys. Lett.* **1989**, *157*, 200.
- [75] R. Krishnan, J. S. Binkley, R. Seeger, J. A. Pople, *J. Chem. Phys.* **1980**, *72*, 650.
- [76] A. Konopacka, Z. Pawelka, *J. Phys. Org. Chem.* **2005**, *18*, 1190.
- [77] T. Schnitzer, H. Wennemers, *J. Am. Chem. Soc.* **2017**, *139*, 15356.
- [78] F. A. Bovey, *Nuclear Magnetic Resonance Spectroscopy*, Academic Press, New York, **1969**.
- [79] H. A. Pople, W. G. Schneider, H. J. Bernstein, *High Resolution Nuclear Magnetic Resonance*, McGraw-Hill, New York, **1967**.
- [80] H. Shanan-Atidi, K. H. Bar-Eli, *J. Phys. Chem.* **1970**, *74*, 961.
- [81] J. H. Frank, Y. L. Powder-George, R. S. Ramsewak, W. F. Reynolds, *Molecules* **2012**, *17*, 7914.
- [82] M. Peterca, M. R. Imam, C. H. Ahn, V. S. K. Balagurusamy, D. A. Wilson, B. M. Rosen, V. Percec, *J. Am. Chem. Soc.* **2011**, *133*, 2311.
- [83] Y. Takahashi, T. Hirokawa, M. Watanabe, S. Fujita, Y. Ogura, M. Enomoto, S. Kuwahara, *Tetrahedron Lett.* **2015**, *56*, 5670.
- [84] M. A. Thorn, G. H. Denny, R. D. Babson, *J. Org. Chem.* **1975**, *40*, 1556.
- [85] A. K. Khandpur, S. Förster, F. S. Bates, I. W. Hamley, A. J. Ryan, W. Bras, K. Almdal, K. Mortensen, *Macromolecules* **1995**, *28*, 8796.
- [86] T. Kato, J. Uchida, T. Ichikawa, T. Sakamoto, *Angew. Chem. Int. Ed.* **2018**, *57*, 4355.
- [87] J. Y. Cheng, C. A. Ross, H. I. Smith, E. L. Thomas, *Adv. Mater.* **2006**, *18*, 2505.
- [88] M. H. C. van Son, A. M. Berghuis, F. Eisenreich, B. de Waal, G. Vantomme, J. Gómez Rivas, E. W. Meijer, *Adv. Mater.* **2020**, DOI 10.1002/adma.202004775.

-
- [89] M. Gsänger, E. Kirchner, M. Stolte, C. Burschka, V. Stepanenko, J. Pflaum, F. Würthner, *J. Am. Chem. Soc.* **2014**, *136*, 2351.
- [90] Y. Van De Burgt, A. Melianas, S. T. Keene, G. Malliaras, A. Salleo, *Nat. Electron.* **2018**, *1*, 386.
- [91] P. Gkoupidenis, N. Schaefer, B. Garlan, G. G. Malliaras, *Adv. Mater.* **2015**, *27*, 7176.
- [92] C. Zhang, K. Nakano, M. Nakamura, F. Araoka, K. Tajima, D. Miyajima, *J. Am. Chem. Soc.* **2020**, *142*, 3326.
- [93] H. Shin, B. Moon, *J. Polym. Sci. A Polym. Chem.* **2018**, *56*, 527.
- [94] P. J. Launer, *Silicon Compounds: Silanes and Silicones*, Gelest Inc., Morisville, **2013**.

Chapter 3

Helicity control in the aggregation of achiral squaraine dyes in solution and thin films

Abstract:

The chiroptical properties of chiral and achiral squaraine dyes that comprise either *N,N*-dimethylamino or hydroxy substituents in the *para* positions to the quadratic core are investigated in detail. The *p-N,N*-dimethylamino-based dyes exhibit an intense green color in the molecularly dissolved state, which changes to violet upon protonation. In contrast, a sky-blue color is observed for the molecularly dissolved hydroxy-substituted dyes. This color is altered to red upon single deprotonation and again to blue upon double deprotonation. A spectroscopic study shows that the *p-N,N*-dimethylamino substituted squaraine dyes form aggregates in aqueous solution. Co-assembly experiments of chiral and achiral dyes indicate self-sorting of the two compounds. When the mixtures are prepared in the good solvent chloroform and spin-coated on glass substrates, thin films containing co-assembled aggregates are formed. Intriguingly, the circular dichroism (CD) of the co-assembled materials reaches its maximum when the fraction of the chiral dye is just 25%. The spectroscopic study shows that at this ratio, the chiral dye does not form its native aggregate structure but acts as a chiral dopant which directs the aggregation of the achiral dye into helical columns with preferred helicity. Since the electrochemical oxidation and reduction of the *p-N,N*-dimethylamino substituted squaraine dyes is fully reversible, their application potential in organic electronic devices is investigated. Magnetic-conductive atomic force microscopy shows that co-assembled thin films can be used as organic non-magnetic electron spin filters. The measured spin polarization of the transmitted electrons correlates with the optical properties of material. The highest spin-selective electron transport is measured for the material that contains only 25% chiral dye.

Part of his work has been published:

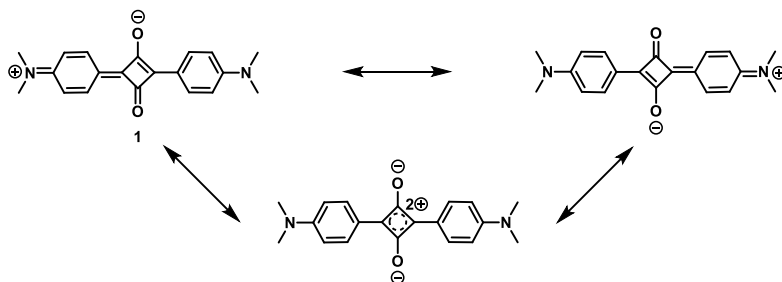
[A.T. Rösch](#), Q. Zhu, J. Robben, F. Tassinari, S.C.J. Meskers, R. Naaman, A.R.A. Palmans, and E.W. Meijer, *Chem. Eur. J.* **2021**, *27*, 298.

3.1 Introduction

The high absorption of light in the visible and near-infrared regime that is displayed by squaraine dyes has intrigued many research groups in the last decades.^[1-7] The high absorptivity with molar extinction coefficients of $10^5 \text{ L mol}^{-1} \text{ cm}^{-1}$ or higher stems from the S_0 - S_1 transition in the dyes' conjugated π -system.^[8] Most of the studies on squaraine dyes that have been reported so far were focused on the optical properties and applications of achiral derivatives.^[2,8] In contrast, research on chiral squaraine dyes is only at the beginning.^[9-13] The reported studies investigated the fundamentals of the formation of CD active superstructures.^[11,12,14-16] Whereas a few articles already suggested an application in organic photodiodes for the detection of circularly polarized light,^[10,13,17] other types of applications such as organic spintronics^[18] remain yet to be explored.

3.1.1 Mesomerism and pH dependent optical properties

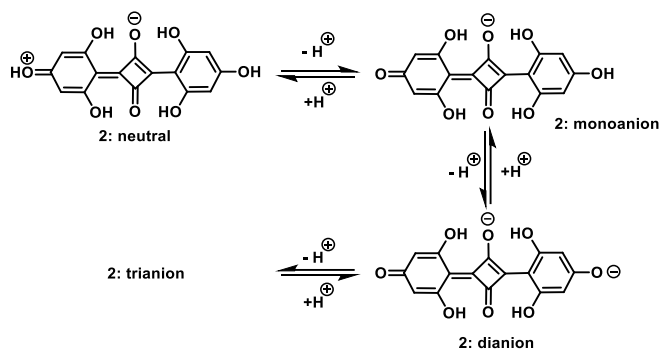
The molecular structure of squaraine dyes is typically represented as resonance-stabilized zwitterion as depicted for squaraine dye **1** in Scheme 3.1.^[2,8] The mesomeric form in which both oxygen atoms are charged (Scheme 3.1 III) is formally attractive since it is in agreement with the aromatic system following Hückel's rule ($N = 0$). The similarity of the absorption spectra of squaraine dyes and cyanine dyes^[19] and their commonly low solubility in organic solvents suggest, however, that dipolar structures (Scheme 3.1 I and II) are the major resonance forms.^[20] Theoretical calculations suggest that both the ground and the excited singlet state of squaraine dyes involve significant intramolecular charge transfer (ICT). As a result, the S_0 - S_1 electronic transition is also considered as an ICT transition.^[8]



*Scheme 3.1: I and II: Major mesomeric forms of the para-N,N-dimethylamino substituted squaraine dye **1**. III: Minor mesomeric form following Hückel's rule. Image adapted with permission from reference [8] (copyright 2016 Nature Publishing Group).*

A study on the phloroglucinol derived squaraine dye **2** by Griffiths and Mama showed that the stabilization of the partial charge can result in pronounced pH-dependent optical properties of dye.^[21] Owing to the stabilization of the partial charge, the hydroxy groups in *para*-position to the quadratic core are highly acidic. **2** was reported to react with small amounts of water present in organic solvents and could be deprotonated multiple times when KOH in ethanol was added (Scheme 3.2). Each deprotonation step could be monitored

by absorption spectroscopy since the removal of each proton affected the optical properties.^[21,22]



Scheme 3.2: Dissociation reactions of the phloroglucinol derived squaraine dye **2**. Image adapted with permission from reference [21] (copyright 2000 Elsevier).

3.1.2 Formation of H- and J-type aggregates

Besides the reports on the optical properties of squaraine dyes in the molecularly dissolved state,^[2] many research groups investigated the dyes' pronounced tendency to form H- and J-type aggregates in solution.^[15,23–29] A study by Buncel *et al.*^[27] described the solvent-controlled aggregation of a squaraine dye in dimethyl sulfoxide (DMSO)/water mixtures. Whereas the dye was molecularly dissolved in pure DMSO, a water content of more than 50 vol% induced the formation of H-type aggregates. Mixtures with an even higher water content (50–80 vol%), showed the formation of J-type aggregates. Interestingly, these J-type aggregates were converted into H-type aggregates after an equilibration period.^[27] The conversion of the aggregates was assigned to the J-type aggregate being formed under kinetic control and the H-type aggregates being the thermodynamically more stable form. The reported system is one of the very early examples of pathway complexity in supramolecular chemistry.^[30–32]

In addition to the aggregation studies in solution,^[15,23–29] the aggregation of squaraine dyes was also studied in thin films^[11,12] and at multiple interfaces.^[16,33–35] A study by Law and Chen^[35] investigated the aggregation of octadecyl-appended squaraine dyes in Langmuir-Blodgett films at the water/air interface. A spectroscopic study showed that the formed type of aggregates depended on the relative positions of the two octadecyl chains attached to the squaraine dye. When the hydrophobic side chains were attached to only one side of the squaraine dye (Figure 3.1a), a blue-shift of the wavelength of maximum absorption was noticed upon aggregation. The blue-shift was assigned to the formation of H-type aggregates stemming from the perpendicular orientation of the squaraine cores to the interface. The stabilization of the H-types aggregates formed by **3** was assigned to the formation of C-O dipole-dipole interactions. When the octadecyl chains were positioned on opposite sides of the dye (Figure 3.1b), a red-shift of the wavelength of maximum

absorption was noticed after aggregation. The red-shift was indicative of the formation of J-type aggregates that stemmed from the parallel orientation of the squaraine cores to the interface. This type of aggregation was suggested to exhibit intermolecular CT interactions between D and A groups of neighboring **4**. Interestingly, the J-type aggregates formed by **4** were thermodynamically unstable after the transfer from the water/air interface to a glass surface and were converted into H-type aggregates after an equilibration period.^[35]

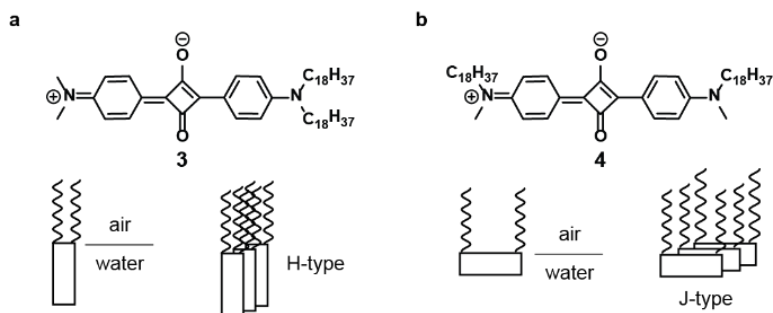


Figure 3.1: H- (a) and J-type (b) aggregates formed by squaraine dyes **3** and **4** at the water/air interface. Image adapted with permission from reference [35] (copyright 1989 American Chemical Society).

3.1.3 Emission of fluorescence in the molecularly dissolved and aggregated state

Owing to their D- π -A- π -D architecture, squaraine dyes have been reported to exhibit (fluoro-)solvatochromism^[36–40] and the emission of dual fluorescence^[36,41] in the molecularly dissolved state. After aggregation, either aggregation-caused quenching (ACQ) or aggregation-induced emission (AIE) of fluorescence is observed. Since ACQ occurs when the planar squaraine cores aggregate into π -stacked architectures, this phenomenon has been observed for the majority of squaraine dyes and enabled applications as fluorescent probes for microscopy imaging of biological samples.^[42,43] In contrast, AIE is realized when π -stacking is prevented.^[36,38] A molecular design that prevents the formation of π -stacked architectures has been proposed by Yu *et al.*^[36] The study used X-ray crystallography to show that the bulky 3,5-dimethylpiperidine moieties attached to the quadratic core prevented π -stacking in the aggregates of squaraine dyes **5** and **6** (Figure 3.2). Instead, the aggregated structures exhibited C-H \cdots O and C-H \cdots π interactions.^[36] Furthermore, fluorescence quenching in squaraine dyes has been induced by chemical reactions, too.^[38,44] For example, squaraine dye **7** was used as a chemical sensor for the detection of cyanide ions in aqueous solution. The corresponding detection limit was 1.7 μ M.^[38]

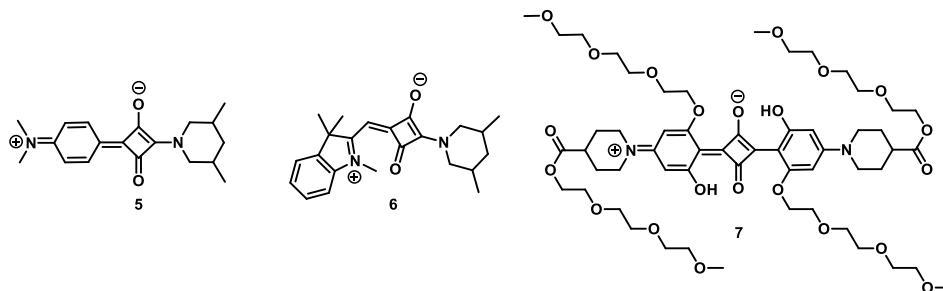


Figure 3.2: Molecular structures of 3,5-dimethylpiperidine substituted squaraine dyes **5** and **6** that exhibit AIE as reported by Yu *et al.*^[36] and triethylene glycol monomethyl ether substituted squaraine dye **7** reported by Liu *et al.*^[38]

3.1.4 Chiral squaraine dyes

One of the first studies that investigated the formation of chiral supramolecular assemblies of squaraine dyes in detail focused on the aggregation of a cholesterol-appended derivative in solution and in thin films.^[11] The study showed that the dye aggregated in helical columns with preferred handedness. Interestingly, the type of preferred handedness depended on the preparation technique of the sample. Similar to the findings by Buncel *et al.*^[27] the formation of a kinetic product was observed when an aliquot of molecularly dissolved dye was added to a solution with a high volume fraction of poor solvent. Thermodynamically stable aggregates were prepared when only a small volume fraction of poor solvent was used, or a heating and cooling cycle was performed. The spectroscopic study on the thin films prepared from the solutions showed that only the thermodynamically stable aggregate retained its optical properties in the solvent-free state. Drop-casting the solutions that contained kinetically formed aggregates or the molecularly dissolved dye resulted in the formation of aggregates with optical properties that differed from the optical properties of the two helical aggregates from the solution experiments which indicated the complexity of the aggregation pathways. Stoll *et al.*^[16] introduced chirality into a squaraine dye by the implementation of enantiopure alkylated prolines (compound **8** in Figure 3.3) and reported the formation of CD active aggregates in solution. Schiek and coworkers prepared homologues of the dye and showed that the derivative with longer terminal alkyl chains (compound **9** in Figure 3.3) could be used to prepare thin films with the hitherto highest intrinsic circular dichroism measured for an organic material.^[12] Additionally, a derivative with shorter alkyl chains (compound **10** in Figure 3.3) was successfully used to prepare organic photodiodes for the detection of circularly polarized light.^[13,17]

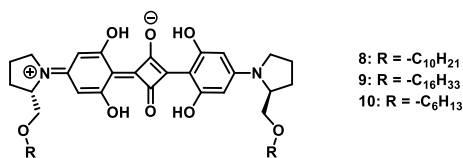


Figure 3.3: Prolinol-appended chiral squaraine dyes. Compound **8** has been reported by Stoll et al.^[16] and compounds **9** and **10** by Schulz et al.^[12,13,17]

In Chapter 2, we discussed the preparation and molecular characterization of the squaraine dyes depicted in Figure 3.4. In this chapter, we continue our study with an investigation of the chiroptical properties, the aggregation behavior and test the usability of the compounds in two different (opto-)electronic applications. We note that the compounds exhibited rotational isomerism in the molecularly dissolved state which can potentially influence both the aggregation and the emerging material properties. Literature reports on the crystal structures of various squaraine dyes indicated that squaraine dyes that contain two oxo-substituents at the quadratic core crystallized exclusively in the *anti*-form.^[45,46] Since we were unfortunately not able to grow crystals for a structural analysis and did not investigate the role of the rotational isomerism in the assembly studies. We assumed, however, that the aggregates will be formed from the thermodynamically most stable isomer. For clarity, we limited the display of the chemical structures of the dyes in this chapter to the *anti*-forms.

Initially, we investigated the absorption and fluorescence of the compounds in the molecularly dissolved state and found that their optical properties could be tuned by the addition of acids and bases. Owing to their better solubility and good chemical stability, we limited the presented results of the aggregation study to the chiral and achiral *para-N,N*-dimethylamino based **S-SQ-1** and **a-SQ-1**. In aqueous solution, **S-SQ-1** formed J-type aggregates and **a-SQ-1** formed H-type aggregates. A spectroscopic study revealed that mixtures of chiral and achiral dye preferred the formation of self-sorted aggregates after equilibration. When concentrated mixtures of the dyes were spin-coated from chloroform solution, a kinetically controlled aggregation process induced the formation of co-assembled J-type aggregates. Intriguingly, the co-assembled material with the highest CD effect was obtained for a feed ratio of a 1:3 mixture of chiral and achiral dye when chiral **S-SQ-1** was used exclusively. We used cyclic voltammetry to demonstrate that both electrochemical oxidation and reduction of the *p-N,N*-dimethylamino substituted dyes were chemically fully reversible. With fulfilling this pivotal requirement for the usage in electronic devices, we moved on to testing the materials in optoelectronic applications. We showed that the compounds act as non-magnetic spin-filters. The highest spin-selectivity of the transmitted electrons was achieved in the material based on the 1:3 mixture of chiral and achiral dye which gave insight into the correlations between the presence of stereogenic centers, optical activity and spin-filtering properties of a material.

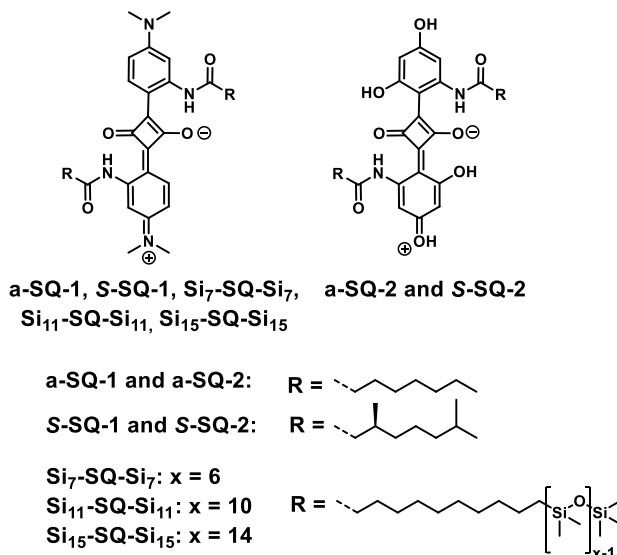


Figure 3.4: Molecular structures of *p*-*N,N*-methylamino substituted squaraine dyes **a-SQ-1**, **S-SQ-1**, **Si₇-SQ-Si₇**, **Si₁₁-SQ-Si₁₁** and **Si₁₅-SQ-Si₁₅** as well as the *p*-hydroxy substituted squaraine dyes **a-SQ-2** and **S-SQ-2**.

3.2 Photophysical properties in the molecularly dissolved state

We started our study with the investigation on the optical properties of our compounds in the molecularly dissolved state. Figure 3.5a shows the molar extinction coefficients ϵ of **a-SQ-1** and **S-SQ-1** as function of the wavelength in tetrahydrofuran (THF) solution. The dyes showed a sharp maximum of ϵ around 670 nm and a weak shoulder at 620 nm. The molar extinction coefficients ϵ determined at λ_{\max} are $3.3 \cdot 10^5$ for **a-SQ-1** and $3.2 \cdot 10^5$ L mol⁻¹ cm⁻¹ for **S-SQ-1**. The absorption spectra of the *p*-hydroxy-substituted squaraine dyes **a-SQ-2** and **S-SQ-2** are depicted in Figure 3.5b. For these dyes, the wavelength of maximum absorption λ_{\max} was 606 nm. In contrast to **a-SQ-1** and **S-SQ-1**, the shoulder at shorter wavelengths was barely noticed. Solutions of the oligo(dimethylsiloxanes) (oDMS) appended squaraine dyes **Si₇-SQ-Si₇**, **Si₁₁-SQ-Si₁₁** and **Si₁₅-SQ-Si₁₅** showed identical optical properties as **a-SQ-1** and **S-SQ-1** (Figure 3.5c). Fluorescence spectroscopy indicated that only the *p*-*N,N*-dimethylamino substituted squaraine dyes were fluorescent in the molecularly dissolved state. The emission spectra recorded for the THF solutions represented mirror images of the absorption spectra and the corresponding Stokes shifts were 15 nm (dashed lines in Figure 3.5c).

The recorded absorption spectra were consistent with literature reports on structurally related squaraine dyes in the molecularly dissolved state.^[2,11,34] The small shoulder in the absorption spectra of **a-SQ-1** and **S-SQ-1** was assigned to the vibronic progression of the absorption band. The high ϵ in combination with the narrow absorption bandwidths and

the low intensity of the vibronic progression indicated a weak vibronic coupling for the electronic S_0 - S_1 transition along the long molecular axis of the squaraine backbone.^[28] Weak vibronic coupling is commonly caused by a low configurational displacement between the initial and the final state of an electronic transition. A theory for quantifying the vibrational progressions in the absorption spectrum has been developed by Huang and Rhys.^[47] The theory introduces the Huang-Rhys parameter S as the ratio of the transitions I_{0-1} and I_{0-0} . Our calculations (given in the experimental part) showed that S was 0.16 for both compounds, which corroborated that the vibronic coupling was weak.^[48] The lack of the I_{0-1} band in the spectra of **a-SQ-2** and **S-SQ-2** suggested an even weaker vibronic coupling for the squaraine dyes with the *p*-hydroxy-substituent. The weaker vibronic coupling was ascribed to the formation of additional intramolecular hydrogen bonds between the hydroxy groups in *ortho*-position to the quadratic core and the oxygen atoms attached to the quadratic core which were suggested to stiffen the molecular backbone. The absorption spectra indicated that ϵ determined at λ_{\max} of the dyes was $1.6 \cdot 10^5 \text{ L mol}^{-1} \text{ cm}^{-1}$ for **a-SQ-2** and $1.5 \cdot 10^5 \text{ L mol}^{-1} \text{ cm}^{-1}$ for **S-SQ-2**. When comparing the spectroscopic data of the two sets of dyes, distinct differences were noticed. For **a-SQ-2** and **S-SQ-2** both the wavelength of maximum absorption and ϵ were lower than for **a-SQ-1** and **S-SQ-1**. The decrease of the values suggested the less pronounced intramolecular charge transfer in the *p*-hydroxy-substituted derivatives with respect to the *p*-*N,N*-methylamino substituted dyes.

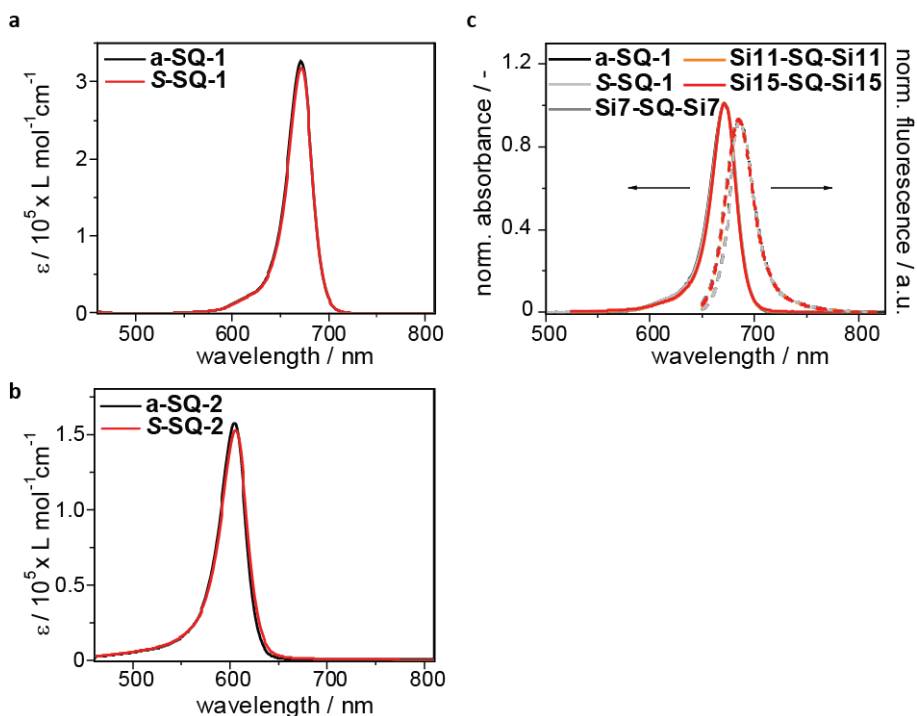


Figure 3.5: Molar extinction coefficients ϵ (solid lines) of (a) **a-SQ-1** and **S-SQ-1** as well as (b) **a-SQ-2** and **S-SQ-2**. Fluorescence (dashed lines in c) was measured for all *p-N,N*-dimethylamino substituted dyes ($\lambda_{\text{ex}} = 640 \text{ nm}$). All spectra were recorded in dry tetrahydrofuran. The concentrations were $2.6 \cdot 10^{-6} \text{ mol L}^{-1}$ for **a-SQ-1**, **S-SQ-1** and the siloxane appended squaraine dyes as well as $1.3 \cdot 10^{-5} \text{ mol L}^{-1}$ for **a-SQ-2** and **S-SQ-2**. Optical path length: 10 mm.

In Chapter 2, we used FT-IR spectroscopy to show that the *p-N,N*-dimethylamino-based dyes formed intramolecular hydrogen bonds. We wondered whether the dyes could form hydrogen bonds to solvent molecules, too. Since the absence of positive or negative solvatochromism (e.g. the absence of a linear correlation of λ_{max} and the solvent polarity) is a common indicator for the formation of hydrogen bonds between solute and solvent,^[49] we investigated the optical properties of the dyes in a range of solvents (acetonitrile (ACN), chloroform (CHCl_3), heptane (C_7H_{16}), and methanol (MeOH)), which differ in polarity. The normalized absorption and fluorescence spectra that were recorded during the experiments for **S-SQ-1** are depicted in Figure 3.6a. When $1/\lambda_{\text{max}}$ was plotted as a function of the solvent's $E_{\text{T}}(30)$ value, Figure 3.6b was obtained. The graph showed that the data are scattered and hardly any linear solvatochromism was observed. The absence of the linear correlation between $1/\lambda_{\text{max}}$ and the solvent's polarity suggested that additional solute-solvent interactions, such as hydrogen bond formation were present.^[49] We note that **S-SQ-1** showed similar fluorescence spectra in most tested solvents, too. Interestingly, the

spectrum recorded in heptane showed a small shoulder at shorter wavelengths. The development of such a shoulder in the fluorescence spectrum recorded in apolar solvent has also been mentioned in a literature report on squaraine dyes.^[36] In the report, the shoulder has been ascribed to two different photophysical process that may occur upon photoexcitation and could potentially be related to LE and ICT state.^[36]

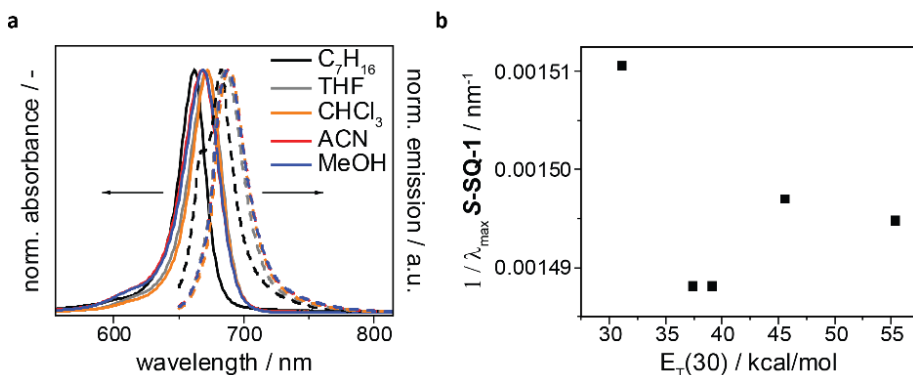


Figure 3.6: (a) Absorption and emission spectra recorded for **S-SQ-1** in various solvents. (b) Variation of $1/\lambda_{max}$ with increasing solvent polarity (as expressed by the $E_T(30)$ value). Concentration: $2.6 \cdot 10^{-6} \text{ mol L}^{-1}$. Optical path length: 10 mm.

During the investigation of the optical properties of **a-SQ-2** and **S-SQ-2** in various solvents, we found a strong impact of the solvent on the absorption spectrum (Figure 3.7). Whereas the absorption band indicative of the molecular dissolved species was clearly observed in dry THF and dry chloroform, the formation of a very broad absorption band was observed in heptane. Additionally, blue-shifted absorption bands around 500 nm were found in acetonitrile, methanol and dry *N,N*-dimethylformamide. The formation of the broad absorption band in heptane was assigned to the formation of aggregates. Interestingly, the formation of the blue-shifted absorption bands was only noticed in solvents that were not water-free or in *N,N*-dimethylformamide which is a base. Owing to the structural similarity of **a-SQ-2** and **S-SQ-2** to the phloroglucinol based squaraine dye whose pH dependent optical properties^[21,22] were presented in the introduction, we concluded that the observed spectral changes stemmed from the dissociation of the hydroxy groups in *para*-position to the quadratic core when water or bases were present.

Stimulated by this finding, we were interested in investigating the pH-dependent properties of both sets of squaraine dyes in detail. Since the type of side chain had a negligible effect on the absorbance or fluorescence of the dyes in molecularly dissolved state, we limit the presented results to the achiral dyes **a-SQ-1** and **a-SQ-2**.

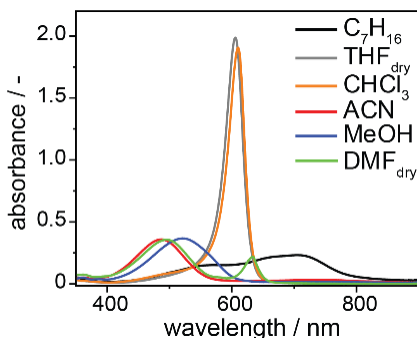


Figure 3.7: Absorption spectra recorded for **S-SQ-2** in various solvents. Concentration: $1.3 \cdot 10^{-5} \text{ mol L}^{-1}$. Optical path length: 10 mm.

As depicted in Figure 3.8a, the green solution of **a-SQ-1** in THF changed its color to violet upon the addition of trifluoroacetic acid (TFA). The color change was accompanied by the formation of new absorption bands around 540 and 570 nm. The band at 570 nm was assigned to the molecularly dissolved and protonated form of **a-SQ-1**. The band at 540 nm was assigned to a corresponding vibronic progression. In contrast to the neutral form, the protonated form did not exhibit fluorescence. We found that the acid-base reaction was reversible and showed a distinct equilibrium character. The absorption bands of unprotonated **a-SQ-1** were still noticed at TFA concentrations that were four orders of magnitude higher than the concentration of **a-SQ-1**. The low basicity of the compound was assigned to the electronic configuration that results in the positive partial charge on the substituents in *para*-position to the quadratic core.

As depicted in Figure 3.8b, the blue color of a solution of molecularly dissolved **a-SQ-2** was changed to red after the addition of one droplet of triethylamine (TEA). The corresponding absorption spectrum revealed a blue shift of λ_{max} to 500 nm. In accordance with literature reports, we assigned the spectral changes to the single deprotonation of the dye.^[21,22] After the addition of KOH in ethanol, the color of the solution was changed again to blue. The corresponding absorption spectrum showed spectral broadening, that λ_{max} was moved to 610 nm and that the formed species emitted fluorescence (excitation at 620 nm). The spectral changes that were in accordance with literature reports on the phloroglucinol derived squaraine dye indicated that the addition of KOH induced the formation of a double deprotonated species.^[21,22]

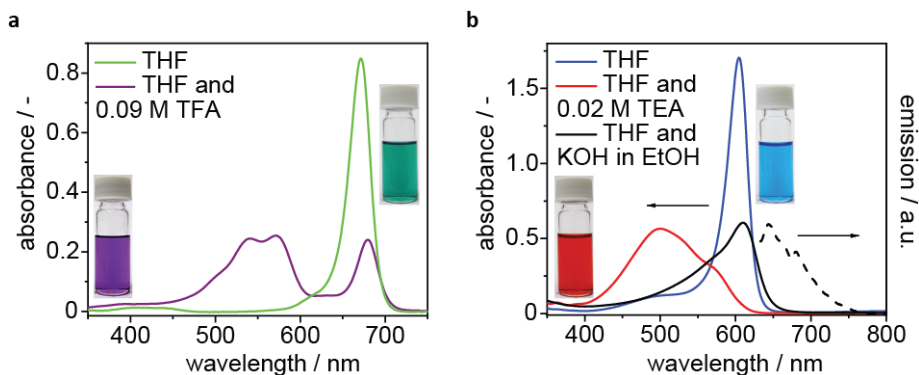


Figure 3.8: Photophysical properties recorded for molecularly dissolved solutions of **a-SQ-1** and **a-SQ-2** in dry THF. (a) The amine group of **SQ-1** was protonated by the addition of TFA (0.09 M). (b) The hydroxyl group of addition of **a-SQ-2** was deprotonated by the addition of a droplet of TEA. A second hydroxy group was deprotonated by the addition of a saturated solution of KOH in ethanol. Doubly deprotonated **a-SQ-2** exhibited fluorescence. Concentrations: **a-SQ-1**: $2.6 \cdot 10^{-6}$ M, **a-SQ-2**: $1.3 \cdot 10^{-5}$ M. Optical path length: 10 mm. The insets show the color of the samples after increasing the concentration of the dyes. Violet: solution of **a-SQ-1** after the addition of TFA, green: solution of **a-SQ-1** in THF, red: solution of **a-SQ-2** in THF after the addition of TEA, blue: solution of **a-SQ-2** in before and after the addition KOH in ethanol solution.

The geometries of the uncharged dyes in the ground and the first excited state were very similar to each other which was indicated by the narrow absorption bandwidths and λ_{\max} noticed at long wavelengths. The stabilization of the single charge resulted in electronically unsymmetrical structures. These species had to adjust their geometries during photoexcitation which required additional energy as noticed by blue shift of their λ_{\max} . Additionally, these increased configurational displacements during photoexcitation resulted in the increased vibronic progressions noticed as spectral broadening.^[21] After characterizing the optical properties of all dyes in the molecularly dissolved state we continued our study with investigating the aggregation behavior of the dyes in solution.

3.3 Formation of CD active aggregates of **a-SQ-1** and **S-SQ-1** in aqueous solution

Having characterized the optical properties of the dyes in the molecularly dissolved state, we continued our study with the investigation of the aggregation in solution. We focussed on the optical properties of aqueous solutions containing the *p-N,N*-dimethylamino substituted dyes **a-SQ-1** and **S-SQ-1** since these dyes exhibited a higher solubility and better chemical stability than **a-SQ-2** and **S-SQ-2** (see 2.2.6 for the chemical instability of *p*-hydroxy substituted squaraine dyes **a-SQ-2** and **S-SQ-2**).

We added concentrated aliquots of **a-SQ-1** and **S-SQ-1** in THF to water. Upon the addition, an immediate color change from green to blue was observed which suggested that the aqueous solution containing 1 vol% THF induced the formation of aggregates. UV/Vis spectroscopy of the prepared samples indicated pronounced spectral broadening (black lines in Figure 3.9a and b). Noticing the absorption band of the molecularly dissolved species only as a small shoulder corroborated the conversion to aggregates. The absorption spectrum of aggregated **a-SQ-1** (Figure 3.9a) showed one absorption maximum around 590 nm with a broad shoulder at longer wavelengths. λ_{\max} was blue-shifted (H-band) with respect to the absorption band of the molecularly dissolved species (670 nm). **S-SQ-1** in turn showed the formation of a very broad absorption band with λ_{\max} around 800 nm, which was indicative of the formation of a J-type aggregate (Figure 3.9b). CD spectroscopy indicated that the aggregates that were formed by **S-SQ-1** exhibited circular dichroism whereas aggregates formed by **a-SQ-1** did not, as expected (Figure 3.9c). Since no CD effect was observed for the molecularly dissolved neutral or charged forms, and the sample did not exhibit linear dichroism (LD), it was concluded that the CD effect stemmed from supramolecular interactions.^[50–52] The helical structure of the aggregates of **S-SQ-1** was indicated by the absorption band around 820 nm, which displayed a strong bisignate Cotton effect in the CD spectrum. We note that the aggregates were non-fluorescent. Aggregation-induced fluorescence quenching is well-known for squaraine dyes and typically occurs when the chromophores form a π -stacked architecture in the aggregates.^[36,53]

Since literature reports on the formation of supramolecular aggregates often mention kinetic traps in the aggregation process,^[54,55] we assessed whether kinetic traps were present in our system as well. We equilibrated the samples by heating and stirring at 90 °C for 30 min, followed by sonication and slow cooling to room temperature before a second investigation by absorption and CD spectroscopy. The absorption spectra depicted as red lines in Figure 3.9a show that the H-type aggregates formed by **a-SQ-1** were retained after equilibration and only the shoulder at longer wavelengths was slightly decreased in intensity. The absorption spectrum of aggregated **S-SQ-1** was barely affected by equilibration (red line in Figure 3.9b). However, the CD spectra recorded for **S-SQ-1** before and after equilibration showed distinct differences. After the equilibration, the CD spectrum was mirrored at the x-axis with respect to the initial spectrum (Figure 3.9c). The mirror symmetry of both CD spectra and the similarity of the absorption spectra suggested that the structural changes that occurred during equilibration were relatable to the inversion of

helicity. A similar inversion of helicity has been reported for squaraine dyes by Jyothish *et al.*^[11] who found that one type of helicity was formed under kinetic and the other under thermodynamic control.

We further investigated the temperature of the helix inversion by a temperature-dependent CD experiment. The ellipticity of a freshly prepared sample was recorded continuously at the wavelength of 875 nm during a heating cycle (blue line in Figure 3.9d). As soon as the temperature was increased above 50 °C, an increase of the ellipticity signal to positive values was observed. This process was not abrupt but happened over the temperature range from 50 °C to 60 °C (scanning rate: 10 °C/min). When the temperature was increased close to the boiling point of water, the sample was still CD active suggesting a high stability of the aggregates.

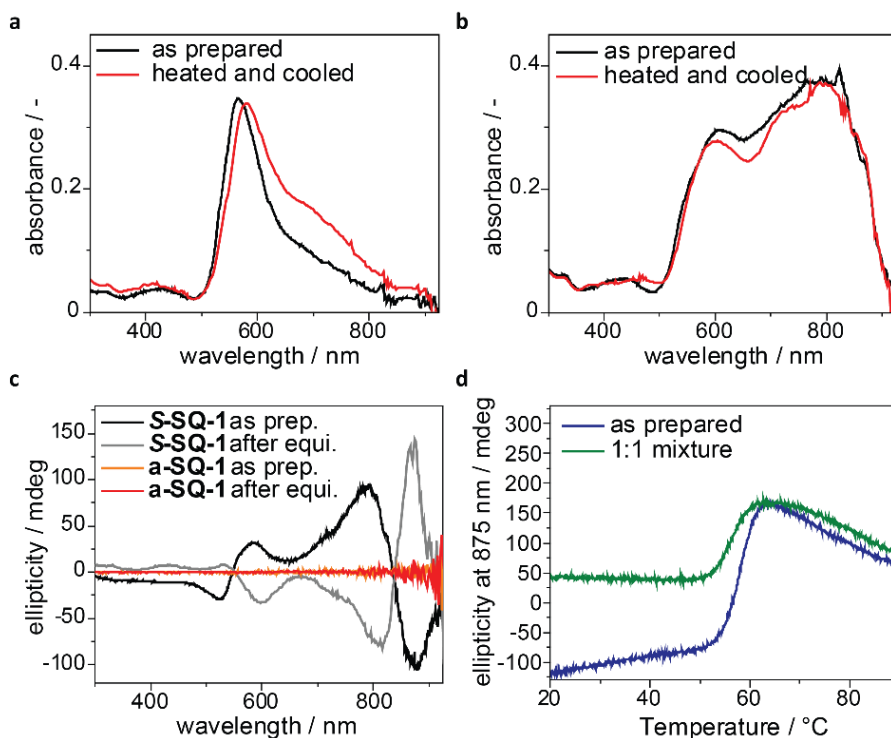


Figure 3.9: Photophysical properties of the aggregates of (a) **a-SQ-1** and (b,c) **S-SQ-1** measured directly after preparation and again after equilibration following the protocol; Concentration: $1.3 \cdot 10^{-5} \text{ mol L}^{-1}$; Solvent: H_2O containing 1 vol% THF. (a,b) UV/Vis spectra; (c) CD spectra; (d) Variation of the ellipticity at 875 nm while heating to 90 °C (heating rate: 10 °C/min). Blue line: Variation of the ellipticity during heating the as-prepared solution. Green line: Variation of the ellipticity for the sample which contained a 1:1 mixture of an as prepared solution and an equilibrated solution. Optical path length: 10 mm.

In a second temperature-dependent experiment, we investigated whether thermodynamically stable aggregates could act as nuclei to facilitate the conversion of the kinetically formed aggregates. The corresponding sample was prepared by mixing the aqueous solution containing the kinetically formed aggregates (concentration: $1.3 \cdot 10^{-5}$ mol L⁻¹) to an equal volume of the aqueous solution containing the thermodynamically stable aggregates (concentration: $1.3 \cdot 10^{-5}$ mol L⁻¹). During the experiment, the mixed solution was heated up to 90 °C while recording the ellipticity continuously at the wavelength of 875 nm (green line in Figure 3.9d). Similar to the previous experiment, the helix inversion occurred between 50 and 60 °C. Since the presence of thermodynamically stable aggregates did not affect the temperature at which helix inversion was observed, we concluded that the thermodynamically stable aggregates were not able to nucleate the conversion of kinetically trapped species on the experimental time scale.

Having investigated the aggregation behavior of the individual dyes, we continued our study with the investigation of the aggregation of samples containing mixtures of **a-SQ-1** and **S-SQ-1**. In order to ensure the reproducibility of the experiments, the investigated samples were equilibrated following the above-mentioned equilibration protocol. When the feed of the dyes was tuned from **a-SQ-1** to **S-SQ-1**, the gradual increase of the J-band was noticed which was most pronounced for pure **S-SQ-1** (Figure 3.10a). Additionally, the CD effect determined at 868 nm increased predominantly in a linear fashion (Figure 3.10b and c). This correlation suggested that the aggregates formed by **a-SQ-1** and **S-SQ-1** in water were either barely mixing or the ability of **S-SQ-1** to bias one helical sense was low.

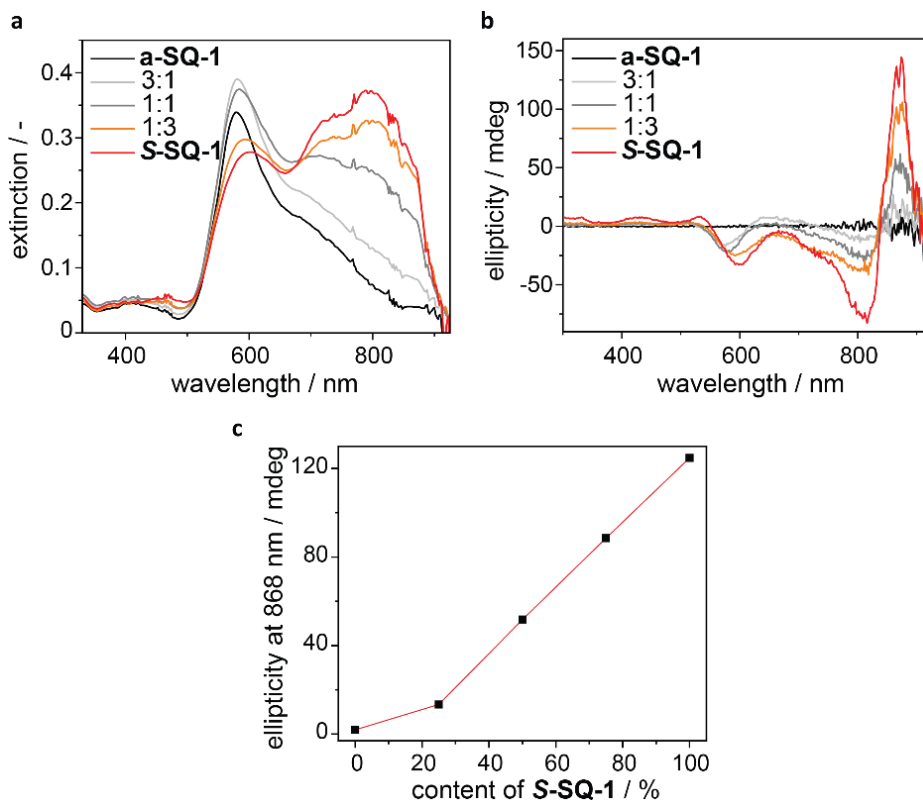


Figure 3.10 Photophysical properties of the aggregates of **a-SQ-1** and **S-SQ-1** and mixtures thereof, recorded at a total concentration of $1.3 \cdot 10^{-5} \text{ mol L}^{-1}$ in H_2O containing 1 vol% THF. (a) UV/Vis spectra; (b) CD spectra; (c) Ellipticity measured at 868 nm. Optical path length: 10 mm.

3.4 Formation of CD active aggregates of **a-SQ-1** and **S-SQ-1** in thin film

We continued our study by investigating the chiroptical properties of **a-SQ-1** and **S-SQ-1** in thin film. Thin films with thicknesses of approximately 40 nm were prepared by spin-coating a solution of **a-SQ-1** or **S-SQ-1** in chloroform onto microscope glass slides. At first, the thin films were characterized by UV/Vis spectroscopy. The spectra depicted in Figure 3.11a showed noticeable differences from those previously recorded in solutions. Both dyes showed broad absorption bands with λ_{max} being red-shifted with respect to the absorption band of the molecularly dissolved species. For **a-SQ-1**, λ_{max} was found at 790 nm and for **S-SQ-1** at 834 nm. Additionally, the absorption spectra of both compounds exhibited a shoulder at 620 nm which was in turn blue-shifted with respect to the absorption band of the molecularly dissolved species. Since the shapes of the absorption spectra of **a-SQ-1** and **S-SQ-1** were rather similar, a structurally related packing of the chromophores in the aggregated thin films was likely which motivated us to probe for the formation of co-

assembled aggregates by spin-coating mixtures of **a-SQ-1** and **S-SQ-1**. As shown in Figure 3.11a, all UV/Vis spectra recorded for the thin films that contained 5-50% **S-SQ-1** looked very similar to the spectrum that was recorded for pure **a-SQ-1**. λ_{\max} was retained at 790 nm. Increasing the content of **S-SQ-1** to 75% in the mixture resulted in a red shift of λ_{\max} to 799 nm which was still somewhat lower than λ_{\max} previously recorded for pure **S-SQ-1** (834 nm).

Next, CD spectroscopy was used to investigate the chiroptical properties of the thin films (Figure 3.11b). Obviously, the thin film consisting of pure **a-SQ-1**, did not show any CD effect. In contrast, thin films which contained a mixture of **a-SQ-1** and **S-SQ-1** or pure **S-SQ-1** showed clear Cotton effects in the CD spectrum. LD had no contribution to the CD spectra (vide infra). As noticed in Figure 3.11c, the measured CD effect increased strongly when 5-25% **S-SQ-1** was added to the feed. The highest CD effect was measured for the thin film prepared from the 3:1 mixture of **a-SQ-1** and **S-SQ-1**. When the amount of **S-SQ-1** was increased further, the ellipticity decreased. We note that the CD spectra that were measured when **S-SQ-1** became the main fraction in the thin film (75% and 100% **S-SQ-1** in the feed) did not only exhibit a reduced maximum ellipticity but had a different shape, too.

This observation was in sharp contrast to the results obtained in the aqueous solutions, where the spectra recorded for mixtures of **a-SQ-1** and **S-SQ-1** resembled linear combinations of the spectra of the individual parts. Since the addition of less than 25% of **S-SQ-1** to the feed induced optical activity but did not impact the absorption spectra of the materials, we concluded that in this regime, **S-SQ-1** was incorporated structurally into the helical aggregates formed by **a-SQ-1**. As a result of the structural incorporation, the stereogenic centers of **S-SQ-1** induced aggregation with preferred helicity. In helical supramolecular systems formed in solution, this effect has commonly been referred to as the “sergeants-and-soldiers” effect.^[56] Whereas the “sergeants-and-soldiers” effect in supramolecular systems that are formed in solution is typically operative for most mixing ratios between achiral and chiral compounds,^[57,58] it was only observed for a rather small range for our co-assembled thin films. Decreasing the CD effect by increasing the amount of **S-SQ-1** above 25% suggested a less effective packing of **S-SQ-1** in the helical columns formed by **a-SQ-1** which induced changes in the absorption spectra once **S-SQ-1** became the major fraction in the feed. The observed trend is fascinating since it shows that the maximization of the amount of stereogenic centers in the aggregates – by increasing the amount of **S-SQ-1** in the feed – does not yield the thin films with the highest CD effect. The highest CD effect was achieved when **S-SQ-1** is solely used as a director for **a-SQ-1**, rather than a structural component.

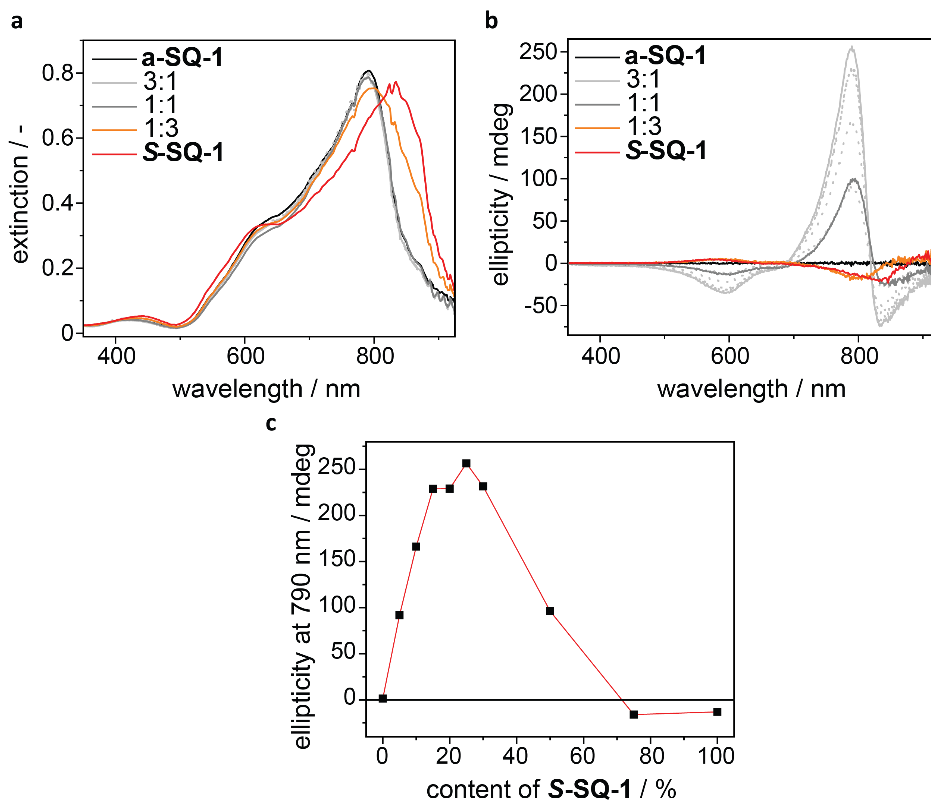


Figure 3.11: Photophysical properties of thin films that were prepared by spin-coating chloroform solutions of **a-SQ-1**, **S-SQ-1** and mixtures thereof. (a) UV/Vis spectra; (b) CD spectra; dotted lines: spectra recorded for the samples with feed ratios of 5, 10, 15, 20 and 30% **S-SQ-1**. (c) Variation of the ellipticity determined at 790 nm for samples with an increasing content of **S-SQ-1**. All thin films had a thickness of approximately 40 nm.

In order to elucidate whether the measured ellipticity was caused by purely excitonic coupling or also stemmed from other effects such as cholesteric ordering, thin films with different thicknesses were prepared by spin-coating. The spin-coating parameters to obtain thin films with thicknesses ranging from 11 to 81 nm are shown in Table 3.1. The absorption and CD spectra recorded for all spin-coated thin films are shown in Figure 3.12a and b. All spectra except the spectra that were recorded for the 81 nm thick film looked very similar. Macroscopically, the 81 nm thick film differed from the others since it was not as smooth as the other. Partial dewetting suggested that 80 nm was the upper limit for the films' thickness that we could achieve with spin-coating our squaraine dye mixtures. As depicted in Figure 3.12c, the ratio of the measured ellipticity and the film's thickness was relatively constant for the thin film with the lowest thickness in the series (thicknesses between 11 and 24 nm). When the film thickness was increased to 43 nm or higher, an increase of the ratio was noticed. In very thin films, the CD effect can only originate from the mechanism

operative at the nm scale, which suggested that similar to the aggregates formed in solution, excitonic coupling was the origin for measuring CD effect in the thin films. The increase of the ratio of measured ellipticity and the film's thickness with an increasing film thickness suggested that the recorded CD effect also stemmed partly from other effects such as cholesteric ordering in bulk.^[59] In all thin films, the aggregates are still very small since the films did not show birefringence when investigated by polarized optical microscopy. We also probed the presence of LD in the films with an increased thickness. For the 81 nm thick film, the measured LD was 0.002 when expressed as the differential absorbance of vertically and horizontally linear polarized light (Figure 3.12d). This value was compared with the ellipticity value that was obtained by CD spectroscopy in order to assess whether this LD signal added a substantial contribution to the ellipticity spectra of the thin films. For a comparison, we first converted the ellipticity value to circular differential absorbance of right and left circularly polarized light $\Delta A = A_L - A_R$. For the 81 nm thick sample, the maximum value of 342 mdeg ellipticity corresponded with a differential absorbance ΔA of 0.01. This value is five times higher than the linear differential absorbance. Considering the fact that the linear birefringence is typically of limited magnitude (typically < 0.1), we conclude that an artificial, LD induced contribution to the circular dichroism spectrum must be very small even in the thicker films.

*Table 3.1: Spin-coating parameters for obtaining co-assembled film containing 75% ***α -SQ-1*** and 25% ***S-SQ-1***.*

Rotation speed ^[a] [rpm]	Concentration ^[b] [mM]	Measured thickness ^[c] [nm]	ellipticity _{790nm} [mdeg]	ellipticity _{790nm} / thickness [mdeg/nm]
2000	20	54	325	6.02
2000	10	24	56	2.31
2000	5	11	22	1.95
1000	20	81	333	4.10
1000	10	43	153	3.55
1000	5	15	30	2.00

^[a] A liquid sample was deposited on top of a microscope glass slide before 45 s of rotation at the given rotation speed. ^[b] Total concentration of a mixture of 75% ***α -SQ-1*** and 25% ***S-SQ-1***. ^[c] The surface was scratched, and the height profile was measured using a surface profilometer.

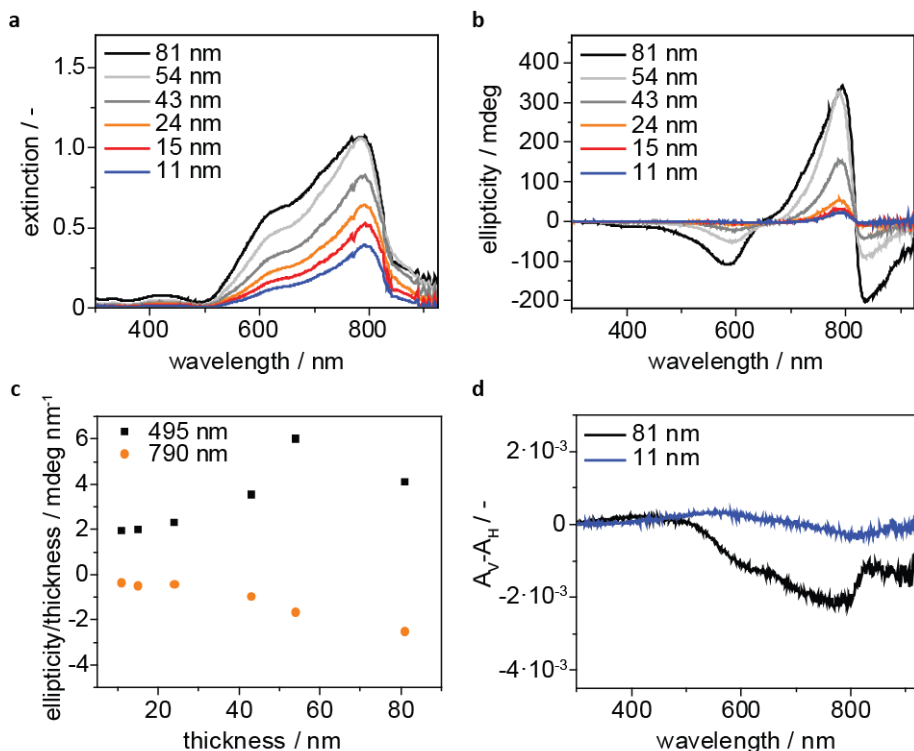


Figure 3.12: Increasing absorption (a) and ellipticity (b) when increasing the thickness of a co-assembled thin film containing 25% **S-SQ-1** and 75% **a-SQ-1**. For the 81 nm thick sample, dewetting started to occur. (c): Variation of the ellipticity/thickness ratio with increasing film thickness. (d): linear dichroism as expressed as the difference in absorbance for vertically and horizontally polarized light $A_V - A_H$ for the 11 nm and 81 nm thick samples.

Since the previously conducted solution experiments indicated that annealing influenced the optical properties of the formed aggregates, a possible impact of annealing was also investigated for the thin films. All thin films were annealed for 10 min at 210 °C under nitrogen atmosphere which was well below the molecules' decomposition temperature (240 °C). Subsequently, the optical properties were investigated. The absorption spectra which were recorded after annealing are depicted in Figure 3.13a. The thin films with low **S-SQ-1** content (0-30%) exhibited a decrease of the former band of maximum absorbance around 790 nm and the rise of two new absorption bands around 600 nm and 700 nm, respectively. For thin films with a higher **S-SQ-1** content (50-100%), the absorption band at λ_{max} was retained and the absorbance of the band around 600 nm intensified slightly. Besides changes in the UV/Vis spectra, the CD spectra recorded for all samples showed differences after annealing, too. As depicted in Figure 3.13b, samples with low **S-SQ-1** content (0-30%) showed a blue-shift of the wavelength of the maximum CD effect. After annealing, the maximum CD effect was noticed around 690 nm (790 nm before

annealing). For the 50% **S-SQ-1** sample, the CD effect was decreased and for the 75% and 100% **S-SQ-1** samples, the CD effect was increased. The changes in both UV/Vis and CD spectra upon annealing suggested that the aggregates which were formed during spin-coating were kinetic products. Interestingly, annealing seemed to have induced the formation of aggregates with optical properties that were somewhat resembling the optical properties found for the equilibrated mixtures in aqueous solution: The thin films that contained a high content of **a-SQ-1** showed the formation of an absorption band that was blue-shifted with respect to the absorption band of the molecularly dissolved dyes and indicative of H-type aggregates. Thin films that contained a high content of **a-SQ-1** retained the red-shifted absorption bands indicative of J-type aggregates. An additional parallel between the aggregation in aqueous solution and the annealed thin films was that the sample with highest amount of **S-SQ-1** exhibited the highest CD effect within the series. The LD spectra recorded after annealing indicate that LD has negligible contribution to the absorption properties after the structural rearrangement, still (Figure 3.14).

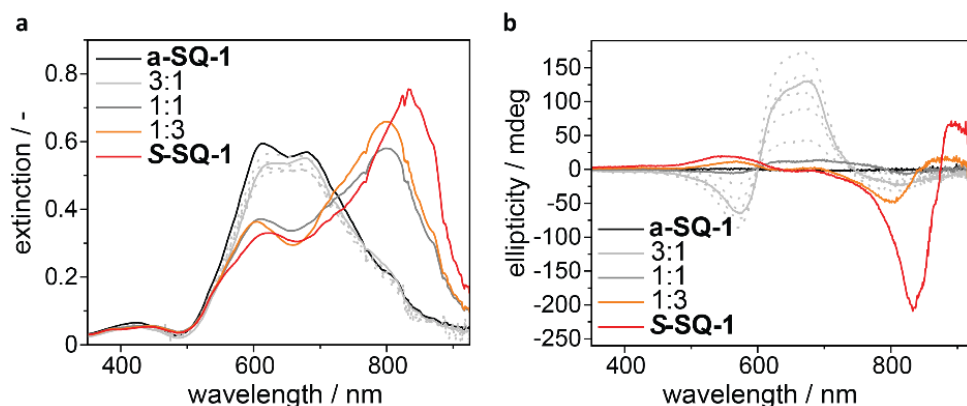


Figure 3.13: Photophysical properties of annealed (10 min, 210°C under nitrogen atmosphere) thin films prepared from **S-SQ-1** and **a-SQ-1** and mixtures thereof. (a) UV/Vis spectra; (b) CD spectra; dotted lines: spectra recorded for samples with feed ratios of 5, 10, 15, 20 and 30% **S-SQ-1**.

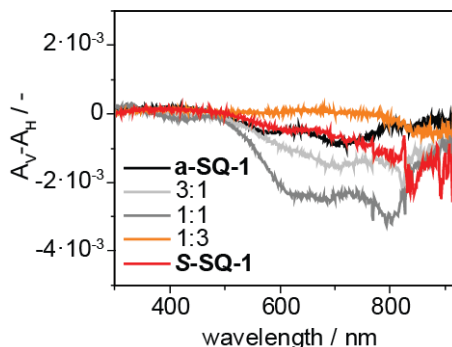


Figure 3.14: Linear dichroism spectra that were measured for spin-coated thin films with an increasing content of **S-SQ-1** in a mix of **a-SQ-1** and **S-SQ-1** after annealing for 10 min at 210 °C under nitrogen atmosphere.

3.5 Aggregation of the siloxane-appended squaraine dyes

The study on the bulk properties of **Si7-SQ-Si7**, **Si11-SQ-Si11** and **Si15-SQ-Si15** in Chapter 2 indicated that all three soft materials exhibited highly ordered nanostructures. We measured the absorption spectra for the thin films of **Si7-SQ-Si7**, **Si11-SQ-Si11** and **Si15-SQ-Si15** to probe the aggregation of the squaraine motifs in the siloxane matrix. The absorption spectra depicted in Figure 3.15 were recorded directly after drop-casting and again after a heating and cooling cycle. Interestingly, the absorption spectra of the as prepared thin films show the formation of H-type aggregates ($\lambda_{\max} = 562$ nm) with shoulder to longer wavelengths similar to the aggregates formed by **a-SQ-1** in water (Figure 3.15a). After the thin films were heated to the isotropic melt and cooled down to room temperature, broad absorption bands were noticed which were indicative of the formation of J-type aggregates similar to **S-SQ-1** aggregated in water (Figure 3.15b). The formation of both H- and J-type aggregates by the siloxane appended squaraine dyes highlighted that also in siloxane matrix, the two main modes of squaraine dye aggregation could be achieved. H-types aggregates have been reported to be stabilized by C-O dipole-dipole interactions and J-type aggregates by intermolecular CT interactions between D and A groups.^[35]

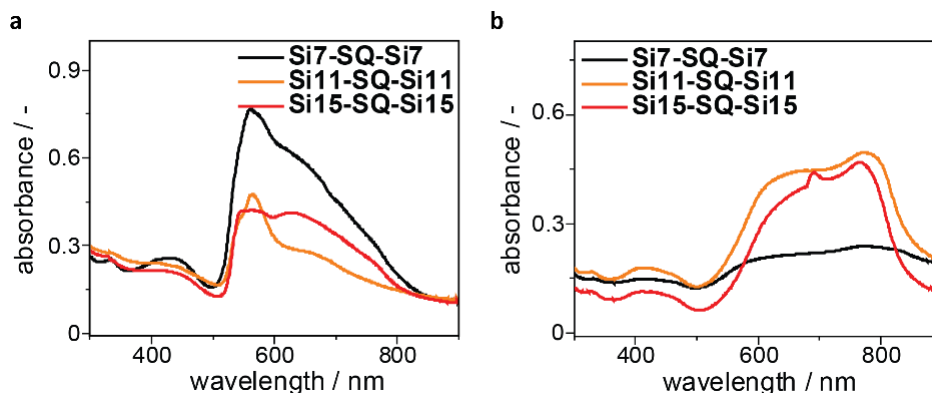


Figure 3.15: Optical properties of **Si7-SQ-Si7**, **Si11-SQ-Si11** and **Si15-SQ-Si15** measured after (a) drop-casting from chloroform solution and (b) after heating to the isotropic melt and cooling back to room temperature.

The aggregation study of **a-SQ-1** and **S-SQ-1** showed that the spin-coating was a suitable technique for preparing co-assembled aggregates of the dyes in a reproducible fashion. In order to investigate possible consequences of chirality on optoelectronic applications, we continued our study by an electrochemical characterization of the dye and applied them in two different devices.

3.6 Cyclic voltammetry (CV)

Since squaraine dyes are well-known for their semiconducting properties, they have often been applied in organic electronic applications.^[60–62] An important requirement for the usability of an organic molecule in an electronic device is its electrochemical stability, i.e. the electrochemical oxidation and reduction of the compound must be fully reversible and should not result in kinetically trapped species or irreversible degradation. In the following section, we investigate the squaraine dyes by CV, which was done in collaboration with Koen Hendriks at the Eindhoven University of Technology. For the experiments, three electrodes (graphite working electrode, platinum counter electrode and Ag/AgCl reference electrode) were connected to a potentiostat and immersed into a 5 mM dichloromethane solution of the squaraine dye (containing 200 mM tetrabutylammonium hexafluorophosphate as background salt to facilitate the electrochemical measurement). The applied voltage between working and counter electrode was referenced to the electrode potential of the reference electrode and varied to oxidize and reduce the compound electrochemically. The electron transfer processes resulted in the generation of electrical current that was measured by the potentiostat.

Figure 3.16 shows the voltammogram that was obtained by CV for the solution of **S-SQ-1** in dichloromethane. For a better comparison with the literature reports, the applied potential was referenced to ferrocene (Fc). The plot shows that increasing the applied

potential above of 0.14 V vs Fc resulted in measuring current with a positive algebraic sign. After reaching the turning point at 0.67 V vs Fc, the applied potential was decreased which was accompanied by a decrease of the current that turned even negative. The minimum current was measured at 0.21 V. When the potential was lowered further to -1.1 V vs Fc, current with negative algebraic sign was noticed for the second time. After the turning point at -1.52 V vs Fc, the applied potential was increased. Increasing the potential resulted in increasing the current to positive values (maximum at -0.64 V vs Fc). After passing the applied potential of 0 V vs Fc, the second cycle of the CV, which looked almost identical as the first, was started.

Whereas positive currents in CV indicate the formation of an oxidized species, negative currents indicate the formation of a reduced species. The matching shapes of the first and the second cycle indicated that all induced electrochemical oxidation and reduction processes were fully reversible. As a result, the positive current that was measured starting from the applied potential of 0.14 V vs Fc was ascribed to the formation of an oxidized species which was reduced to the neutral form when the applied potential was reduced below 0.35 V vs Fc (after passing the first turning point at 0.67 V vs Fc). Analogously, the negative current that was measured starting from the applied potential of -1.1 V vs Fc was ascribed to the formation of a reduced species which was oxidized back to the neutral form when the applied potential was increased to -0.64 V vs Fc (after passing the second turning point at -1.52 V vs Fc). The onsets of the oxidation and reduction peaks from the CV are commonly used to determine the highest occupied molecular orbital (HOMO) and lowest unoccupied molecular orbital (LUMO) of the investigated compound. In the literature, the values are often referenced to the electrode potential of Fc in vacuum to exclude solvent effects.^[34] By performing the additional referencing step for data recorded for **S-SQ-1**, the HOMO was determined at -5.3 eV and the LUMO at -4.1 eV. These values are similar to those reported in the literature for squaraine dyes that do not contain amide groups, suggesting that the amide functionalization did neither cause a decreased electrochemical stability nor has a strong impact on the redox potential of the dyes.^[34,60]

Having shown that the oxidation and reduction of our dyes is electrochemically reversible, we moved on the using the compounds as organic semiconductors in organic electronic devices.

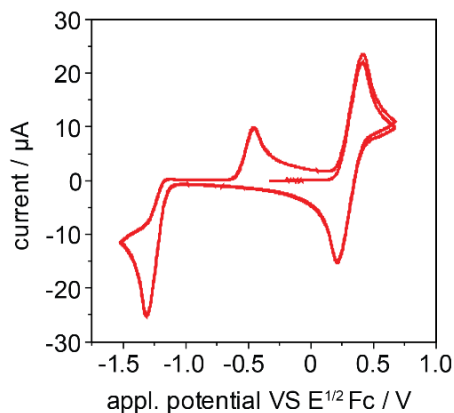


Figure 3.16: Cyclic voltammetry was performed using a 5 mM solution of **S-SQ-1** in dichloromethane solution with 200 mM tetrabutylammonium hexafluorophosphate as background salt to facilitate the electrochemical measurement. The scanning rate was 0.1 V s^{-1} . The reference electrode for the measurement was an Ag/AgCl electrode. The applied potential was referenced to the half potential of Fc after adding Fc to the solution and repeating the measurement.

3.7 Organic field effect transistors (OFET)

Squaraine dyes have recently been highlighted as high-performance materials in organic thin-film field effect transistors, and yielded hole mobilities of $0.1 \text{ cm}^2 \text{ V}^{-1} \text{ s}^{-1}$.^[62] Therefore, we explored the semiconducting properties of **a-SQ-1**, **S-SQ-1** and mixtures thereof. The following organic field effect transistor (OFET) study was performed in collaboration with Mengmeng Li from prof. René Janssen's group at the Eindhoven University of Technology. Figure 3.17 shows the transfer characteristics of a top-gate, bottom-contact OFET that was fabricated from **S-SQ-1**. The mobility extraction from transfer curves was not conducted since the leakage current I_{GS} was in the range of $I_{GS} < I_{DS} < 10 I_{GS}$. The high leakage current is a consequence of a rather low charge carrier mobility in the spin-coated thin film which also resulted in the necessity to apply the relatively high gate-source voltage of -80 V. In contrast to **S-SQ-1**, **a-SQ-1** could not be used as semiconducting material in an OFET since the film formation on top of the Si/SiO₂ substrates used for OFET fabrication was hampered by dewetting. Gsänger *et al.* reported that the mobilities of the squaraine dye based OFETs were greatly enhanced when vacuum-deposition was used for sample preparation instead of spin-coating.^[62] However, as **S-SQ-1** decomposes at its melting temperature of 220 °C, vacuum-deposition for OFET fabrication was not performed and the device performance of the **S-SQ-1**-based OFET could unfortunately not be increased.

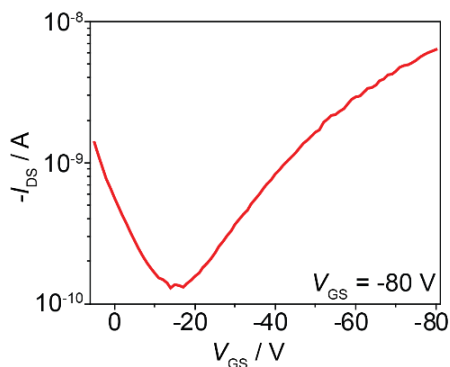


Figure 3.17: Transfer characteristics of a top-gate, bottom-contact OFET of **S-SQ-1**. The organic material was deposited by spin-coating.

3.8 Investigation of spin-filtering properties by magnetic-conductive atomic force microscopy

Magnetic-conducting atomic force microscopy (mc-AFM) is an efficient method for studying the spin-selectivity in the electron transport through chiral structures including the effect of the interface between the probed material and the substrate.^[63–67] The mc-AFM studies described in the following were performed in collaboration with Qirong Zhu and Francesco Tassinari from prof. Ron Naaman’s group at the Weizmann Institute of Science. The electrical AFM-measurement is recording the current, which is transported through a thin film of organic matter that is deposited on top of a gold-coated nickel surface. During the measurements, the sample is magnetized with its magnetization perpendicular to the surface. Owing to the magnetization direction of the Ni/Au substrate, the electrons that are injected into the organic material have a bias in their populations of electron spin orientations. Depending on the orientation of the magnet, either spin-up or spin-down orientation of the electron spin is favored. Depending on the handedness of their helicity, chiral, non-racemic materials favor the transmission of electrons with either spin-up or spin-down orientation of the electron spin. As a result, a higher number of electrons is transmitted when the magnet is oriented in a way that the majority of the injected electrons has the spin alignment that is transmitted preferably. When the orientation of the magnet is reversed, the majority of the injected electrons has the spin alignment that is not transmitted preferably. The amount of transmitted electrons is hence reduced.^[68,69] As a result, one orientation of the magnet results in a higher current than the other when investigating a chiral sample that is deposited on a Ni/Au substrate by mc-AFM.^[70] It is important to note that the values are determined in the nonlinear regime which makes the measurement sensitive to detect the spin polarization for the electron conduction.

The mc-AFM experiments on the squaraine dyes were performed on spin-coated thin films using pure **a-SQ-1**, pure **S-SQ-1** and the 3:1 mixture thereof. The thin films were not

annealed. Figure 3.18 shows the results obtained from recording 100 *I*-*V* curves for both orientations of the magnet. The orientation of the magnet did not have an influence on the *I*-*V* curves that were recorded for **a-SQ-1** which was ascribed to the absence of preferred handedness in the helical aggregates. For the sample containing purely **S-SQ-1**, an effect of the orientation of the magnet was found. The most pronounced dependency of the *I*-*V* curves on the orientation of the magnet was found for the 3:1 mixture of both **a-SQ-1** and **S-SQ-1**. From the recorded measurements, the spin polarization *SP* was determined using $SP = \left[\frac{I_{up} - I_{down}}{I_{up} + I_{down}} \right] \cdot 100$. The spin polarization at 3 V is 0% for **a-SQ-1**, $17 \pm 5\%$ for **S-SQ-1** and $56 \pm 8\%$ for the 3:1 mixture. Figure 3.18d shows that similar values were also found for lower potentials. The upper limit of 60% *SP* corresponds to a ratio of about four to one between the two spin states. For various systems, which are based on a homochiral compound, a similar *SP* has been reported.^[64,69,71-76] One recent study that reported on the correlation of *SP* and optical activity of a supramolecular material investigated aggregates of chiral coronene bisimides. The compounds formed nanofibers in poor solvent. Depending on the temperature, one type of handedness was formed preferably. At 20 °C, P-type helicity was preferred and at -10 °C, M-helicity. mc-AFM showed that samples prepared and dried at 20 °C or -10 °C preferred the transmission of electrons with one particular spin alignment. However, the direction of the spin alignment of the electrons that were transported preferably were opposite for the two samples. The observation was ascribed to the dependency of the spin-filtering properties of a material on the type of helicity in its aggregate structure and not its type and number of stereogenic centers.^[65] The system presented by us corroborates these findings and indicates that not only supramolecular nanofibers, but also spin-coated thin films can be used as spin filters. Although the number of stereogenic centers is increased when comparing the **S-SQ-1** sample with the 3:1 mixture of **a-SQ-1** and **S-SQ-1**, a pronounced decrease in spin polarization is noticed which coincides with the decrease of optical activity.

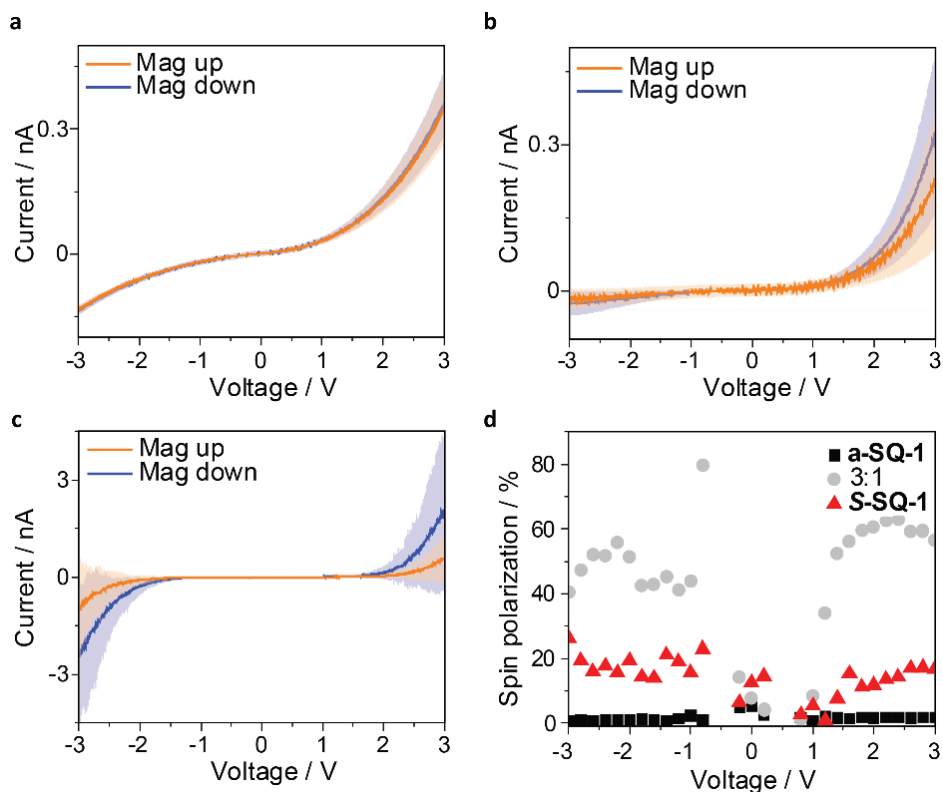


Figure 3.18: Spin-dependent conduction through thin films consisting of (a) **a-SQ-1**, (b) **S-SQ-1** and (c) the 3:1 mixture thereof. The I-V plots show the averages and standard deviations over 100 individual measurements. For each sample, the measurements were performed with the Ni film magnetized with the north pole pointing up (orange) or down (blue). (d) Spin polarization was calculated from the results of the mc-AFM measurements.

3.9 Conclusions

We investigated the optical properties of two sets of novel amide functionalized squaraine dyes. Molecular solutions of all dyes exhibited intense colors that were tuned by the addition of acids or bases. The *p*-*N,N*-dimethylamino substituted squaraine dyes **a-SQ-1** and **S-SQ-1** changed their color from green to violet upon protonation. Blue *p*-hydroxyl substituted squaraine dyes **a-SQ-2** and **S-SQ-2** changed their color to red when singly deprotonated and to blue when deprotonated twice. The aggregates formed by **a-SQ-1** and **S-SQ-1** in aqueous solution and in thin film were studied by optical spectroscopy. When mixtures of **a-SQ-1** and **S-SQ-1** were aggregated in aqueous solution, the CD effect increased predominantly linearly when increasing the amount of chiral **S-SQ-1** in the feed. The linear increase indicated that the aggregates of **a-SQ-1** and **S-SQ-1** were either barely mixing or the ability of **S-SQ-1** to bias one helical sense in the mix was low.

In contrast, spin-coated thin films of **a-SQ-1** and **S-SQ-1** resulted in co-assembled structures that displayed a non-linear increase of the CD effect. Surprisingly, the highest CD effect was measured for a thin film that contained a 3:1 mixture of **a-SQ-1** and **S-SQ-1**. The similarity of the absorption spectrum of the 3:1 mixture to the absorption spectrum of pure **a-SQ-1** indicated that co-assembled **S-SQ-1** was structurally incorporated into the helical aggregates formed by **a-SQ-1** and induced aggregation with preferred helicity. Annealing of the spin-coated films resulted in changes of the UV/Vis and CD spectra which suggested that the co-assembly during spin-coating is a kinetically controlled process.

Cyclic voltammetry indicated that the electrochemical oxidation and reduction of the dyes were fully reversible. As a result, we tested the compounds for application as organic semiconductors to probe for a correlation between the optical activity and device characteristics. Whereas the results from OFETs indicated only low charge carrier mobilities, mc-AFM measurements showed that the highest spin polarization of transmitted electrons was found for the 3:1 mixture, i.e. the material with the highest CD-effect (and not the material containing the highest amount of stereogenic centers). Considering the emerging work on spintronic applications e.g. photoelectrochemical water splitting,^[67,77] the system presented here stresses the importance of supramolecular chirality rather than the mere presence of stereogenic centers for achieving spin polarization during electron transport.

3.10 Experimental Section

3.10.1 Optical measurements

The stock solutions which are used for the optical measurements and spin-coating were prepared by weighing the required amount of compound and transferring it into a screw-capped vial. The desired concentration of the stock solution was adjusted by the addition of the chosen solvent by using Gilson MICROMAN Positive-Displacement Pipets. The samples were heated and sonicated until the solids were dissolved completely and homogeneous solutions were obtained. In case of sensitive **a-SQ-2** and **S-SQ-2**, stock solutions were not sonicated but thoroughly shaken manually. The solutions were freshly prepared on each day when the measurements were performed. The solutions for the subsequently conducted optical measurements were prepared by the dilution of the stock solutions to adjust the desired target concentration. In order to ensure the complete dissolution and equilibration during the experiments which were performed in aqueous solutions, the samples were heated and stirred at 90 °C for 20 min, followed by the slow cooling to room temperature. Spectroscopic measurements were performed in high precision cells made of quartz suprasil (Hellma analytics). The optical path length was 10 mm. For spin-coating, quadratic microscope glass slides (2 cm side length) were cleaned by sonication in acetone, demineralized water and isopropanol for 5 min each. 50 µL of the solution which was containing the dye were deposited on top of the microscope glass slide and subsequently spun (Headway Research Inc.; concentrations: 5 mM, 10 mM or 20 mM; spinning speed: 1000 rpm or 2000 rpm; spinning time: 45 sec). For the determination of the optical properties after annealing, the spin-coated samples were annealed at 210 °C for 10 min under nitrogen atmosphere. UV/Vis, CD and LD spectroscopy were performed on a JASCO J-815 CD spectrometer with either a JASCO Peltier MPTC-490S temperature controller with a temperature range of 278 - 373 K or a JASCO Peltier PFD-425S/15 with a temperature range of 263 - 383 K. Separate UV/Vis spectra were recorded on a JASCO V-750 UV/Vis spectrometer. Fluorescence spectroscopy was performed on a Perkin Elmer LS 50 B luminescence spectrometer. Reflectivity and Muller matrix spectroscopy was performed on a W-VASE ellipsometer from J.A. Wollam.

3.10.2 Investigation of thin film morphology and spin-filtering properties

Optical microscopy using crossed polarizers was performed on an optical microscope from Jenaval. Images were recorded using an Infinity1 camera purchased from Lumenera. AFM imaging was performed using an Asylum Research MFP-3D mounted on an anti-vibration stage. Silicon tips were supplied by Nanoworld (SIN 89229F10L1333). The dimensions of the tips were: length of 150 μm , width of 27 μm and thickness of 2.8 μm . The spring constant was 7.4 N/m and soft tapping-mode was used to obtain an image. A resolution of 512 points and lines was used for the images. The images were processed using Gwyddion (v. 2.53) software. mc-AFM measurements were performed on 10 nm thick thin films deposited by spin-coating from a chloroform solution on top of a gold-coated nickel surface (Ni/Au 120/8 nm thicknesses). The AFM set-up was a custom-designed RHK machine capable of reaching a magnetic field of 1 T. During the AFM measurement (contact mode), the substrate was magnetized with the magnetic pole up or down by external magnetic field of 0.5 T. The AFM cantilevers were platinum-coated silicon tips supplied by Micromasch (HQ:DPE-XSC11, spring constant: 2.7 N/m). During each measurement, an 8-10 nN force was exerted with the tip onto the probed surface. The AFM tip is grounded while the potential at the Au/Ni substrate was varied from -3 to +3 V.

3.10.3 Determination of the Huang-Rhys parameter S

The Huang-Rhys parameter S is defined as

$$\frac{I_{0-0}}{I_{0-1}} = \frac{1}{S} \quad (\text{a})$$

In order to calculate S , the relative contributions of the I_{0-0} and the I_{0-1} transition to the absorption band have to be determined. The information was obtained by the integration of the two vibronic bands noticed in Figure 3.19.

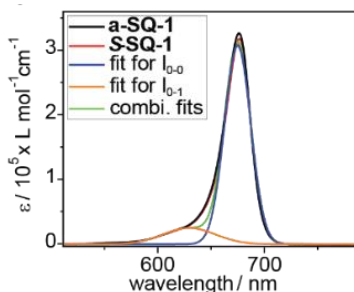


Figure 3.19: Molar extinction coefficients ϵ of **a-SQ-1** and **S-SQ-1** as well as Gaussian fit-functions for S_{0-0} and S_{0-1} . The spectra were recorded in dry tetrahydrofuran. The concentrations were $2.6 \cdot 10^{-6} \text{ mol L}^{-1}$ and the optical path length 10 mm

The spectra of the extinction coefficients ϵ of **S-SQ-1** and **a-SQ-1** were approximated using the software Origin 2019 and the Levenberg Marquardt algorithm. The chosen function consisted of two Gaussians to fit the I_{0-0} and I_{0-1} transitions. The fit-function was

$$\epsilon = -1200 + 618326 * e^{-0.5 * \left(\frac{E-1.8505}{0.03499}\right)^2} + 50170 * e^{-0.5 * \left(\frac{E-1.98}{0.07}\right)^2}.$$

Origin 2019 was used to plot and integrate this function. An area of 55642.9 was obtained.

By integrating $\epsilon = -1200 + 50170 * e^{-0.5 * \left(\frac{E-1.98}{0.07}\right)^2}$, the area under the baseline and the I_{0-1} transition was 1263.2. We note that this integral stems from an error of the baseline. The error is so small that it does not affect the values stated for ϵ in the corresponding subchapter. For the calculation of S the error is compensated by subtraction. The area under the I_{0-0} transition is 54379.7 and the area under the I_{0-1} transition band is 8803.

After transposing equation (a), the calculated integrals were used to determine the Huang-Rhys parameter $S = 0.16$. The value corroborates the weak vibronic coupling.^[48] The energy difference between the S_{0-0} and S_{0-1}

absorption bands corresponds with 1040 cm^{-1} . A corresponding vibration is not found in the FT-IR spectrum in Chapter 2 due to the symmetrical character of the molecule.

3.10.4 Cyclic voltammetry

The dyes **a-SQ-1** and **S-SQ-1** were dissolved in dry dichloromethane containing 200 mM tetrabutyl ammonium hexafluorophosphate as the background salt to obtain 5 mM solutions of the dyes. The working electrode was made from graphite and the counter electrode from platinum. The reference electrode for the measurement was an Ag/AgCl electrode. A potentiostat / galvanostat (PGSTAT12 from AutoLab) was used for the CV measurement. The scanning rate was 0.1 V s^{-1} . The determined electrode potentials were referenced to Fc in vacuum by addition of -5.16 eV .^[34]

3.10.5 Organic field effect transistors

A top-gate bottom-contact architecture was used for transistor fabrication. Au electrodes were thermally evaporated onto Si/SiO₂ substrates as source and drain. The semiconductor layer was spin-coated from a 10 mM solution of **S-SQ-1** in chloroform (60 μL , 1000 rpm, 45 s). Afterwards, a CYTOP® fluoropolymer insulating layer was spin-coated as dielectric, and 60 nm Ag were thermally evaporated as gate electrode. A Keithley 4200-SCS was used for all standard OFET measurements which were performed in vacuum.

3.11 References

- [1] A. Treibs, K. Jacob, *Angew. Chem. Int. Ed.* **1965**, *4*, 694.
- [2] K. Y. Law, *Chem. Rev.* **1993**, *93*, 449.
- [3] G. Xia, H. Wang, *J. Photochem. Photobiol. C Photochem. Rev.* **2017**, *31*, 84.
- [4] H. E. Sprenger, W. Ziegenbein, *Angew. Chem. Int. Ed.* **1967**, *6*, 553.
- [5] C. Qin, W. Y. Wong, L. Han, *Chem. Asian J.* **2013**, *8*, 1706.
- [6] K. a. Bello, S. N. Corns, J. Griffiths, *J. Chem. Soc. Chem. Commun.* **1993**, 452.
- [7] U. Mayerhöffer, M. Gsänger, M. Stolte, B. Fimmel, F. Würthner, *Chem. Eur. J.* **2013**, *19*, 218.
- [8] S. Sreejith, P. Carol, P. Chithra, A. Ajayaghosh, *J. Mater. Chem.* **2008**, *18*, 264.
- [9] A. Ajayaghosh, P. Chithra, R. Varghese, *Angew. Chem. Int. Ed.* **2007**, *46*, 230.
- [10] S. Brück, C. Krause, R. Turrisi, L. Beverina, S. Wilken, W. Saak, A. Lützen, H. Borchert, M. Schiek, J. Parisi, *Phys. Chem. Chem. Phys.* **2014**, *16*, 1067.
- [11] K. Jyothish, M. Hariharan, D. Ramaiah, *Chem. Eur. J.* **2007**, *13*, 5944.
- [12] M. Schulz, J. Zablocki, O. S. Abdullaeva, S. Brück, F. Balzer, A. Lützen, O. Arteaga, M. Schiek, *Nat. Commun.* **2018**, *9*, 2413.
- [13] M. Schulz, F. Balzer, D. Scheunemann, O. Arteaga, A. Lützen, S. C. J. Meskers, M. Schiek, *Adv. Funct. Mater.* **2019**, *29*, 1900684.
- [14] H. Chen, K.-Y. Law, J. Perlstein, D. G. Whitten, *J. Am. Chem. Soc.* **1995**, *117*, 7257.
- [15] H. Chen, M. S. Farahat, K. Y. Law, D. G. Whitten, *J. Am. Chem. Soc.* **1996**, *118*, 2584.
- [16] R. S. Stoll, N. Severin, J. P. Rabe, S. Hecht, *Adv. Mater.* **2006**, *18*, 1271.
- [17] M. Schulz, M. Mack, O. Kollege, A. Lützen, M. Schiek, *Phys. Chem. Chem. Phys.* **2017**, *19*, 6996.
- [18] V. Varade, T. Z. Markus, K. Vankayala, N. Friedman, M. Sheves, D. H. Waldeck, R. Naaman, *Phys. Chem. Chem. Phys.* **2017**, DOI 10.1039/C7CP06771B.
- [19] R. W. Bigelow, H.-J. Freund, *Chem. Phys.* **1986**, *107*, 159.
- [20] P. M. Kazmaier, G. K. Hamer, R. A. Burt, *Can. J. Chem.* **1990**, *68*, 530.
- [21] J. Griffiths, J. Mama, *Dye. Pigment.* **2000**, *44*, 9.
- [22] S. Das, K. G. Thomas, M. V. George, *J. Chem. Soc., Faraday Trans.* **1992**, *88*, 3419.
- [23] Y. Zhang, B. Kim, S. Yao, M. V. Bondar, K. D. Belfield, *Langmuir* **2013**, *29*, 11005.
- [24] Y. Xu, Z. Li, A. Malkovskiy, S. Sun, Y. Pang, *J. Phys. Chem. B* **2010**, *114*, 8574.
- [25] U. Mayerhöffer, F. Würthner, *Chem. Sci.* **2012**, *3*, 1215.
- [26] S. H. Kim, J. H. Kim, J. Z. Cui, Y. S. Gal, S. H. Jin, K. Koh, *Dye. Pigment.* **2002**, *55*, 1.
- [27] E. Buncel, A. J. McKerrow, P. M. Kazmaier, *J. Chem. Soc. Chem. Commun.* **1992**, 1242.
- [28] C. Lambert, F. Koch, S. F. Völker, A. Schmiedel, M. Holzapfel, A. Humeniuk, M. I. S. Röhr, R. Mitric, T. Brixner, *J. Am. Chem. Soc.* **2015**, *137*, 7851.
- [29] J. Wojtyk, A. McKerrow, P. Kazmaier, E. Buncel, *Can. J. Chem.* **1999**, *77*, 903.

- [30] P. A. Korevaar, S. J. George, A. J. Markvoort, M. M. J. Smulders, P. A. J. Hilbers, A. P. H. J. Schenning, T. F. A. De Greef, E. W. Meijer, *Nature* **2012**, *481*, 492.
- [31] D. Van Der Zwaag, P. A. Pieters, P. A. Korevaar, A. J. Markvoort, A. J. H. Spiering, T. F. A. De Greef, E. W. Meijer, *J. Am. Chem. Soc.* **2015**, *137*, 12677.
- [32] S. Ogi, C. Grzeszkiewicz, F. Würthner, *Chem. Sci.* **2018**, *9*, 2768.
- [33] K. Liang, K.-Y. Law, D. G. Whitten, *J. Phys. Chem.* **1994**, *98*, 13379.
- [34] K. Gräf, M. A. Rahim, S. Das, M. Thelakkat, *Dye. Pigment.* **2013**, *99*, 1101.
- [35] K. Y. Law, C. C. Chen, *J. Phys. Chem.* **1989**, *93*, 2533.
- [36] F. Yu, Q. Yan, K. Liang, Z. Cong, Q. Shao, Y. Wang, L. Hong, L. Jiang, G. Ye, H. Wang, B. Chi, G. Xia, *J. Lumin.* **2021**, *233*, 117882.
- [37] C. A. T. Laia, S. M. B. Costa, *Phys. Chem. Chem. Phys.* **1999**, *1*, 4409.
- [38] T. Liu, X. Liu, M. A. Valencia, B. Sui, Y. Zhang, K. D. Belfield, *Eur. J. Org. Chem.* **2017**, 3957.
- [39] K. M. Shafeekh, S. Das, C. Sissa, A. Painelli, *J. Phys. Chem. B* **2013**, *117*, 8536.
- [40] D. D. S. Pisoni, C. L. Petzhold, M. P. De Abreu, F. S. Rodembusch, L. F. Campo, *C. R. Chim.* **2012**, *15*, 454.
- [41] Q. Shao, K. Liang, H. Ling, Y. Wang, Z. Yan, G. Xia, H. Wang, *J. Mater. Chem. C* **2020**, *8*, 4549.
- [42] I. A. Karpenko, M. Collot, L. Richert, C. Valencia, P. Villa, Y. Mély, M. Hibert, D. Bonnet, A. S. Klymchenko, *J. Am. Chem. Soc.* **2015**, *137*, 405.
- [43] M. Collot, R. Kreder, A. L. Tatarets, L. D. Patsenker, Y. Mely, A. S. Klymchenko, *Chem. Commun.* **2015**, *51*, 17136.
- [44] J. Griffiths, S. Park, *Tetrahedron Lett.* **2002**, *43*, 7669.
- [45] P. F. Santos, L. V. Reis, P. Almeida, D. E. Lynch, *CrystEngComm* **2011**, *13*, 1333.
- [46] J. Bernstein, E. Goldstein, *Mol. Cryst. Liq. Cryst.* **1988**, *164*, 213.
- [47] K. Huang, A. Rhys, *Proc. R. Soc. Lond. A* **1950**, *204*, 406.
- [48] H. Moustroph, A. Towns, *ChemPhysChem* **2018**, *19*, 1016.
- [49] C. Reichardt, *Chem. Rev.* **1994**, *94*, 2319.
- [50] G. Pescitelli, L. Di Bari, N. Berova, *Chem. Soc. Rev.* **2014**, *43*, 5211.
- [51] M. Liu, L. Zhang, T. Wang, *Chem. Rev.* **2015**, *115*, 7304.
- [52] N. Berova, K. Nakanishi, R. Woody, *Circular Dichroism: Principles And Applications*, John Wiley&Sons, New York, USA, **2000**.
- [53] M. Huang, R. Yu, K. Xu, S. Ye, S. Kuang, X. Zhu, Y. Wan, *Chem. Sci.* **2016**, *7*, 4485.
- [54] S. H. Shin, S. Chung, B. Sani, L. R. Comolli, C. R. Bertozzi, J. J. De Yoreo, *Proc. Natl. Acad. Sci.* **2012**, *109*, 12968.
- [55] S. Ogi, T. Fukui, M. L. Jue, M. Takeuchi, K. Sugiyasu, *Angew. Chem. Int. Ed.* **2014**, *53*, 14363.
- [56] M. M. Green, M. P. Reidy, R. J. Johnson, G. Darling, D. J. O'Leary, G. Willson, *J. Am. Chem. Soc.* **1989**, *111*, 6452.
- [57] P. J. M. M. Stals, J. C. Everts, R. De Bruijn, I. A. W. W. Pilot, M. M. J. J. Smulders, R. Martín-Rapún, E. A. Pidko, T. F. A. A. De Greef, A. R. A. A. Palmans, E. W. Meijer, *Chem. Eur. J.* **2010**, *16*, 810.
- [58] S. Vela, J. A. Berrocal, C. Atienza, E. W. Meijer, N. Martín, *Chem. Commun.* **2017**, *53*, 4084.
- [59] M. R. Craig, P. Jonkheijm, S. C. J. Meskers, A. P. H. J. Schenning, E. W. Meijer, *Adv. Mater.* **2003**, *15*, 1435.
- [60] A. M. Della Pelle, P. J. Homnick, Y. Bae, P. M. Lahti, S. Thayumanavan, *J. Phys. Chem. C* **2014**, *118*, 1793.
- [61] L. V. Govor, J. Parisi, *Phys. Status Solidi A* **2019**, 1900112.
- [62] M. Gsänger, E. Kirchner, M. Stolte, C. Burschka, V. Stepanenko, J. Pflaum, F. Würthner, *J. Am. Chem. Soc.* **2014**, *136*, 2351.
- [63] A. C. Aragonès, E. Medina, M. Ferrer-Huerta, N. Gimeno, M. Teixidó, J. L. Palma, N. Tao, J. M. Ugalde, E. Giralte, I. Díez-Pérez, V. Mujica, *Small* **2017**, *13*, 1.
- [64] B. P. Bloom, V. Kiran, V. Varade, R. Naaman, D. H. Waldeck, *Nano Lett.* **2016**, *16*, 4583.
- [65] C. Kulkarni, A. K. Mondal, T. K. Das, G. Grinbom, F. Tassinari, M. F. J. Mabesoone, E. W. Meijer, R. Naaman, *Adv. Mater.* **2020**, *32*, 1.
- [66] R. Naaman, D. H. Waldeck, *Annu. Rev. Phys. Chem.* **2015**, *66*, 263.
- [67] W. Mtangi, F. Tassinari, K. Vankayala, A. Vargas Jentsch, B. Adelizzi, A. R. A. A. Palmans, C. Fontanesi, E. W. Meijer, R. Naaman, *J. Am. Chem. Soc.* **2017**, *139*, 2794.
- [68] R. Naaman, D. H. Waldeck, *J. Phys. Chem. Lett.* **2012**, *3*, 2178.
- [69] B. Göhler, V. Hamelbeck, T. Z. Markus, M. Kettner, G. F. Hanne, Z. Vager, R. Naaman, H. Zacharias, *Science* **2011**, *331*, 894.
- [70] T. Benincori, S. Arnaboldi, M. Magni, S. Grecchi, R. Cirilli, C. Fontanesi, P. R. Mussini, *Chem. Sci.* **2019**, *10*, 2750.

-
- [71] M. Kettner, B. Göhler, H. Zacharias, D. Mishra, V. Kiran, R. Naaman, C. Fontanesi, D. H. Waldeck, S. Sek, J. Pawowski, J. Juhaniwicz, *J. Phys. Chem. C* **2015**, *119*, 14542.
- [72] K. M. Alam, S. Pramanik, *Adv. Funct. Mater.* **2015**, *25*, 3210.
- [73] S. P. Mathew, P. C. Mondal, H. Moshe, Y. Mastai, R. Naaman, *Appl. Phys. Lett.* **2014**, *105*, 242408.
- [74] J. M. Abendroth, K. M. Cheung, D. M. Stemer, M. S. El Hadri, C. Zhao, E. E. Fullerton, P. S. Weiss, *J. Am. Chem. Soc.* **2019**, *141*, 3863.
- [75] M. Suda, Y. Thathong, V. Promarak, H. Kojima, M. Nakamura, T. Shiraogawa, M. Ehara, H. M. Yamamoto, *Nat. Commun.* **2019**, *10*, 2455.
- [76] M. Á. Niño, I. A. Kowalik, F. J. Luque, D. Arvanitis, R. Miranda, J. J. De Miguel, *Adv. Mater.* **2014**, *26*, 7474.
- [77] B. Adelizzi, A. T. Rösch, D. J. van Rijen, R. S. Martire, S. Esiner, M. Lutz, A. R. A. Palmans, E. W. Meijer, *Helv. Chim. Acta* **2019**, e201900065.

Chapter 4

Towards novel graphitic carbon nitrides: a supramolecular approach

Abstract:

Graphitic carbon nitride ($g\text{-C}_3\text{N}_4$) based materials are used as catalysts for a variety of applications such as electrochemical water splitting. So far, the preparation of these functional materials has been performed by solid state chemistry. Here, we present a possible novel and facile approach for the preparation of $g\text{-C}_3\text{N}_4$ -like materials by supramolecular chemistry. We synthesize and characterize two novel supramolecular building blocks that contain the nitrogen-rich *s*-heptazine motif and amide functionalized side chains. One derivative contains additional urethane groups to enable the thermally induced cleavage of the catalytically inactive side chains. Whereas both compounds form optically active aggregates in solution, only the thin film formed by the derivative without the urethane groups is optically active. Studying the thermal properties of the materials indicates that the melting temperatures of the thin films formed by both building blocks are higher than the thermal decomposition temperature of the compound that contains the additional urethane groups. Atomic force microscopy indicates that heating and annealing the smooth thin film prepared from the urethane functionalized building block above its thermal decomposition but below its melting temperature does not result in dewetting. Instead, the formation of a surface morphology that contains band-shaped structures is observed. Retaining or even increasing the surface area while increasing the relative content of nitrogen atoms by the cleavage of the side chains is expected to promote the catalytic activity of the supramolecular $g\text{-C}_3\text{N}_4$ material.

4.1 Introduction

An important class of materials that is currently captivating chemists' attention for designing metal-free catalysts for hydrogen evolution^[1–10] and water splitting reactions^[11–16] are graphitic carbon nitrides ($g\text{-C}_3\text{N}_4$). The ideal, defect-free structure of $g\text{-C}_3\text{N}_4$ is depicted in Figure 4.1a and obtained when melon,^[17–19] one of the oldest synthetic polymers (Figure 4.1b, c),^[17,18] is formally condensed until no hydrogen atoms are left.^[10]

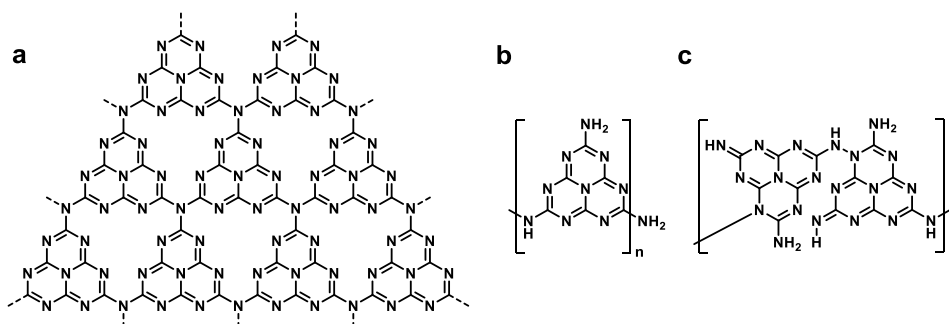


Figure 4.1: (a) Ideal, defect-free chemical structure of the graphitic carbon nitride ($g\text{-C}_3\text{N}_4$) sheet,^[10] (b,c) chemical structures of melon as (b) reported by Liebig^[17,18] and (c) by Komatsu.^[19]

Realizing the cost-efficient production of hydrogen gas by the electrolysis of water is of particular socioeconomic interest since it is an important step towards a sustainable energy production.^[20] Although the electrolysis of water has already been described more than 200 years ago and a variety of catalytic systems has meanwhile been developed, it is still not possible to produce and handle hydrogen gas in technical processes that are economically more favorable than the use of fossil fuels.^[21–28] One disadvantage that limits the usage of today's $g\text{-C}_3\text{N}_4$ materials as catalysts for the production of hydrogen gas is their preparation method that typically involves time and energy intensive solid state chemistry.^[11]

In contrast to solid state chemistry, supramolecular chemistry is well-known for forming reversible non-covalent bonds already at room temperature.^[29–32] The purposeful design of supramolecular polymers^[33–42] has led to the development of functional materials with a variety of applications.^[43–51] One particular example for such an application is the usage of homochiral supramolecular polymers as electrode coatings when performing electrochemical water splitting.^[52,53] The corresponding literature reports suggested that the chiral materials introduced spin-selective chemistry which reduced both the overpotential required to split water and the production of the undesired byproduct hydrogen peroxide.^[52,53] Hitherto, the number of such supramolecular systems that implement spin selective chemistry into the water splitting reaction is still very limited and the reported hydrogen gas production has been too low for practical applications.^[54] Since chiral $g\text{-C}_3\text{N}_4$ -materials prepared by solid state chemistry have already been reported and exhibited enhanced photocatalytic activity,^[55,56] the preparation of chiral, $g\text{-C}_3\text{N}_4$ -like materials by

supramolecular chemistry is an intriguing concept for exploring potential future systems for hydrogen evolution.

Here, we report on the synthesis and characterization of two novel, chiral building blocks, **AHA** and **UAHA**, for the formation of supramolecular g - C_3N_4 -like materials. The molecular structures of both compounds are depicted in Figure 4.2 and contain the nitrogen-rich *s*-heptazine motif. Since C_3 -symmetrical *s*-heptazine derivatives have already been reported to form hexagonal columnar liquid crystals,^[57,58] we anticipated that the combination of the disc-shaped geometry of the molecules and their amide functionalized side chains induces the formation of helical aggregates. We implemented the thermally degradable urethane groups^[59] in the molecular structure of **UAHA** to be able to increase the relative amount of nitrogen atoms in the material by cleaving off the catalytically inactive side chains. We investigated the aggregation of both compounds in solution and in the thin film. Moreover, we studied the thermal properties of both compounds in thin film and in the bulk to investigate whether increasing the nitrogen content by cleaving off the side chains was possible without melting and dewetting the thin film.

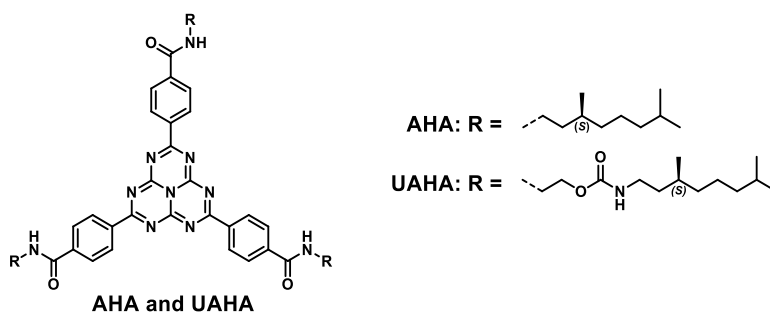
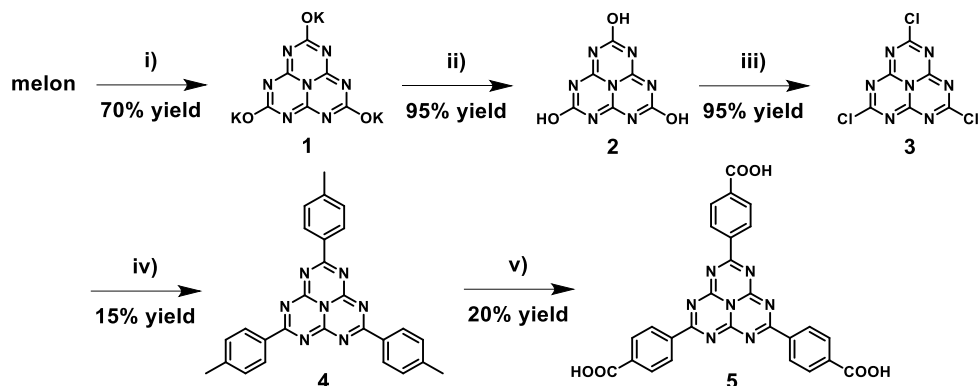


Figure 4.2: Molecular structures of the supramolecular building blocks **AHA** and **UAHA**.

4.2 Synthesis of supramolecular building blocks containing the *s*-heptazine motif

4.2.1 Synthesis of *s*-heptazine tribenzoic acid **5**

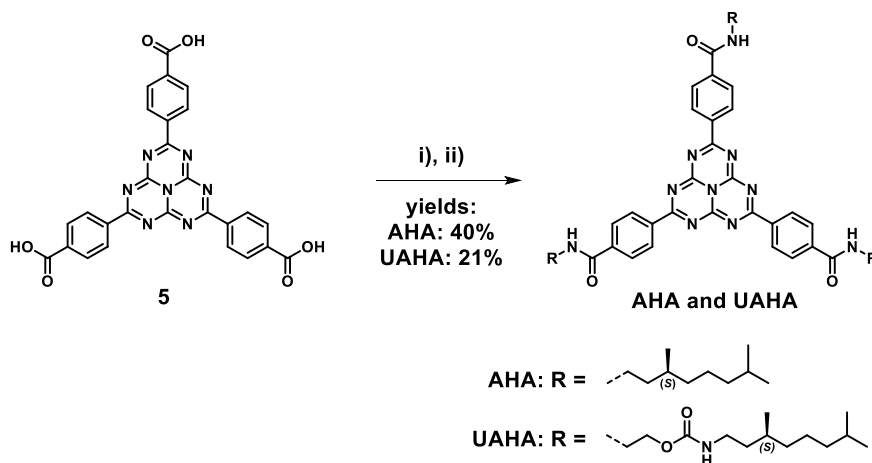
The synthesis of *s*-heptazine tribenzoic acid **5** was performed in collaboration with Nils Jansen and Joep Sanders during their master graduation projects in the group. The synthetic strategy starting from technical grade melon (generously supplied by Durferrit GmbH) is depicted schematically in Scheme 4.1 and was inspired by literature reports.^[60,61] Initially, melon was hydrolyzed by boiling in aqueous potassium hydroxide solution. The obtained potassium cyamelurate **1** was dissolved in water and protonated by the addition of hydrochloric acid. Cyameluric acid **2** was chlorinated by a reaction with PCl_5 to prepare cyameluric chloride **3**. Friedel-Crafts arylation of **3** in toluene using aluminum chloride yielded the toluene functionalized *s*-heptazine **4**. Subsequently, the three methyl groups of **4** were oxidized using chromic acid. Pure tribenzoic acid functionalized *s*-heptazine **5** was obtained after recrystallization from *N,N*-dimethylformamide (DMF).



Scheme 4.1: Synthesis of s-heptazine tribenzoic acid. Reagents and conditions: i) KOH, H₂O, 100 °C, 4h; ii) HCl, H₂O, R.T., 30 min.; iii) PCl₅, POCl₃, 106 °C, 2 h.; iv) toluene, AlCl₃, 60 °C - R.T., 14 h; v) CrO₃, acetic acid, sulfuric acid, acetic anhydride, 0 °C - R.T.

4.2.2 Synthesis of amide functionalized s-heptazines

To enable the synthesis of chiral supramolecular building blocks with high enantiopurity, we selected commercially available (*S*)-(-)- β -citronellol (obtained from Takasago International Corporation) as an affordable commercially accessible starting material with high enantiomeric excess (98.4% ee).^[62] The conversion of (*S*)-(-)- β -citronellol to (*S*)-3,7-dimethyloctan-1-amine and 2-(12-azaneyl)ethyl (*S*)-(3,7-dimethyloctyl)carbamate was performed according to literature procedures^[63,64] by Marcin L. Ślęczkowski and Hao Su, respectively. The synthesis of the amide functionalized *s*-heptazine **AHA** and both amide and urethane functionalized *s*-heptazine **UAHA** was performed in two steps (Scheme 4.2). At first, **5** was converted to the corresponding triacid chloride using the reagent oxalyl chloride and catalytic amounts DMF. The full conversion to the triacid chloride was confirmed by Fourier-transform infrared (FT-IR) spectroscopy before the excess of oxalyl chloride was evaporated. The generated triacid chloride was reacted with a primary amine (**AHA**: (*S*)-3,7-dimethyloctan-1-amine, **UAHA**: 2-(12-azaneyl)ethyl (*S*)-(3,7-dimethyloctyl)carbamate) to yield the supramolecular building blocks **AHA** or **UAHA**, respectively. After purification by column chromatography, precipitation and finally recrystallization, the pure products were obtained in medium to low yields (**AHA**: 40% and **UAHA**: 21%). The chemical structures were confirmed by ¹H and ¹³C nuclear magnetic resonance (NMR), FT-IR spectroscopy and matrix-assisted laser ionization time of flight mass spectrometry (MALDI-TOF-MS).



*Scheme 4.2: Synthetic strategy for the preparation of **AHA** and **UAHA**. i) oxalyl chloride (in excess), DMF, 50 °C, 2h; ii) primary amine (**AHA**: (S)-3,7-dimethyloctan-1-amine, **UAHA**: 2-(12-azaneyl)ethyl (S)-(3,7-dimethyloctyl) carbamate), triethylamine, dry tetrahydrofuran (THF), 0 °C - 66°C, 1 h.*

4.3 Characterization in the solid state

Having confirmed the chemical structures of the supramolecular building blocks by standard characterization techniques, we continued our study with the investigation of the bulk properties. We wanted to assess the presence of hydrogen-bonds in the bulk materials as well as determine the melting temperature of **AHA** and thermal decomposition temperature of **UAHA** that contains the additional urethane groups.

4.3.1 Fourier-transform infrared spectroscopy

We started our study by performing FT-IR spectroscopy to probe for the formation of hydrogen bonds in the solid state. As noticed in Figure 4.3, the spectra recorded for both compounds showed absorption bands around 3300 cm^{-1} which stemmed from the N-H-stretching vibration of protons that are involved in hydrogen bonds.^[46] The C=O-stretching vibrations were found at 1643 cm^{-1} for **AHA** and at 1698 cm^{-1} as well as 1644 cm^{-1} for **UAHA**. These results indicate that both compounds form strong hydrogen bonds, most probably of the amides, and **UAHA** exhibits the formation of additional weak hydrogen bonds, most probably of the urethane.^[46,65] We note that both compounds exhibit an absorption band at 828 cm^{-1} (**AHA**) or at 829 cm^{-1} (**UAHA**) that is indicative for the vibration of the contained C_6N_7 -core.^[66,67]

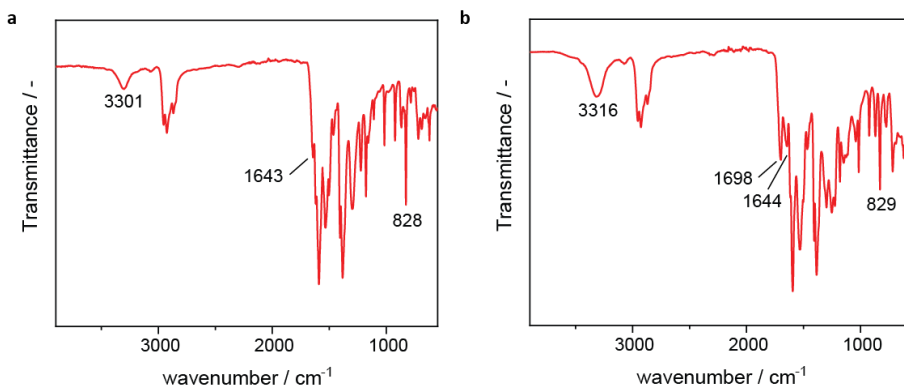


Figure 4.3: FT-IR spectra recorded for (a) **AHA** and (b) **UAHA** in bulk.

4.3.2 Thermal properties of amide functionalized *s*-heptazines **AHA** and **UAHA**

The thermal phase transitions of **AHA** were investigated by dynamic scanning calorimetry (DSC) and polarized optical microscopy (POM). For the DSC measurements, the sample was heated to the isotropic melt, equilibrated, and cooled at a constant rate of $10\text{ }^{\circ}\text{C min}^{-1}$ to standardize the thermal history. The DSC trace that was obtained in the second heating and cooling cycle (scanning rate of $10\text{ }^{\circ}\text{C min}^{-1}$) is depicted in Figure 4.4a. For the POM study, a small amount of substance was placed in between two microscope glass slides and heated until it was isotropically molten. Microscopy images were taken while the sample was cooled to $50\text{ }^{\circ}\text{C}$ and subsequently reheated. As depicted as inset in Figure 4.4a, **AHA** showed the formation of birefringent textures upon solidification (crystallization temperature $T_c = 271\text{ }^{\circ}\text{C}$) which did not change their shape during the cooling and heating cycle. Heating **AHA** to $287\text{ }^{\circ}\text{C}$ resulted in melting and the loss of the birefringent textures in the POM image.

Due to the expected decomposition of **UAHA** by the cleavage of the urethane groups when heating to temperatures above $200\text{ }^{\circ}\text{C}$ ^[59] and observing decomposition in the melt of **UAHA** in the POM study, we did not investigate the thermal properties by DSC but assessed the thermal stability by thermogravimetric analysis (TGA). Figure 4.4b shows the relative decrease of mass of **UAHA** upon heating at a constant rate of $5\text{ }^{\circ}\text{C min}^{-1}$. After the onset of the thermal decomposition around $240\text{ }^{\circ}\text{C}$, a rapid loss of weight is noticed. The temperature at which 45% of the mass is lost, which corresponds roughly with cleaving and removing the expected part of the side chains, was reached at $385\text{ }^{\circ}\text{C}$.

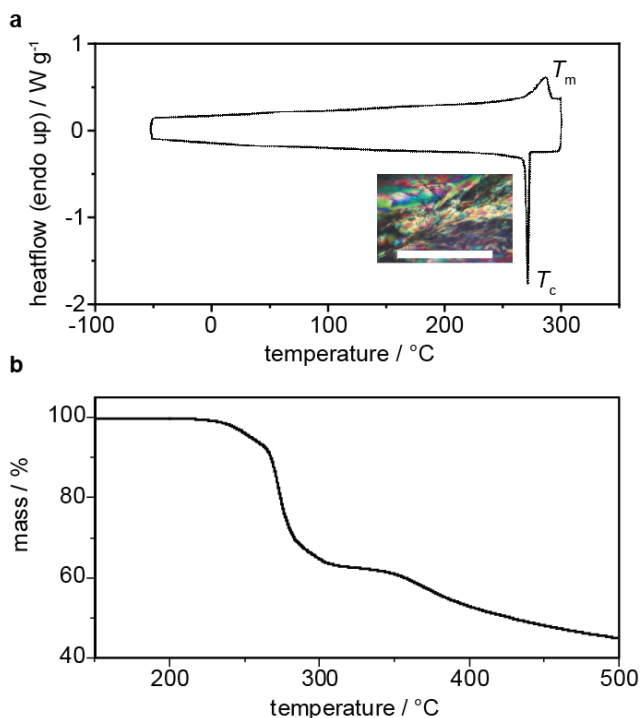


Figure 4.4: (a) DSC trace (second cycle, heating rate $10\text{ }^{\circ}\text{C min}^{-1}$) recorded for **AHA**. Inset: birefringent structures observed by POM. White bar: $50\text{ }\mu\text{m}$. (b) Thermogravimetric analysis of **UAHA** (heating rate $5\text{ }^{\circ}\text{C min}^{-1}$).

Since the evaluation of the bulk properties showed that both compounds formed hydrogen-bonded, crystalline bulk materials, we were motivated to study the aggregation behavior of both compounds in solution and in thin films.

4.4 Assessing the formation of CD active aggregates by AHA and UAHA in solution and in thin film

We started our optical study by performing ultraviolet–visible (UV/Vis), circular dichroism (CD) and linear dichroism (LD) spectroscopy on solutions of **AHA** and **UAHA**. The spectroscopic solutions were prepared by adding concentrated stock solutions of the compounds in chloroform to either good or poor solvents. We note that in case of **UAHA**, 1 vol% trifluoroacetic acid (TFA) was required as co-solvent to chloroform in the stock solution to achieve full dissolution. Before the optical measurements, all samples were heated slightly below the boiling point of the solvent, sonicated, and cooled slowly to room temperature. The solid lines in Figure 4.5a and b show the absorption spectra of **AHA** and **UAHA** in chloroform and in heptane (containing 2 vol% chloroform) solutions. In chloroform solution, the molar extinction coefficient ϵ was $1.1 \cdot 10^5\text{ L mol}^{-1}\text{ cm}^{-1}$ for **AHA** ($\lambda_{\text{max}} = 336\text{ nm}$) and $1.2 \cdot 10^5\text{ L mol}^{-1}\text{ cm}^{-1}$ for **UAHA** ($\lambda_{\text{max}} = 334\text{ nm}$). Replacing the good solvent chloroform

by the poor solvent heptane induced spectral broadening and blue-shifting λ_{\max} for **AHA** ($\lambda_{\max} = 315$ nm). For **UAHA**, the blue-shift was very small ($\lambda_{\max} = 331$ nm) and the spectrum showed a more pronounced spectral broadening. CD spectroscopy indicated that the chloroform solutions of **AHA** and **UAHA** were CD silent. In contrast, optical activity was measured for the heptane solutions (dashed lines in Figure 4.5a and b). For **AHA**, two bands of negative CD effect (minima at $\lambda = 268$ nm and 316 nm) and two bands of positive CD effect (maxima at $\lambda = 291$ and 344 nm) were found. For **UAHA**, the Cotton effects were much smaller and only one band of negative CD effect (minimum at $\lambda = 364$ nm) was noticed. LD spectroscopy indicated the absence of LD for all samples (Figure 4.5c).

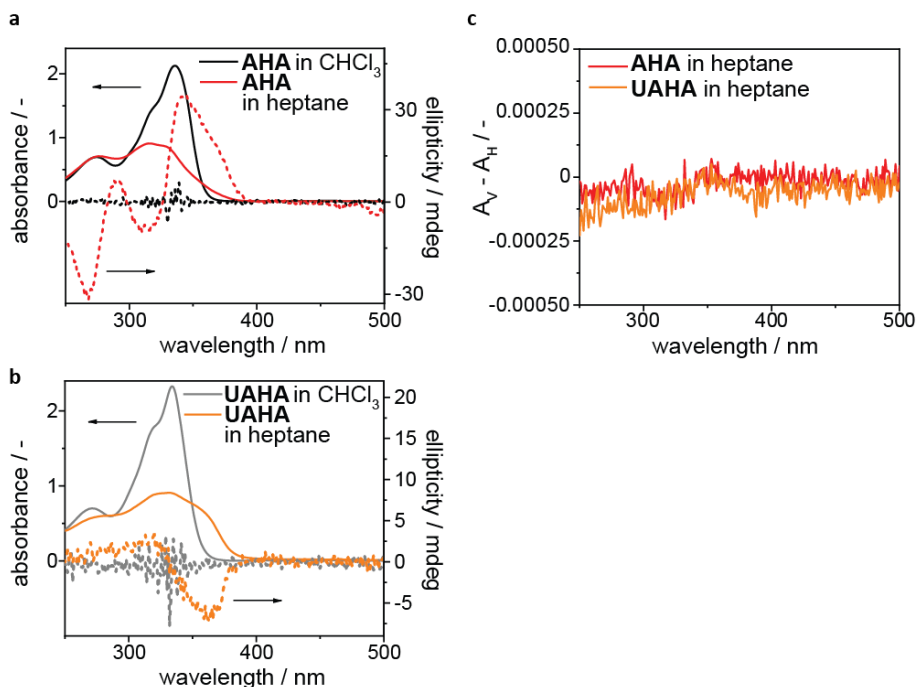


Figure 4.5: Photophysical properties of **AHA** and **UAHA** in chloroform and heptane (containing 2 vol% chloroform) solutions. Solid lines in (a): absorption spectra, dashed lines in (a): CD spectra. (b) LD spectra. Concentrations: 20 μM . Optical path lengths: 10 mm. LD is expressed as the difference in absorbance for vertically and horizontally polarized light $A_V - A_H$. We note that the addition of 9.6 μmol triethylamine to the solutions of **UAHA** to neutralize the contained TFA did not affect the recorded CD spectrum.

The blue-shift of λ_{\max} in the absorption spectrum of **AHA** recorded in heptane solution suggested the formation of H-type aggregates similar to π -stacked and hydrogen-bonded supramolecular systems reported in the literature.^[38,68–70] The formation of nanofibers which is indicative of such a one-dimensional π -stacked architecture was also assessed by atomic force microscopy (vide infra). The differences of the absorption spectra recorded for

the heptane solutions of **AHA** and **UAHA** suggested that both types of molecules were arranged differently in their respective aggregate structures which was corroborated by the differences in the CD spectra. Nevertheless, measuring ellipticity in the absence of LD for the heptane solutions of both compounds suggested the efficient transfer of point chirality from the stereogenic centers in the side chains to the supramolecular aggregates.

Having investigated the optical properties of **AHA** and **UAHA** in solution, we continued our study with the investigation of the optical properties of the thin films formed by both compounds. The investigated thin films were prepared by spin coating 4 mM solutions of each compound in chloroform (in case of **UAHA**, again 1 vol% TFA was required as co-solvent to achieve full dissolution) onto quartz glass slides. The UV/Vis spectrum that was recorded for the thin film of **AHA** is presented as black line in Figure 4.6a and the corresponding λ_{\max} is noticed at 330 nm. The CD spectrum of the thin film of **AHA** is noticed as black line in Figure 4.6b and contains bands of negative and positive CD effect. LD spectroscopy indicated the absence of LD (Figure 4.6c). The UV/Vis spectrum recorded for the thin film of **UAHA** is noticed as grey line in Figure 4.6a and exhibits its λ_{\max} at 336 nm. CD spectroscopy indicated that the thin film formed by this compound was optically inactive (grey line in Figure 4.6b). Comparing the absorption spectra of the thin films with the absorption spectra recorded in the chloroform solutions suggested the absence of blue-shifts of λ_{\max} which was in contrast to the results from the heptane solutions and suggested different aggregation pathways in both media. The structural differences of the aggregates formed by each compound in the two media were corroborated by the differences in the corresponding CD spectra. Whereas the shape of the CD spectrum of **AHA** was strongly changed, the thin film of **UAHA** was completely optically inactive. We note that the aggravation of **UAHA**'s aggregation into optically active structures can potentially stem from TFA protonating **UAHA** during spin coating. The presence of TFA in the spin-coated thin film can be investigated by techniques such as total reflection X-ray fluorescence spectrometry.

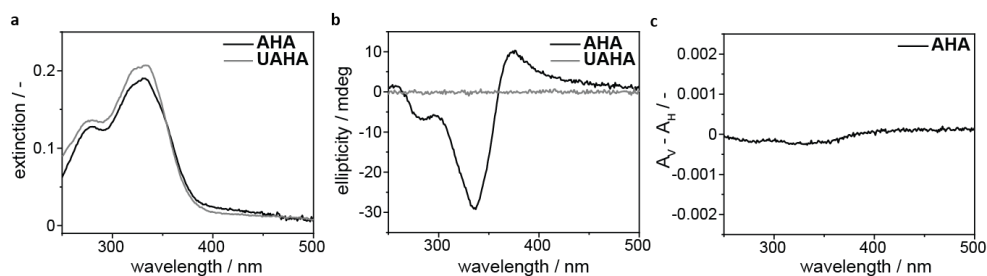


Figure 4.6: (a) UV/Vis spectra, (b) CD spectra and (c) LD spectra recorded for thin films prepared from **AHA** and **UAHA**. Owing to the presence of a scattering contribution, the y-axis in (a) is labelled extinction. LD is expressed as the difference in absorbance for vertically and horizontally polarized light $A_V - A_H$.

Since **AHA** and **UAHA** formed smooth thin films and DSC indicated that the melting temperature of **AHA** was higher than the thermal decomposition temperature of **UAHA** as

determined by TGA, we investigated the thin films in variable temperature experiments to determine whether the urethane groups of **UAHA** could be decomposed below the melting temperature to avoid dewetting of the thin film and retaining a high surface area while increasing the nitrogen content of the material.

4.5 Investigating the thermal stability of the morphologies of thin films and the impact of heating on optical properties

Optical microscopy indicated a smooth surface morphology for the thin films formed by both **AHA** and **UAHA**, as exemplarily shown for the thin film of **UAHA** in Figure 4.7a. The surfaces of the thin films remained smooth until their melting temperature was reached. Melting induced dewetting and the formation of blob-like structures which did not change their shape upon cooling, as exemplarily shown for the thin film of **UAHA** in Figure 4.7b. According to the Linkam heating element that was used to perform temperature-dependent experiments, the melting temperature of the thin film formed by **AHA** was 275 °C. For the thin film formed by **UAHA**, the melting temperature was 270 °C (scanning rate 20 °C min⁻¹). We note that the melting temperature of the thin film of **AHA** was lower than the melting temperature determined by DSC for the bulk material. We ascribed the discrepancy to the thicknesses of the thin films which were below 100 nm.

Since the melting temperature of the thin film formed by **UAHA** was higher than **UAHA**'s thermal decomposition temperature, we wanted to explore the structural consequences of cleaving off the side chains when performing a heating and annealing experiment just below the melting temperature of the thin film. We heated and annealed the thin film for 20 minutes at 265 °C. After cooling, the thin film was investigated by optical microscopy. The microscopy image depicted in Figure 4.7c indicated the formation of crack-like structures. Since these structural features were too small to be resolved clearly by optical microscopy, we performed atomic force microscopy (AFM). To better compare the surface morphology before and after heating and annealing, we also imaged the untreated thin film by AFM. The height profile depicted in Figure 4.7d indicated maximum height differences of 20 nm within the imaged area of 400 μm² which corroborated the smooth surface morphology noticed in the optical microscopy images. Upon close-examination, a blob-like substructure of the smooth surface was noticed (Figure 4.7e, height difference between white and black elements: 6 nm). AFM-imaging performed after heating and annealing suggested that the crack-like structures noticed in optical microscopy image stemmed from the formation of a surface morphology that contained band-shaped textures (Figure 4.7f). The AFM images suggested that this new morphology had an increased surface roughness (maximum height difference between white and black elements: 60 nm; this height difference is also responsible for the measurement artifacts in the AFM image). Imaging the sample with increased magnification suggested that the band-shaped structures consisted of smaller, fiber-like elements as noticed in Figure 4.7g. The changes in the surface morphology which were induced by heating and annealing the thin film suggested that cleaving off the side chains resulted in a local rearrangement of the supramolecular structure. Interestingly,

increasing the relative amount of nitrogen atoms in the thin film was not accompanied by dewetting but seemed to even increase the surface area.

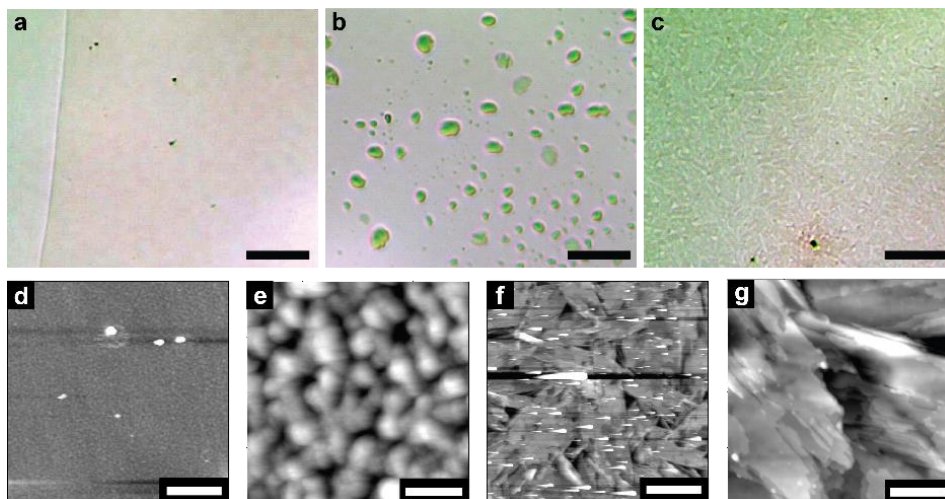


Figure 4.7: (a-c) Optical microscopy of thin films prepared by spin coating 4 mM chloroform solutions of **UAHA** containing 1 vol% TFA as cosolvent. Images of the thin films were taken (a) directly after preparation, (b) after melting and cooling, (c) after heating and annealing for 20 minutes at 265 °C. Black bars: 20 μm . We note that birefringent textures were absent in all images when crossing the polarizers. (d-g) AFM height traces of the thin films after preparation (d,e) and after heating and annealing for 20 minutes at 265 °C(f,g); White bars: 5 μm in (d,f) and 500 nm in (e,g).

We note that **AHA** formed fibrous structures, too. The AFM image of a sample prepared by drop-casting a 2 mM chloroform solution of **AHA** onto mica is depicted in Figure 4.8 (image recorded by Elisabeth Weyandt). The height difference of 8 nm between the fibrous structures that are highlighted in white and the grey mica surface indicates the formation of bundles of nanofibers.

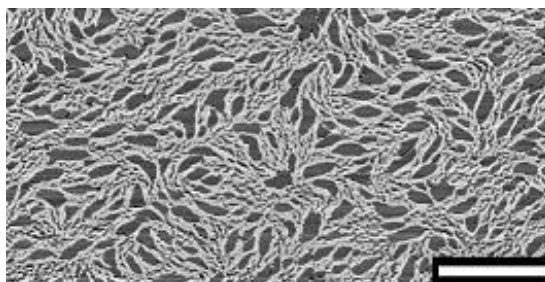


Figure 4.8: AFM height image of bundles of nanofibers formed by **AHA**. The sample was prepared by drop casting a chloroform solution (concentration = 2 mM) onto mica. White bar: 1 μm .

To investigate the consequences of the observed structural rearrangements during the variable temperature experiments on the optical properties of the thin films, we performed optical spectroscopy. As noticed in Figure 4.9a, performing heating and cooling experiments below the melting temperature of the thin film of **AHA** induced a red-shift of λ_{\max} from 330 nm to 349 nm in the UV/Vis spectrum. Melting and cooling induced additional spectral broadening. CD spectroscopy indicated that heating and cooling experiments affected the ellipticity spectrum of the thin film, too (Figure 4.9b). When the thin film was heated to 230 °C, an ellipticity signal of 23 mdeg was measured at 351 nm. We note that this CD signal corresponded with a circular differential absorbance $\Delta A = A_L - A_R$ of $6 \cdot 10^{-4}$ which was smaller than the linear differential absorbance $\Delta A = A_L - A_R$ of $4 \cdot 10^{-3}$ noticed in the corresponding LD spectrum (Figure 4.9c). Both ellipticity and LD effect were lost when the thin film was melted and cooled. In contrast to **AHA**, λ_{\max} of the UV/Vis spectrum of the thin film of **UAHA** was barely affected by the thermal treatment (336 nm in Figure 4.6a and 338 nm in Figure 4.9d). Interestingly, a small ellipticity signal was measured for the thin film after heating and annealing for 20 minutes at 265 °C (Figure 4.9e). The corresponding maximum circular differential absorbance ($\lambda = 326$ nm) of $5 \cdot 10^{-5}$ was smaller than the linear differential absorbance of $1.6 \cdot 10^{-3}$ noticed in the corresponding LD spectrum (Figure 4.9f).

The red-shift of λ_{\max} that was noticed in the UV/Vis spectrum of the thin film of **AHA** after heating and cooling suggested a local structural rearrangement that was corroborated by the changes in the CD spectrum and the generation of LD. LD can, in combination with linear birefringence in either the optical setup or the sample itself, lead to an artificial contribution to the circular dichroism. Although linear birefringence is of limited magnitude (typically below 0.1), the comparable magnitudes of linear and circular differential absorption in the heated and cooled thin film of **AHA** suggested a distinct LD contamination in the CD spectrum. Analogously to this argumentation, the measured ellipticity of the thin film of **UAHA** after heating and annealing for 20 minutes at 265 °C was ascribed to the sample's LD effect.

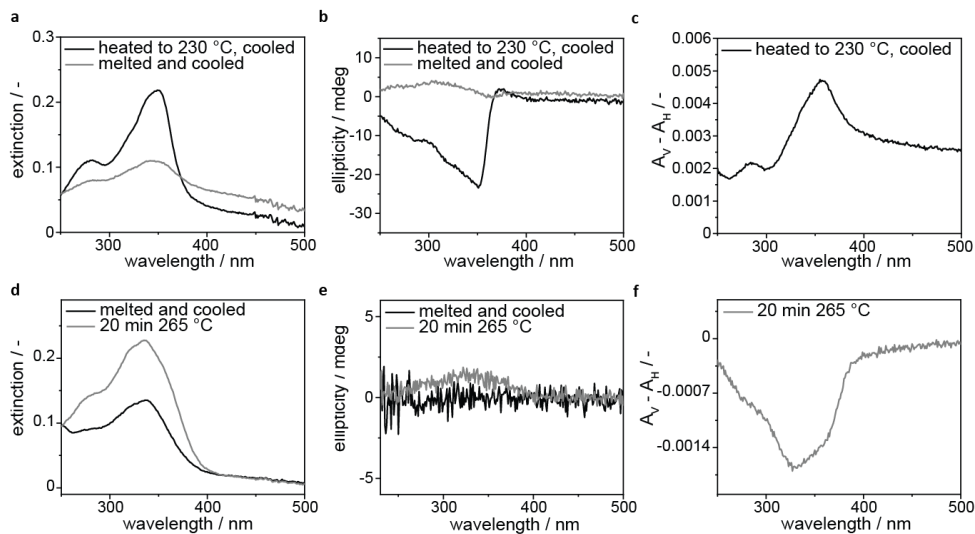


Figure 4.9: (a) UV/Vis spectra, (b) CD spectra and (c) LD spectra recorded at room temperature for the thin films of **AHA** after conducting the indicated heating and annealing experiments. (d) UV/Vis spectra, (e) CD spectra and (f) LD spectra recorded at room temperature for the thin films of **UAHA** after conducting the indicated heating and annealing experiments. LD is expressed as the difference in absorbance for vertically and horizontally polarized light $A_V - A_H$.

4.6 Conclusions and outlook

We presented here the synthesis and characterization of two novel chiral supramolecular building blocks **AHA** and **UAHA** that contain the *s*-heptazine motif as the core and amide functionalized side chains for the preparation of novel supramolecular *g*- C_3N_4 -like materials. The investigation of the optical properties indicated that both compounds formed optically active aggregates in poor solvents. Interestingly, the optical activity of these aggregates was more pronounced for **AHA** than for **UAHA** that contained additional, thermally degradable urethane groups. Both compounds could be used to prepare smooth thin films by spin coating. The spectroscopic investigation indicated that only **AHA** formed optically active aggregates in thin film. Since the melting temperature of the thin film of **UAHA** was higher than its thermal decomposition temperature, the catalytically inactive side chains could be cleaved off by thermal curing. Heating and annealing did not result in dewetting but in the formation of band-shaped surface textures. Since initial results from using thin films of **AHA** as electrode coating in an electrochemical cell used for water splitting indicated catalytic activity, we conclude that structurally approaching *g*- C_3N_4 in supramolecular systems introduces functionality. Increasing the relative amount of nitrogen atoms via the cleavage of the side chains is suggested to increase the catalytic activity. Since the thin film formed by **UAHA** was however not optically active, the presented system needs further optimization to allow for the preparation of

chiral supramolecular g -C₃N₄-like materials in which catalytically inactive side chains can be removed by a curing step.

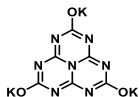
4.7 Experimental Section

4.7.1 Materials and Methods

Melon was generously supplied by Durferrit GmbH. All other chemicals were purchased from commercial sources and used without further purification. The solvents were purchased and treated as stated in Chapter 2. Silica column purification and chemical characterization (¹H and ¹³C NMR, FT-IR and MALDI-TOF) was performed on the machines stated in Chapter 2. DSC was performed on a Q2000 from TA Instruments. TGA was performed on a Q500 from TA Instruments. The stock solutions which are used for the optical measurements and spin-coating were prepared by weighing the required amount of compound and transferring it into a screw-capped vial. The desired concentrations of the used solutions were adjusted by the addition of the chosen solvent by using Gilson MICROMAN Positive-Displacement Pipets. The samples were heated and sonicated until the solids were dissolved completely and homogeneous solutions were obtained. The optical path length was 10 mm. For spin-coating, quadratic quartz glass slides (2 cm side length) were cleaned by sonication in acetone, demineralized water and isopropanol for 5 min each. For the preparation of the thin films, 70 μL of the stock solution were deposited on top of the microscope glass slide and subsequently spun (Headway Research Inc.; concentrations: 4 mM; spinning speed: 2000 rpm; spinning time: 45 sec). UV/Vis, CD and LD spectroscopy were performed on the spectrometers stated in Chapter 3. Optical microscopy using crossed polarizers was performed on an optical microscope from Jenaval. Images were recorded using an Infinity1 camera purchased from Lumenera. Atomic force microscopy was performed as stated in Chapter 3.

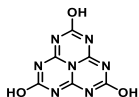
4.7.2 Synthetic procedures

Synthesis of potassium cyamelurate (1)

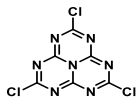


Melon pellets were pulverized with a pestle a mortar. The yellow powder (10 g, 45 mmol, 1 eq.) was added to a round bottom flask filled with aqueous 3 M KOH solution (90 mL, 275 mmol, 6 eq). Subsequently, the reaction mixture was heated to 100 °C. Heating and stirring was continued at for 3 h before the reaction mixture was filtrated using a warmed Büchner funnel. Upon cooling down, white crystals were formed in the filtrate. The white crystals were filtered off and washed with ethanol thrice. After drying, potassium cyamelurate was obtained as a white powder in 70% yield (10.5 g, 31.2 mmol). FT-IR (cm⁻¹): 3064 (b) 1644 (m), 1515 (m), 1471 (s), 1404 (s), 1151(m), 813 (s).

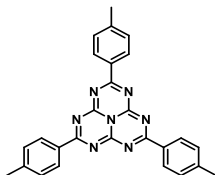
Synthesis of cyameluric Acid (2)



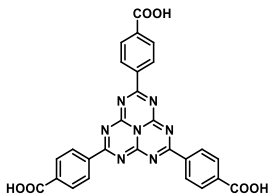
Potassium cyamelurate (10.8 g, 32.2 mmol, 1 eq.) was dissolved in 50 mL water. Subsequently, 1M HCl (130 mL, 130 mmol, 4 eq.) was added dropwise which induced the formation of a white precipitate. Stirring was continued for 10 minutes before the precipitate was filtered off and washed three times with water. Cyameluric acid was obtained as a white powder in 95% yield (6.8 g, 30.9 mmol). MALDI-TOF-MS found: 221.14 m/z (calculated: 221.03). FT-IR (cm⁻¹): 2985 (b), 1610 (s), 1474 (s), 1399 (s), 1310 (s), 1168 (m), 952(m), 826(m), 786 (s), 628 (m), 537 (m).

Synthesis of cyameluric chloride (3)

The reaction was carried out in dried glassware under argon atmosphere. A round Schleck bottom flask was charged with cyameluric acid (2 g, 9.04 mmol, 1 eq.) and 50 mL POCl₃. PCl₅ (8.5 g, 40.7 mmol, 4.5 eq.) was added portion wise to the mixture before heating to 106 °C. The HCl gas which was formed during the reaction was neutralized by passing it through an aqueous NaOH 1M solution. After 2 h of heating and stirring, the reaction mixture was more turbid than in the beginning and the color had changed from white to yellow. POCl₃ was removed via distillation before the temperature was raised to 140°C. Exposing the mixture to an argon flow resulted in the complete removal of excessive and unreacted PCl₅ sublimation. Cyameluric chloride was obtained as a yellow powder in 95% yield (2.4 g, 8.60 mmol). ¹³C NMR (101 MHz, THF-*d*₆): δ [ppm] = 175.4, 158.6. FT-IR (cm⁻¹): 1601 (s), 1498 (s), 1302 (s), 1200 (s), 1088 (s), 970 (s), 824 (s), 648 (s), 579(w).

Synthesis of 2,5,8-tri-*p*-tolyl-1,3,3a1,4,6,7,9-heptaazaphenalene (4)

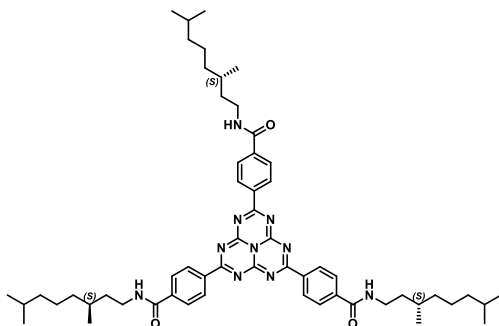
A round bottom flask was charged with toluene (40 mL, 376 mmol, 40 eq.) and anhydrous AlCl₃ (2.5 g, 18.82 mmol, 2 eq.). The suspension was stirred and heated to 60°C. Cyameluric chloride (2.6 g, 9.41 mmol, 1 eq.) was added portion wise which induced the formation of a dark red color. The reaction was cooled down to R.T. and stirring was continued for 14 h. Upon the addition of 100 mL water a color change to yellow and the formation of a precipitate was observed. The precipitate was collected by filtration. 2,5,8-tri-*p*-tolyl-1,3,3a1,4,6,7,9-heptaazaphenalene was purified by recrystallization from DMF. The pure product was obtained as yellow crystals in 15% yield (626 mg, 1.41 mmol). ¹H NMR (400 MHz, C₆D₆-*d*₆): δ [ppm] = 8.80 (d, 6H), 7.04 (d 6H), 2.02 (s, 9H). ¹³C NMR (101 MHz, C₆D₆-*d*₆): δ [ppm] = 180.62, 168.01, 145.18, 133.11, 130.66, 129.84, 21.57. MALDI-TOF-MS found: 444.20m/z (calculated: 444.20). FT-IR (cm⁻¹): 3033 (b), 1621 (m), 1587 (s), 1509 (m), 1492 (m), 1405 (m), 1384 (s), 1296 (w), 1223 (m), 1174 (s), 1037 (w) 1019 (m), 929 (m), 851 (w), 815 (s), 796 (m), 738 (s), 684 (m), 609 (m), 516 (m), 477 (s).

Synthesis of 4,4',4''-(1,3,3a1,4,6,7,9-heptaazaphenalene-2,5,8-triyl)tribenzoic acid (5)

2,5,8-Tri-*p*-tolyl-1,3,3a1,4,6,7,9-heptaazaphenalene (1.21 grams, 2.73 mmol, 1 eq.) was added to a round bottom flask containing a mixture of acetic acid (36.2 g, 602.81 mmol, 220 eq.) and sulfuric acid (4.02 g, 41.02 mmol, 15 eq.) that was cooled to 0°C. The mixture was stirred for 10 minutes before CrO₃ (4.92 g, 49.23 mmol, 18 eq) was added portion wise which induced a color change to green. Subsequently, acetic anhydride (2.2 g, 21.88 mmol, 8 eq.) was added and stirring at room temperature was continued for 16 h. The reaction mixture was poured into 300 mL water which induced the formation of a yellow solid. The solid was collected by filtration and redissolved in 100 mL of aqueous NaOH solution (conc. = 6 M). The resulting mixture was acidified by the addition of 50 mL aqueous HCl solution (conc. = 12 M) which resulted in the formation of a yellow precipitate which was collected via filtration. Purification was performed by recrystallization from hot DMF and washing with 100 mL aqueous HCl solution (conc. = 1 M). Pure 4,4',4''-(1,3,3a1,4,6,7,9-heptaazaphenalene-2,5,8-triyl)tribenzoic acid was obtained as

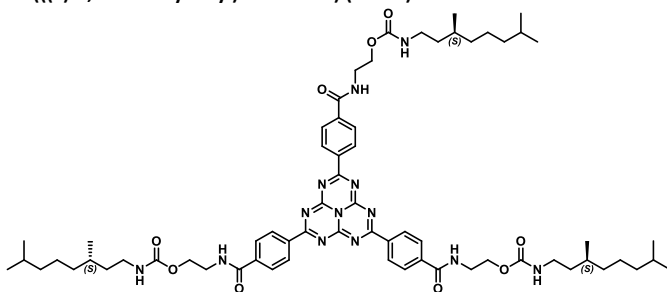
a yellow powder in 20% yield (302 mg, 0.55 mmol). ^1H NMR (400 MHz, DMF- d_7): δ [ppm] = 13.79 (s, 3H), 8.62 (d, 6H), 8.27 (d, 6H). ^{13}C NMR (101 MHz, DMF- d_7): δ [ppm] = 174.6, 167.0, 160.5, 138.4, 136.2, 130.15, 129.9. MALDI-TOF-MS found: 533.19 m/z (calculated: 533.11). FT-IR (cm^{-1}): 3056 (b), 1715(m), 1589(s), 1498 (s), 1408 (w), 1373(m), 1303(w), 1220 (m), 1105 (m), 1014 (s), 924 (s), 875 (m), 830(s), 789 (s), 718 (s).

4,4',4''-(1,3,3a1,4,6,7,9-Heptaazaphenalene-2,5,8-triyl)tris(*N*-((*S*)-3,7-dimethyloctyl)benzamide) (AHA)



The reaction was carried out under inert conditions in dried glassware under argon. 4,4',4''-(1,3,3a1,4,6,7,9-Heptaazaphenalene-2,5,8-triyl)tribenzoic acid (100 mg, 0.19 mmol, 1 eq.) was added to 10 mL oxalyl chloride. One drop of DMF was added as catalyst. The mixture was stirred for 2 h at 50 °C. Oxalyl chloride was removed by evaporation. The generated acid chloride was redispersed in 10 mL dry THF and added to a 10 mL THF solution of (*S*)-3,7-dimethyloctan-1-amine (103.8 mg, 0.66 mmol, 3.5 eq.) and triethylamine (0.66 mmol, 3.5 eq.). The mixture was stirred at 66 °C for one hour. The reaction mixture was cooled down and concentrated. Purification was performed by silica column chromatography with methanol (0-5%) in chloroform as eluent and subsequent precipitation in methanol. The pure product was obtained a yellow orange powder in 41% yield (74 mg, 0.08 mmol). ^1H NMR (400 MHz, Chloroform- d_3): δ [ppm] = 7.68 (d, J = 7.6 Hz, 6H), 7.54 (s, 3H), 7.04 (s, 6H), 3.36 (d, J = 10.6 Hz, 6H), 1.77 – 1.63 (m, 3H), 1.61 – 1.42 (m, 9H), 1.42 – 1.09 (m, 18H), 0.97 (d, J = 6.3 Hz, 9H), 0.89 (d, J = 6.6 Hz, 18H). ^{13}C NMR (101 MHz, Chloroform- d_3): δ [ppm] = 174.71, 168.12, 158.10, 140.42, 134.87, 130.11, 127.02, 39.44, 38.73, 37.46, 36.70, 31.24, 28.14, 24.92, 22.90, 22.79, 19.73. MALDI-TOF-MS found: 950.73 m/z (calculated: 950.63). FT-IR (cm^{-1}): 3301 (w), 2953 (m), 2926 (m), 2870 (m), 1698 (m), 1644 (m), 1595 (s), 1529 (s), 1466 (m), 1407 (s), 1385 (s), 1298 (m), 1252 (m), 1224 (m), 1180 (m), 1148 (w), 1042 (w), 1015 (m) 924 (m), 870 (w), 829 (m), 774 (w), 717 (m), 621 (m).

((4,4',4''-(1,3,3a1,4,6,7,9-Heptaazaphenalene-2,5,8-triyl)tris(benzoyl)tris(azanediyl)tris(ethane-2,1-diyl)tris(((*S*)-3,7-dimethyloctyl)carbamate) (UAHA)



The reaction was carried out under inert conditions in dried glassware under argon. 4,4',4''-(1,3,3a1,4,6,7,9-Heptaazaphenalene-2,5,8-triyl)tribenzoic acid (100 mg, 0.19 mmol, 1 eq.) was added to 10 mL oxalyl chloride. One drop of DMF was added as catalyst. The mixture was stirred for 2 h at 50 °C. Oxalyl chloride was removed by evaporation. The generated acid chloride was redispersed in 10 mL dry THF and added to a 10 mL THF solution of 2-(12-azaneyl)ethyl (*S*)-(3,7-dimethyloctyl)carbamate (365 mg, 1.5 mmol, 8 eq.). The mixture was stirred at 66 °C for one hour. The reaction mixture was cooled down and concentrated. Purification was performed by silica

column chromatography with methanol (0-3%) in chloroform as eluent and subsequent precipitation in methanol. The pure product was obtained a yellow orange powder in 21% yield (48 mg, 0.04 mmol).

^1H NMR (400 MHz, Chloroform- d_3 , 3 vol% TFA- d_1): δ [ppm] = 8.49 (d, J = 8.2 Hz, 6H), 7.85 (d, J = 8.2 Hz, 6H), 7.49 (t, J = 5.6 Hz, 3H), 4.41 (br, 6H), 3.80 (br, 6H), 3.29 – 3.10 (m, J = 7.0, 6.4 Hz, 6H), 1.55 – 1.40 (m, 9H), 1.37 – 1.02 (m, 21H), 0.86 (t, J = 7.0 Hz, 27H). ^{13}C NMR (101 MHz, Chloroform- d_3 , 3 vol% TFA- d_1): 175.34, 169.19, 169.12, 158.75, 138.24, 138.21, 136.80, 131.04, 127.73, 63.93, 40.75, 39.79, 39.29, 37.13, 36.65, 30.52, 28.07, 24.70, 22.73, 22.63, 19.34. MALDI-TOF-MS found: 1211.75 m/z (calculated: 1211.72). FT-IR (cm^{-1}): 3316 (br), 1702 (m), 1592 (s), 1501 (s), 1408 (s), 1377 (s), 1304 (s), 1220 (m), 1195 (s), 1108 (m), 1015 (m), 925 (m), 872 (s), 831 (s), 791 (s), 720 (s), 689 (s), 641 (m), 586 (m), 528 (m).

4.8 References

- [1] G. Liu, P. Niu, C. Sun, S. C. Smith, Z. Chen, G. Q. Lu, H. M. Cheng, *J. Am. Chem. Soc.* **2010**, *132*, 11642.
- [2] V. W. Lau, M. B. Mesch, V. Duppel, V. Blum, J. Senker, B. V. Lotsch, *J. Am. Chem. Soc.* **2015**, *137*, 1064.
- [3] S. Cao, J. Yu, *J. Phys. Chem. Lett.* **2014**, *5*, 2101.
- [4] K. Schwinghammer, B. Tuffy, M. B. Mesch, E. Wirnhier, C. Martineau, F. Taulelle, W. Schnick, J. Senker, B. V. Lotsch, *Angew. Chem. Int. Ed.* **2013**, *52*, 2435.
- [5] G. Zhang, J. Zhang, M. Zhang, X. Wang, *J. Mater. Chem.* **2012**, *22*, 8083.
- [6] X. Wang, K. Maeda, A. Thomas, K. Takanebe, G. Xin, J. M. Carlsson, K. Domen, M. Antonietti, *Nat. Mater.* **2009**, *8*, 76.
- [7] V. W. H. Lau, I. Moudrakovski, T. Botari, S. Weinberger, M. B. Mesch, V. Duppel, J. Senker, V. Blum, B. V. Lotsch, *Nat. Commun.* **2016**, *7*, DOI 10.1038/ncomms12165.
- [8] K. Kailasam, M. B. Mesch, L. Möhlmann, M. Baar, S. Blechert, M. Schwarze, M. Schröder, R. Schomäcker, J. Senker, A. Thomas, *Energy Technol.* **2016**, *4*, 744.
- [9] K. Schwinghammer, S. Hug, M. B. Mesch, J. Senker, B. V. Lotsch, *Energy Environ. Sci.* **2015**, *8*, 3345.
- [10] J. Zhang, G. Zhang, X. Chen, S. Lin, L. Möhlmann, G. Dolega, G. Lipner, M. Antonietti, S. Blechert, X. Wang, *Angew. Chem. Int. Ed.* **2012**, *51*, 3183.
- [11] M. A. Wahab, J. Joseph, L. Atanda, U. K. Sultana, J. N. Beltramini, K. Ostrikov, G. Will, A. P. O'Mullane, A. Abdala, *ACS Appl. Energy Mater.* **2020**, *3*, 1439.
- [12] C. Zhang, B. Wang, X. Shen, J. Liu, X. Kong, S. S. C. Chuang, D. Yang, A. Dong, Z. Peng, *Nano Energy* **2016**, *30*, 503.
- [13] W. Niu, K. Marcus, L. Zhou, Z. Li, L. Shi, K. Liang, Y. Yang, *ACS Catal.* **2018**, *8*, 1926.
- [14] V. S. Kale, U. Sim, J. Yang, K. Jin, S. I. Chae, W. J. Chang, A. K. Sinha, H. Ha, C. C. Hwang, J. An, H. K. Hong, Z. Lee, K. T. Nam, T. Hyeon, *Small* **2017**, *13*, DOI 10.1002/sml.201603893.
- [15] J. Zhang, J. Sun, K. Maeda, K. Domen, P. Liu, M. Antonietti, X. Fu, X. Wang, *Energy Environ. Sci.* **2011**, *4*, 675.
- [16] M. Bledowski, L. Wang, A. Ramakrishnan, O. V. Khavryuchenko, V. D. Khavryuchenko, P. C. Ricci, J. Strunk, T. Cremer, C. Kolbeck, R. Beranek, *Phys. Chem. Chem. Phys.* **2011**, *13*, 21511.
- [17] J. Liebig, *Ann. Pharm.* **1834**, *10*, 1.
- [18] J. Liebig, *Ann. Phys.* **1835**, *110*, 570.
- [19] T. Komatsu, *Macromol. Chem. Phys.* **2001**, *202*, 19.
- [20] H. B. Gray, *Nat Chem* **2009**, *1*, 7.
- [21] G. Pearson, *Phil. Trans. R. Soc. Lond.* **1797**, *87*, 142.
- [22] J. W. Ager, M. R. Shaner, K. A. Walczak, I. D. Sharp, S. Ardo, *Energy Environ. Sci.* **2015**, *8*, 2811.
- [23] A. J. Bard, M. A. Fox, *Acc. Chem. Res.* **1995**, *28*, 141.
- [24] R. E. Blankenship, D. M. Tiede, J. Barber, G. W. Brudvig, G. Fleming, M. Ghirardi, M. R. Gunner, W. Junge, D. M. Kramer, A. Melis, T. A. Moore, C. C. Moser, D. G. Nocera, A. J. Nozik, D. R. Ort, W. W. Parson, R. C. Prince, R. T. Sayre, *Science* **2011**, *332*, 805.
- [25] Y. Tachibana, L. Vayssieres, J. R. Durrant, *Nat Phot.* **2012**, *6*, 511.
- [26] S. Y. Reece, J. A. Hamel, K. Sung, T. D. Jarvi, A. J. Esswein, J. J. H. Pijpers, D. G. Nocera, *Science* **2011**, *334*, 645 LP.
- [27] Z. Han, R. Eisenberg, *Acc. Chem. Res.* **2014**, *47*, 2537.
- [28] B. D. Yuhas, A. L. Smeigh, A. P. Douvalis, M. R. Wasielewski, M. G. Kanatzidis, *J. Am. Chem. Soc.* **2012**, *134*, 10353.
- [29] S. Sheu, D. Yang, H. L. Selzle, E. W. Schlag, **2003**, *100*, 12683.

- [30] S. J. Grabowski, *Chem. Rev.* **2011**, *111*, 2597.
- [31] J. Emsley, *Chem. Soc. Rev.* **1980**, *9*, 91.
- [32] O. Markovitch, N. Agmon, *J. Phys. Chem. A* **2007**, *111*, 2253.
- [33] T. F. A. De Greef, E. W. Meijer, **2008**, 453.
- [34] J. H. K. K. Hirschberg, L. Brunsveld, A. Ramzi, J. A. J. M. Vekemans, R. P. Sijbesma, E. W. Meijer, *Nature* **2000**, *407*, 167.
- [35] R. P. Sijbesma, E. W. Meijer, *Chem. Commun.* **2003**, 5.
- [36] R. P. Sijbesma, F. H. Beijer, L. Brunsveld, B. J. B. Folmer, J. H. K. K. Hirschberg, **1997**, 278, DOI 10.1126/science.278.5343.1601.
- [37] S. Cantekin, T. F. A. A. De Greef, A. R. A. A. Palmans, *Chem. Soc. Rev.* **2012**, *41*, 6125.
- [38] M. P. Lightfoot, F. S. Mair, R. G. Pritchard, J. E. Warren, *Chem. Commun.* **1999**, 1945.
- [39] M. A. J. Gillissen, M. M. E. Koenigs, J. J. H. Spiering, J. A. J. M. Vekemans, A. R. A. Palmans, I. K. Voets, E. W. Meijer, *J. Am. Chem. Soc.* **2014**, *136*, 336.
- [40] P. J. M. M. Stals, J. C. Everts, R. De Bruijn, I. A. W. W. Pilot, M. M. J. J. Smulders, R. Martín-Rapún, E. A. Pidko, T. F. A. A. De Greef, A. R. A. A. Palmans, E. W. Meijer, *Chem. Eur. J.* **2010**, *16*, 810.
- [41] P. A. Korevaar, S. J. George, A. J. Markvoort, M. M. J. Smulders, P. A. J. Hilbers, A. P. H. J. Schenning, T. F. A. De Greef, E. W. Meijer, *Nature* **2012**, *481*, 492.
- [42] T. F. A. A. De Greef, M. M. J. J. Smulders, M. Wolfs, A. P. H. J. H. J. Schenning, R. P. Sijbesma, E. W. Meijer, *Chem. Rev.* **2009**, *109*, 5687.
- [43] G. Morgese, B. F. M. De Waal, S. Varela-aramburu, A. R. A. Palmans, L. Albertazzi, E. W. Meijer, **2020**, 1.
- [44] S. I. S. Hendrikse, S. Spaans, E. W. Meijer, P. Y. W. Dankers, *Biomacromolecules* **2018**, *19*, 2610.
- [45] A. Bernet, R. Q. Albuquerque, M. Behr, S. T. Hoffmann, H.-W. Schmidt, *Soft Matter* **2012**, *8*, 66.
- [46] A. Timme, R. Kress, R. Q. Albuquerque, H. W. Schmidt, *Chem. Eur. J.* **2012**, *18*, 8329.
- [47] H. Misslitz, K. Kreger, H. W. Schmidt, *Small* **2013**, *9*, 2053.
- [48] J. J. Van Gorp, J. A. J. M. Vekemans, E. W. Meijer, *J. Am. Chem. Soc.* **2002**, *124*, 14759.
- [49] M. Blomenhofer, S. Ganzleben, D. Hanft, H. W. Schmidt, M. Kristiansen, P. Smith, K. Stoll, D. Mäder, K. Hoffmann, *Macromolecules* **2005**, *38*, 3688.
- [50] K. E. Broaders, S. J. Pastine, S. Grandhe, J. M. J. Fréchet, *Chem. Commun.* **2011**, *47*, 665.
- [51] J. Kluin, H. Talacua, A. I. P. M. Smits, M. Y. Emmert, M. C. P. Brugmans, E. S. Fioretta, P. E. Dijkman, S. H. M. Söntjens, R. Duijvelshoff, S. Dekker, M. W. J. T. Janssen-van den Broek, V. Lintas, A. Vink, S. P. Hoerstrup, H. M. Janssen, P. Y. W. Dankers, F. P. T. Baaijens, C. V. C. Bouten, *Biomaterials* **2017**, *125*, 101.
- [52] W. Mtangi, F. Tassinari, K. Vankayala, A. Vargas Jentszsch, B. Adelizzi, A. R. A. A. Palmans, C. Fontanesi, E. W. Meijer, R. Naaman, *J. Am. Chem. Soc.* **2017**, *139*, 2794.
- [53] B. Adelizzi, A. T. Rösch, D. J. van Rijen, R. S. Martire, S. Esiner, M. Lutz, A. R. A. Palmans, E. W. Meijer, *Helv. Chim. Acta* **2019**, e201900065.
- [54] B. P. Bloom, Y. Lu, T. Metzger, S. Yochelis, Y. Paltiel, C. Fontanesi, S. Mishra, F. Tassinari, R. Naaman, D. H. Waldeck, *Phys. Chem. Chem. Phys.* **2020**, *22*, 21570.
- [55] W. Lin, W. Hong, L. Sun, D. Yu, X. Chen, *ChemSusChem* **2018**, *11*, 114.
- [56] Y. Zheng, L. Lin, X. Ye, F. Guo, X. Wang, *Angew. Chem.* **2014**, *126*, 12120.
- [57] I. Bala, H. Singh, V. R. Battula, S. P. Gupta, J. De, S. Kumar, K. Kailasam, S. K. Pal, *Chem. Eur. J.* **2017**, *23*, 14718.
- [58] S. Irla, V. A. Raghunathan, S. Kumar, *J. Mol. Liq.* **2020**, *314*, 113631.
- [59] J. Chambers, J. Jiricny, C. B. Reese, *Fire Mater.* **1981**, *5*, 133.
- [60] C. E. Redemann, H. J. Lucas, *J. Am. Chem. Soc.* **1940**, *62*, 842.
- [61] H. Schroeder, E. Kober, *J. Org. Chem.* **1962**, *27*, 4262.
- [62] P. J. M. Stals, M. M. J. Smulders, R. Martín-Rapún, A. R. A. Palmans, E. W. Meijer, *Chem. Eur. J.* **2009**, *15*, 2071.
- [63] T. Terashima, T. Mes, T. F. A. De Greef, M. A. J. Gillissen, P. Besenius, A. R. A. Palmans, E. W. Meijer, *J. Am. Chem. Soc.* **2011**, *133*, 4742.
- [64] P. Panchaud, T. Bruyère, A. C. Blumstein, D. Bur, A. Chambovey, E. A. Ertel, M. Gude, C. Hubschwerlen, L. Jacob, T. Kimmerlin, T. Pfeifer, L. Prade, P. Seiler, D. Ritz, G. Rueedi, *J. Med. Chem.* **2017**, *60*, 3755.
- [65] S. Zhang, Z. Ren, S. He, Y. Zhu, C. Zhu, *Spectrochim. Acta - Part A Mol. Biomol. Spectrosc.* **2007**, *66*, 188.
- [66] E. Kroke, M. Schwarz, E. Horath-Bordon, P. Kröll, B. Noll, A. D. Norman, *New J. Chem.* **2002**, *26*, 508.
- [67] Y. Ke, D. J. Collins, D. Sun, H. C. Zhou, *Inorg. Chem.* **2006**, *45*, 1897.
- [68] F. Helmich, C. C. Lee, M. M. L. L. Nieuwenhuizen, J. C. Gielen, P. C. M. M. Christianen, A. Larsen, G. Fytas, P. E. L. G. L. G. Leclère, A. P. H. J. H. J. Schenning, E. W. Meijer, *Angew. Chem. Int. Ed.* **2010**, *49*, 3939.

- [69] S. Ogi, K. Sugiyasu, S. Manna, S. Samitsu, M. Takeuchi, *Nat. Chem.* **2014**, *6*, 188.
- [70] A. T. Haedler, K. Kreger, A. Issac, B. Wittmann, M. Kivala, N. Hammer, J. Köhler, H.-W. Schmidt, R. Hildner, *Nature* **2015**, *523*, 196.

Chapter 5

Tuning the pitch of N,N' -bis(n -alkyl)-naphthalenediimide double lamellae in 2D and 3D

Abstract:

The fabrication of nanostructured surfaces with high order is currently a hot topic in supramolecular chemistry and envisaged to bolster advances in heterogenous catalysis and microelectronic applications. Here, we report on the self-assembly of a set of novel alkylated double N,N' -bis(n -alkyl)-naphthalenediimides (NDIs) into double lamellar morphologies on highly oriented pyrolytic graphite (HOPG) surfaces. A detailed analysis of the two-dimensional (2D) monolayers by scanning tunneling microscopy (STM) reveals that the pitch of the double lamellae is tuned precisely by the variation of the length of the alkyl spacer that covalently connects two NDI cores. We find that the combination of our molecular design and flow deposition can be used to obtain the desired large-scaled ordered domains that exceed $1 \mu\text{m}^2$ in surface area. In addition to the surface experiments, we investigate the bulk properties for the entire series of compounds to determine structure-property relationships. Small angle X-ray scattering reveals that all bulk materials exhibit nanophase-separated lamellar phases whose domain spacings are slightly larger than the repeating units of the double-lamellar structures formed on HOPG surface. We assign the discrepancy to the partial desorption of the alkyl spacer from the HOPG surface. The desorption becomes more pronounced for longer alkyl spacers and decreases the predictability of the structural details of the self-assembled monolayers. The finding has important implications for the molecular design of future materials for functional interfaces that are based on electron donor - electron acceptor couples.

Part of this work will be published:

A.T. Rösch, R. Reynaerts, B.A.G. Lamers, K.S. Mali, S. De Feyter, A.R.A. Palmans, and E.W. Meijer

5.1 Introduction

The realization of highly regular surface patterns has become a major goal in the fields of supramolecular chemistry and nanotechnology^[1–6] since it is considered a crucial step towards achieving novel functional surfaces with applications in organic electronics,^[7,8] analyte-recognition^[9] and heterogenous catalysis.^[10] As an attractive alternative to top-down methods that commonly involve lithographic steps,^[11] bottom-up chemistry aims for the precise and highly regular positioning of molecules via the formation of directional, non-covalent interactions.^[12–14]

The non-covalent interactions that are used to generate patterned surfaces are well-known from supramolecular chemistry^[15] and comprise van der Waals interactions,^[16–19] hydrogen-bonding,^[20–26] halogen-bonding^[27,28] and coordination chemistry.^[29–31] In contrast to the supramolecular structures formed in solution or in bulk systems, the morphologies formed at surfaces depend on additional parameters. When designing adsorbates rationally, adsorbate-adsorbate, adsorbate-solvent and substrate-adsorbate interactions need to be considered.^[32] Achieving a suitable interplay of the interactions between all components and optimizing the preparation techniques results in the formation of two dimensional (2D) supramolecular monolayers in highly regularity.^[33] A structural investigation of monolayers is often performed by atomic force microscopy (AFM)^[34,35] or scanning tunneling microscopy (STM)^[36] since these techniques offer a (sub-)molecular resolution.^[37] Typical examples for the morphologies that have been observed for self-assembled monolayers are honeycomb patterns or lamellae^[38] which can exhibit structural details such as chiral textures^[39] and vertical nanophase separation.^[40] In addition, monolayers formed by a series of homologues may exhibit a periodical structural rearrangement that is governed by an odd-even effect.^[41,42]

Odd-even effects are well-known phenomena in chemistry and physics.^[41–47] One of the most prominent examples is the non-linear increase of the melting temperatures of *n*-alkanes.^[48,49] The addition of one methylene group to an *n*-alkane of odd chain length is accompanied by a rather distinct increase of the melting temperature. When a methylene group is added to an *n*-alkane of even chain length, however, the melting temperature is increased only marginally if not is decreased.^[48,49] The odd-even effect of the melting temperatures stems from differences in the crystal packing within the series of homologues. Although all compounds crystallize in the all-*anti* conformation, homologues with an even number of methylene groups form more densely packed crystals. Owing to the denser crystal packing, the homologues with an even number of methylene groups exhibit somewhat higher melting temperatures than their neighbors that contain an odd-number of methylene groups.^[48,50] On highly oriented pyrolytic graphite (HOPG) surface, adsorbed *n*-alkanes arrange in an all-*anti* conformation, since the epitaxial adsorption energy for each methylene group in a 2D monolayer is 64 meV (1.5 kcal/mol).^[32] Owing to this all-*anti* conformation, the terminal methylene groups are pointing either to one side (*syn*) or to opposite sides (*anti*) of the molecule. As a result, supramolecular monolayers prepared

from alkyl chain functionalized molecules typically exhibit a periodic modulation of surface structures that follows an odd-even trend.^[41] An exemplary STM study describing such an odd-even effect on HOPG surface has been conducted by Kim et al.^[51] Their study investigated the adsorption of dicarbamates that were both connected and terminated by alkyl chains on HOPG surface. Given by the all-*anti* conformation of the adsorbed alkyl chains, an even number of methylene groups in the central alkyl chain resulted in an *anti*-arrangement of the terminal alkyl chains with respect to each other. Analogously, a *syn*-arrangement was observed for derivatives containing an odd number of methylene groups in the central alkyl chain (Figure 5.1).

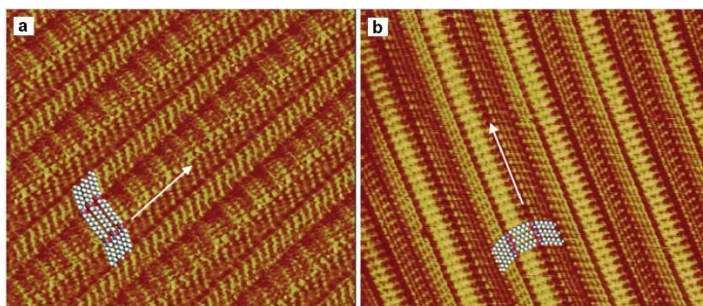


Figure 5.1: STM images showing an odd-even in the morphologies of monolayers of alkylated dicarbamates on HOPG surface. (a) An even number of methylene groups in the central alkyl chain resulted in an *anti*-arrangement of the terminal alkyl chains with respect to each other. (b) Analogously, an odd number resulted in a *syn*-arrangement. Figure adapted with permission from reference [51] (copyright 2000 American Chemical Society).

When the adsorption process continues, multilayers and finally thin films and bulk materials are generated. Since AFM and STM only image the surface morphologies, other techniques such as nuclear magnetic resonance (NMR),^[52] differential scanning calorimetry (DSC),^[52] attenuated total internal reflection infrared spectroscopy (ATR-IR),^[53] electron diffraction,^[54] neutron^[52,53,55,56] and X-ray scattering^[56–58] become more suitable to obtain structural information of such multilayered materials.^[54] Literature studies that compared the self-assembled structures of compounds in a 2D monolayer and in bulk material reported that the complex nature of the additional interactions at the interface with respect to the bulk often induces structural differences in both media.^[59,60] One particular example for a type of compounds that has already been investigated upon the formation of self-assembled structures in crystalline bulk material^[58,61–64] and on surface^[14,38,40,59,65] are *N,N'*-bis(*n*-alkyl)naphthalenediimides (NDIs). The class of compounds is of particular interest due to its *n*-type semiconducting properties^[62,66–69] and its straightforward chemical modification.^[62,63,70] The determination of the crystal structures of various alkylated NDIs indicated that in bulk, the compounds are typically arranged in lamellar phases.^[58] The domain spacings of the investigated crystals were defined by the molecular dimensions of the microphase segregated NDI cores and the alkyl chains of the molecules.^[58] In contrast

to bulk materials, the self-assembled monolayers formed on HOPG surface (exemplary STM images depicted in Figure 5.2) showed the formation of lamellar structures only for very short or rather long alkyl chains ($N_{\text{methylene groups}} \leq 4$ or ≥ 13).^[38] For the derivatives that contained alkyl chains of intermediate length ($4 < N_{\text{methylene groups}} < 13$), the formed morphologies were identified as honeycomb patterns.^[38] The hexagonal packing of the NDI cores in these honeycomb patterns was ascribed to a partial desorption of the alkyl chains.^[38]

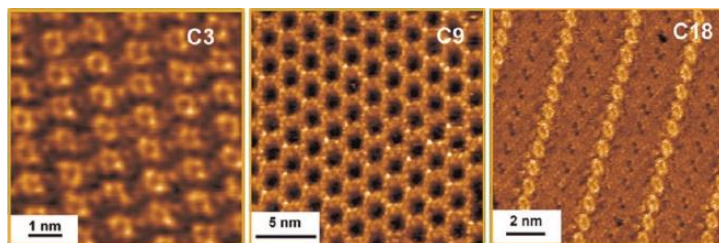
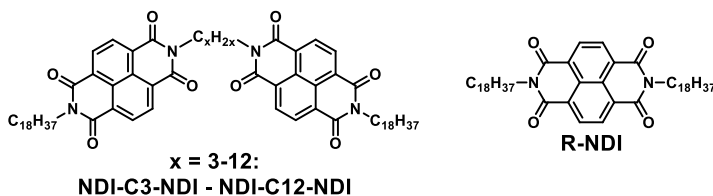


Figure 5.2: STM images of supramolecular monolayers formed by propyl (left), nonyl (middle) and octadecyl (right) appended NDIs at the HOPG/1-tetradecene interface. Figure adapted with permission from reference [38] (copyright 2012 American Chemical Society).

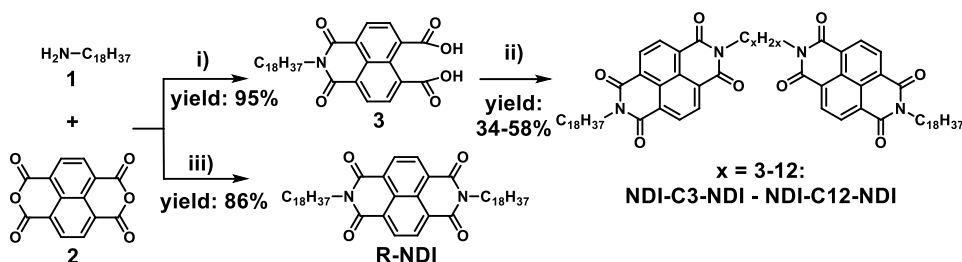
Inspired by a recent report on engineering long-range order in supramolecular assemblies of alkylated NDIs,^[14] we designed a series of novel double NDIs (Scheme 5.1). We terminated the double NDIs with octadecyl chains to induce the formation of lamellar morphologies on HOPG surface.^[14,38] The central alkyl chain was anticipated to act as an additional restriction during the self-assembly process. The length of the alkyl spacer was varied from three to twelve carbon atoms to systematically investigate structure-property relationships of both self-assembled monolayers and bulk phases. We conducted a STM study to investigate the morphologies formed on HOPG surface and performed X-ray scattering to investigate the morphologies and corresponding domain spacing in the bulk phase.



Scheme 5.1: Molecular structures of double *N,N'*-bis(*n*-alkyl)-naphthalenediimides **NDI-C3-NDI – NDI-C12-NDI** and reference **R-NDI**.

5.2 Synthesis and characterization of *N,N'*-bis(*n*-alkyl)-naphthalene-diimides

The synthesis of all NDIs was performed according to Scheme 5.2. Following a modified protocol by Tambara et al.,^[71] *n*-octadecylamine **1** was reacted with 1,4,5,8-naphthalenetetracarboxylic dianhydride **2**. The condensation was sped up by using a microwave reactor. Compound **2** was used in excess to form predominantly octadecyl naphthalene monoimide **NMI** and reduce the formation of double alkyl functionalized **R-NDI**. During the work-up, unreacted **2** was solubilized in water by hydrolysis in aqueous NaOH solution (1 M). Insoluble **NMI** was isolated by filtration and dispersed in aqueous hydrochloric acid solution (3 M) to protonate the carboxylic acid groups. The protonation was required to increase the electrophilicity of the compound for the subsequent condensation reaction. Dried **NMI** was reacted with aliphatic α,ω -diamines (ranging from 1,3-diaminopropane to 1,12-diaminododecane) using the microwave reactor. All double NDIs **NDI-C3-NDI** – **NDI-C12-NDI** were purified by recrystallization from chloroform or toluene and obtained as crystalline compounds in medium to high yields (34-81%). In addition to the double NDIs, 1,4,5,8-naphthalenetetracarboxylic dianhydride was also reacted twice with *n*-octadecylamine to prepare the reference compound **R-NDI**. After recrystallization from toluene, **R-NDI** was obtained as a crystalline material in high yield (86%).



*Scheme 5.2: Synthetic route for the preparation of double NDIs **NDI-C3-NDI** - **NDI-C12-NDI** and **R-NDI**. All reactions were performed in a microwave reactor. Reagents and conditions: i) 1) 2.5 eq. naphthalene-tetracarboxylic dianhydride, 50/50 DMF/THF, 75 °C - 140 °C, 10 min, 2) NaOH(aq.), 3) HCl(aq.), ii) aliphatic α,ω -diamines, DMF/THF, 75 °C - 140 °C, 30 min, iii) 2 eq. octadecylamine, DMF/THF, 75 °C - 140 °C, 10 min.*

All compounds were fully characterized by ^1H and ^{13}C nuclear magnetic resonance (NMR) and Fourier-transform infrared (FT-IR) spectroscopy and matrix-assisted laser ionization time of flight mass spectrometry (MALDI-TOF-MS). The MALDI-TOF-MS spectra showed peaks which corresponds well with the exact mass of the NDIs. Mass peaks which would indicate monosubstitution were absent. The FT-IR spectra of all NDIs looked very similar. The spectra show C-H stretching vibrations at 3065 cm^{-1} and 2920 cm^{-1} which were assigned to protons attached to sp^3 and sp^2 -hybridized carbon atoms, respectively. The C=O vibration of the imide was noticed at 1703 cm^{-1} .

5.3 Optical properties of the NDIs

Having proven the molecular structures of all NDIs, we moved on to determining the optical properties of the series of homologues in chloroform solution ($1.3 \cdot 10^{-5}$ mol/L) and in drop-casted thin films. The spectroscopic solutions were prepared by dissolving the NDIs in chloroform. Full dissolution of the compounds was achieved by heating the samples slightly below 61 °C and sonicating until the solutions were transparent. When the spectroscopic samples were stored for several hours at room temperature, the samples became turbid. Precipitation of the compounds indicated a poor solubility and was more pronounced for the even than for the odd homologous. During the spectroscopic study, the samples were hence warmed up just before each measurement to ensure that all experiments were performed on transparent solutions. The absorption and fluorescence spectra recorded for **R-NDI**, **NDI-C6-NDI** and **NDI-C7-NDI** are good examples to highlight the similarities and differences of the optical properties within the series of homologues. The corresponding spectra recorded for these compounds are shown in Figure 5.3a. The shapes of the absorption spectra of these three NDIs were identical with the absorption spectra of the remaining homologues. All compounds showed strong absorption bands with local maxima at 382 nm (molecular extinction coefficients of the double NDIs $\epsilon = 5.6 \cdot 10^4$ L mol⁻¹ cm⁻¹), 361 nm ($\epsilon = 5.1 \cdot 10^4$ L mol⁻¹ cm⁻¹) and 343 nm ($\epsilon = 3.0 \cdot 10^4$ L mol⁻¹ cm⁻¹). We note that the normalization of the spectra was performed because **R-NDI** had only one NDI chromophore and hence only half the molecular absorptivity as the double NDIs. In contrast to the fluorescence spectrum recorded for **R-NDI**, the spectra recorded for the double NDIs showed additional fluorescence at longer wavelengths (around 550 nm). Within the series, the additional fluorescence band was most apparent for **NDI-C6-NDI** and least apparent for **NDI-C7-NDI**. As noticed in Figure 5.3b, the intensity of the additional fluorescence band followed an odd-even effect for the series of homologues. Upon the transition from an odd to an even homologue, the fluorescence intensity was strongly increased. In contrast, the transition from an even homologue to an odd homologue resulted only in a small increase or in most cases even a decrease of the fluorescence intensity. The noticed absorption bands were assigned to characteristic π - π^* transitions of the NDI chromophore in the molecularly dissolved state.^[72] Since the absorption spectra did hence not indicate the formation of aggregates and all spectra were also recorded in dilute solutions ($1.3 \cdot 10^{-5}$ mol/L), the additional fluorescence band that was noticed for the double NDIs at 550 nm was ascribed to intramolecular excited dimer (excimer) formation.^[63,73]

Literature studies on compounds containing two or more chromophores that were connected by a flexible alkyl spacer reported on a strong impact of the length of the spacer and the formation of intramolecular excimers, too. Hirayama^[74] reported on the intramolecular excimer formation in diphenyl and triphenyl alkanes. The study showed that excimers were formed only when the alkyl spacer that connected the two phenyl rings contained exactly three methylene groups. The absence of excimer formation for compounds with different alkyl spacer lengths was ascribed to conformational restrictions

which prevented the formation of the π -stacked arrangement of the excimer.^[74] Mattice and coworkers investigated the excimer formation of bifunctional compounds containing the naphthalene,^[75] naphthol^[76] or pyrene^[77] chromophores which are structurally related to the NDI motif. For bifunctional naphthalene and naphthol derivatives, the formation of excimers was noticed for alkyl spacers containing two to six methylene groups. The highest excimer emission with respect to the emission of the monomer was found when the chromophores were connected by two or three methylene groups.^[75,76] For the bispyrenes, the intensity of the excimer fluorescence was found to depend both on the length of the alkyl spacer and the viscosity of the solvent. In a 9:1 solvent mixture of methanol and ethylene glycol, the highest relative excimer fluorescence within the series was found when the chromophores were linked by five or six methylene groups. When the relative excimer fluorescence within the series was determined in pure ethylene glycol which is more viscous, a different trend was found. The series exhibited an odd-even effect and the highest relative fluorescence was measured when the pyrenes were connected by three methylene groups.^[77] Since pyrene and NDI chromophores are structurally related and chloroform is a low viscosity solvent such as the 9:1 solvent mixture of methanol and ethylene glycol, determining the highest relative excimer fluorescence for **NDI-C6-NDI** was in agreement with this literature report. The somewhat unexpectedly low excimer fluorescence of **NDI-C5-NDI** and remaining discrepancies between the two systems were ascribed to the differences in the chemical structures that include the type of chromophores and the attachment position of alkyl spacer as well as the different solvent.

Thin films were prepared by drop-casting concentrated chloroform solutions onto microscope glass slides. Owing to the preparation technique, the thin films were not uniform and the absorption spectra were normalized to simplify the comparison of the data. The absorption spectra recorded for all thin films looked very similar, contained scattering contributions and showed a 10 nm red-shift of the characteristic π - π^* transitions with respect to the absorption spectra recorded in solution (Figure 5.3c). All samples exhibited broad fluorescence bands that showed an increasing intensity with an increasing wavelength. After the fluorescence data was corrected for differences in absorption and normalized, also here, an odd-even effect was observed (Figure 5.3d). Both scattering contributions and the red-shifts of the absorption bands were ascribed to the aggregation of the compounds and were in accordance with literature reports on structurally related single NDIs.^[65]

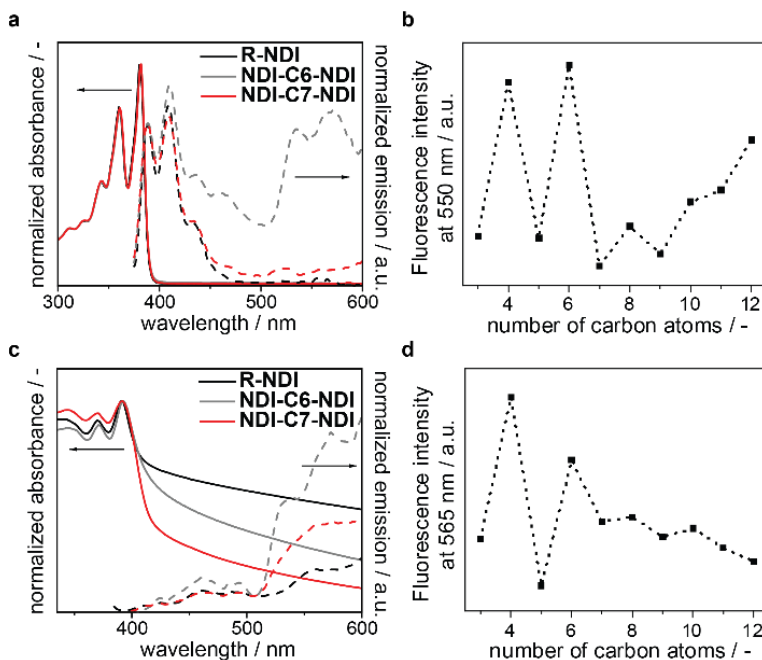


Figure 5.3: (a) UV/Vis (solid trace) and fluorescence (dashed trace, $\lambda_{ex} = 356$ nm) spectra recorded for chloroform solutions of **NDI-C6-NDI** and **NDI-C7-NDI**, concentration $1.3 \cdot 10^{-5}$ mol/L. (b) Variation of the fluorescence intensity measured at 550 nm for all homologues. (c) UV/Vis (solid trace) and emission (dashed trace, $\lambda_{ex} = 365$ nm) spectra recorded for drop-casted thin films of **NDI-C6-NDI** and **NDI-C7-NDI**. (d) Variation of the fluorescence intensity measured at 565 nm for all homologues. Before normalization, the fluorescence spectra were corrected for differences in thickness via division by the measured optical density.

5.4 Physisorbed self-assembled monolayers formed at the solution/HOPG interface

5.4.1 Structural details of the monolayers formed within the series of homologues

In order to characterize the surface morphologies formed by the double NDIs with different spacer lengths at the HOPG/1-phenyloctane interface, physisorbed self-assembled monolayers were prepared and studied by STM. The study was performed in collaboration with Robby Reynaerts and Kunal Mali from prof. Steven De Feyter's group at the Katholieke Universiteit Leuven. Given the low solubility of the double NDIs in 1-phenyloctane (boiling point of 261-263 °C), a typical solvent used for STM experiments, the self-assembled monolayers were obtained by drop casting saturated solutions onto freshly cleaved HOPG substrates. Drop-casting was followed immediately by creating a solution flow by absorbing the excess solution using a clean tissue paper since flow-deposition is a known procedure to increase the domain size of physisorbed self-assembled monolayers.^[33] Flow-deposition was followed by annealing the samples at 100 °C for 10 minutes. The HOPG substrates were

allowed to slowly cool down to room temperature before the STM measurements were performed.

Using these conditions to prepare the samples, all double NDIs (except for **NDI-C4-NDI** whose solubility was too low) could be imaged. High resolution STM (HR-STM) images of the monolayers are provided in Figure 5.4. Corresponding unit cell parameters are given in Table 5.1. The images indicate the formation of double lamellar structures for all compounds. In general, the double lamellar structures consist of alternating bright and dark columns. The bright columns always have a similar width and are separated by a narrower dark column on the one side (grey arrows in Figure 5.4) and a wider dark column on the other (green arrows in Figure 5.4). Within the series of compounds, the STM images clearly reveal a variation of the width of the narrower dark column. The narrower dark column was assigned to the adsorption of the alkyl spacer connecting two NDI cores. The broader dark columns were attributed to the terminal octadecyl chains and the bright columns to the adsorbed NDI cores.

To analyze the morphologies of the monolayers in more detail, we built molecular models. The molecular models are also shown in Figure 5.4 and positioned right next the STM images of the monolayer of the corresponding double NDI. Figure 5.4a and b show the HR-STM image of the monolayer and corresponding molecular model of **NDI-C3-NDI**. Both images show two different modes of adsorption and also the front at which these two regimes meet. In the hereinafter-called 'collinear' conformation (marked in red in Figure 5.4 b), the octadecyl chains attached to one NDI lamella are collinear and fully interdigitated with the octadecyl chains attached to the neighboring NDI lamella. In the second type of adsorption the hereinafter-called 'non-collinear' conformation (marked in blue in Figure 5.4 b), the octadecyl chains are non-collinear with respect to each other and not fully interdigitated with the octadecyl chains of the neighboring NDI lamella. We note that the width of the octadecyl lamella remains the same irrespective of the adsorption conformation. Additionally, the two covalently connected NDI cores of **NDI-C3-NDI** are always in a *syn*-arrangement with respect to each other. Similar to **NDI-C3-NDI**, **NDI-C5-NDI** showed the adsorption into double lamellar structures in which collinear and non-collinear regimes coexisted. Additionally, the two covalently connected NDI cores were arranged in the *syn*-conformation, too. In contrast, all remaining double NDIs (**NDI-C6-NDI – NDI-C12-NDI**) strongly preferred the adsorption in the non-collinear conformation. The STM images of the monolayers formed by these homologues indicated that the covalently connected NDI cores were always adsorbed in the *anti*-arrangement.

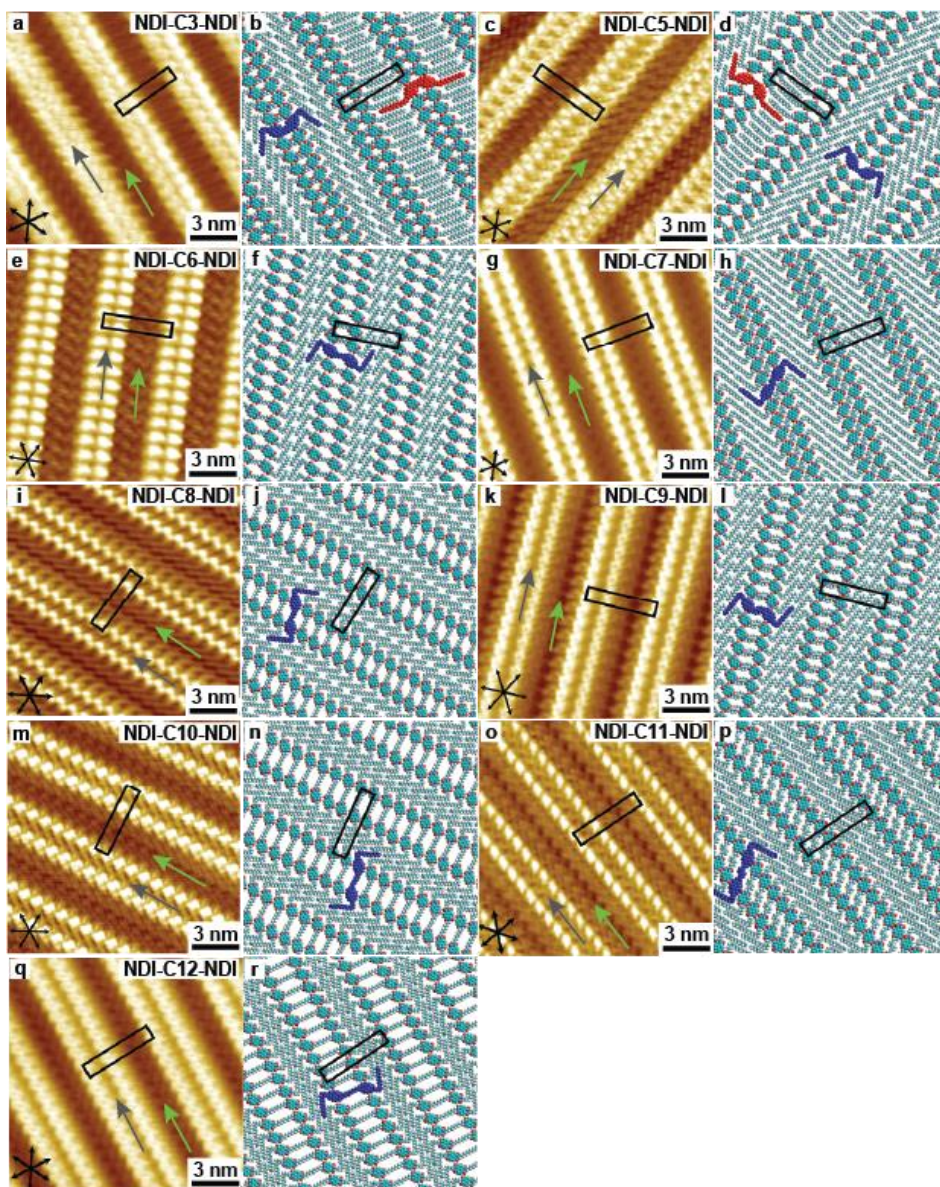


Figure 5.4: Representative high-resolution STM images (a, c, e, g, i, k, m, o, q) and corresponding molecular models (b, d, f, h, j, l, n, p, r) of the monolayers formed by the double NDIs at the 1-phenyloctane/HOPG interface. Imaging parameters: (a) $V_{bias} = -1.0$ V, $I_{set} = 90$ pA; (c) $V_{bias} = -1.1$ V, $I_{set} = 110$ pA; (e) $V_{bias} = -0.5$ V, $I_{set} = 120$ pA; (g) $V_{bias} = -0.6$ V, $I_{set} = 100$ pA; (i) $V_{bias} = -0.6$ V, $I_{set} = 130$ pA; (k) $V_{bias} = 0.8$ V, $I_{set} = 110$ pA; (m) $V_{bias} = 0.5$ V, $I_{set} = 110$ pA; (o) $V_{bias} = -0.7$ V, $I_{set} = 130$ pA; (p) $V_{bias} = -1.35$ V, $I_{set} = 80$ pA. The orientation of the HOPG axes and the unit cell are given in black.

The common structural element that distinguishes the non-collinear regime from the collinear regime in the monolayers of our double NDIs, is the sharp bend (between 30° to 60°) that is observed in the terminal octadecyl chains. While alkyl chains are flexible and thus can form curved structures upon surface adsorption, the sharp bend indicates the formation of a kink that involves the partial desorption of the otherwise straight alkyl chain from the surface.^[78] The molecular models presented above enforce this kink by introducing a gauche defect between the C2 and the C3 carbons of the terminal octadecyl chains. The coinciding presence of two modes of adsorption of the alkyl sidechains has also been reported for self-assembled monolayers of single NDIs and has been ascribed to the very similar potential energies of the two states.^[14,38] Similar sharp angles as observed for our double NDIs have also been reported for the on-surface self-assembly of a hexadecyl substituted single NDI.^[59] Based on DFT calculations, it was argued that the partial desorption of the methylene group in the kinked conformation avoids the steric repulsion between the carbonyl group of the NDI core and the α -CH₂ group of the alkyl chain. In addition, the bent conformation was also found to increase the overall density of the lamellar structures which added an energetically favorable contribution to the overall adsorption energy of the monolayer.^[59]

Observing the *syn*- and *anti*-arrangement of the covalently connected NDI core is somewhat similar to the work by Kim *et al.*^[51] The literature report described the adsorption of dicarbamates on HOPG surface which were both connected and terminated by alkyl chains. Depending on the number of the methylene groups in the central alkyl chain that was absorbed flat and in all-*anti* conformation to the HOPG surface, either a *syn*- or an *anti*-arrangement of the carbamates and the terminal side chains was observed. The *syn*-arrangement was observed for the compounds that contained alkyl spacers with an odd number of methylene groups. Analogously, the *anti*-arrangement was observed for compounds containing alkyl spacers with an even number of methylene groups. Since **NDI-C3-NDI** and **NDI-C5-NDI** contained alkyl spacers with an odd parity, the observed *syn*-arrangement of the NDI cores in the monolayers satisfied our expectations. Analogously, the *anti*-arrangement for **NDI-C6-NDI**, **NDI-C8-NDI**, **NDI-C10-NDI** and **NDI-C12-NDI** fulfilled the rational, too. In contrast, observing the *anti*-arrangement for the monolayers of **NDI-C7-NDI**, **NDI-C9-NDI** and **NDI-C11-NDI** was somewhat surprising. The suspension of the odd-even effect suggested that for these homologues, the central alkyl chain was not adsorbed flat in the all-*anti* conformation. In order to understand the structural origin of the observation better, we compared the unit cell parameters '*b*' of the monolayers formed by **NDI-C7-NDI – NDI-C11-NDI**. As easily noticed in Table 5.1, '*b*' was either not increased or even slightly decreased upon the transition from a homologue with an even parity to the following homologue with an odd parity. In contrast, the addition of one methylene group to a homologue with an odd parity resulted in a notable increase of '*b*'. The peculiar odd-even trend corroborated the partial desorption of the alkyl spacers with an odd number of methylene groups. As noticed in Figure 5.4h, l and p, we simply pointed the central methylene group of the alkyl spacer away from the surface while keeping the rest in the

same plane to fit the observed structure with the molecular models. Possible reasons for the suspension of the odd-even effect are the systems' striving to the highest packing density, a higher entropy by the partial desorption of the alkyl spacer and a better interaction of the monolayer with the surface when both NDI cores were arranged in the *anti*-conformation along one axis of the HOPG surface.

Table 5.1: Unit cell parameters of the lamellar domains formed by **NDI-C3-NDI** – **NDI-C12-NDI** at the 1-phenyloctane/HOPG interface.

Entry	Unit cell parameters (STM)			rel. orientation of the NDI cores
	<i>a</i> [nm]	<i>b</i> [nm]	α [°]	
NDI-C3-NDI	0.9 ± 0.1	4.4 ± 0.1	87 ± 2	<i>syn</i>
NDI-C5-NDI	0.9 ± 0.1	4.4 ± 0.1	87 ± 2	<i>syn</i>
NDI-C6-NDI	0.9 ± 0.1	4.4 ± 0.1	88 ± 1	<i>anti</i>
NDI-C7-NDI	0.9 ± 0.1	4.4 ± 0.1	89 ± 1	<i>anti</i>
NDI-C8-NDI	0.9 ± 0.1	4.6 ± 0.2	89 ± 2	<i>anti</i>
NDI-C9-NDI	0.9 ± 0.1	4.5 ± 0.1	89 ± 1	<i>anti</i>
NDI-C10-NDI	0.9 ± 0.1	4.8 ± 0.1	86 ± 4	<i>anti</i>
NDI-C11-NDI	0.9 ± 0.1	4.7 ± 0.1	87 ± 2	<i>anti</i>
NDI-C12-NDI	0.9 ± 0.1	4.8 ± 0.1	85 ± 1	<i>anti</i>

5.4.2 Structural details at the boundaries of the domains

Imaging the self-assembled monolayer of **NDI-C12-NDI** at decreased magnification shows that the columns in adjacent domains were oriented at an angle of approximately 60° with respect to each other. This relative arrangement highlights the influence of the underlying graphite substrate lattice on the self-assembly process. The lamellae of **NDI-C12-NDI** often showed defects along the lamellar axis as marked by the purple oval in Figure 5.5. The defect possibly stemmed from two lamellae meeting each other which initially grew in opposite directions and had a slight mismatch in the propagation axis (inset on the right in Figure 5.5). The structural transition at this defect is also depicted as a simplified schematic next to the STM image.

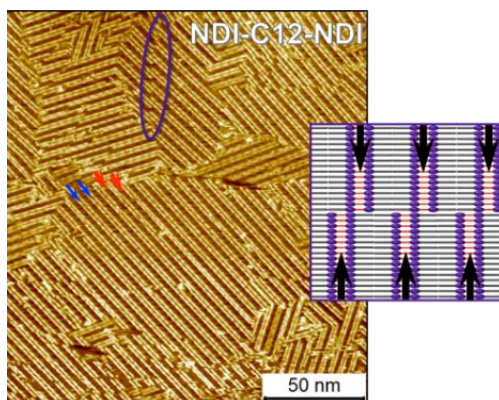


Figure 5.5: Representative large scale STM images showing the self-assembled monolayers formed by **NDI-C12-NDI** at the 1-phenyloctane/HOPG interface. The blue and the red arrows show the narrow and the dark columns indicating the adsorption of the spacer and the terminal octadecyl chains. The purple oval highlights defects that are formed when two lamellae with a slight mismatch in the propagation axes meet. The defect is illustrated schematically on the right. Imaging parameters: $V_{bias} = 0.9$ V, $I_{set} = 100$ pA.

5.4.3 Transformation of the collinear to the non-collinear regime

Although the non-collinear adsorption conformation of the octadecyl chains was strongly preferred for **NDI-C6-NDI** – **NDI-C12-NDI**, we occasionally observed the collinear regime for **NDI-C11-NDI**, too. When investigating the structure over time in a time-dependent STM experiment, we found that the collinear conformation was transformed into the non-collinear conformation (Figure 5.6). The conversion typically occurred within two to four minutes and indicated the higher thermodynamic stability of the non-collinear regime with respect to the collinear regime.

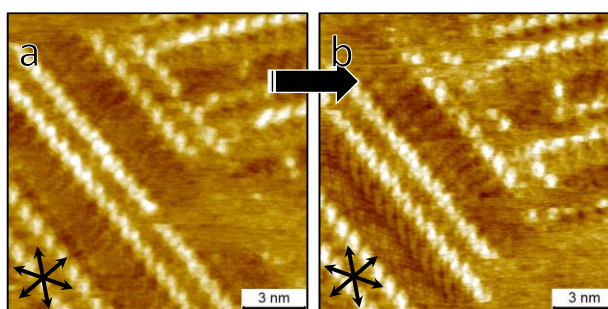


Figure 5.6: STM images of **NDI-C11-NDI** at the 1-phenyloctane/HOPG interface showing the transition of the collinear surface domain (a) to the non-collinear arrangement (b) within a time span of 2 minutes. Imaging conditions: $V_{bias} = -0.7$ V, $I_{set} = 130$ pA.

5.4.4 Formation of very large domains by flow-deposition

Samples prepared by drop-casting (without the flow deposition step) showed the formation of disordered aggregates. After annealing, ordered domains that typically spanned 120 nm to 300 nm were obtained. Applying flow deposition^[33] resulted in the preparation of the largest domains. In some cases, we observed the formation of domains that exceeded the surface area of 1 μm^2 (Figure 5.7) which suggested that the molecular design was excellent for the fabrication of supramolecular structures with long range order.

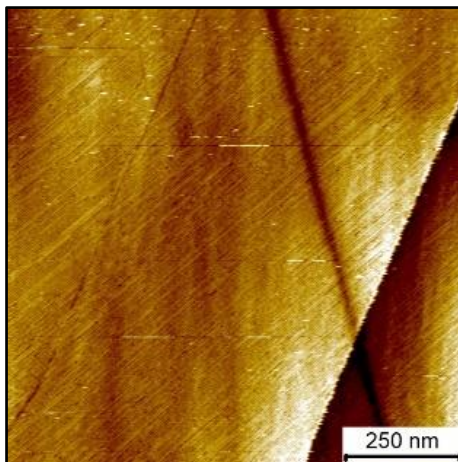


Figure 5.7: Large scale image of **NDI-C12-NDI** spanning $1 \times 1 \mu\text{m}$. Imaging conditions: $V_{\text{bias}} = 1.4 \text{ V}$, $I_{\text{set}} = 90 \text{ pA}$.

5.5 Thermal properties of all NDIs

Having characterized the structural details of the surface morphologies, we continued our study with the investigation of the bulk properties. The thermal behavior of all compounds was investigated in detail by differential scanning calorimetry (DSC) and polarized optical microscopy (POM). For the DSC measurements, all samples were heated to the isotropic melt, equilibrated and cooled down at a constant rate of 10 K min^{-1} to standardize the thermal history. Subsequently, two heating and cooling cycles were recorded by DSC. The data obtained from the second heating cycle (heating rate of 10 K/min) are summarized in Table 5.2. For the POM study, a small amount of substance was placed in between two microscope glass slides and heated until it was isotropically molten. POM images were taken while the sample was cooled from the isotropic melt to room temperature and heated again to the isotropic melt. Being exemplary for the series, the DSC trace of **NDI-C11-NDI** is depicted in Figure 5.8. Upon heating from room temperature, two thermal transitions were noticed. The first transition, whose maximum heat flow is indicated by T_1 , was only weakly endothermic and occurred over a broad temperature window that ranged from $90 \text{ }^\circ\text{C}$ to $150 \text{ }^\circ\text{C}$. POM images which were taken below and above

T_1 showed the presence of similar birefringent textures. Interestingly, fissures appeared when cooling the material below T_1 and disappeared when heating above T_1 . A second thermal transition was noticed when the temperature was increased to 230 °C. At this temperature, the solid material was melted into an isotropic liquid, as evidenced by the loss of the birefringence in the POM image. The corresponding thermal phase transition temperature was assigned to the melting temperature T_m .

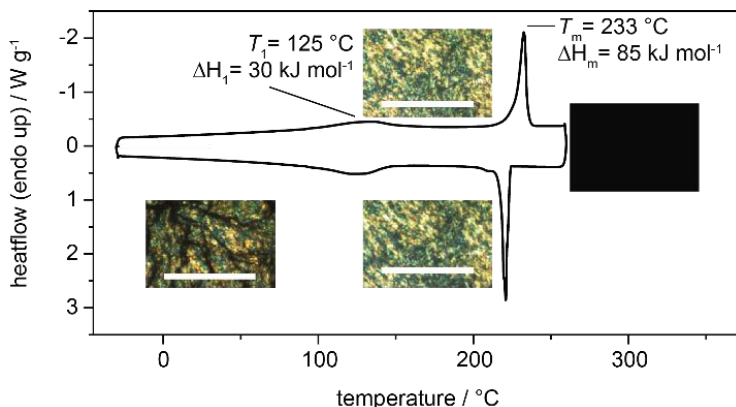


Figure 5.8: Second heating and cooling runs recorded by DSC for **NDI-C11-NDI** (heating and cooling rate = 10 K min⁻¹). The insets are POM images. The images were taken for the isotropic melt, after crystallization, when cooled down to 50 °C and after reheating closely beneath T_m . White scale bar: 100 μ m.

The remaining homologues showed a very similar thermal phase behavior which consisted of two thermal transitions during the heating cycle (except for **NDI-C8-NDI** that showed an additional third thermal transition at $T_2 = 229$ °C; $\Delta H_2 = 7$ kJ mol⁻¹) and two thermal transitions during the cooling cycle. Since the first thermal transitions of all homologues occurred over a similar and rather wide temperature range, it was not possible to detect an odd-even effect for T_1 . In contrast, the melting temperatures T_m of the series of homologues depended strongly on the length of the alkyl spacer. As noticed in Figure 5.9a, T_m of the double NDIs was governed by an odd-even effect. Double NDIs with an even parity of the alkyl spacer always had higher melting temperatures T_m than their neighbors with an odd parity. Within the series, **NDI-C4-NDI** showed the highest ($T_m = 328$ °C) and **NDI-C11-NDI** ($T_m = 230$ °C) the lowest T_m . This observation suggested that T_m was overall decreased when the length of the alkyl spacer was increased. For the melting enthalpies ΔH_m , an odd-even effect was noticed, too (Figure 5.9b). In contrast to the odd-even effect of T_m , the odd-even effect of ΔH_m was not noticed through-out the entire series. **NDI-C8-NDI**, the only homologue that contained a third thermal transition, was an exception from the trend.

Since the POM images taken below and above T_1 always showed birefringent structures and the samples remained non-shearable until heated to T_m , the transitions occurring at T_1

were suggesting crystal-crystal transitions. Interestingly, the birefringent structures noticed in the POM images above and below T_1 looked very similar and were distinguished only by the formation of fissures when the sample was cooled below T_1 . The observation of similar fissures during cooling perylene bisimides has been reported by Chesterfield *et al.*^[79] In this literature system, the formation of fissures was ascribed to differences in the thermal expansion coefficients of the organic material and the microscope glass slide and could be avoided completely by reducing the cooling rate to 1 K/min. In case of our double NDIs, fissure formation was still observed when cooling was performed at the rate of 1 K/min. A recent report on the thermal phase transitions of alkylated single NDIs reported that within the series of homologues, T_m was decreased when the length of the side chains was increased.^[64] The somewhat unexpected trend of decreasing T_m while increasing the molecular weight was ascribed to an increasing fusion entropy that stemmed either from the larger conformational freedom of the longer alkyl chains in the melt or from their more ordered crystal packing in the solid.^[64] The structural similarity of our double NDIs with the reported single NDIs suggested that the increase of the length of the alkyl spacer resulted in increasing the fusion entropy of the double NDIs, too. In line with this argumentation, **R-NDI**, which contains exclusively long alkyl chains, was found to reach the isotropic melt already at 147 °C which was also in accordance with a literature report on the thermal properties of compound by Ichikawa *et al.*^[80] The similarity of the DSC traces recorded for the series of the double NDIs was somewhat surprising, since the above-mentioned literature report on the single NDIs described the presence of multiple polymorphic transitions and liquid crystalline phases for several homologues within the series.^[64] We conclude that while the length of alkyl spacer in the double NDIs induced strong differences in T_m within the series, its size was too small to counter the structural directing effect of the terminal octadecyl sidechains which induced the formation of lamellar structures for all homologues.

Since the odd-even effect that was observed for T_m stemmed from periodic changes in the crystal packing,^[64] and the similarity of the DSC traces indicated no polymorphism for the double NDIs, we continued our study with a structural investigation of the bulk morphologies at room temperature and the rearrangements occurring at T_1 by performing X-ray scattering.

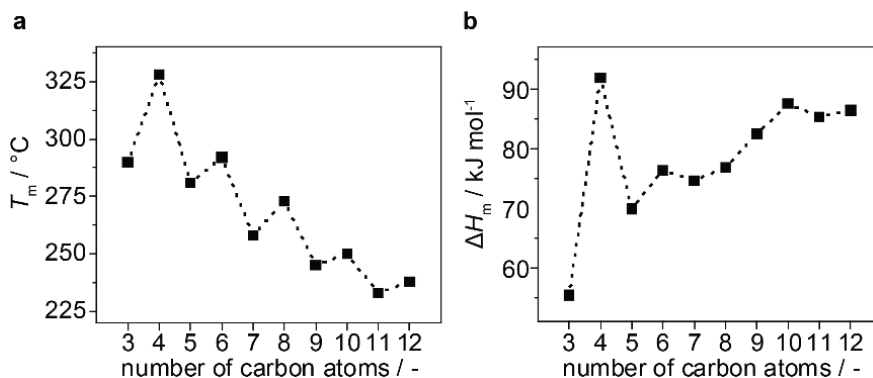


Figure 5.9: (a) Decrease of T_m in an odd-even fashion when increasing the length of the alkyl chain connecting the NDI cores. (b) Variation of the melting enthalpy with the series.

Table 5.2: Thermal properties of the double NDIs **NDI-C3-NDI** – **NDI-C12-NDI** as well as **R-NDI**.

entry	NDI ^[a]	T_1 ^[b] [°C]	ΔH_1 ^[c] [kJ mol ⁻¹]	T_m ^[b] [°C]	ΔH_m ^[c] [kJ mol ⁻¹]
1	NDI-C3-NDI	96	41	290	55
2	NDI-C4-NDI	133	38	328	92
3	NDI-C5-NDI	121	41	281	70
4	NDI-C6-NDI	124	50	292	76
5	NDI-C7-NDI	130	45	258	75
6	NDI-C8-NDI	128	38	273	77
7	NDI-C9-NDI	124	35	245	83
8	NDI-C10-NDI	132	27	250	88
9	NDI-C11-NDI	125	30	233	85
10	NDI-C12-NDI	132	37	239	86
11	R-NDI ^[e]	139	15	147	47

[a] Molecules as depicted in Scheme 5.1; [b] Tabularized temperatures for the first endothermic transition (T_1) and second endothermic transition (T_m) are the local maxima in heatflow during the second heating cycle in the DSC trace using a heating rate of 10 K min⁻¹; [c] corresponding enthalpy of fusion per mole molecule (ΔH_1 and ΔH_m , respectively); [d] **NDI-C8-NDI** showed an addition transition at $T_2 = 229$ °C, $\Delta H_2 = 7$ kJ mol⁻¹; [e] **R-NDI** melts at T_1 and forms a liquid crystalline phase. For this compound, T_m represents the clearing temperature.

5.6 Morphologies observed by X-ray scattering in bulk

To determine the bulk morphologies and corresponding domain spacings, the packing of the NDI bulk materials was investigated by X-ray scattering. Since we were not able to grow single crystals of our compounds, we could not determine the crystal structure by single crystal X-ray crystallography and performed the X-ray scattering study on polycrystalline samples instead. The samples were prepared by placing the NDIs in SAXS capillaries, heating them to the isotropic melt and cooling down slowly. Subsequently, 2D transmission scattering data were acquired in medium- and wide-angle modes (MAXS and WAXS, $0.1 < q < 30 \text{ nm}^{-1}$). Radial averaging resulted in one-dimensional (1D) transmission scattering profiles that captured feature sizes in a range of 0.2 – 60 nm. The scattering profiles of all double NDIs are depicted in Figure 5.10, with the **R-NDI** as a reference. All NDIs exhibited well-structured, lamellar lattices, as indicated by the sharp, equally spaced scattering peaks in the MAXS region (labelled with q^* , $\sqrt{4}q^*$, $\sqrt{9}q^*$, ...). For **NDI-C6-NDI** and **NDI-C8-NDI**, the presence of a second lamellar lattice was noticed. For these two compounds, the sets of scattering peaks were labelled as q^* and q_2^* , respectively. Both sets of reflections remained unaltered after heating the samples again and annealing for several minutes before cooling slowly to room temperature. The lamellar spacings d_{LAM} of all crystal lattices are listed in Table 5.3. The graph in Figure 5.11 shows the variation of d_{LAM} with an increasing length of the alkyl spacer. With **NDI-C8-NDI** being an exception, d_{LAM} was always increased by lengthening the alkyl spacer. Additionally, the increase of d_{LAM} followed an odd-even trend. Until reaching **NDI-C8-NDI**, d_{LAM} was increased noticeably upon the transition from a homologue with an odd number of methylene groups in the alkyl spacer to a homologue with an even parity. In contrast, the transition from a homologue with an even number of methylene groups in the alkyl spacer to a homologue with an odd parity resulted in a small increase of d_{LAM} only. The odd-even effect of d_{LAM} was less apparent for the homologues that succeeded **NDI-C8-NDI**.

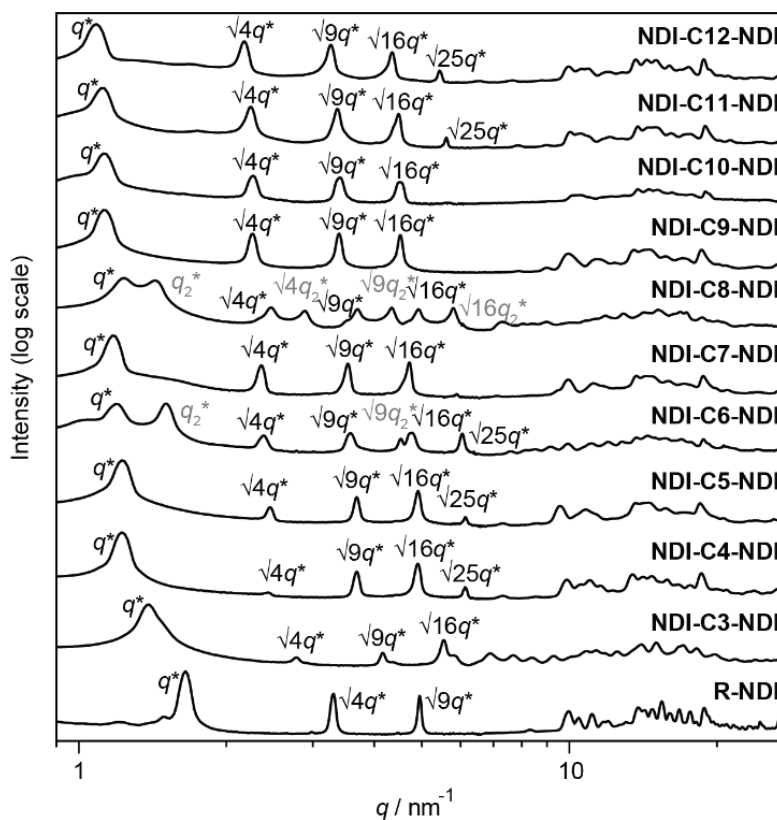


Figure 5.10: 1D transmission scattering profiles obtained for the double NDIs at room temperature.

The scattering peaks at $18.5 - 18.7 \text{ nm}^{-1}$ were indicative of the crystallization of the alkyl chains in the all-*anti* conformation.^[81] The combination of the lamellar morphology and the observed crystalline alkyl chain domains suggested the formation of microphase-segregated 2D sheets that contained alternating crystalline NDI and alkyl lamellae. This type of microphase-segregation has also been described for alkylated single NDIs and was assigned to the formation of van der Waals interactions between the alkyl chains and the aggregation of the NDI cores.^[14,38,58,82] To further probe for the suggested formation of the microphase-segregated NDI and alkyl sheets, we used molecular modelling to calculate the lengths of the NDI-C_xH_{2x}-NDI-C₁₈H₃₇-elements in the fully stretched conformation. The comparison of the calculated values with the experimentally determined d_{LAM} (Table 5.3) shows that d_{LAM} of the first set of reflexes was always very similar but slightly larger than the length of the NDI-C_xH_{2x}-NDI-C₁₈H₃₇-element. Considering that in the crystal, the octadecyl chains were only interdigitated and not covalently linking two NDI cores, the somewhat bigger size of the experimentally determined d_{LAM} was in agreement with the proposed arrangement of the double NDIs in the fully stretched conformation (illustrated

schematically in Figure 5.12a). The second set of reflexes found for **NDI-C6-NDI** and **NDI-C8-NDI** was indicative the formation of a second lamellar lattice stemming from a second crystalline polymorph which interestingly had not been noticed in the DSC traces. When comparing the dimensions of the two lamellar lattices for each derivative, we found noticed that d_{LAM} of the second lattice was approximately 1 nm (1.1 nm for **NDI-C6-NDI** and 0.7 nm for **NDI-C8-NDI**) smaller than d_{LAM} of the first lattice. One possible arrangement that can explain the reduced d_{LAM} and still contains fully stretched terminal alkyl chains was achieved by the backfolding of the second NDI core on the first. The proposed structure of this second crystal polymorph is shown schematically in Figure 5.12b).

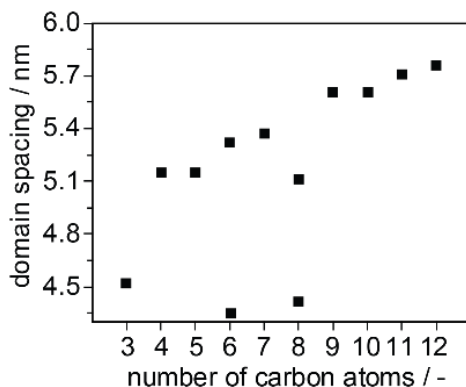


Figure 5.11: Lamellar domain spacing d_{LAM} of double NDIs obtained from X-ray scattering as a function of the number of carbon atoms in the alkyl chain connecting the two NDI motifs. For **NDI-C6-NDI** and **NDI-C8-NDI**, two lamellar structures with different lamellar thickness were observed.

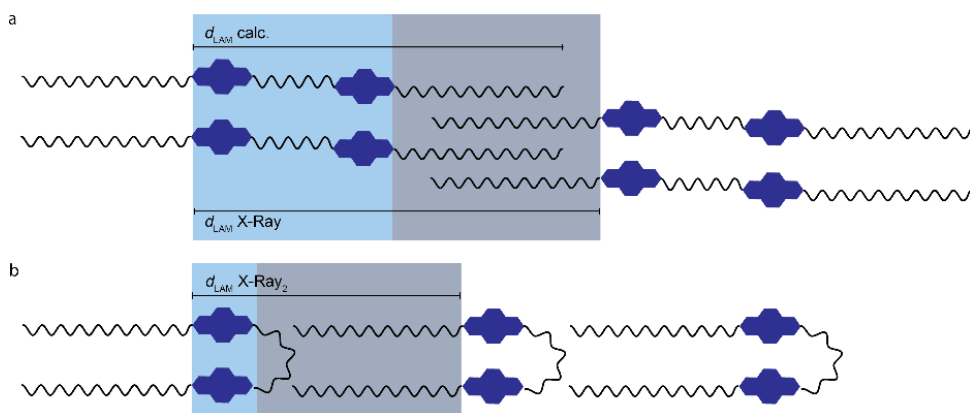


Figure 5.12: (a) Pictorial representations of the molecular packing of NDIs in bulk as a fully stretched and (b) backfolded arrangement.

Subsequently, variable-temperature (VT) X-ray measurements were performed to capture structural transformations that related to the transition observed at T_1 in the DSC traces. **NDI-C11-NDI** was chosen for this type of experiment since it had the lowest melting temperature T_m . A selection of 1D transmission scattering profiles recorded at variable temperatures is depicted in Figure 5.13. When the temperature of the heating element was increased to 260 °C, **NDI-C11-NDI**'s temperature was well above T_1 but still below T_m . In this regime we observed an increase of d_{LAM} from 5.7 nm to 6.0 nm. Furthermore, the scattering peaks in the wide-angle region ($q > 8 \text{ nm}^{-1}$) changed. A third lamellar lattice appeared next to the second lamellar lattice when the heating element that contained the sample was heated to 270 °C. The reflexes of the lattice are labelled by q_3^* and its integer multiples ($\sqrt{4}q_3^*$, $\sqrt{9}q_3^*$...). The corresponding d_{LAM} was increased further to 7.0 nm. At 280 °C, only this third lamellar structure remained. Heating and annealing the sample for a longer period at this temperature induced melting which was accompanied by the scattering peaks in the WAXS region disappearing.

Changes of the scattering peaks in the wide-angle region ($q > 8 \text{ nm}^{-1}$) during heating indicated a transition in the local crystal packing. The successive widening of the lamellar lattice of **NDI-C11-NDI** upon heating was most likely stemming from the aliphatic side chains becoming somewhat mobile. The thermal behavior was in contrast to the thermal rearrangements reported for several alkylated single NDIs where heating was found to induce the formation of more complex crystal structures.^[64] The observed widening of the lamellar lattice was also corroborating the proposed microphase-segregated sheetlike structure. Initially, heating only weakened the cohesion of the octadecyl chain sheets. Strongly aggregated NDI cores retained the 2D sheet morphology and were melted only at higher temperatures.

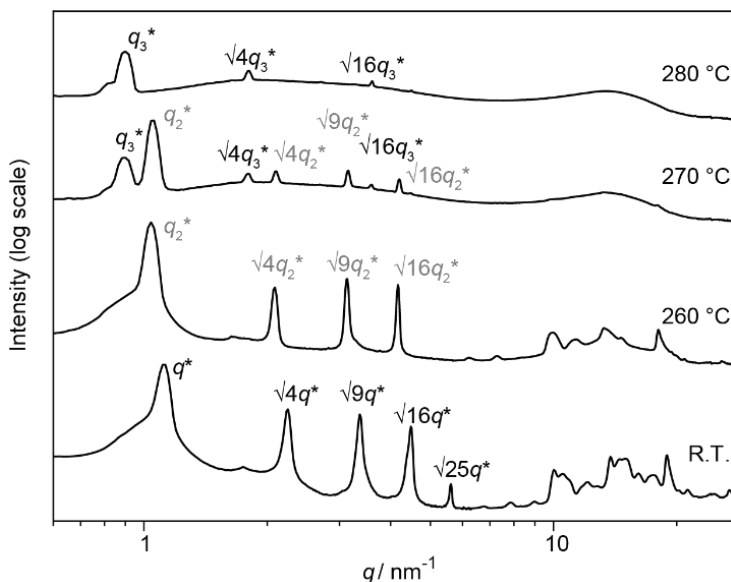


Figure 5.13: 1-D transmission scattering profiles for **NDI-C11-NDI** at various temperatures. The indicated temperatures state the temperature of the heating element and not the temperature of the sample with is presumably lower.

5.7 Comparison of the morphologies formed on surface and in bulk

Although we observed the formation of lamellar phases both on surface and in bulk material, a direct comparison between the structures formed in both media is not straightforward due to the differences in the interactions between the molecules in the two environments.³⁸ The two main differences between the two media are the confined nature of the 2D self-assembly process and the presence of the solid substrate and solvent molecules at the solution-solid interface. These two factors are absent in the bulk crystallization scenario. The ‘structure directing’ effect of the graphite lattice on self-assembled monolayers of alkylated systems is well-documented^[32,83] and was also noticed in the present case. In the conformations that were observed in the self-assembled monolayers, the terminal alkyl chains and possibly also the long alkyl spacers (although not observed clearly in STM images) are always oriented along one of the symmetry axes of the underlying HOPG substrate. Such ‘structure directing’ influence of the substrate is absent in the case of the bulk crystalline phase. The non-collinear adsorption regime observed in monolayers indicated that the molecule-substrate interaction at the level of the single molecule was a dominant factor in the stabilization of the monolayer. Intermolecular interactions such as the van der Waals interactions between the terminal alkyl chains also contribute to the stabilization of the monolayers on the HOPG surface.^[14,38] In the case of bulk crystallization, the van-der-Waals interactions between the alkyl chains and dipolar (π -stacking) interactions between the NDI cores are expected to have a dominant influence on

the structure formation. We note that both these factors were absent in the case of monolayers. The impact of the respective interactions on the size of the structural repeating units in both media can be investigated by comparing d_{LAM} with the unit cell parameter ' b ' on surface. In bulk material, d_{LAM} is always slightly larger than the corresponding $\text{H}_{37}\text{C}_{18}\text{-NDI-C}_x\text{H}_{2x}\text{-NDI}$ -element (Table 5.3) which suggests interdigitated molecules in a fully stretched conformation. The unit cell parameters ' b ' on surface represents the same crystal axis of the lamellar phase in bulk. In contrast to d_{LAM} , ' b ' increases only marginally with an increasing length of the central alkyl chain. When the length of the alkyl spacer is five methylene groups or more, ' b ' becomes even smaller than the corresponding $\text{H}_{37}\text{C}_{18}\text{-NDI-C}_x\text{H}_{2x}\text{-NDI}$ -element. Since a literature report on octadecyl substituted NDIs^[38] and the STM images suggested that the octadecyl chains are stretched out flat, the central alkyl chains have to be partially desorbed to reduce the unit cell along the long axis which is also similar to a system reported by Schwab *et al.*^[78]

Table 5.3: Domain spacings of the lamellar morphologies formed by the double NDIs **NDI-C3-NDI** – **NDI-C12-NDI** as well as **R-NDI** and in bulk and at the 1-phenyloctane/HOPG interface. The length of the double NDI derivatives was also estimated based on the molecular dimensions.

entry	NDI ^[a]	d_{LAM} X-Ray ^[b] [nm]	d_{LAM} calc. ^[c] [nm]	b (STM) [nm]
1	NDI-C3-NDI	4.5	4.2	4.4 ± 0.1
2	NDI-C4-NDI	5.2	4.4	n.d.
3	NDI-C5-NDI	5.2	4.5	4.4 ± 0.1
4	NDI-C6-NDI	5.3 (4.2) ^[d]	4.6	4.4 ± 0.1
5	NDI-C7-NDI	5.4	4.7	4.4 ± 0.1
6	NDI-C8-NDI	5.1 (4.4) ^[d]	4.8	4.6 ± 0.2
7	NDI-C9-NDI	5.6	5.0	4.5 ± 0.1
8	NDI-C10-NDI	5.6	5.1	4.8 ± 0.1
9	NDI-C11-NDI	5.7	5.2	4.7 ± 0.1
10	NDI-C12-NDI	5.8	5.4	4.8 ± 0.1
11	R-NDI	3.8	3.2	n.d.

[a] Molecules as depicted in Scheme 5.1; [b] Lamellar domain spacing of the bulk phase examined with MAXS at room temperature and calculated from $d = 2\pi/q^*$; [c] Length of the $\text{H}_{37}\text{C}_{18}\text{-NDI-C}_x\text{H}_{2x}\text{-NDI}$ -element determined by molecular modelling which is the structural repeating unit as depicted in Figure 5.12; [d] The double lamellar domain spacing was observed. The smaller spacing, which is corresponding to q_2^* (Figure 5.10), is reported in brackets.

5.8 Conclusions

A novel series of ten double NDIs was prepared and their self-assembly was explored on HOPG surfaces and in bulk. All materials (except **NDI-C4-NDI** whose solubility was too low for an investigation) formed self-assembled monolayers on HOPG surface. The monolayers formed by all compounds had a double lamellar morphology in common which stemmed from the double NDIs being arranged in a fully stretched conformation. The investigation of the structural details of the monolayers showed that the adsorption of the terminal octadecyl chains occurred in two modes, namely in the collinear and in the non-collinear orientation. The length of the NDI connecting alkyl chain set the distance between the adsorbed NDI cores which were arranged either in the *syn*- or an *anti*-orientation. Whereas the *syn* orientation was observed for the compounds with an alkyl spacer that was containing three or five methylene groups, an *anti*-orientation was observed for all other derivatives. The unexpected *anti*-orientation of the derivatives with an alkyl spacer containing seven, nine or eleven methylene groups was ascribed to the partial desorption of the spacer. X-ray scattering experiments indicated the formation of lamellar lattices for all compounds in the solid state. Within the lattices, NDI cores and alkyl chains were arranged in alternating 2D sheets. When comparing the domain spacings of the crystalline bulk materials with the unit cells of the monolayers, we observed that the structural repeating units of the surface patterns were always slightly shorter than those of the bulk materials. The discrepancy of the values was relatively small for compounds with a short NDI connecting alkyl chain and increased with an increasing length of the alkyl chain. In congruence with molecular models of the imaged structures, this observation was ascribed to the partial desorption of the central alkyl chain.

Despite the fundamental differences of the interactions inducing the formation of supramolecular structures at the HOPG/1-phenyloctane interface and in bulk material, all presented double NDIs formed structurally similar lamellae in both media. However, subtle differences were identified when investigating the structural details. Whereas the partial desorption of the central alkyl chain was observed for several derivatives on surface, the formation of a second crystalline polymorph was noticed in bulk material. We found that the similarities of the structures formed in both media were decreased when the length of the central alkyl chain was increased. Such an increasing conformational freedom reduces the predictability of the formed structures and needs to be considered when designing multicomponent systems for the generation of functional interfaces. In the following chapter, we will investigate the stepwise formation of multicomponent assemblies on HOPG surface by the addition of mono- and bifunctional electron-rich compounds on top of the NDI double lamellae.

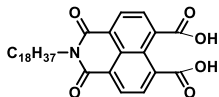
5.9 Experimental Section

5.9.1 Materials and Methods

All chemicals were purchased from commercial sources (TCI Chemicals, Sigma-Aldrich and abcr) and used without further purification. The solvents were purchased and treated as stated in Chapter 2. Silica column purification and chemical characterization (^1H and ^{13}C NMR, FT-IR and MALDI-TOF) was performed on the machines stated in Chapter 2. Samples for polarized optical microscopy (POM) imaging were drop casted on glass coverslips, heated up above the isotropic melt and slowly cooled ($10\text{ }^\circ\text{C}/\text{min}$) prior to the measurement. POM, DSC and SAXS was performed as stated in Chapter 2. The stock solutions used for the optical measurements were prepared by weighing the necessary amount of compound for the given concentration and transferring into a screw-capped vial. The desired concentration was adjusted by the addition of solvent using Gilson™ MICROMANTM Positive-Displacement Pipets. UV/Vis solution measurements were performed using quartz cuvettes with 1 cm optical path. Glass substrates for UV/vis and fluorescence measurements of drop-casted films were cleaned by sonication in AR grade acetone, water and, finally, AR grade i-propanol for 10 min each. The NDIs were deposited by drop casting 5×10^{-3} M CHCl_3 solutions of each compound on top of the clean and dry glass substrates. The solvent was removed by evaporation. UV/Vis spectra of NDI solutions and thin films were recorded on a JASCO V-750 UV/Vis spectrometer. Fluorescence spectroscopy was performed on a Perkin Elmer LS 50 B luminescence spectrometer. STM samples were prepared by applying a drop of the saturated solution of a given double NDI derivative onto a freshly cleaved HOPG surface (HOPG, grade ZYB, Advanced Ceramics Inc., Cleveland, OH) followed by creating a solution flow by touching one corner of the HOPG sample with a clean Kimwipe tissue paper after which the sample was heated at 100°C for 10 minutes. This annealing step led to evaporation of the solvent. Hence a drop of neat solvent was applied to the surface prior to imaging. The STM experiments were carried out using a PicoSPM (Agilent) operating in the constant-current mode with the tip immersed in the solution at room temperature. STM tips were prepared by mechanical cutting from Pt/Ir wire (80%/20%, diameter 0.2 mm). For analysis purposes, the imaging of a molecular layer was immediately followed by recording at a lower bias voltage the graphite lattice, under otherwise identical experimental conditions. The STM images were corrected for drift via Scanning Probe Image Processor (SPIP) software (Image Metrology ApS), using the recorded graphite images for calibration purposes, allowing a more accurate unit cell determination. The unit cell parameters were determined by examining at least 5 images and only the average values are reported. After the determination of the unit cell from the acquired STM images, a molecular model of the observed monolayer was constructed using HyperChem™ Professional 8.0.1 program. First, a molecular model for a single molecule was built. The model of the entire monolayer was constructed by placing the molecules in accordance with the unit cell parameters obtained from the analysis of the calibrated STM images. The imaging parameters are indicated in the figure caption: tunneling current (I_{set}), and sample bias (V_{bias}).

5.9.2 Synthetic procedures

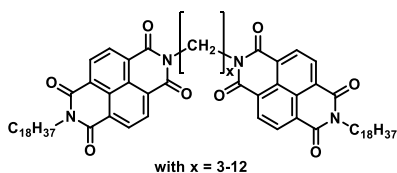
Synthesis of 2-octadecyl-1,3-dioxo-2,3-dihydro-1H-benzo[de]isoquinoline-6,7-dicarboxylic acid (NMI)



1,4,5,8-Naphthalenetetracarboxylic dianhydride (1.80 g, 6.7 mmol, 2.5 eq.) and octadecylamine (0.72 g, 2.7 mmol, 1 eq.) were suspended in 12 mL DMF and 10 mL THF. The mixture was sonicated for 3 minutes. A microwave reactor was used to heat the mixture to 75 °C. The temperature was held for 5 min and subsequently increased to 140 °C. After the temperature had been held for another 5 min, the reaction mixture was allowed to cool down to room temperature again. The mixture was added to 150 mL 1 M aqueous NaOH solution. The mixture was filtered and the filter cake was dispersed in 100 mL 1 M HCl. A second filtration and subsequent drying afforded a beige solid that was used without further purification. 2-Octadecyl-1,3-dioxo-2,3-dihydro-1H-benzo[de]isoquinoline-6,7-dicarboxylic acid was obtained in 95% yield (1.38 g, 2.6 mmol).

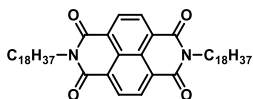
FT-IR (cm⁻¹): 2917 (s), 2849 (s), 1703 (s), 1655 (s), 1582 (w), 1519 (w), 1452 (m), 1389 (w), 1348 (s), 1271 (m), 1256 (m), 1242 (m), 1155 (w), 1091 (m), 1026 (w), 944 (w), 877 (w), 831 (w), 805 (w), 766 (s), 720 (m), 689 (w), 644 (w), 594 (w), 561 (w), 483 (w), 429 (m).

Synthesis of the double NDIs NDI-C3-NDI - NDI-C12-NDI



2-Octadecyl-1,3-dioxo-2,3-dihydro-1H-benzo[de]isoquinoline-6,7-dicarboxylic acid **1** and a diamine (the scope of substrates was 1,3-diaminopropane to 1,12-diaminododecane) were suspended in 12 mL DMF and 10 mL THF. The exact amounts of the used materials for the individual reactions are given in Table 4.4. The mixture was sonicated for 3 minutes. A microwave reactor was used to heat the mixture to 75 °C. The temperature was held for 5 min and subsequently increased to 140 °C. After the temperature had been held for another 25 min, the reaction mixture was allowed to cool down to room temperature again. The mixture was added to 150 mL water and filtration was performed. The filter cake was dried and recrystallized from chloroform. In case of 1,3-diaminopropane, recrystallization was performed from toluene. All compounds were obtained as beige solids.

Synthesis of 2,7-dioctadecylbenzo[Imn][3,8]phenanthroline-1,3,6,8(2H,7H)-tetraone (R-NDI)



1,4,5,8-Naphthalenetetracarboxylic dianhydride (0.6 g, 2.2 mmol, 1 eq.) and octadecylamine (1.2 g, 4.5 mmol, 2 eq.) were suspended in 12 mL DMF and 10 mL THF. The mixture was sonicated for 3 minutes. A microwave reactor was used to heat the mixture to 75 °C. The temperature was held for 5 min and subsequently increased to 140 °C. After the temperature had been held for further 25 min, the reaction mixture was allowed to cool down to room temperature again. The mixture was added to 150 mL 1 M aqueous NaOH solution. Filtration afforded a beige solid that was recrystallized from toluene. 2,7-dioctadecylbenzo[Imn][3,8]phenanthroline-1,3,6,8(2H,7H)-tetraone was obtained in 86% yield (1.47 g, 1.9 mmol).

Table 5.4: Overview over the amounts of substance used for the synthesis of **NDI-C3-NDI** - **NDI-C12-NDI** as well as the isolated yields.

No	NDI	Amount of 3	Used amine	Amount of amine	yield
1	NDI-C3-NDI	814 mg (1.5 mmol, 2.1 eq.)	1,3-Diaminopropane	53 mg (0.72 mmol, 1 eq.)	291 mg (0.27 mmol, 38%)
2	NDI-C4-NDI	600 mg (1.1 mmol, 2.1 eq.)	1,4-Diaminobutane	46 mg (0.53 mmol, 1 eq.)	203 mg (0.18 mmol, 35%)
3	NDI-C5-NDI	600 mg (1.1 mmol, 2.1 eq.)	1,5-Diaminopentane	54 mg (0.53 mmol, 1 eq.)	476 mg (0.43 mmol, 81%)
4	NDI-C6-NDI	1 g (1.86 mmol, 2 eq.)	1,6-Diaminohexane	108 mg (0.84 mmol, 1 eq.)	565 mg (0.50 mmol, 60%)
5	NDI-C7-NDI	700 mg (1.3 mmol, 2.1 eq.)	1,7-Diaminoheptane	80 mg (0.6 mmol, 1 eq.)	415 mg (0.37 mmol, 61%)
6	NDI-C8-NDI	700 mg (1.3 mmol, 2.1 eq.)	1,8-Diaminooctane	98 mg (0.6 mmol, 1 eq.)	240 mg (0.21 mmol, 34%)
7	NDI-C9-NDI	600 mg (1.1 mmol, 2 eq.)	1,9-Diaminononane	88 mg (0.6 mmol, 1 eq.)	442 mg (0.38 mmol, 62%)
8	NDI-C10-NDI	651 mg (1.2 mmol, 2.1 eq.)	1,10-Diaminodecane	99 mg (0.6 mmol, 1 eq.)	425 mg (0.36 mmol, 60%)
9	NDI-C11-NDI	620 mg (1.2 mmol, 2.1 eq.)	1,11-Diaminoundecane	102 mg (0.6 mmol, 1 eq.)	434 mg (0.36 mmol, 66%)
10	NDI-C12-NDI	600 mg (1.1 mmol, 2 eq.)	1,12-Diaminododecane	111 mg (0.6 mmol, 1 eq.)	423 mg (0.35 mmol, 58%)

Chemical characterization of all NDIs:

NDI-C3-NDI: ^1H NMR (500 MHz, TCE- d_2) δ [ppm] = 8.74 (q, J = 7.6 Hz, 8H), 4.41 (t, J = 7.1 Hz, 4H), 4.23 (t, J = 7.1 Hz, 4H), 2.35 (p, J = 7.4 Hz, 2H), 1.80 (p, J = 7.3 Hz, 4H), 1.32 (s, 60H), 0.93 (t, J = 6.8 Hz, 6H).

^{13}C NMR (126 MHz, TCE- d_2): δ [ppm] = 162.65, 162.45, 130.72, 130.58, 126.72, 126.56, 126.32, 40.88, 38.61, 32.99, 29.45, 29.43, 29.40, 29.38, 29.35, 29.31, 29.06, 27.95, 26.94, 26.57, 22.42, 16.25. MALDI/TOF found 1076.70 m/z (calculated 1077.46). FT-IR: 2956 (w), 2920 (s), 2850 (m), 1703 (m), 1661 (s), 1581 (m), 1455 (m), 1383 (m), 1345 (s), 1270 (w), 1250 (s), 1220 (w), 1161 (m), 1089 (m), 1061 (m), 960 (w), 891 (m), 809 (w), 770 (s), 720 (m), 711 (w), 614 (w), 563 (m), 439 (m), 427 (m).

NDI-C4-NDI: ^1H NMR (500 MHz, TCE- d_2): δ [ppm] = 8.76 (s, 8H), 4.32 (t, J = 7.6 Hz, 4H), 4.23 (t, J = 7.6 Hz, 4H), 1.91 – 1.25 (m, 68H), 0.94 (d, J = 7.0 Hz, 6H).⁴ MALDI/TOF found 1090.72 m/z (calculated 1090.68). FT-IR: 2955 (w), 2919 (s), 2847 (m), 1704 (m), 1654 (s), 1581 (m), 1463 (m), 1454 (m), 1376 (m), 1337 (s), 1269 (s), 1242 (s), 1160 (m), 1087 (m), 977 (m), 889 (m), 807 (w), 769 (s), 723 (m), 617 (w), 565 (m).

NDI-C5-NDI: ^1H NMR (500 MHz, TCE- d_2): δ [ppm] = 8.78 – 8.69 (m, 8H), 4.23 (t, J = 7.4 Hz, 4H), 4.22 (t, J = 7.4 Hz, 4H), 1.91 (p, J = 7.8 Hz, 4H), 1.80 (p, J = 7.6 Hz, 4H), 1.62 (p, J = 7.8 Hz, 2H), 1.31 (s, 60H), 0.93 (t, J = 6.7 Hz, 6H). ^{13}C NMR (126 MHz, TCE- d_2): δ [ppm] = 162.58, 162.50, 130.66, 130.59, 126.61, 126.47, 48.88, 45.18, 29.45, 29.41, 29.31, 29.11, 29.07, 27.95, 27.58, 22.42, 13.85. MALDI/TOF found 1104.73 m/z (calculated 1104.69). FT-IR: 2919 (s), 2847 (m), 1703 (m), 1654 (s), 1581 (m), 1455 (m), 1375 (m), 1332 (s), 1244 (s), 1196 (w), 1154 (w), 1090 (w), 1075 (m), 975 (m), 889 (m), 808 (w), 768 (s), 723 (m), 612 (w), 599 (m), 566 (m).

NDI-C6-NDI: ^1H NMR (500 MHz, TCE- d_2) δ [ppm] = 8.75 (s, 8H), 4.23 (t, J = 7.4 Hz, 4H), 4.22 (t, J = 7.4 Hz, 4H), 1.88 – 1.74 (m, 12H), 1.31 (s, 60H), 0.93 (t, J = 6.8 Hz, 6H).

^{13}C NMR (126 MHz, TCE- d_2) δ [ppm] = 162.58, 162.54, 130.67, 130.63, 126.86, 126.60, 126.51, 40.90, 35.56, 31.69, 29.46, 29.44, 29.42, 29.37, 29.32, 29.11, 29.09, 27.96, 27.81, 26.94, 26.56, 23.09, 22.44, 18.58, 13.86. MALDI/TOF

⁴ The solubility of **NDI-C4-NDI** was too low to obtain ^{13}C nuclear magnetic resonance spectra.

Tuning the pitch of *N,N'*-bis(*n*-alkyl)-naphthalenediimide double lamellae

found 1118.79 m/z (calculated 1118.71). FT-IR: 2919 (s), 2847 (m), 1703 (m), 1655 (s), 1581 (m), 1454 (m), 1374 (m), 1338 (s), 1329 (s), 1251 (s), 1157 (m), 1086 (m), 1015 (w), 993 (m), 965 (w), 890 (m), 807 (w), 768 (s), 724 (m), 609 (w), 568 (m), 439 (m), 425 (m).

NDI-C7-NDI: ^1H NMR (500 MHz, TCE-*d*₂): δ [ppm] = 8.76 (s, 8H), 4.23 (t, *J* = 7.6 Hz, 8H), 1.81 (h, *J* = 8.0, 7.2 Hz, 8H), 1.55 – 1.24 (m, 66H), 0.93 (t, *J* = 6.8 Hz, 6H). ^{13}C NMR (126 MHz, TCE-*d*₂): δ [ppm] = 162.56, 162.54, 130.65, 130.62, 126.58, 126.52, 40.87, 40.73, 31.69, 29.46, 29.44, 29.42, 29.37, 29.32, 29.11, 29.09, 28.72, 27.96, 27.83, 26.94, 26.73, 22.44, 13.86. MALDI/TOF found 1132.79 m/z (calculated 1133.57). FT-IR: 2919 (s), 2848 (m), 1704 (m), 1654 (s), 1581 (m), 1455 (m), 1374 (m), 1333 (s), 1257 (w), 1243 (s), 1185 (w), 1154 (w), 1082 (m), 998 (w), 969 (w), 890 (m), 807 (w), 768 (s), 723 (m), 609 (w), 566 (m), 422 (m).

NDI-C8-NDI: ^1H NMR (500 MHz, TCE-*d*₂): δ [ppm] = 8.77 (s, 8H), 4.22 (t, *J* = 7.5 Hz, 8H), 1.80 (br, 8H), 1.58 – 1.25 (m, 68H), 0.93 (t, *J* = 6.8 Hz, 6H). ^{13}C NMR (126 MHz, TCE-*d*₂): δ [ppm] = 162.55, 130.65, 126.54, 31.69, 29.46, 29.44, 29.42, 29.37, 29.32, 29.11, 29.09, 28.94, 26.94, 26.82, 22.98, 22.22, 13.86.

MALDI/TOF found 1146.75 m/z (calculated 1146.74). FT-IR: 2920 (m), 2850 (s), 1702 (m), 1657 (s), 1582 (m), 1455 (m), 1376 (m), 1338 (s), 1283 (w), 1245 (s), 1182 (w), 1157 (w), 1085 (m), 1018 (w), 967 (w), 890 (m), 809 (w), 768 (s), 724 (m), 607 (w), 565 (m), 421 (m).

NDI-C9-NDI: ^1H NMR (500 MHz, TCE-*d*₂): δ [ppm] = 8.76 (s, 8H), 4.22 (t, *J* = 7.4 Hz, 8H), 1.80 (p, *J* = 7.5 Hz, 8H), 1.51 – 1.25 (m, 70H), 0.93 (t, *J* = 6.7 Hz, 6H). ^{13}C NMR (126 MHz, TCE-*d*₂): δ [ppm] = 162.54, 130.63, 126.56, 40.80, 31.69, 29.46, 29.44, 29.42, 29.37, 29.32, 29.11, 29.09, 28.93, 27.96, 27.88, 26.93, 26.83, 22.44, 13.86. MALDI/TOF found 1160.84 m/z (calculated 1160.75). FT-IR: 2919 (m), 2848 (s), 1705 (m), 1655 (s), 1581 (m), 1455 (m), 1374 (m), 1333 (s), 1271 (w), 1243 (s), 1181 (w), 1154 (w), 1084 (m), 972 (w), 889 (m), 808 (w), 768 (s), 723 (m), 608 (w), 565 (m), 419 (m).

NDI-C10-NDI: ^1H NMR (500 MHz, TCE-*d*₂): δ [ppm] = 8.76 (s, 8H), 4.22 (t, *J* = 7.5 Hz, 8H), 1.80 (p, *J* = 7.6 Hz, 8H), 1.51 – 1.26 (m, 72H), 0.93 (d, *J* = 6.8 Hz, 6H). ^{13}C NMR (126 MHz, TCE-*d*₂): δ [ppm] = 162.55, 130.63, 126.56, 40.87, 40.83, 31.69, 29.46, 29.44, 29.42, 29.37, 29.32, 29.17, 29.11, 29.09, 29.01, 27.95, 27.92, 26.94, 26.87, 22.44, 13.86. MALDI/TOF found 1174.82 m/z (calculated 1175.65). FT-IR: 2920 (m), 2848 (s), 1705 (m), 1656 (s), 1581 (m), 1455 (m), 1374 (m), 1347 (m), 1338 (m), 1243 (s), 1220 (w), 1155 (m), 1087 (m), 1058 (w), 1021 (w), 970 (m), 889 (m), 769 (s), 723 (m), 609 (m), 566 (m), 439 (m), 417 (m).

NDI-C11-NDI: ^1H NMR (500 MHz, TCE-*d*₂): δ [ppm] = 8.76 (s, 8H), 4.22 (t, *J* = 7.4 Hz, 8H), 1.80 (p, *J* = 7.4 Hz, 8H), 1.51 – 1.26 (m, 74H), 0.93 (t, *J* = 6.8 Hz, 6H). ^{13}C NMR (126 MHz, TCE-*d*₂): δ [ppm] = 162.54, 130.63, 126.55, 40.85, 31.69, 29.46, 29.42, 29.37, 29.32, 29.20, 29.11, 29.09, 29.02, 27.95, 27.93, 26.94, 26.89, 22.44, 13.86. MALDI/TOF found 1188.82 m/z (calculated 1188.82). FT-IR: 2919 (m), 2848 (s), 1704 (m), 1654 (s), 1581 (m), 1454 (m), 1374 (m), 1346 (m), 1333 (m), 1257 (m), 1243 (s), 1220 (w), 1154 (m), 1084 (m), 1066 (w), 1025 (w), 969 (m), 889 (m), 768 (s), 723 (m), 607 (m), 566 (m), 439 (m), 413 (m).

NDI-C12-NDI: ^1H NMR (500 MHz, TCE-*d*₂): δ [ppm] = 8.76 (s, 8H), 4.22 (t, *J* = 7.4 Hz, 8H), 1.80 (p, *J* = 7.1 Hz, 8H), 1.51 – 1.24 (m, 76H), 0.93 (t, *J* = 6.9 Hz, 6H). ^{13}C NMR (126 MHz, TCE-*d*₂): δ [ppm] = 162.54, 130.63, 126.55, 40.86, 31.69, 29.46, 29.44, 29.42, 29.37, 29.32, 29.27, 29.23, 29.11, 29.09, 29.06, 27.95, 27.93, 26.93, 26.91, 22.44, 13.86. MALDI/TOF found 1202.89 m/z (calculated 1202.89). FT-IR: 2920 (m), 2848 (s), 1705 (m), 1656 (s), 1581 (m), 1455 (m), 1374 (m), 1348 (m), 1333 (m), 1258 (m), 1243 (m), 1219 (w), 1155 (m), 1087 (m), 1071 (w), 1030 (w), 971 (m), 890 (m), 769 (s), 724 (m), 608 (m), 567 (m), 439 (m), 409 (m).

R-NDI: ^1H NMR (500 MHz, TCE-*d*₂): δ [ppm] = 8.76 (s, 4H), 4.22 (t, *J* = 7.5 Hz, 4H), 1.80 (p, *J* = 7.4 Hz, 4H), 1.31 (s, 60H), 0.93 (t, *J* = 6.8 Hz, 6H). ^{13}C NMR (126 MHz, TCE-*d*₂): δ [ppm] = 162.53, 130.61, 126.56, 40.86, 33.00, 31.68, 29.45, 29.41, 29.36, 29.31, 29.08, 27.95, 26.93, 22.42, 13.83. MALDI/TOF found 770.60 m/z (calculated 770.66). FT-IR: 2955 (w), 2918 (s), 2847 (m), 1704 (m), 1655 (s), 1581 (m), 1462 (m), 1455 (m), 1373 (m), 1348 (m), 1331 (m), 1244 (s), 1220 (w), 1154 (m), 1086 (m), 1073 (m), 970 (w), 890 (m), 769 (s), 724 (s), 710 (w), 607 (m), 566 (m), 439 (m), 423 (m).

5.10 References

- [1] D. P. Goronzy, M. Ebrahimi, F. Rosei, Arramel, Y. Fang, S. De Feyter, S. L. Tait, C. Wang, P. H. Beton, A. T. S. Wee, P. S. Weiss, D. F. Perepichka, *ACS Nano* **2018**, *12*, 7445.
- [2] K. S. Mali, N. Pearce, S. De Feyter, N. R. Champness, *Chem. Soc. Rev.* **2017**, *46*, 2520.

- [3] A. G. Slater, P. H. Beton, N. R. Champness, *Chem. Sci.* **2011**, *2*, 1440.
- [4] M. T. Räisänen, F. Mögele, S. Feodorow, B. Rieger, U. Ziener, M. Leskelä, T. Repo, *Eur. J. Inorg. Chem.* **2007**, 4028.
- [5] M. A. Van Hove, *Catal. Today* **2006**, *113*, 133.
- [6] J. A. A. W. Elemans, S. Lei, S. De Feyter, *Angew. Chem. Int. Ed.* **2009**, *48*, 7298.
- [7] A. Ringk, X. Li, F. Gholamrezaie, E. C. P. Smits, A. Neuhold, A. Moser, C. Van Der Marel, G. H. Gelinck, R. Resel, D. M. De Leeuw, P. Strohriegel, *Adv. Funct. Mater.* **2013**, *23*, 2016.
- [8] E. C. P. Smits, S. G. J. Mathijssen, P. A. Van Hal, S. Setayesh, T. C. T. Geuns, K. A. H. A. Mutsaers, E. Cantatore, H. J. Wondergem, O. Werzer, R. Resel, M. Kemerink, S. Kirchmeyer, A. M. Muzafarov, S. A. Ponomarenko, B. De Boer, P. W. M. Blom, D. M. De Leeuw, *Nature* **2008**, *455*, 956.
- [9] A. M. Andringa, M. J. Spijkman, E. C. P. Smits, S. G. J. Mathijssen, P. A. van Hal, S. Setayesh, N. P. Willard, O. V. Borschhev, S. A. Ponomarenko, P. W. M. Blom, D. M. de Leeuw, *Org. Electron.* **2010**, *11*, 895.
- [10] S. Casalini, C. A. Bortolotti, F. Leonardi, F. Biscarini, *Chem. Soc. Rev.* **2017**, *46*, 40.
- [11] J. W. Lathrop, *IEEE Ann. Hist. Comput.* **2013**, *35*, 48.
- [12] H. E. Katz, J. Huang, *Annu. Rev. Mater. Res.* **2009**, *39*, 71.
- [13] B. K. Pathem, S. A. Claridge, Y. B. Zheng, P. S. Weiss, *Annu. Rev. Phys. Chem.* **2013**, *64*, 605.
- [14] J. A. Berrocal, G. H. Heideman, B. F. M. De Waal, M. Enache, R. W. A. Havenith, M. Stöhr, E. W. Meijer, B. L. Feringa, *J. Am. Chem. Soc.* **2020**, *142*, 4070.
- [15] J.-M. Lehn, *Angew. Chem. Int. Ed.* **1990**, *29*, 1304.
- [16] P. N. Dickerson, A. M. Hibberd, N. Oncel, S. L. Bernasek, *Langmuir* **2010**, *26*, 18155.
- [17] J. L. Atwood, L. J. Barbour, M. W. Heaven, C. L. Raston, *Angew. Chem. Int. Ed.* **2003**, *42*, 3254.
- [18] E. R. McNellis, J. Meyer, K. Reuter, *Phys. Rev. B - Condens. Matter Mater. Phys.* **2009**, *80*, 1.
- [19] J. Sauer, P. Ugliengo, E. Garrone, V. R. Saunders, *Chem. Rev.* **1994**, *94*, 2095.
- [20] B. Feringán, P. Romero, J. L. Serrano, C. L. Folcia, J. Etxebarria, J. Ortega, R. Termine, A. Golemme, R. Giménez, T. Sierra, *J. Am. Chem. Soc.* **2016**, *138*, 12511.
- [21] J. V. Barth, J. Weckesser, C. Cai, P. Günter, L. Bürgi, O. Jeandupeux, K. Kern, *Angew. Chem. Int. Ed.* **2000**, *39*, 1230.
- [22] A. G. Slater, L. M. A. Perdigão, P. H. Beton, N. R. Champness, *Acc. Chem. Res.* **2014**, *47*, 3417.
- [23] H. Zhou, H. Dang, J. H. Yi, A. Nanci, A. Rochefort, J. D. Wuest, *J. Am. Chem. Soc.* **2007**, *129*, 13774.
- [24] S. Griessl, M. Lackinger, M. Edelwirth, M. Hietschold, W. M. Heckl, *Single Mol.* **2002**, *3*, 25.
- [25] J. Van Esch, S. De Feyter, R. M. Kellogg, F. De Schryver, B. L. Feringa, *Chem. E* **1997**, 1238.
- [26] S. De Feyter, P. C. M. Grim, J. Van Esch, R. M. Kellogg, B. L. Feringa, F. C. De Schryver, *J. Phys. Chem. B* **1998**, *102*, 8981.
- [27] R. Gutzler, C. Fu, A. Davvand, Y. Hua, J. M. MacLeod, F. Rosei, D. F. Perepichka, *Nanoscale* **2012**, *4*, 5965.
- [28] J. K. Yoon, W. J. Son, K. H. Chung, H. Kim, S. Han, S. J. Kahng, *J. Phys. Chem. C* **2011**, *115*, 2297.
- [29] S. Vijayaraghavan, D. Ecija, W. Auwärter, S. Joshi, K. Seufert, M. Drach, D. Nieckarz, P. Szabelski, C. Aurisicchio, D. Bonifazi, J. V. Barth, *Chem. Eur. J.* **2013**, *19*, 14143.
- [30] G. De Ruiter, M. Lahav, M. E. Van Der Boom, *Acc. Chem. Res.* **2014**, *47*, 3407.
- [31] S. Stepanow, M. Lingenfelder, A. Dmitriev, H. Spillmann, E. Delvigne, N. Lin, X. Deng, C. Cai, J. V. Barth, K. Kern, *Nat. Mater.* **2004**, *3*, 229.
- [32] B. Ilan, G. M. Florio, M. S. Hybertsen, B. J. Berne, G. W. Flynn, *Nano Lett.* **2008**, *8*, 3160.
- [33] S. L. Lee, C. Y. J. Chi, M. J. Huang, C. H. Chen, C. W. Li, K. Pati, R. S. Liu, *J. Am. Chem. Soc.* **2008**, *130*, 10454.
- [34] G. Binnig, C. F. Quate, *Phys. Rev. Lett.* **1986**, *56*, 930.
- [35] J. M. Topple, S. A. Burke, S. Fostner, P. Grütter, *Phys. Rev. B - Condens. Matter Mater. Phys.* **2009**, *79*, 1.
- [36] G. Binnig, H. Rohrer, *IBM J. Res. Dev.* **1986**, *30*, 355.
- [37] A. M. Sweetman, S. P. Jarvis, H. Sang, I. Lekkas, P. Rahe, Y. Wang, J. Wang, N. R. Champness, L. Kantorovich, P. Moriarty, *Nat. Commun.* **2014**, *5*, DOI 10.1038/ncomms4931.
- [38] Y. Miyake, T. Nagata, H. Tanaka, M. Yamazaki, M. Ohta, R. Kokawa, T. Ogawa, *ACS Nano* **2012**, *6*, 3876.
- [39] T. Chen, Q. Chen, G. B. Pan, L. J. Wan, Q. L. Zhou, R. Ben Zhang, *Chem. Commun.* **2009**, 2649.
- [40] J. A. J. A. Berrocal, J. Teyssandier, O. J. G. M. G. M. Goor, S. De Feyter, E. W. Meijer, S. De Feyter, E. W. Meijer, *Chem. Mater.* **2018**, *30*, 3372.
- [41] F. Tao, S. L. Bernasek, *Chem. Rev.* **2007**, *107*, 1408.
- [42] H. Fang, L. C. Giancarlo, G. W. Flynn, *J. Phys. Chem. B* **1998**, *102*, 7421.
- [43] P. J. M. Stals, M. M. J. Smulders, R. Martín-Rapún, A. R. A. Palmans, E. W. Meijer, *Chem. Eur. J.* **2009**, *15*, 2071.
- [44] H. Zhang, Q. Yin, Z. Liu, J. Gong, Y. Bao, M. Zhang, H. Hao, B. Hou, C. Xie, *J. Chem. Thermodyn.* **2014**, *77*,

- 91.
- [45] A. Blumstein, O. Thomas, *Macromolecules* **1982**, *15*, 1264.
- [46] S. Yang, X. Xu, Y. Zhu, R. Niu, C. Xu, Y. Peng, X. Cheng, X. Jia, X. Xu, J. Lu, Y. Ye, *Phys. Rev. X* **2021**, *11*, 011003.
- [47] F. Ben Amara, E. R. Dionne, S. Kassir, C. Pellerin, A. Badia, **2020**, DOI 10.1021/jacs.0c04288.
- [48] K. Yang, Z. Cai, A. Jaiswal, M. Tyagi, J. S. Moore, Y. Zhang, *Angew. Chem. Int. Ed.* **2016**, *55*, 14090.
- [49] "Boiling points and structures of hydrocarbons," can be found under <http://chemistry.elmhurst.edu/vchembook/501hcboilingpts.html>, **2020**.
- [50] V. R. Thalladi, R. Boese, H. C. Weiss, *J. Am. Chem. Soc.* **2000**, *122*, 1186.
- [51] K. Kim, K. E. Plass, A. J. Matzger, *J. Am. Chem. Soc.* **2005**, *127*, 4879.
- [52] M. D. Alba, M. A. Castro, S. Clarke, S. Medina, L. Messe, C. Millán, M. M. Orta, A. C. Perdígón, *J. Phys. Chem. C* **2009**, *113*, 3176.
- [53] X. Wang, S. Y. Lee, K. Miller, R. Welbourn, I. Stocker, S. Clarke, M. Casford, P. Gutfreund, M. W. A. Skoda, *Langmuir* **2013**, *29*, 5520.
- [54] Z. P. L. Laker, A. J. Marsden, O. De Luca, A. Della Pia, L. M. A. Perdígão, G. Costantini, N. R. Wilson, *Nanoscale* **2017**, *9*, 11959.
- [55] M. A. Castro, S. M. Clarke, A. Inaba, C. C. Dong, R. K. Thomas, *J. Phys. Chem. B* **1998**, *102*, 777.
- [56] K. W. Herwig, B. Matthies, H. Taub, *Phys. Rev. Lett.* **1995**, *75*, 3154.
- [57] S. Labat, C. Guichet, O. Thomas, B. Gilles, A. Marty, *Appl. Surf. Sci.* **2002**, *188*, 182.
- [58] X. Jiao, S. Maniam, S. J. Langford, C. R. McNeill, *Phys. Rev. Mater.* **2019**, *3*, 1.
- [59] C. Fu, H. P. Lin, J. M. Macleod, A. Krayev, F. Rosei, D. F. Perepichka, *Chem. Mater.* **2016**, *28*, 951.
- [60] Y. Kaneda, M. E. Stawasz, D. L. Sampson, B. A. Parkinson, *Langmuir* **2001**, *17*, 6185.
- [61] J. Hak, S. Sabin-Lucian, W. Y. Lee, M. Könemann, H. W. Höffken, C. Röger, R. Schmidt, Y. Chung, W. C. Chen, F. Würthner, Z. Bao, *Adv. Funct. Mater.* **2010**, *20*, 2148.
- [62] M. Al Kobaisi, S. V. S. V. Bhosale, K. Latham, A. M. Raynor, S. V. S. V. Bhosale, *Chem. Rev.* **2016**, *116*, 11685.
- [63] T. D. M. Bell, S. V. Bhosale, C. M. Forsyth, D. Hayne, K. P. Ghiggino, J. A. Hutchison, C. H. Jani, S. J. Langford, M. A. P. Lee, C. P. Woodward, *Chem. Commun.* **2010**, *46*, 4881.
- [64] S. Milita, F. Liscio, L. Cowen, M. Cavallini, B. A. Drain, T. Degousée, S. Luong, O. Fenwick, A. Guagliardi, B. C. Schroeder, N. Masciocchi, *J. Mater. Chem. C* **2020**, *8*, 3097.
- [65] J. A. Berrocal, R. H. Zha, B. F. M. De Waal, J. A. M. Luggier, M. Lutz, E. W. Meijer, *ACS Nano* **2017**, *11*, 3733.
- [66] A. Dey, A. Kalita, P. K. Iyer, *ACS Appl. Mater. Interfaces* **2014**, *6*, 12295.
- [67] T. Kakinuma, H. Kojima, M. Ashizawa, H. Matsumoto, T. Mori, *J. Mater. Chem. C* **2013**, *1*, 5395.
- [68] Z. Ma, H. Geng, D. Wang, Z. Shuai, *J. Mater. Chem. C* **2016**, *4*, 4546.
- [69] B. A. Jones, A. Facchetti, M. R. Wasielewski, T. J. Marks, *J. Am. Chem. Soc.* **2007**, *129*, 15259.
- [70] B. Baumgartner, A. Svirikova, J. Bintinger, C. Hametner, M. Marchetti-Deschmann, M. M. Unterlass, *Chem. Commun.* **2017**, *53*, 1229.
- [71] K. Tambara, N. Nonnuswamy, G. Hennrich, G. D. Pantoş, *J. Org. Chem.* **2011**, *76*, 3338.
- [72] M. B. Avinash, T. Govindaraju, *Nanoscale* **2011**, *3*, 2536.
- [73] F. Fennel, J. Gershberg, M. Stolte, F. Würthner, *Phys. Chem. Chem. Phys.* **2018**, *20*, 7612.
- [74] F. Hirayama, *J. Chem. Phys.* **1965**, *42*, 3163.
- [75] F. Mendicuti, B. Patel, W. L. Mattice, *Polymer* **1990**, *31*, 453.
- [76] F. Mendicuti, E. Saiz, I. Zúñiga, B. Patel, W. L. Mattice, *Polymer* **1992**, *33*, 2031.
- [77] F. Mendicuti, E. Saiz, W. L. Mattice, *J. Polym. Sci. Part B Polym. Phys.* **1993**, *31*, 213.
- [78] M. G. Schwab, M. Takase, A. Mavrinsky, W. Pisula, X. Feng, J. A. Gámez, W. Thiel, K. S. Mali, S. De Feyter, K. Müllen, *Chem. Eur. J.* **2015**, *21*, 8426.
- [79] R. J. Chesterfield, J. C. McKeen, C. R. Newman, P. C. Ewbank, D. A. Da Silva Filho, J. L. Brédas, L. L. Miller, K. R. Mann, C. D. Frisbie, *J. Phys. Chem. B* **2004**, *108*, 19281.
- [80] M. Ichikawa, Y. Yokota, H. G. Jeon, G. D. R. Banoukepa, N. Hirata, N. Oguma, *Org. Electron.* **2013**, *14*, 516.
- [81] B. Van Genabeek, B. F. M. De Waal, A. R. A. Palmans, E. W. Meijer, *Polym. Chem.* **2018**, *9*, 2746.
- [82] J. Park, S. H. Lee, M. Y. Choi, C. J. Moon, T. H. Kim, *Acta Crystallogr. Sect. E Crystallogr. Commun.* **2019**, *75*, 934.
- [83] A. J. Groszecz, *Proc. R. Soc. A* **1970**, *314*, 473.

Chapter 6

Stepwise formation of charge transfer complexes at the 1-phenyloctane/HOPG interface

Abstract:

The generation of highly ordered multicomponent architectures on surfaces by the stepwise addition of supramolecular building blocks is currently a hot topic in the field of nanotechnology and expected to bring tremendous innovation to microelectronics. Since we have shown in Chapter 5 that our electron accepting (A) double naphthalenediimides (NDIs) form highly regular double lamellar structures on highly oriented pyrolytic graphite (HOPG) surface, we aim for decorating these monolayers with electron donating chromophores (D). We present a library of D molecules to investigate the formation of charge transfer (CT) complexes by the co-adsorption with the NDIs on HOPG surface. We use mono- and bifunctional D molecules to probe for the impact of bivalency. Similar as for the double NDIs, we systematically vary the length of the alkyl spacers within the series of bifunctional D molecules to probe for molecular geometries that induce D-A co-adsorption. Scanning tunneling microscopy (STM) indicates that several D-A mixtures form new surface structures that potentially stem from co-adsorption. Analyzing the structural details suggests that D-A co-adsorption occurs in either new two-dimensional (2D) lattices or in D-A stacks. The close proximity of D and A chromophores in the D-A stacks suggests the achievement of CT complexes on HOPG surface. In bulk material, we also find CT complexes that are however not arranged in a periodical fashion. The discrepancy between the surface and bulk systems highlights the importance of controlling adsorbate-solvent and adsorbate-substrate interactions when arranging D and A molecules on HOPG surface.

Part of this work will be published:

A.T. Rösch, R. Reynaerts, K.S. Mali, S. De Feyter, A.R.A. Palmans, and E.W. Meijer
R. Reynaerts, A.T. Rösch, K.S. Mali, A.R.A. Palmans, E.W. Meijer, and S. De Feyter

6.1 Introduction

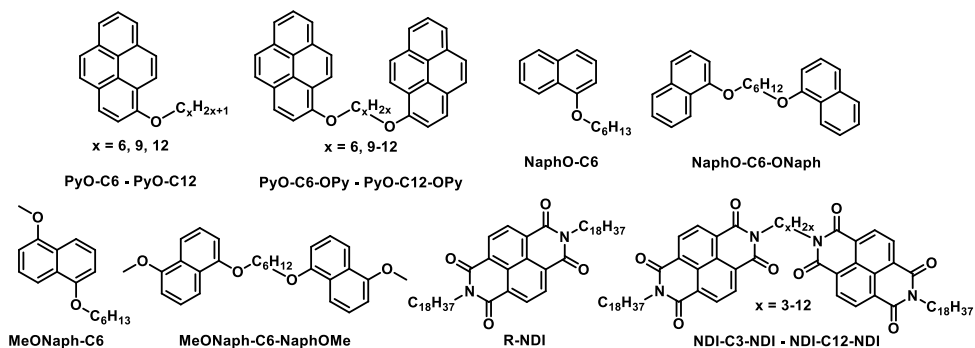
Dipolar interactions between electron-rich and electron-poor arene systems are often referred to as “aromatic interactions”^[1] or “ π -stacking”.^[2] When an electron-rich donor (D) and an electron-poor acceptor chromophore (A) are brought in close proximity, a fraction of the electronic charge is transferred from D to A. The formed adduct is called charge transfer (CT) complex.^[3] A very prominent example for an organic CT complex is formed between tetrathiafulvalene (TTF) and 7,7,8,8-tetracyanoquinodimethane (TCNQ).^[4] This CT material shows a very high electron conductance for an organic material and behaves like a metal over a wide temperature range. The finding of the TTF-TCNQ CT complex has triggered a plethora of investigations that have resulted in organic CT systems with potential applications as organogelators,^[5–8] hydrogelators,^[9] liquid crystals,^[10] polymers,^[11–16] foldamers,^[17] rotaxanes and catenanes,^[18] nanoparticles,^[19] synthetic ion channels^[20] and artificial photosystems.^[21]

Another example for a particularly well-studied CT complex is the adduct between the electron-rich pyrene and the electron-poor *N,N'*-bis(*n*-alkyl)-naphthalenediimide (NDI) chromophores.^[22] Compounds based on the NDI motif are of particular interest due to the combination of the NDI's strong tendency to form π -stacked aggregates and its *n*-type semiconductivity.^[23,24] Depending on the chemical structure of the NDI, CT complexes with pyrene derivatives were obtained as co-crystal,^[25] polymer blend^[26] or as NDI-based vesicles with intercalated pyrene derivatives.^[27] In the NDI-pyrene cocrystal, a parallel sandwich arrangement in D-A stacks was found which exhibited a rotational angle of 53° between the two chromophores.^[25] The interplanar distance was 3.4 Å which was smaller than interplanar distance of 3.5 Å in the crystal of pure pyrene and hence indicative of attractive hetero-interactions.^[22,25,28] Yeh *et al.* investigated the non-covalent interactions between the NDI and the pyrene chromophores in more detail by density-functional theory (DFT).^[29] Corroborating the structural information gained by X-ray crystallography,^[22,25] a parallel face-to-face packing of the aromatic compounds was calculated since this arrangement maximized the attractive dispersion forces between the molecules similar as also known from other large polycyclic systems.^[29,30] DFT calculations suggested further that the attractive interactions stemmed from the overlap of the wavefunctions of LUMO_{NDI} and the HOMO_{pyrene} and occurred only for rotational angles of 50° and more between the stacked molecules which was in good agreement with the experimentally found rotational angle of 53°. ^[29]

Whereas D-A co-assembly and the formation of CT complexes is well-described for many solution-based systems^[5–7] and bulk materials,^[11–15] research on co-assembly and especially CT complex formation at interfaces is relatively unexplored. The paucity of the reports likely stems from the complex interplay of substrate-adsorbate, adsorbate-adsorbate and adsorbate-solvent interactions which all need to be considered when preparing self-assembled structures on surfaces and complicate the design of multicomponent systems further.^[31–33] The existing literature studies on multicomponent surface systems often used

scanning tunneling microscopy (STM)^[34] as characterization technique since it offers a (sub-)molecular resolution of the prepared structures.^[35] The studies reported on the formation of co-adsorbed structures by the combination of van-der-Waals interactions and geometrical restrictions,^[36–38] hydrogen-bonding^[39–42] and/or fluorophilicity^[43] but not by the formation of CT complexes, yet. Due to the absence of such literature reports and many prospective applications such as microelectronics or heterogenous catalysis,^[44] research on the co-adsorption of D-A mixtures is gaining increasing scientific attention. Velpula *et al.*^[45] reported on the co-adsorption of D-A mixtures in a 2D layer driven by the combination of the molecules' geometry and the formation of hydrogen bonds as an additional directional interaction. Owing to the types of interactions, a geometrical arrangement was obtained which did however not indicate the formation of CT complexes. In contrast to co-adsorption in plane, stacked systems allow for a closer proximity of the two types of chromophores. Such stacked multicomponent systems have been described already, however mostly in systems that used metal-ligand coordination.^[46–48] In a recent study, Heideman *et al.*^[49] reported on the stepwise functionalization of surfaces with D-A mixtures. At first, a monolayer of NDI was prepared at the 1-phenyloctane/HOPG interface. In a second step, pyrene molecules were adsorbed on top. Since the pyrene chromophores were, however, not adsorbed directly on top of the NDI cores but on adjacent alkyl chains, the formation of CT complexes at the HOPG surface remained elusive.^[49]

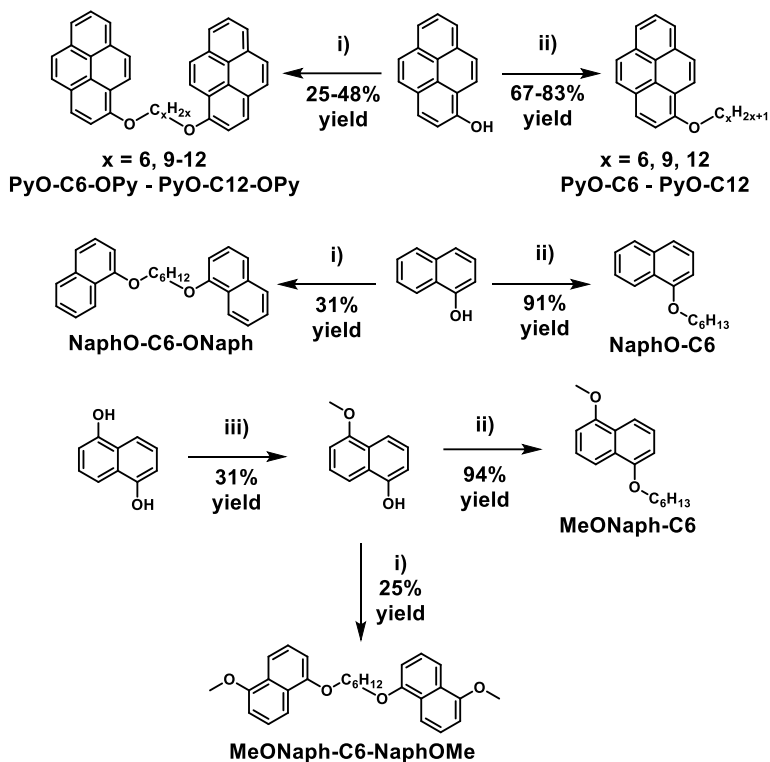
In order to gain more fundamental insight into the formation of co-adsorbed D-A systems at interfaces and to achieve CT complex formation, we investigated the co-adsorption of mono- and bifunctional D and A pairs at the 1-phenyloctane/HOPG interface. The molecular structures of all compounds are shown in Scheme 6.1. The electron-rich D compounds contained either the pyrene, the naphthalene or the 1-methoxynaphthalene chromophore(s). The electron-poor A compounds were the NDIs which have already been described in Chapter 5. Within the series of bifunctional compounds, the lengths of the alkyl spacers were varied to systematically probe for matching geometries that result in the formation of co-adsorbed structures and ideally also CT complexes at the 1-phenyloctane/HOPG interface. Whereas the surface morphologies of D-A mixtures were investigated by STM, the morphologies formed in bulk material were determined by X-ray scattering. Finally, a comparison of the data was performed to probe for potential similarities of the co-assembly in both media.



Scheme 6.1: Molecular structures of mono- and bifunctional D and A compounds based on the electron-rich pyrene and naphthalene and the electron-poor NDI chromophores.

6.2 Synthesis and characterization of pyrene and naphthalene-based compounds

The preparation of the electron-rich D compounds was inspired by a protocol from David *et al.*^[50] The synthetic strategies are shown schematically in Scheme 6.2. The etherification of the hydroxy-functionalized chromophores with mono- and bifunctional bromoalkanes of various chain lengths was performed using potassium carbonate as base and potassium iodide as catalyst. In all cases except for the methylation of 1,5-naphthalenediol, the solvent was dry *N,N*-dimethylformamide (DMF). For the methylation reaction, we found that DMF favored double substitution and the formation of undesired 1,5-dimethoxy-naphthalene as main product. Replacement of the solvent by acetonitrile yielded a statistical mixture of unreacted, mono- and double substituted naphthalenes, which was separated by column chromatography. A second etherification step, again performed in DMF, was used to prepare the final methoxy naphthol-based compounds. The chemical structures of all final compounds were proven by ¹H and ¹³C nuclear magnetic resonance (NMR) and Fourier-transform infrared (FT-IR) spectroscopy as well as matrix-assisted laser ionization time of flight mass spectrometry (MALDI-TOF-MS). We used all pure compounds to prepare supramolecular 2D monolayers in HOPG surface. Since an initial screening experiment indicated that the double pyrenes showed the best adsorption at the 1-phenyloctane/HOPG interface and displayed less polymorphism than the other compounds, we focused our study on the adsorption behavior of the double pyrenes.



Scheme 6.2: Synthetic route for the preparation of the donor compounds containing pyrene or the naphthalene chromophores. Reagents and conditions: i) aliphatic α,ω -dibromoalkane, K_2CO_3 , KI, DMF, 60 °C, 16 h; ii) aliphatic α -bromoalkane, K_2CO_3 , KI, DMF, 60 °C, 16 h; iii) methyl iodide, K_2CO_3 , acetonitrile, 60 °C, 16 h.

6.3 Physisorbed self-assembled monolayers formed by double pyrenes at the solution/HOPG interface

We started our study by applying the electron-rich double pyrenes to the solution/HOPG interface and used STM to probe for the formation of self-assembled monolayers. The STM study was performed in collaboration with Robby Reynaerts and Kunal Mali from prof. Steven De Feyter's group at the Katholieke Universiteit Leuven. The samples were prepared by drop casting 1-phenyloctane solutions of the compounds onto a freshly cleaved HOPG substrate. The morphologies formed by **PyO-C6-OPy**, **PyO-C9-OPy** and **PyO-C10-OPy** are depicted in Figure 6.1. The STM images show that **PyO-C6-OPy** (Figure 6.1a) and **PyO-C10-OPy** (Figure 6.1c) formed lamellar lattices. In contrast, **PyO-C9-OPy** (Figure 6.1b) exhibited the formation of a grid-like structure. In addition, the bulk properties of the compounds such as bulk morphology and thermal properties were investigated, too (*vide infra*).

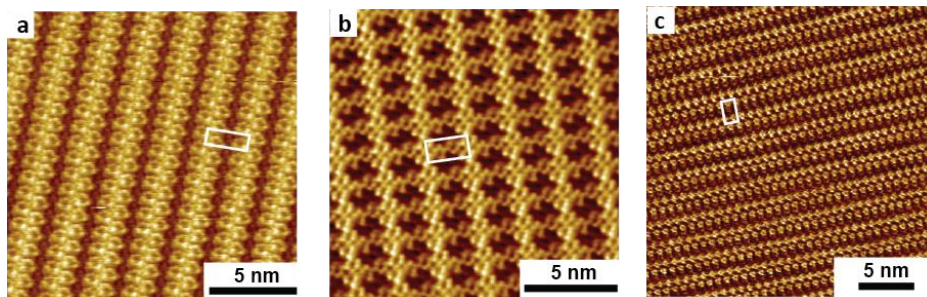


Figure 6.1: Representative STM images showing the self-assembled networks formed by (a) **PyO-C6-OPy**, (b) **PyO-C9-OPy** and (c) **PyO-C10-OPy**. The unit cells are given in white.

Since the structures of the monolayers formed by the NDIs have already been described extensively in Chapter 5, we continued our study with an investigation of the monolayer formed when applying D-A mixtures.

6.4 Physisorbed self-assembled monolayers formed in D-A mixtures of double pyrene and double NDIs at the solution/HOPG interface

Being able to clearly identify the morphologies of the native monolayers of the D and A molecules, we moved on to performing the D-A mixing experiments. We systematically investigated the morphologies of the D-A mixtures of bifunctional molecules by STM as summarized in Table 6.1 to identify structure-property relationships required for achieving the desired D-A co-adsorption. The preparation of the samples was performed in two steps. At first, a saturated solution of the NDI derivative in 1-phenyloctane was drop-casted onto a freshly cleaved HOPG substrate. After annealing for 10 minutes at 100 °C, the sample was slowly cooled to room temperature to prepare the supramolecular monolayer of the NDI as reported in Chapter 5. Subsequently, one drop of a solution of a double pyrene in 1-phenyloctane was drop-casted on top. The surface morphology of the sample was investigated by STM. The STM images recorded for the D-A mixtures were compared with the STM images of the native monolayers of the used D and A molecules. D-A mixtures that exhibited the formation of structures that deviated from the structures of the native D and A monolayers were labelled as 'new structure' (Table 6.1). We want to point out that for the majority of the investigated D-A mixtures, the formation of new structures which are potentially indicative of co-adsorption was not observed. For most samples, only two types of phase separated surface domains were noticed which resembled the morphologies of the native monolayers of the used D and A molecules. Since periodic interactions between these two domains were absent, we ascribed this coexistence to the similar affinity of both compounds to the HOPG surface and the system trying to achieve an energetically favorable high surface coverage. Upon a close examination, we found that the formation of such phase separated D and A domains occurred either laterally or vertically. An example for lateral phase separation is depicted in Figure 6.2a. The STM image shows **NDI-C9-NDI**

double lamellae in the center which are surrounded by **PyO-C6-OPy** domains. The formation of the vertically phase separated lattices was indicated by the absence of periodic interaction in stacked D-A monolayers. The formation of such systems was easily identified by time dependent STM experiments. As exemplarily shown in Figure 6.2b and c for the mixture of **PyO-C6-OPy** with **NDI-C8-NDI**, we observed the nucleation of double pyrene on top of the NDIs' double lamellae (Figure 6.2b) which induced the formation of a dense double pyrene lattice on top which showed its native morphology (Figure 6.2c). In the following, we will focus on comparing the structural features of the new surface morphologies.

Table 6.1: Results from the structural investigation of the D-A mixtures of double pyrenes and double NDIs as investigated by STM; n.d.: no data available.

entry	NDI	PyO-C6-OPy	PyO-C9-OPy	PyO-C10-OPy
1	NDI-C3-NDI	n.d.	lateral phase separation	n.d.
3	NDI-C5-NDI	n.d.	new structure	n.d.
4	NDI-C6-NDI	vertical phase separation	lateral phase separation	n.d.
5	NDI-C7-NDI	n.d.	lateral phase separation	lateral phase separation
6	NDI-C8-NDI	new structure	lateral phase separation	n.d.
7	NDI-C9-NDI	lateral phase separation	new structure	n.d.
8	NDI-C10-NDI	vertical phase separation	lateral phase separation	n.d.
9	NDI-C11-NDI	n.d.	new structure	n.d.
10	NDI-C12-NDI	n.d.	vertical phase separation	new structure

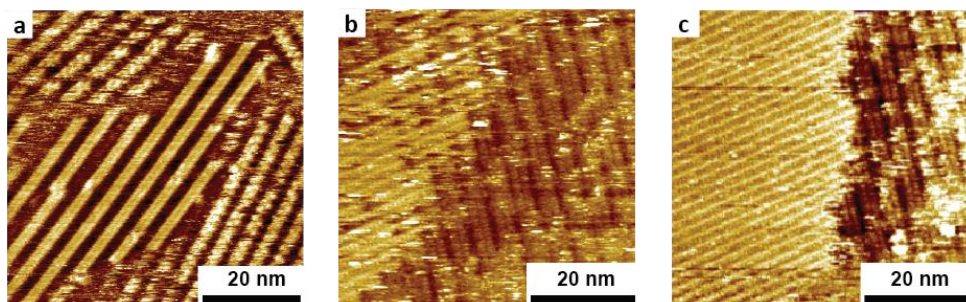


Figure 6.2: Representative STM images showing the morphologies of laterally or vertically phase separated double pyrene and double NDI domains. (a) A domain of **NDI-C9-NDI** double lamellae (center) is surrounded by **PyO-C6-OPy** domains. (b) Nucleation of **PyO-C6-OPy** on top of **NDI-C10-NDI** double lamellae resulted in (c) the formation of a vertically phase separated **PyO-C6-OPy** domain (left) on top of the NDI lattice (right).

6.4.1 New surface structures formed by D-A co-adsorption

As noticed in Table 6.1, we found that five of the investigated D-A mixtures exhibited the formation of new surface domains. In this context, ‘new’ means that the surface morphology of one domain found in the D-A mixture did not resemble the native surface structures of the contained D or A molecules. The formation of such a new structure is potentially indicative of D-A co-adsorption within one surface domain. To allow for a better comparison of the new surface morphologies among themselves and with the native lattices of the contained D and A components, STM images of all new surface morphologies and the native lattices of the contained compounds are provided in Figure 6.3. As noticed in Figure 6.3b and e, the new morphologies found in the D-A mixtures of **PyO-C6-OPy** with **NDI-C8-NDI** and **PyO-C10-OPy** with **NDI-C12-NDI** exhibited lamellar structures that were structurally related with the double lamellae of the contained NDI derivatives. In contrast, the remaining three new morphologies depicted in Figure 6.3h, k and m had grid-like morphologies that were clearly distinguished from the native lattices of the contained D and A molecules. Investigating the formed morphologies in more detail by recording STM images at increased resolution and by performing molecular modelling suggested that the observed patterns did indeed stem from the desired D-A co-adsorption. Depending on the molecular geometries, co-adsorption occurred either in plane or in stacked systems. In the following, we highlight one example for each of these two modes of co-adsorption. We describe the co-adsorption of **PyO-C6-OPy** and **NDI-C8-NDI** in new type of 2D monolayer and the formation of D-A stacks in the mixture of **PyO-C9-OPy** and **NDI-C5-NDI**.

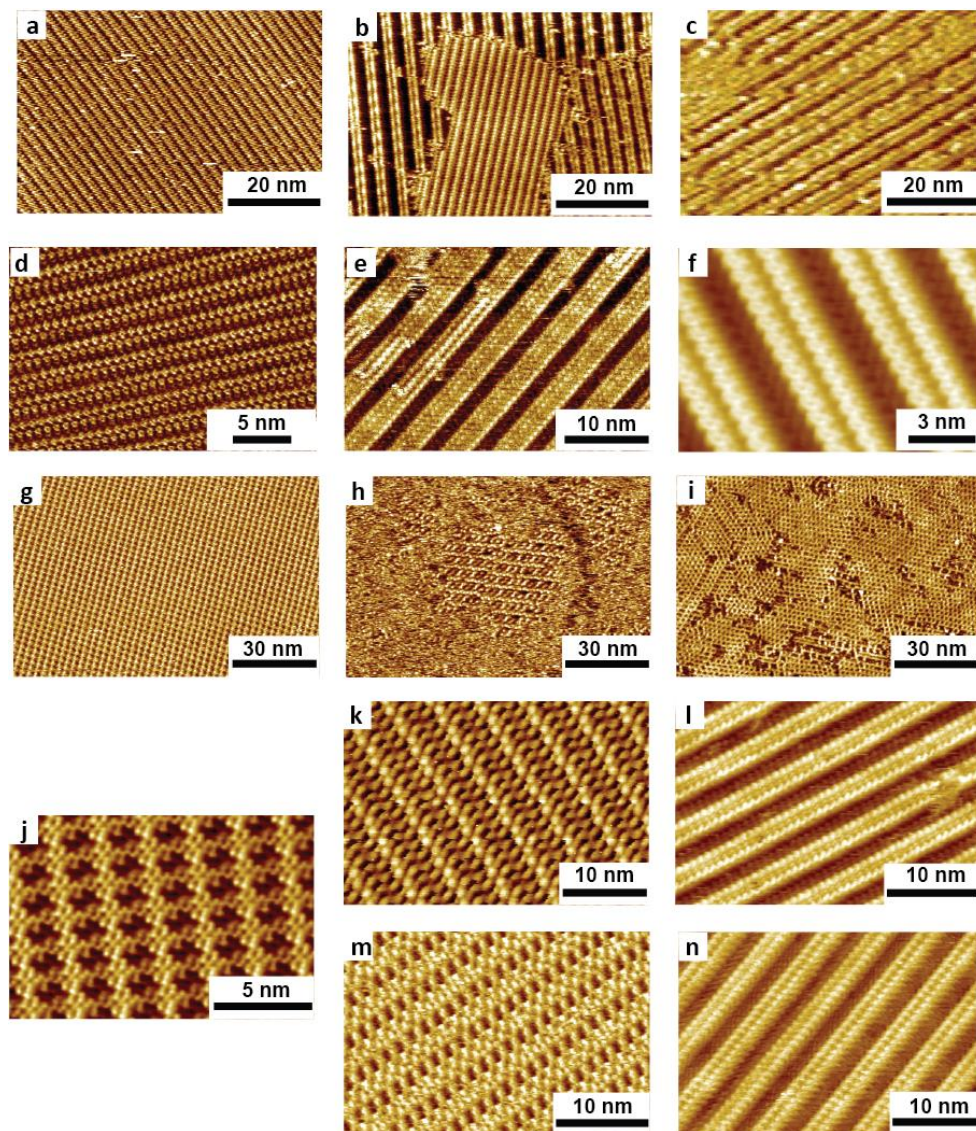


Figure 6.3: Representative STM images showing the self-assembled networks formed by (a) **PyO-C6-OPy**, (b) the D-A mixture of **PyO-C6-OPy** and **NDI-C8-NDI**, (c) **NDI-C8-NDI**, (d) **PyO-C12-OPy**, (e) the D-A mixture of **PyO-C12-OPy** and **NDI-C10-NDI**, (f) **NDI-C10-NDI**, (g) **PyO-C11-OPy**, (h) the D-A mixture of **PyO-C11-OPy** and **NDI-C9-NDI**, (i) **NDI-C9-NDI**, (j) **PyO-C9-OPy**, (k) the D-A mixture of **PyO-C9-OPy** and **NDI-C9-NDI**, (l) **NDI-C9-NDI**, (m) the D-A mixture of **PyO-C9-OPy** and **NDI-C5-NDI**, (n) **NDI-C5-NDI**. We note that the grid-like morphology shown in (i) is a polymorph of **NDI-C11-NDI** that was formed over time and not the lamellar structure shown in Chapter 5.

6.4.2 Structural details of laterally co-adsorbed PyO-C6-OPy and NDI-C8-NDI

Since the new surface morphology that was formed in the D-A mixture of **PyO-C6-OPy** and **NDI-C8-NDI** was structurally very similar to the double lamellae that were formed by **PyO-C6-OPy** and **NDI-C8-NDI**, a further investigation of the structure by determining the unit cell parameters and by creating a molecular model was possible. The unit cell parameters of the three lattices of **PyO-C6-OPy**, **NDI-C8-NDI** and the co-adsorbed structure are summarized in Table 6.2. For all structures, the unit cell parameter a was 0.9 nm and the angle α was very close to 90° . The unit cell parameter b was 2.3 nm for **PyO-C6-OPy** and 4.6 nm for **NDI-C8-NDI**. In the co-adsorbed structure, b was 3.2 nm which suggested that the unit cell of the new structure was representing almost the median of the unit cells found for the native supramolecular monolayers of **PyO-C6-OPy** and **NDI-C8-NDI**. When the new structure was imaged at higher magnification (Figure 6.4b), strong differences in STM contrast between the individual aromatic cores in the double lamellar patterns were noticed. A common origin for differences in contrast in STM micrographs is the interference effect stemming from the superposition of differently sized repeating units of the adsorbed monolayer and the HOPG lattice which is also called Moiré-pattern.^[51] Since an interference effect results in periodic changes of the STM contrast and the observed contrast differences in the STM image (Figure 6.4b) were irregular, we excluded Moiré-pattern as origin. Instead, the darker and brighter spots were likely to originate from two chemical species with a different electronic configuration. The STM image hence suggested that this new type of domain consisted of D and A molecules which were co-adsorbed next to each other. As a result, a double lamellar morphology similar to the native lattices of **PyO-C6-OPy** and **NDI-C8-NDI** was formed. Comparing the molecular models of **PyO-C6-OPy** (Figure 6.4d) and **NDI-C8-NDI** (Figure 6.4f) with a simplified structure proposed for the co-adsorbed domain (Figure 6.4e) corroborated that the formation of a fully covered surface by D-A co-adsorption with unit cell parameters comparable to the experimentally obtained data.

Table 6.2: Unit cell parameters of the lamellar structures of **PyO-C6-OPy**, **NDI-C8-NDI** and the co-adsorbed structure formed at the 1-phenyloctane/HOPG interface as derived from the STM micrographs.

Structure	PyO-C6-OPy	NDI-C8-NDI	co-adsorbed
a [nm]	0.9 ± 0.1	0.9 ± 0.1	0.9 ± 0.1
b [nm]	2.3 ± 0.1	4.6 ± 0.1	3.2 ± 0.1
α [°]	85 ± 2	89 ± 1	89 ± 1

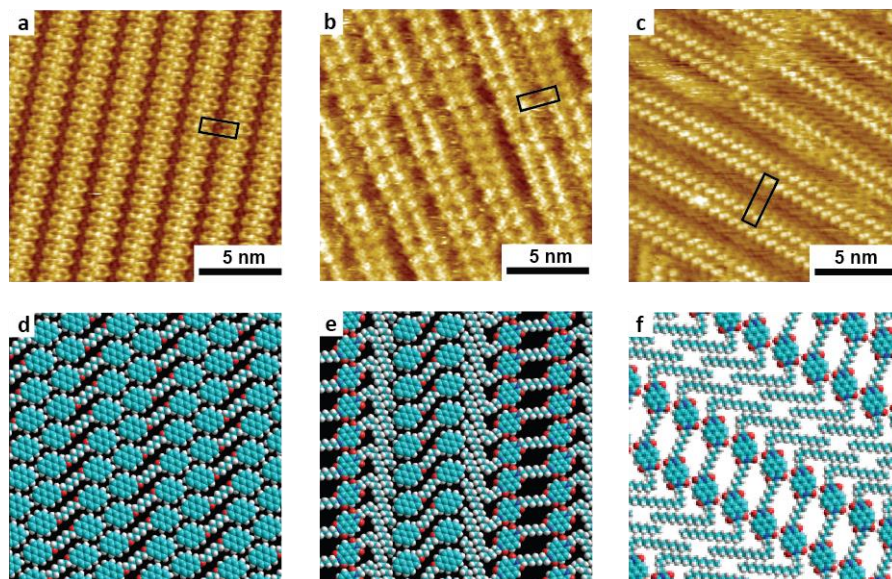


Figure 6.4: Representative STM images showing the self-assembled networks formed by (a) **PyO-C6-OPy**, (c) **NDI-C8-NDI** and (b) the mixtures thereof. Molecular models of the corresponding 2D monolayers are shown in (d-f). The unit cells are given in black.

6.4.3 Structural details of vertically co-adsorbed **PyO-C9-OPy** and **NDI-C5-NDI**

The new type of surface morphology that was formed in the D-A mixture of **PyO-C9-OPy** and **NDI-C5-NDI** exhibited a grid-like morphology (Figure 6.5b) that differed clearly from the native grid-like 2D monolayer of **PyO-C9-OPy** (Figure 6.5a) or the double lamellar morphologies of **NDI-C5-NDI** (Figure 6.5c). The structural details of the surface morphology became apparent when the resolution was increased. As shown in Figure 6.5d, the morphology consisted of bright and rather broad lamellae (orientated along the blue arrow in Figure 6.5d) that were decorated with brick-shaped elements (highlighted by the red circle in Figure 6.5d). Owing to the high resolution of the STM image, we were able to develop a molecular model that recreated the observed structural details. The molecular model is depicted in Figure 6.5e and suggests the formation of a stacked D-A system. The broad lamellar structures (orientated along the blue arrow in Figure 6.5d) were assigned to the native **NDI-C5-NDI** double lamellae. The bright bricks that were arranged perpendicularly to the NDI double lamellae (red circle in Figure 6.5d), were assigned to the pyrene chromophores of **PyO-C9-OPy** molecules which were adsorbed on top of the alkyl lamellae of the NDI lattice. Owing to the length of the **PyO-C9-OPy** molecule and the differences in contrast in the STM images, the molecular model suggested that the second pyrene chromophore of the **PyO-C9-OPy** molecule was located on top of the NDI columns. Thereby, the remaining part of the molecule was also covering the narrower alkyl lamella in between the covalently connected bright NDI lamellae (only noticed in the native

monolayer of **NDI-C5-NDI** in Figure 6.5c). According to the model, the rotational angle between the long axes of the stacked pyrene and the NDI chromophores was 65° .

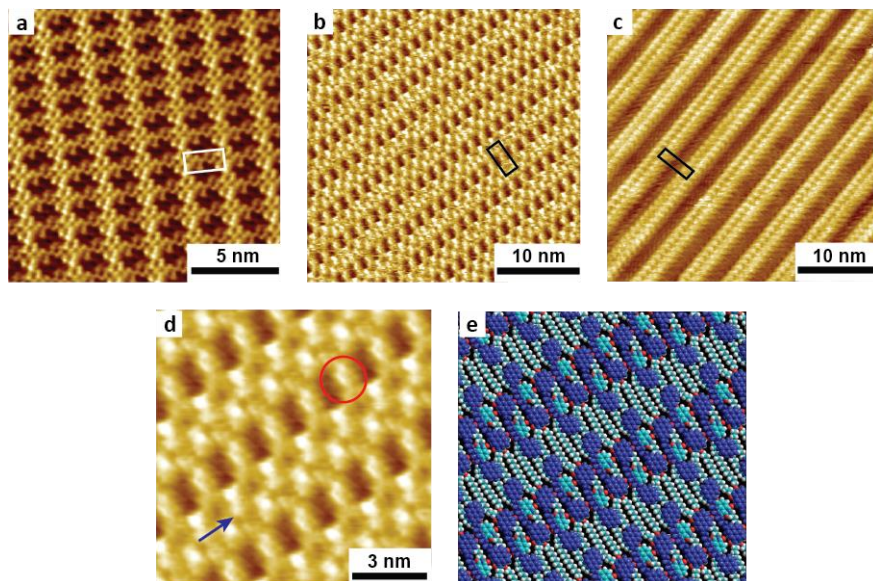


Figure 6.5: Representative STM images showing the self-assembled networks formed by (a) **NDI-C5-NDI**, (c) **PyO-C9-OPy** and (b) in the mixture thereof; (d) magnified STM image of the D-A mixture; (e) Proposed molecular model showing the arrangement of **PyO-C9-OPy** molecules on top of the **NDI-C5-NDI** layer. The unit cells are given in white or black, respectively.

6.4.4 Discussion on the new surface morphologies formed by D-A co-adsorption

The above presented structural investigation of the morphologies formed by the D-A mixtures on HOPG surface suggested that applying several combinations of double pyrenes and double NDIs to HOPG surface resulted in the formation of structurally new surface domains. Due to the complexity of some of the structures, we were not able to perform a detailed analysis in all cases. Nevertheless, our results already indicate the existence of two different modes of D-A co-adsorption, namely the co-adsorption in plane and the co-adsorption in D-A stacks.

The STM image and the molecular model for the co-adsorbed structure formed by **PyO-C6-OPy** and **NDI-C8-NDI** indicated that co-adsorbed pyrene and NDI chromophores were laterally separated by alkyl chains. This spatial separation suggested the absence of CT complexes. We concluded that the driving force to form this 2D monolayer was no D-A interaction but the generation of an energetically favorable high surface coverage similar as reported in the literature for the co-adsorption of electron-rich hexabenzocoronenes and an electron-poor perylene diimide on the HOPG surface.^[45] In contrast, we found a close

proximity of the pyrene and NDI chromophores in the co-adsorbed D-A stacks formed by **PyO-C9-OPy** and **NDI-C5-NDI**. The rotational angle of 65° between the stacked pyrene and NDI chromophores was similar to the angle of 53° that has been reported for the co-crystal of structurally related pyrene and NDI derivatives.^[25] Since DFT calculations performed by another group suggested that attractive interactions in a pyrene-NDI stack occur when the torsion angle between the chromophores is greater than 50° ,^[29] the noticed close proximity and of the chromophores in the D-A stacks and the determined rotational angle were indicative of the formation of CT complexes on HOPG surface. The adsorption of the second pyrene chromophore of the **PyO-C9-OPy** molecules occurred however on top of the alkyl chains. This distinct off-set of the adsorption location from the NDI columns was structurally resembling the results from Heideman *et al.*^[49] We note that the system described here and that from Heideman *et al.* clearly differ from each other. In the system described by Heideman *et al.*, the adsorption of monofunctional pyrenes occurred exclusively on top of unsaturated bonds in close proximity to the NDI columns and never directly on top of the NDI cores. In our case, one pyrene chromophore of the bifunctional **PyO-C9-OPy** molecule was adsorbed on top of an NDI core. The other one was positioned on top of the alkyl chains as defined by the length of the alkyl spacer arranged in a fully stretched conformation, and not by the presence of an unsaturated bond.

Owing to the synthetic strategy, the linkers of the two pyrene chromophores in the double pyrenes contained two ether groups, whereas the alkyl spacers in the double NDIs did not. As a result, equal distances between the covalently linked pyrenes and NDIs were achieved in the following investigated D-A mixtures: **PyO-C6-OPy** and **NDI-C8-NDI**, **PyO-C9-OPy** and **NDI-C11-NDI** as well as **PyO-C10-OPy** and **NDI-C12-NDI**. As noticed in Table 6.1, each of these three tested D-A mixtures showed the formation of a new surface structure. The D-A mixtures of **PyO-C6-OPy** and **NDI-C8-NDI** as well as **PyO-C10-OPy** and **NDI-C12-NDI** formed lamellar structures. The detailed structural investigation of **PyO-C6-OPy** and **NDI-C8-NDI** indicated the formation of a laterally D-A co-adsorbed structure. In contrast, the STM image of the D-A mixture of **PyO-C10-OPy** and **NDI-C12-NDI** suggested the formation of D-A stacks structurally related to the new structure formed by **PyO-C9-OPy** and **NDI-C5-NDI** as indicated by the absence of the narrower dark column in between the NDI double lamellae (Figure 6.3e). Owing to the complexity of the grid-like structure of **PyO-C9-OPy** and **NDI-C11-NDI**, a detailed structural investigation was not possible. Although applying a D-A mixture of bifunctional molecules with equal lengths of the chromophore connecting spacers seemed to promote the formation of new surface morphologies, the complexity and strong differences in the formed surface structures prevented the identification of a correlation between the molecular structures in the D-A mixture and the formed surface morphologies.

One possible explanation for the complexity of the observed structures was the partial desorption of the alkyl spacer of the double NDIs as described in detail in Chapter 5. We conclude that with the current data set, it is too early to deduce definitive structure-

property relationships for D-A co-adsorption which in turn suggests that engineering architectures at interfaces is equally challenging as crystal engineering.

6.5 Co-assembly of pyrene-NDI mixtures in bulk material

We continued our study with the investigation of the co-assembly in bulk material of the D-A mixtures to eventually be able to probe for structural parallels between D-A systems formed in bulk and on HOPG surface. The investigated samples were equimolar mixtures of double pyrenes and double NDIs which were prepared by heating D-A mixtures to the isotropic melt and cooling slowly to room temperature. Additionally, the mixture of monofunctional **PyO-C6** with **R-NDI** was prepared to investigate the impact of bifunctionality. The bulk properties were investigated by ultraviolet–visible (UV/Vis) spectroscopy and X-ray scattering.

6.5.1 Optical properties of pyrene-NDI mixtures

When the solid D-A mixtures were heated to the isotropic melt, an intense red color was developed which is exemplarily shown for the D-A mixture of **PyO-C6** and **R-NDI** in the left inset in Figure 6.6a. Upon cooling the melted materials to room temperature, solidification was observed. In case of the mixture of **PyO-C6** and **R-NDI**, the solidification resulted in a loss of the red color (right inset in Figure 6.6a). In contrast, D-A mixtures that contained bifunctional compounds did not lose their red color but changed their appearance to a more violet hue instead (inset in Figure 6.6b). Since the formation of the red color was indicative of CT complex formation,^[52] we investigated the optical properties of the materials quantitatively by variable-temperature UV/Vis spectroscopy. Exemplary absorption spectra recorded for melted and solidified D-A mixtures are depicted in Figure 6.6. In the melt, the D-A mixtures exhibited absorption bands below 400 nm as well as a very broad absorption band at 560 nm. In the solid state, the broad absorption band at 560 nm was depleted for the D-A mixture of **PyO-C6** and **R-NDI** and retained for the D-A mixture of **PyO-C6-OPy** and **NDI-C8-NDI**. The absorption bands below 400 were assigned to the absorption bands of the pyrene^[53] and the NDI chromophores.^[24] The broad absorption band at 560 nm indicated the formation of CT complexes since it was red-shifted with respect to the absorption bands of the individual chromophores and also in accordance with literature reports on the CT complex of structurally related pyrene and NDI derivatives.^[6,54] The absence of the red color and the depletion of the absorption band at 560 nm in the solid mixture of **PyO-C6** and **R-NDI** was ascribed to the dissociation of the CT complexes. The dissociation of the CT complexes was not unexpected since CT complexes commonly have low association constants when no additional attractive interactions such as hydrogen bonds are present between the D and A chromophores.^[39,42] Retaining the red color and the absorption band at 560 nm in the solid mixture of **PyO-C6-OPy** and **NDI-C8-NDI** (blue line in Figure 6.6b) suggested that bifunctionality stabilized the CT complexes or partially hindered the formation of self-sorted D and A crystals. All spectra recorded at room temperature contained scattering contributions indicative of the formation of rather large aggregates.

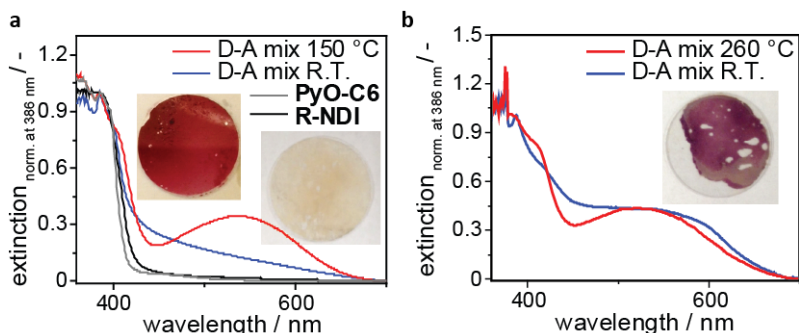


Figure 6.6: Optical properties (a) of melted **PyO-C6** and **R-NDI** as well as the equimolar mixture thereof (at 150 °C and at R.T.) and (b) of the equimolar mixture of **PyO-C6-OPy** and **NDI-C8-NDI**. The left inset in (a) shows the red color of the molten material. The insets on the right both in (a) and (b) show the optical appearances of the corresponding D-A mixtures after cooling to room temperature.

6.5.2 X-Ray scattering profiles of pyrene-NDI mixtures

Since all solid D-A mixtures of bifunctional compounds exhibited a red-violet color indicative of CT complex formation, we conducted an X-ray scattering study to investigate the bulk morphologies of the D-A mixtures and to be able to determine possible structural parallels between the co-adsorption on surface and the co-assembly in bulk. We first focused on the D-A mixtures of **PyO-C6-OPy** and **NDI-C8-NDI** or **NDI-C6-NDI**. The scattering profiles of the individual compounds and the D-A mixtures are shown in Figure 6.7a and b. The determined bulk morphologies and corresponding domain spacings are summarized in Table 6.3. For pure **PyO-C6-OPy**, no bulk morphology could be determined since the sample showed scattering peaks in the WAXS region only. As already described in Chapter 5, pure **NDI-C6-NDI** or **NDI-C8-NDI**, respectively, showed scattering peaks that were indicative of two lamellar lattices. In the D-A mixture of **NDI-C6-NDI** and **PyO-C6-OPy**, the intensities of the scattering peaks of the second lattice of **NDI-C6-NDI** were reduced but the corresponding scattering vectors q were unaffected. In contrast, the scattering profile recorded for the D-A mixture of **NDI-C8-NDI** and **PyO-C6-OPy** indicated that the domain spacing of the second lattice of **NDI-C8-NDI** was increased by approximately 1 nm with respect to the corresponding second lattice of pure **NDI-C8-NDI**.

Table 6.3: X-Ray scattering peaks and bulk morphologies determined for **PyO-C9-OPy**, all double NDIs and the D-A mixtures. All measurements were performed at room temperature.

compound	morphology	number of sharp scattering peaks	domain spacing first lattice [nm]	domain spacing second lattice [nm]
PyO-C6-OPy	-	0	-	-
NDI-C6-NDI	Lamellar	7	5.3	4.2
D-A mixture	Lamellar	7	5.3	4.2
NDI-C8-NDI	Lamellar	8	5.0	4.4
D-A mixture	Lamellar	8	5.0	5.7

We continued the X-ray scattering study with the investigation of the D-A mixtures containing **PyO-C9-OPy**. We note that pure **PyO-C9-OPy** showed two scattering peaks in the SAXS region (grey line in Figure 6.7c) which we assigned to the formation of a lamellar bulk morphology with a domain spacing of 2.5 nm. The bulk morphologies and domain spacings determined for all D-A mixtures containing **PyO-C9-OPy** are summarized in Table 6.4. Out of this series, we want to highlight the scattering profiles recorded for the D-A mixtures of **PyO-C9-OPy** and **NDI-C6-NDI** as well as of **PyO-C9-OPy** and **NDI-C8-NDI**. The scattering profile recorded for the D-A mixture of **PyO-C9-OPy** and **NDI-C6-NDI** is exemplary for all other D-A mixtures in this series and shown in Figure 6.7c. The scattering profile did not contain scattering peaks stemming from crystalline **PyO-C9-OPy**. The number of scattering peaks stemming from crystalline **NDI-C6-NDI** was reduced with respect to the scattering peaks of pure **NDI-C6-NDI** bulk material. However, the scattering vectors q corresponding to crystal lattices of **NDI-C6-NDI** were hardly affected by the presence of **PyO-C9-OPy**. In the scattering profile of the D-A mixture of **PyO-C9-OPy** and **NDI-C8-NDI**, no scattering peaks were found for **PyO-C9-OPy** either (Figure 6.7c). However, we found that the domain spacing of the second lattice of **NDI-C8-NDI** was increased by approximately 0.4 nm with respect to the native lattice of **NDI-C8-NDI** which makes this D-A mixture unique in the series.

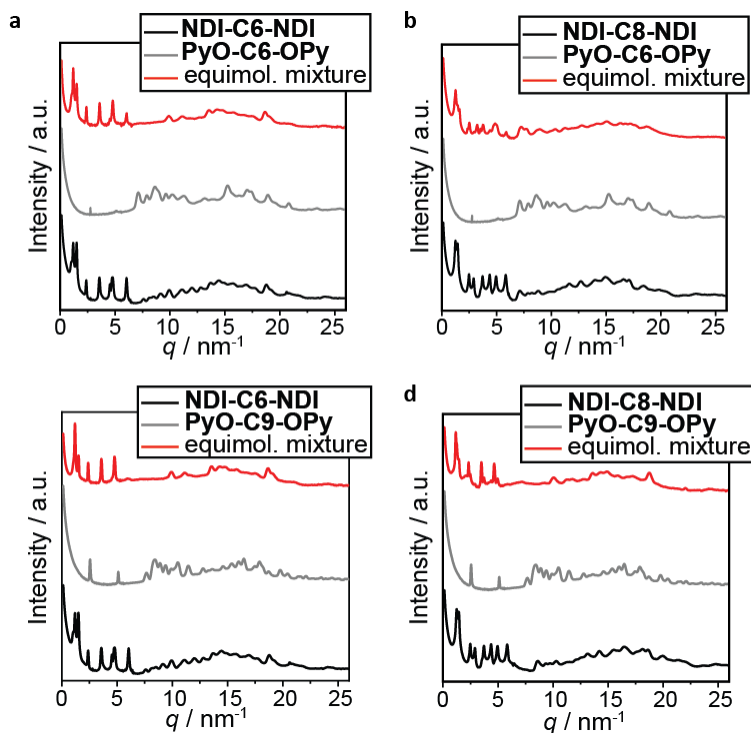


Figure 6.7: 1D transmission scattering profiles obtained for pure compounds and D-A mixtures of (a) **NDI-C6-NDI** and **PyO-C6-OPy**, (b) **NDI-C8-NDI** and **PyO-C6-OPy**, (c) **NDI-C6-NDI** and **PyO-C9-OPy** and (d) **NDI-C8-NDI** and **PyO-C9-OPy** the mixture thereof. The scattering vector is ranging from 0.1 to 25 nm⁻¹.

The absence of new scattering peaks and the only marginal alteration (0-0.2 nm) of the domain spacings of the lamellar lattices of the double NDIs in most D-A bulk mixtures suggested that the CT complexes formed in bulk material were typically not arranged in a periodic fashion. The decreased number of sharp scattering peaks with respect to the corresponding pure NDI material suggested that mixing merely reduced the crystalline order. The only exceptions from these trends were the D-A mixtures that contained **NDI-C8-NDI**. Here, the domain spacing of one crystal lattice was increased when a double pyrene was present, which suggested also an alternation in the periodic packing of the **NDI-C8-NDI** molecule.

Since the previously described surface experiments showed that the formation of co-adsorbed structures occurred only for certain combinations of D and A and these structures were highly periodic, a comparison with the co-assembly in bulk indicates stark differences between both media. The absence of a structural correlation suggested that substrate-adsorbate and adsorbate-solvent interactions were pivotal for the formation of the observed co-adsorbed architectures on the HOPG surface.

Table 6.4: X-Ray scattering peaks and bulk morphologies determined individually for **PyO-C9-OPy**, the double NDIs and the D-A mixtures. All measurements were performed at room temperature.

compound	morphology	number of sharp scattering peaks	domain spacing first lattice [nm]	domain spacing second lattice [nm]
PyO-C9-OPy	Lamellar	2	2.5	-
NDI-C3-NDI	Lamellar	4	4.5	-
D-A mixture	-	1	4.3	-
NDI-C5-NDI	Lamellar	4	5.2	-
D-A mixture	Lamellar	4	5.2	-
NDI-C6-NDI	Lamellar	7	5.3	4.2
D-A mixture	Lamellar	5	5.3	4.2 ^A
NDI-C7-NDI	Lamellar	4	5.4	-
D-A mixture	Lamellar	4	5.4	-
NDI-C8-NDI	Lamellar	8	5.0	4.4
D-A mixture	Lamellar	8	5.4	4.4 ^A
NDI-C9-NDI	Lamellar	4	4.5	-
D-A mixture	Lamellar	4	4.5	-
NDI-C10-NDI	Lamellar	4	4.5	-
D-A mixture	Lamellar	4	4.5	-
NDI-C11-NDI	Lamellar	5	5.6	-
D-A mixture	Lamellar	4	5.8	-
NDI-C12-NDI	Lamellar	5	5.8	-
D-A mixture	Lamellar	4	5.8	-

^A Strong decrease in intensity.

6.6 Conclusions

We prepared a library of electron donor molecules to investigate the formation of CT complexes with the electron accepting NDIs reported in Chapter 5. The STM study on the adsorption of the D molecules at the 1-phenyloctane/HOPG interface indicated that the double pyrenes formed highly regular lattices and did not exhibit polymorphism. Consequently, we focused our D-A co-adsorption study on the mixtures of double pyrenes and double NDIs. The preparation of the samples was performed in two steps. At first a monolayer of double NDI was formed. Subsequently a solution of double pyrene was drop casted on top. The structural investigation of the samples indicated that, in most cases, only phase separated surface domains were formed which contained either the D or the A molecule, but never both. However, we also observed the formation of a third and structurally new type of surface domain for five of the investigated D-A combinations. We were able to develop molecular models for two of these new structures which suggested D-A co-adsorption as structural origin. The molecular models suggested further that depending on the molecular structures of the mixed molecules, co-adsorption occurred either in plane or in D-A stacks. The co-adsorption in plane was ascribed to result from matching molecular geometries that allowed for the formation of a 2D monolayer with high surface coverage. The spatial separation between the pyrene and NDI chromophores in this type of structure suggested that CT complexes were however absent. In contrast, pyrene and NDI chromophores were in close proximity in the D-A stacks. The corresponding molecular model suggested that the relative arrangement of pyrene and NDI cores on top of each other was similar as in the co-crystal formed by these chromophores. The structural similarity suggested that using our sample preparation protocol for this specific D-A mixture induced the desired formation of CT complexes on HOPG surface. Since most of the investigated D-A mixtures did however not show the formation of co-adsorbed domains, the exact structural requirements for the CT complex formation remained unclear. We continued the study with an investigation of the bulk properties of the D-A mixtures. In contrast to the results presented in Chapter 5, where the morphologies of double NDIs which were formed on surface and in bulk differentiated only in structural details, large differences were found when comparing the structures of D-A mixtures in these two media. Whereas the co-adsorption on HOPG surface resulted in highly regular structures and was only observed for a small number of the tested D-A mixtures, CT complex formation was noticed for all bulk samples. An X-ray scattering study indicated that the solid CT complexes were typically not arranged in a periodical fashion. The stark structural differences between the co-adsorption on surface and co-assembly in bulk highlighted the importance of precisely tuning substrate-adsorbate and adsorbate-solvent interactions when aiming for the fabrication of complex CT architectures on HOPG surface.

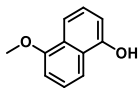
6.7 Experimental Section

6.7.1 Materials and Methods

All chemicals were purchased from commercial sources (TCI Chemicals, Sigma-Aldrich and abcr) and used without further purification. The solvents were purchased and treated as stated in Chapter 2. Silica column purification and chemical characterization (^1H and ^{13}C NMR, FT-IR and MALDI-TOF) was performed on the machines stated in Chapter 2. STM was performed as stated in Chapter 5. Samples for polarized optical microscopy and UV/Vis spectroscopy of bulk materials were mixed in glass vials, melted, cooled and deposited on glass coverslips which were cleaned as stated in Chapter 3. Before each measurement, the samples were melted and cooled slowly ($10\text{ }^\circ\text{C}/\text{min}$) to room temperature. UV/Vis spectra were recorded on a JASCO V-750 UV/Vis spectrometer. Bulk small angle X-ray scattering (SAXS), optical microscopy and DSC was performed as stated in Chapter 2.

6.7.2 Synthetic procedures

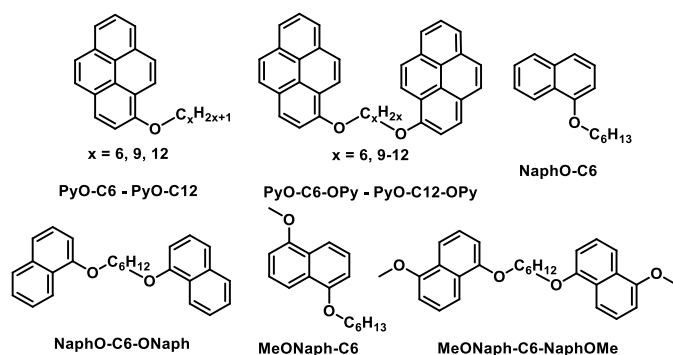
Synthesis of 5-methoxynaphthalen-1-ol



1,5-Dihydroxynaphthalene (4.5 g, 28.1 mmol, 1.0 eq.), methyl iodide (1.75 mL, 28.1 mmol 1.0 eq.) and potassium carbonate (4.27 g, 30.9 mmol, 1.1 eq.) were added to 80 mL acetonitrile. The mixture was stirred at $82\text{ }^\circ\text{C}$ under argon atmosphere for 16 h. The mixture was allowed to cool down to room temperature and concentrated under reduced pressure. The obtained solid was dissolved in 50 mL chloroform and filtered through diatomaceous earth. The solution was extracted twice with saturated NaHCO_3 solution and twice with brine before drying with anhydrous Na_2SO_4 . Subsequently, the solution was filtered, and the filter cake was washed with chloroform before the solution was concentrated to obtain the crude product. The crude product was purified on a silica column (chloroform - methanol, 0-10%) to afford pure 5-methoxynaphthalen-1-ol as white solid in 31% yield (1.69 g, 9.7 mmol).

^1H NMR (400 MHz, Chloroform- d_3): δ [ppm] = 7.85 (dt, J = 8.5, 1.0 Hz, 1H), 7.74 (dt, J = 8.5, 0.9 Hz, 1H), 7.40 (dd, J = 8.5, 7.6 Hz, 1H), 7.30 (dd, J = 8.5, 7.5 Hz, 1H), 6.85 (dd, J = 7.5, 1.0 Hz, 2H), 4.00 (s, 3H).

Synthesis of the electron donor compounds



The synthesis of all compounds was performed according to the following procedure. The exact amounts of used materials for the individual reactions are listed in Table 6.5. The reaction was carried out under inert conditions in dried glassware under argon. Hydroxy arene, bromoalkane, potassium carbonate and 25 mg potassium iodide were added to 25 mL DMF. The reaction mixture was stirred for 16 h at $60\text{ }^\circ\text{C}$ under argon atmosphere. The mixture was allowed to cool down to room temperature and added to 100 mL demi water. The precipitated solid was

filtered off, washed with water and dried. The crude products were purified on a silica column (heptane – ethyl acetate 1:1 and chloroform - methanol, 0-10%) to afford pure compounds as white-beige solids.

Table 6.5: Overview over the amounts of substance used for the synthesis of the donor molecules as well as the obtained yields.

No	compound	hydroxy arene	bromoalkane	K ₂ CO ₃	yield
1	PyO-C6	0.5 g, 2.3 mmol, 1 eq. 1-Hydroxypyrene	378 mg, 2.3 mmol, 1 eq. H ₁₃ C ₆ Br	1.1 g 7.6 mmol, 3.3 eq.	464 mg, 1.5 mmol, 67%
2	PyO-C9	0.5 g, 2.3 mmol, 1 eq. 1-Hydroxypyrene	475 mg, 2.3 mmol, 1 eq. H ₁₉ C ₉ Br	1.1 g 7.6 mmol, 3.3 eq.	658 mg, 1.9 mmol, 83%
3	PyO-C12	0.5 g, 2.3 mmol, 1 eq. 1-Hydroxypyrene	571 mg, 2.3 mmol, 1 eq. H ₁₉ C ₉ Br	1.1 g 7.6 mmol, 3.3 eq.	672 mg, 1.7 mmol, 76%
4	PyO-C6-OPy	212 g, 1.0 mmol, 2 eq. 1-Hydroxypyrene	119 mg, 0.5 mmol, 1 eq. BrH ₁₂ C ₆ Br	446 mg 3.2 mmol, 6.6 eq.	189 mg, 0.36 mmol, 74%
5	PyO-C9-OPy	197 mg, 0.9 mmol, 2 eq. 1-Hydroxypyrene	129 mg, 0.5 mmol, 1 eq. BrH ₁₈ C ₉ Br	424 mg 3.1 mmol, 6.6 eq.	124 mg, 0.22 mmol, 49%
6	PyO-C10-OPy	0.5 g, 2.3 mmol, 1 eq. 1-Hydroxypyrene	327 mg, 1.1 mmol, 1 eq. BrH ₂₀ C ₁₀ Br	994 mg 7.2 mmol, 6.6 eq.	600 mg, 1.0 mmol, 96%
7	PyO-C11-OPy	0.5 g, 2.3 mmol, 1 eq. 1-Hydroxypyrene	342 mg, 1.1 mmol, 1 eq. BrH ₂₂ C ₁₁ Br	994 mg 7.2 mmol, 6.6 eq.	343 mg, 0.6 mmol, 53%
8	PyO-C12-OPy	222 g, 1.0 mmol, 2 eq. 1-Hydroxypyrene	167 mg, 0.5 mmol, 1 eq. BrH ₂₄ C ₁₂ Br	465 mg 3.2 mmol, 6.6 eq.	282 mg, 0.47 mmol, 92%
9	NaphO-C6	1.0 g, 6.9 mmol, 1 eq. 1-naphthol	1.14 g, 6.9 mmol, 1 eq. H ₁₃ C ₆ Br	3.16 g 22.9 mmol, 3.3 eq.	1.4 g, 6.3 mmol, 91%
10	NaphO-C6-ONaph	1.0 g, 6.9 mmol, 2.1 eq. 1-naphthol	0.8 g, 3.3 mmol, 1 eq. BrH ₁₂ C ₆ Br	3.01 g 21.8 mmol, 6.6 eq.	747 mg, 2 mmol, 61%
11	MeO-NaphO-C6	470 mg, 2.7 mmol, 1 eq. 5-methoxy- naphthalen-1-ol	445 mg, 2.7 mmol, 1 eq. H ₁₃ C ₆ Br	1.1 g 7.8 mmol, 2.9 eq.	653 mg, 2.5 mmol, 94%
12	MeO-NaphO-C6-ONaph-OMe	0.7 g, 3.6 mmol, 2.1 eq. 5-methoxy- naphthalen-1-ol	467 mg, 1.9 mmol, 1 eq. BrH ₁₂ C ₆ Br	0.8 g 5.8 mmol, 3.0 eq.	411 mg, 0.95 mmol, 50%

Chemical characterization of all donor compounds:

PyO-C6

^1H NMR (400 MHz, Chloroform- d_2): δ [ppm] = 8.49 (d, J = 9.2 Hz, 1H), 8.10 (ddd, J = 8.6, 7.3, 1.4 Hz, 3H), 8.04 (d, J = 9.2 Hz, 1H), 7.99 – 7.93 (m, 2H), 7.88 (d, J = 9.0 Hz, 1H), 7.54 (d, J = 8.4 Hz, 1H), 4.32 (t, J = 6.5 Hz, 2H), 2.07 – 1.96 (m, 2H), 1.69 – 1.59 (m, 2H), 1.49 – 1.35 (m, 4H), 0.96 (t, J = 7.0 Hz, 3H). ^{13}C NMR (101 MHz, Chloroform- d_2): δ [ppm] = 153.41, 131.91, 131.87, 127.41, 126.39, 126.19, 126.00, 125.63, 125.24, 125.14, 125.01, 124.30, 124.21, 121.46, 120.57, 109.28, 69.14, 31.82, 29.63, 26.11, 22.81, 14.23. MALDI/TOF found 302,20 m/z (calculated 302,17). FT-IR (cm^{-1}): 3045 (w), 2953 (m), 2941 (m), 2926 (m), 2869 (m), 1627 (w), 1599 (m), 1510 (s), 1487 (m), 1472 (m), 1449 (m), 1432 (m), 1407 (m), 1370 (m), 1325 (m), 1308 (w), 1259 (s), 1239 (s), 1213 (m), 1190 (m), 1177 (w), 1148 (m), 1105 (m), 1071 (m), 996 (m), 841 (s), 830 (s), 816 (s), 784 (w) 757 (m), 739 (m), 728 (m), 718 (s), 675 (m), 622 (m), 561 (w), 505 (w).

PyO-C9

^1H NMR (400 MHz, Chloroform- d_2): δ [ppm] = 8.48 (d, J = 9.1 Hz, 1H), 8.10 (dd, J = 8.7, 6.6 Hz, 3H), 8.04 (d, J = 9.2 Hz, 1H), 7.96 (dt, J = 7.7, 3.2 Hz, 2H), 7.88 (d, J = 8.9 Hz, 1H), 7.54 (d, J = 8.4 Hz, 1H), 4.32 (t, J = 6.5 Hz, 2H), 2.01 (p, J = 6.9 Hz, 2H), 1.63 (p, J = 7.3 Hz, 2H), 1.50 – 1.22 (m, 10H), 0.90 (t, J = 6.4 Hz, 3H). ^{13}C NMR (101 MHz, Chloroform- d_2): δ [ppm] = 153.41, 131.90, 131.87, 127.40, 126.38, 126.18, 126.00, 125.63, 125.24, 125.14, 125.00, 124.29, 124.21, 121.47, 120.58, 109.29, 69.15, 32.06, 29.75, 29.67, 29.64, 29.46, 26.44, 22.85, 14.28. MALDI/TOF found 344,24 m/z (calculated 344,21). FT-IR (cm^{-1}): 3044 (w), 2965 (w), 2940 (w), 2925 (m), 2873 (m), 2857 (m) 1627 (w), 1599 (m), 1509 (s), 1487 (w), 1466 (m), 1433 (m), 1407 (m), 1394 (m), 1325 (m), 1306 (w), 1259 (s), 1238 (s), 1213 (m), 1190 (m), 1178 (w), 1148 (m), 1118 (m), 1071 (m), 1036 (m), 1004 (m), 957 (m), 841 (s), 830 (s), 819 (s), 782 (w) 757 (m), 740 (m), 728 (m), 718 (s), 675 (m), 621 (m), 561 (w), 483 (w).

PyO-C12

^1H NMR (400 MHz, Chloroform- d_2): δ [ppm] = 8.48 (d, J = 9.1 Hz, 1H), 8.19 – 8.07 (m, 3H), 8.03 (d, J = 9.2 Hz, 1H), 7.95 (dt, J = 7.7, 3.2 Hz, 2H), 7.88 (d, J = 8.9 Hz, 1H), 7.54 (d, J = 8.4 Hz, 1H), 4.33 (t, J = 6.5 Hz, 2H), 2.01 (p, J = 6.8 Hz, 2H), 1.63 (p, J = 7.4 Hz, 2H), 1.50 – 1.19 (m, 16H), 0.88 (t, J = 6.5 Hz, 3H). ^{13}C NMR (101 MHz, Chloroform- d_2): δ [ppm] = 153.42, 131.91, 131.88, 127.41, 126.39, 126.19, 126.00, 125.64, 125.25, 125.14, 125.01, 124.30, 124.21, 121.47, 120.59, 109.31, 69.17, 32.08, 29.84, 29.82, 29.79, 29.66, 29.63, 29.52, 26.44, 22.85, 14.28. MALDI/TOF found 386,32 m/z (calculated 386,26). FT-IR (cm^{-1}): 3036 (w), 2947 (w), 2925 (m), 2847 (m), 1627 (w), 1600 (m), 1511 (m), 1490 (w), 1463 (m), 1432 (m), 1396 (m), 1325 (m), 1308 (w), 1261 (s), 1236 (m), 1212 (m), 1192 (m), 1149 (m), 1115 (m), 1070 (m), 1021 (m), 999 (m), 946 (w), 886 (w), 838 (m), 828 (s), 766 (w) 742 (m), 727 (m), 711 (s), 676 (m), 622 (m), 615 (m), 562 (w), 481 (w).

PyO-C6-OPy

^1H NMR (400 MHz, Chloroform- d_2): δ [ppm] = 8.40 (d, J = 9.1 Hz, 2H), 8.01 (ddd, J = 8.0, 6.9, 1.4 Hz, 6H), 7.92 – 7.85 (m, 6H), 7.81 (d, J = 8.9 Hz, 2H), 7.48 (d, J = 8.4 Hz, 2H), 4.32 (t, J = 6.3 Hz, 4H), 2.06 (t, J = 5.9 Hz, 4H), 1.82 – 1.73 (m, 4H). ^{13}C NMR (101 MHz, Chloroform- d_2): δ [ppm] = 153.32, 131.89, 131.84, 127.39, 126.45, 126.19, 126.00, 125.62, 125.31, 125.11, 125.06, 124.32, 124.24, 121.36, 120.59, 109.29, 68.93, 29.64, 26.30. MALDI/TOF found 518,21 m/z (calculated 518,22). FT-IR (cm^{-1}): 3041 (w), 2965 (w), 2849 (w), 1597 (w), 1508 (m), 1487 (w), 1459 (m), 1431 (m), 1407 (m), 1400 (w), 1386 (m), 1324 (m), 1302 (w), 1256 (s), 1238 (s), 1213 (m), 1190 (w), 1173 (m), 1178 (w), 1148 (m), 1116 (m), 1106 (m), 1072 (m), 1041 (m), 999 (m), 966 (w), 954 (w), 913 (w), 892 (w) 839 (m), 828 (s), 819 (s), 758 (m), 713 (s), 689 (m), 675 (m), 620 (w).

PyO-C9-OPy

^1H NMR (400 MHz, Chloroform- d_2): δ [ppm] = 8.42 (d, J = 9.1 Hz, 2H), 8.02 (d, J = 7.8 Hz, 6H), 7.97 (d, J = 9.1 Hz, 2H), 7.89 (d, J = 8.3 Hz, 4H), 7.82 (d, J = 8.9 Hz, 2H), 7.46 (d, J = 8.3 Hz, 2H), 4.25 (t, J = 6.4 Hz, 4H), 1.96 (p, J = 6.7 Hz, 4H), 1.60 (dd, J = 10.8, 4.2 Hz, 4H), 1.43 (t, J = 5.2 Hz, 6H). ^{13}C NMR (101 MHz, Chloroform- d_2): δ [ppm] = 153.39, 131.90, 131.86, 127.41, 126.40, 126.19, 126.00, 125.64, 125.25, 125.14, 125.02, 124.31, 124.22, 121.45, 120.57, 109.29, 69.09, 29.68, 29.63, 29.51, 26.39. MALDI/TOF found 560,26 m/z (calculated 560,27). FT-IR (cm^{-1}): 3042 (w), 2945 (w), 2921 (w), 2875 (w), 2855 (w), 1627 (w), 1600 (m), 1510 (m), 1487 (w), 1474 (m), 1433 (m), 1408 (m), 1396 (m), 1326 (m), 1309 (w), 1258 (s), 1237 (s), 1213 (m), 1191 (m), 1175 (w), 1150 (w), 1116 (m), 1070 (m), 1028 (m), 985 (w), 885 (w), 839 (m), 827 (s), 818 (m), 784 (w), 754 (m), 727 (m), 712 (s), 675 (m), 623 (m), 562 (w), 494 (w).

PyO-C10-OPy

^1H NMR (400 MHz, Chloroform- d_3): δ [ppm] = 8.42 (d, J = 9.1 Hz, 2H), 8.05 – 7.99 (m, 6H), 7.96 (d, J = 9.2 Hz, 2H), 7.91 – 7.85 (m, 4H), 7.81 (d, J = 9.0 Hz, 2H), 7.47 (d, J = 8.4 Hz, 2H), 4.25 (t, J = 6.4 Hz, 4H), 1.99 – 1.89 (m, 4H), 1.58 (p, J = 7.0 Hz, 4H), 1.40 (q, J = 6.5, 4.9 Hz, 8H). ^{13}C NMR (101 MHz, Chloroform- d_3): δ [ppm] = 153.40, 131.90, 131.86, 127.41, 126.40, 126.19, 126.00, 125.64, 125.25, 125.14, 125.02, 124.31, 124.22, 121.46, 120.58, 109.30, 69.11, 29.68, 29.63, 29.56, 26.41. MALDI/TOF found 574,27 m/z (calculated 574,29). FT-IR (cm^{-1}): 3042 (w), 2942 (w), 2922 (w), 2849 (w), 1599 (m), 1507 (m), 1473 (m), 1432 (m), 1406 (w), 1392 (m), 1324 (m), 1307 (w), 1255 (s), 1213 (w), 1187 (m), 1151 (w), 1114 (s), 1068 (m), 1038 (w), 983 (w), 839 (m), 828 (s), 783 (w), 752 (m), 727 (m), 713 (s), 675 (m), 622 (m), 563 (w), 490 (w).

PyO-C11-OPy

^1H NMR (400 MHz, Chloroform- d_3): δ [ppm] = 8.42 (d, J = 9.1 Hz, 2H), 8.03 (ddd, J = 7.2, 4.9, 1.4 Hz, 6H), 7.97 (d, J = 9.2 Hz, 2H), 7.92 – 7.85 (m, 4H), 7.81 (d, J = 9.0 Hz, 2H), 7.46 (d, J = 8.4 Hz, 2H), 4.25 (t, J = 6.4 Hz, 4H), 1.94 (dq, J = 8.6, 6.5 Hz, 4H), 1.62 – 1.52 (m, 4H), 1.46 – 1.28 (m, 10H). ^{13}C NMR (101 MHz, Chloroform- d_3): δ [ppm] = 153.41, 131.91, 131.87, 127.41, 126.39, 126.19, 126.00, 125.64, 125.25, 125.14, 125.01, 124.31, 124.22, 121.47, 120.58, 109.30, 69.13, 29.72, 29.67, 29.64, 29.58, 26.40. MALDI/TOF found 588,30 m/z (calculated 588,30). FT-IR (cm^{-1}): 3042 (w), 2942 (w), 2918 (w), 2873 (w), 2854 (w), 1627 (w), 1601 (m), 1511 (m), 1473 (m), 1434 (m), 1407 (w), 1396 (m), 1327 (m), 1310 (w), 1262 (s), 1239 (w), 1192 (w), 1149 (w), 1118 (m), 1071 (m), 1039 (w), 1006 (m), 884 (w), 840 (m), 830 (s), 819 (m), 780 (w), 753 (m), 729 (m), 716 (s), 675 (m), 622 (m), 561 (w), 505 (w).

PyO-C12-OPy

^1H NMR (400 MHz, Chloroform- d_3): δ [ppm] = 8.41 (d, J = 9.1 Hz, 2H), 8.03 (dt, J = 7.2, 3.1 Hz, 6H), 7.97 (d, J = 9.2 Hz, 2H), 7.91 – 7.85 (m, 4H), 7.81 (d, J = 8.9 Hz, 2H), 7.47 (d, J = 8.4 Hz, 2H), 4.25 (t, J = 6.4 Hz, 4H), 1.94 (p, J = 6.5 Hz, 4H), 1.56 (p, J = 7.4 Hz, 4H), 1.46 – 1.28 (m, 12H). ^{13}C NMR (101 MHz, Chloroform- d_3): δ [ppm] = 153.42, 131.91, 131.88, 127.41, 126.40, 126.20, 126.01, 125.64, 125.25, 125.15, 125.02, 124.31, 124.22, 121.47, 120.59, 109.30, 69.14, 29.75, 29.73, 29.64, 29.59, 26.41. MALDI/TOF found 602,30 m/z (calculated 602,32). FT-IR (cm^{-1}): 3042 (w), 2943 (w), 2922 (w), 2856 (w), 1626 (w), 1601 (m), 1511 (m), 1474 (m), 1487 (w), 1435 (m), 1407 (w), 1395 (m), 1326 (m), 1308 (w), 1264 (s), 1213 (w), 1175 (w), 1118 (m), 1071 (m), 1035 (w), 1003 (m), 884 (w), 840 (m), 829 (s), 819 (m), 778 (w), 755 (m), 728 (m), 717 (s), 710 (m), 675 (m), 622 (m), 562 (w), 503 (w).

NaphO-C6

^1H NMR (400 MHz, Chloroform- d_3): δ [ppm] = 8.30 (d, J = 8.4 Hz, 1H), 7.83 – 7.76 (m, 1H), 7.53 – 7.44 (m, 2H), 7.39 (dt, J = 15.5, 8.1 Hz, 2H), 6.81 (d, J = 7.3 Hz, 1H), 4.14 (t, J = 6.4 Hz, 2H), 1.94 (p, J = 6.8 Hz, 2H), 1.58 (t, J = 7.5 Hz, 2H), 1.40 (h, J = 3.3 Hz, 4H), 0.98 – 0.90 (m, 3H). ^{13}C NMR (101 MHz, Chloroform- d_3): δ [ppm] = 155.05, 134.64, 127.54, 126.43, 126.05, 125.91, 125.17, 122.24, 120.05, 104.66, 68.28, 31.79, 29.44, 26.12, 22.80, 14.21. MALDI/TOF found 228.27 m/z (calculated 228,15). FT-IR (cm^{-1}): 3053 (w), 2954 (w), 2929 (w), 2858 (w), 1628 (w), 1595 (m), 1580 (m), 1509 (m), 1460 (m), 1405 (w), 1388 (m), 1347 (w), 1268 (s), 1239 (s), 1214 (w), 1178 (w), 1156 (m), 1099 (s), 1070 (w), 1019 (m), 959 (w), 871 (w), 853 (w), 789 (s), 767 (s), 732 (m), 637 (w), 618 (w), 572 (w).

NaphO-C6-ONaph

^1H NMR (400 MHz, Chloroform- d_3): δ [ppm] = 8.32 (d, J = 8.0 Hz, 2H), 7.81 (d, J = 7.9 Hz, 2H), 7.55 – 7.34 (m, 8H), 6.82 (d, J = 7.4 Hz, 2H), 4.18 (t, J = 6.3 Hz, 4H), 2.02 (t, J = 6.6 Hz, 4H), 1.80 – 1.69 (m, 4H). ^{13}C NMR (101 MHz, Chloroform- d_3): δ [ppm] = 154.97, 134.64, 127.56, 126.46, 126.04, 125.88, 125.21, 122.19, 120.13, 104.69, 68.10, 29.44, 26.29. MALDI/TOF found 370,22 m/z (calculated 370,19). FT-IR (cm^{-1}): 3050 (w), 2942 (w), 2868 (w), 2854 (w), 1724 (w), 1628 (w), 1594 (m), 1578 (m), 1508 (m), 1478 (m), 1461 (m), 1446 (w), 1407 (m), 1388 (s), 1349 (w), 1267 (s), 1241 (s), 1223 (m), 1180 (w), 1159 (m), 1099 (s), 1074 (m), 1065 (m), 1019 (m), 990 (m), 961 (w), 952 (w), 870 (w), 856 (w), 791 (s), 766 (s), 734 (m), 636 (w), 615 (w), 572 (w).

MeO-NaphO-C6

^1H NMR (400 MHz, Chloroform- d_3): δ [ppm] = 7.88 (d, J = 8.5 Hz, 1H), 7.82 (d, J = 8.5 Hz, 1H), 7.38 (td, J = 8.3, 5.1 Hz, 2H), 6.86 (dd, J = 7.8, 3.1 Hz, 2H), 4.14 (t, J = 6.5 Hz, 2H), 1.97 – 1.87 (m, 2H), 1.57 (tt, J = 9.1, 6.7, 4.6 Hz, 2H), 1.39 (p, J = 3.7 Hz, 4H), 0.94 (td, J = 6.6, 2.3 Hz, 3H). ^{13}C NMR (101 MHz, Chloroform- d_3): δ [ppm] = 155.31, 155.28, 154.78, 126.97, 126.79, 126.73, 125.42, 125.33, 125.30, 125.18, 125.10, 125.06, 114.60, 114.13, 105.84, 105.76, 104.82, 68.61, 68.55, 55.84, 55.82, 55.79, 31.78, 29.43, 26.09, 22.79, 14.20. MALDI/TOF found 258,20 m/z

Stepwise formation of charge transfer complexes on HOPG surface

(calculated 258,16). FT-IR (cm^{-1}): 2952 (m), 2929 (m), 2868 (m), 2836 (w), 1590 (m), 1508 (s), 1471 (m), 1463 (m), 1453 (m), 1409 (s), 1382 (s), 1342 (w), 1265 (s), 1212 (m), 1183 (w), 1080 (s), 1069 (s), 1065 (s), 1048 (s), 992 (m), 959 (w), 943 (m), 879 (m), 870 (w), 774 (s), 729 (w), 723 (w), 615 (m), 591 (w), 498 (m).

MeO-NaphO-C6-ONaph-OMe

^1H NMR (400 MHz, Chloroform- d_3): δ [ppm] = 7.87 (d, J = 8.5 Hz, 2H), 7.82 (d, J = 8.5 Hz, 2H), 7.36 (td, J = 8.1, 3.0 Hz, 4H), 6.85 (d, J = 7.6 Hz, 4H), 4.16 (t, J = 6.3 Hz, 4H), 4.00 (s, 6H), 1.99 (t, J = 6.6 Hz, 4H), 1.75 – 1.66 (m, 4H). ^{13}C NMR (101 MHz, Chloroform- d_3): δ [ppm] = 155.32, 154.76, 126.92, 126.77, 125.38, 125.21, 114.50, 114.13, 105.63, 104.72, 68.25, 55.74, 29.43, 26.27. MALDI/TOF found 430,24 m/z (calculated 430,21). FT-IR (cm^{-1}): 3018 (w), 2932 (m), 2922 (m), 2909 (w), 2860 (w), 2834 (w), 1593 (m), 1508 (m), 1475 (m), 1459 (m), 1442 (m), 1408 (s), 1383 (s), 1262 (s), 1215 (m), 1193 (w), 1170 (m), 1079 (s), 1069 (s), 1047 (s), 1034 (s), 997 (m), 960 (w), 912 (m), 888 (m), 853 (w), 834 (w), 771 (s), 737 (w), 671 (m), 614 (m), 592 (m), 551 (w), 504 (w).

Thermal characterization of all donor compounds:

Table 6.6: Phase transition temperatures^A and enthalpies^B recorded for all donor molecules during heating. Heating rate: 10 K min^{-1} .

Phase transition temperatures upon heating									
Compound	T_g	T_1	ΔH_1	T_2	ΔH_2	T_3	ΔH_3	T_m	ΔH_m
PyO-C6-OPy	-	155	2.0					205	31.5
PyO-C9-OPy	19	57	-41,4	105	2,9			132	56,6
PyO-C10-OPy	-							124	80.7
PyO-C11-OPy	-							142	94.3
PyO-C12-OPy	-	134	12.1					152	49.4
PyO-C6	-							111	49.9
PyO-C9	-							75	49.3
PyO-C12	-							78	54.7
NaphO-C6-ONaph ^C	-	5	-11.9	87	5.4			105	35.0
NaphO-C6 ^C	-	-39.4	-14.5	-18.1	2.4	-1.7	8.2	-2.4	16.6
MeO-NaphO-C6-ONaph-OMe	-	124	-5.2					162	68.5
MeO-NaphO-C6	-							60	33.0

^A The peak temperatures in the DSC traces were obtained during the second heating and cooling cycle. T_g glass transition. At T_1 - T_3 , thermal transitions were observed before reaching the melting temperature T_m . ^B values are given in kJ/mol. ^C Heating rate 5 K min^{-1} .

Table 6.7: Phase transition temperatures^A and enthalpies^B recorded for all donor molecules during cooling. Heating rate: 10 K min⁻¹.

Phase transition temperatures upon cooling					
Compound	T_g	T_c	ΔH_c	T_4	ΔH_1
PyO-C6-OPy	-	149	29.1		
PyO-C9-OPy	13	-	-		
PyO-C10-OPy	-	91	73.4		
PyO-C11-OPy	-	113	78.5	92	3.0
PyO-C12-OPy	-	115	45.3		
PyO-C6	-	89	48.7		
PyO-C9	-	65	48.0		
PyO-C12	-	56	51.5		
NaphO-C6-ONaph	-	23	13.7		
NaphO-C6	-	-	-		
MeO-NaphO-C6-ONaph-OMe	-	124	51.7		
MeO-NaphO-C6	-	29	32.5		

^A The peak temperatures in the DSC traces were obtained during the second heating and cooling cycle. T_g glass transition. At T_4 a thermal transition was observed during cooling besides the melting temperature T_m . ^B values are given in kJ/mol.

6.8 References

- [1] C. A. Hunter, K. R. Lawson, J. Perkins, C. J. Urch, *J. Chem. Soc. Perkin Trans. 2* **2001**, 651.
- [2] C. R. Martinez, B. L. Iverson, *Chem. Sci.* **2012**, 3, 2191.
- [3] R. Foster, C. A. Fyfe, *Prog. Nucl. Magn. Reson. Spectrosc.* **1969**, 4, 1.
- [4] J. Ferraris, D. O. Cowan, V. Walatka, J. H. Perlstein, *J. Am. Chem. Soc.* **1973**, 95, 948.
- [5] S. Bartocci, J. A. Berrocal, P. Guarracino, M. Grillaud, L. Franco, M. Mba, *Chem. Eur. J.* **2018**, 24, 2920.
- [6] A. Das, S. Ghosh, *Angew. Chem. Int. Ed.* **2014**, 53, 2038.
- [7] M. Kumar, K. Venkata Rao, S. J. George, *Phys. Chem. Chem. Phys.* **2014**, 16, 1300.
- [8] K. V. Rao, K. Jayaramulu, T. K. Maji, S. J. George, *Angew. Chem. Int. Ed.* **2010**, 49, 4218.
- [9] H. Shao, T. Nguyen, N. C. Romano, D. A. Modarelli, J. R. Parquette, *J. Am. Chem. Soc.* **2009**, 131, 16374.
- [10] W. Pisula, M. Kastler, D. Wasserfallen, J. W. F. Robertson, F. Nolde, C. Kohl, K. Müllen, *Angew. Chem. Int. Ed.* **2006**, 45, 819.
- [11] L. R. Hart, J. H. Hunter, N. A. Nguyen, J. L. Harries, B. W. Greenland, M. E. Mackay, H. M. Colquhoun, W. Hayes, *Polym. Chem.* **2014**, 5, 3680.
- [12] S. Burattini, H. M. Colquhoun, J. D. Fox, D. Friedmann, B. W. Greenland, P. J. F. Harris, W. Hayes, M. E. Mackay, S. J. Rowan, *Chem. Commun.* **2009**, 6717.
- [13] W. X. Xiao, D. Liu, C. J. Fan, Y. Xiao, K. K. Yang, Y. Z. Wang, *Polymer* **2020**, 190, 122228.
- [14] J. Qin, F. Lin, D. Hubble, Y. Wang, Y. Li, I. A. Murphy, S. H. Jang, J. Yang, A. K. Y. Jen, *J. Mater. Chem. A* **2019**, 7, 6773.
- [15] S. Chakraborty, D. Ray, V. K. Aswal, S. Ghosh, *Chem. Eur. J.* **2018**, 24, 16379.
- [16] S. De, S. Ramakrishnan, *Macromolecules* **2009**, 42, 8599.
- [17] V. J. Bradford, B. L. Iverson, *J. Am. Chem. Soc.* **2008**, 130, 1517.
- [18] H. Y. Au-Yeung, G. D. Pantoş, J. K. M. Sanders, *Proc. Natl. Acad. Sci.* **2009**, 106, 10466.
- [19] J. Li, L. Guo, L. Zhang, C. Yu, L. Yu, P. Jiang, C. Wei, F. Qin, J. Shi, *Dalt. Trans.* **2009**, 823.
- [20] P. Talukdar, G. Bollot, J. Mareda, N. Sakai, S. Matile, *J. Am. Chem. Soc.* **2005**, 127, 6528.
- [21] R. Bhosale, J. Mišek, N. Sakai, S. Matile, *Chem. Soc. Rev.* **2010**, 39, 138.
- [22] N. S. S. Kumar, M. D. Gujrati, J. N. Wilson, *Chem. Commun.* **2010**, 46, 5464.
- [23] J. Hak, S. Sabin-Lucian, W. Y. Lee, M. Könemann, H. W. Höffken, C. Röger, R. Schmidt, Y. Chung, W. C. Chen, F. Würthner, Z. Bao, *Adv. Funct. Mater.* **2010**, 20, 2148.
- [24] A. Dey, A. Kalita, P. K. Iyer, *ACS Appl. Mater. Interfaces* **2014**, 6, 12295.
- [25] M. D. Gujrati, N. S. S. Kumar, A. S. Brown, B. Captain, J. N. Wilson, *Langmuir* **2011**, 27, 6554.

- [26] S. Burattini, H. M. Colquhoun, J. D. Fox, D. Friedmann, B. W. Greenland, P. J. F. Harris, W. Hayes, M. E. MacKay, S. J. Rowan, *Chem. Commun.* **2009**, 6717.
- [27] P. Rajdev, M. R. Molla, S. Ghosh, *Langmuir* **2014**, *30*, 1969.
- [28] J. Bernstein, H. Regev, F. H., Herbstein, P. Main, S. H. Rizvi, K. Sasvari, B. Turcsanyi, *Proc. R. Soc. Lond. A Soc. A.* **1967**, *347*, 355.
- [29] M. Y. Yeh, H. C. Lin, *Phys. Chem. Chem. Phys.* **2014**, *16*, 24216.
- [30] S. M. Ryno, C. Risko, J. L. Brédas, *J. Am. Chem. Soc.* **2014**, *136*, 6421.
- [31] K. S. Mali, J. Adisojoso, E. Ghijsens, I. De Cat, S. De Feyter, *Acc. Chem. Res.* **2012**, *45*, 1309.
- [32] J. A. Berrocal, G. H. Heideman, B. F. M. de Waal, E. W. Meijer, B. L. Feringa, *ACS Nano* **2020**, DOI 10.1021/acsnano.0c06274.
- [33] B. Ilan, G. M. Florio, M. S. Hybertsen, B. J. Berne, G. W. Flynn, *Nano Lett.* **2008**, *8*, 3160.
- [34] G. Binnig, H. Rohrer, *IBM J. Res. Dev.* **1986**, *30*, 355.
- [35] A. M. Sweetman, S. P. Jarvis, H. Sang, I. Lekkas, P. Rahe, Y. Wang, J. Wang, N. R. Champness, L. Kantorovich, P. Moriarty, *Nat. Commun.* **2014**, *5*, DOI 10.1038/ncomms4931.
- [36] Y. T. Shen, K. Deng, X. M. Zhang, D. Lei, Y. Xia, Q. D. Zeng, C. Wang, *J. Phys. Chem. C* **2011**, *115*, 19696.
- [37] E. Mena-Osteritz, P. Bäuerle, *Adv. Mater.* **2006**, *18*, 447.
- [38] G. Velpula, T. Takeda, J. Adisojoso, K. Inukai, K. Tahara, K. S. Mali, Y. Tobe, S. De Feyter, *Chem. Commun.* **2017**, *53*, 1108.
- [39] J. A. Theobald, N. S. Oxtoby, M. A. Phillips, N. R. Champness, P. H. Beton, *Nature* **2003**, *424*, 1029.
- [40] M. O. Blunt, J. C. Russell, M. D. C. Gimenez-Lopez, N. Taleb, X. Lin, M. Schröder, N. R. Champness, P. H. Beton, *Nat. Chem.* **2011**, *3*, 74.
- [41] J. Teyssandier, S. De Feyter, K. S. Mali, *Chem. Commun.* **2016**, *52*, 11465.
- [42] M. T. Räisänen, A. G. Slater, N. R. Champness, M. Buck, *Chem. Sci.* **2012**, *3*, 84.
- [43] K. Tahara, K. Kaneko, K. Katayama, S. Itano, C. H. Nguyen, D. D. Amorim, S. De Feyter, Y. Tobe, *Langmuir* **2015**, *31*, 7032.
- [44] S. Casalini, C. A. Bortolotti, F. Leonardi, F. Biscarini, *Chem. Soc. Rev.* **2017**, *46*, 40.
- [45] G. Velpula, M. Li, Y. Hu, Y. Zagranyarski, W. Pisula, K. Müllen, K. S. Mali, S. De Feyter, *Chem. Eur. J.* **2018**, *24*, 12071.
- [46] R. Hahn, F. Bohle, S. Kotte, T. J. Keller, S. S. Jester, A. Hansen, S. Grimme, B. Esser, *Chem. Sci.* **2018**, *9*, 3477.
- [47] J. Visser, N. Katsonis, J. Vicario, B. L. Feringa, *Langmuir* **2009**, *25*, 5980.
- [48] J. V. Barth, *Surf. Sci.* **2009**, *603*, 1533.
- [49] G. H. Heideman, J. A. Berrocal, E. W. Meijer, B. L. Feringa, *Chem. Eur. J.* **2020**, DOI 10.1002/chem.202004008.
- [50] A. H. G. David, R. Casares, J. M. Cuerva, A. G. Campañ, V. Blanco, *J. Am. Chem. Soc.* **2019**, *141*, 18064.
- [51] K. Kobayashi, *Phys. Rev. B* **1996**, *53*, 91.
- [52] V. C. Wakchaure, L. V. Pillai, Goudappagouda, K. C. Ranjeesh, S. Chakrabarty, S. Ravindranathan, P. R. Rajamohanam, S. S. Babu, *Chem. Commun.* **2019**, *55*, 9371.
- [53] A. T. Haedler, H. Misslitz, C. Buehlmeier, R. Q. Albuquerque, A. Köhler, H. W. Schmidt, *ChemPhysChem* **2013**, *14*, 1818.
- [54] S. Bhattacharjee, S. Bhattacharya, *Chem. Asian J.* **2015**, *10*, 572.

Summary

The development of modern organic chemistry enabled the preparation of a large variety of synthetic colorants which soon received an indispensable social role. As already suggested by literature reports from the 19th century, organic materials need to contain certain functional groups, the so-called chromophores to exhibit colors that are visible by eye. Today, we know that the color of an organic material typically arises from light-matter-interactions that involve electronic transitions such as the charge transfer (CT) from an electron donating (D) to electron accepting moiety (A). Modern research has shown that besides being used as colorants, organic CT materials can be used for many more applications that still remain to be explored fully.

In Chapter 1, we introduce the literature-known structure-property relationships of organic CT materials. First, we highlight exemplary systems that exhibit intramolecular CT (ICT). This class of compounds contains many functional dyes with a wide range of (opto-)electronic applications. Subsequently, we present examples of organic CT complexes that are formed as adducts between D and A moieties of two individual chemical species. Finally, we show the recent developments of arranging molecules that contain D and A moieties on surface, a medium where CT complex formation is highly desirable but has not been achieved yet.

In Chapter 2, we report on the design, synthesis and characterization of novel chiral and achiral squaraine dyes that contain the D- π -A- π -D architecture. We show that only highly electron-rich starting materials undergo condensation with squaric acid to form squaraine dyes. We investigate the rotational isomerism of one squaraine dye in detail by the combination of DFT calculations, FT-IR and NMR spectroscopy. Finally, we develop a synthetic strategy to implement a squaraine dye into a soft siloxane matrix.

In Chapter 3, we report on the chiroptical properties, the aggregation behavior and the (opto-)electronic applications of our squaraine dyes. We show that the colors of the dyes are pH responsive and change upon aggregation. Spin-coating the mixtures of chiral and achiral squaraine dye results in the formation co-assembled structures. The combined results of optical spectroscopy and magnetic conducting atomic force microscopy show that the highest optical activity and the most spin-selective electron transport is achieved in the thin film containing 25% chiral and 75% achiral dye.

In Chapter 4, we present a novel supramolecular approach for the preparation of graphitic carbon nitride-like materials. We prepare two novel, chiral supramolecular

building blocks that contain the *s*-heptazine motif and amide groups. We find that both compounds form optically active aggregates in poor solvent. We show that heating and annealing the thin film prepared from the building block that contains additional urethane groups can be used to cleave off the catalytically inactive side chains without melting the thin film. The increase of the relative amount of nitrogen atoms and retaining a high surface area during the thermal curing step are suggested to promote catalytic activity by structurally approaching graphitic carbon nitride in the supramolecular system.

In Chapter 5, we present a series of novel double *N,N'*-bis(*n*-alkyl)-naphthalenediimides (NDIs) for the functionalization of highly oriented pyrolytic graphite (HOPG) surfaces with electron-poor double lamellar structures. The pitch of the NDI lamellae is precisely tuned by the length of the alkyl chain that connects two NDI cores covalently. The investigation of the bulk morphologies by X-ray scattering indicates that in bulk, lamellar structures are formed, too, which have comparable repeating units as the surface structures. Nevertheless, we find subtle differences in the structural details between the lamellae formed in both media which we ascribe to the partial desorption of the alkyl spacers from HOPG surface.

In Chapter 6, we investigate the stepwise functionalization of surfaces with D-A-mixtures. Electron-rich pyrenes are added on top of the NDI double lamellae described in Chapter 5. Depending on the molecular structures of the NDIs and the pyrenes, different morphologies are formed. Whereas most NDI-pyrene combinations show lateral or vertical phase separation, several mixtures show the formation of new surface domains that consist of co-adsorbed structures. The detailed structural analysis shows that co-adsorption occurs either in plane or in D-A stacks. The close proximity and rotational angle between the chromophores in the D-A stacks are indicative of CT complex formation on the HOPG surface.

Some general conclusions and future perspectives

Charge transfer processes and supramolecular chemistry have been identified as pivotal elements in many biological processes. Owing to the complexity of most biological systems, the structure-property relationships that are required to design highly functional artificial supramolecular charge transfer systems remain yet to be explored fully.

This thesis shows several approaches for developing model systems to study the formation and the applications of prospective supramolecular charge transfer systems. The co-assembly of chiral and achiral semiconducting squaraine dyes is a brilliant example for creating a binary mixture that has a greater functionality than the sum of its individual parts. Since applications realized by the usage of organic spin-filtering materials are currently still at their beginning, the demonstrated increase of the spin polarization by mixing two components has important implications for optimizing the materials that are used in future spintronic devices. Since the nitrogen-rich *s*-heptazine motif has already been suggested by many literature reports for a variety photo- and electrocatalytic applications, its potential for spintronic applications is standing to reason. With the synthetic strategy described in this thesis, it is possible to synthesize small molecules that both contain the functional *s*-heptazine motif and form self-assembled nanofibers. Although the presented building blocks need further optimization to enable a thorough investigation of the consequences of side chain cleavage on material and spin-filtering properties, thin films with a high thermal stability could be prepared. The electrocatalytic functionality of these materials remains to be investigated quantitatively.

Next to the preparation of functional thin films, the creation of highly defined mono- and bilayers poses a challenge in the field of nanotechnology and is expected to aid the continuing miniaturization of electronic devices. The presented NDI-pyrene system shows that the stepwise formation of a complex supramolecular architecture that contains charge transfer complexes can be achieved at an interface. Before continuing with an investigation of potential applications, the underlying structure-property relationships need to be understood better which will also give valuable suggestions for the design of other molecular building blocks used to create functional interfaces in a stepwise approach.

Curriculum Vitae



Andreas Thomas Rösch was born on 28 September 1990 in Wertheim (Germany). After finishing his secondary education and basic military service, he started studying chemistry at the University of Bayreuth in 2011. Andreas conducted his graduation project in the group of prof. dr. Georg Papastavrou, where he was working on patterning benzene-1,3,5-tricarboxamide based hydrogels by using atomic force microscopy. Andreas obtained his B.Sc. in 2014 and continued his studies at the University of Bayreuth by enrolling in the master program "Polymer Science". During his master studies, he was supported by the Erasmus Student Mobility Placement to join the Laboratory of Macromolecular and Organic Chemistry at the Eindhoven University where he developed novel chiral materials for organic light emitting devices. During his master graduation project in the group of prof. dr. Hans-Werner Schmidt, Andreas developed novel s-heptazine based supramolecular nanofibers for which he was awarded with the Johann-Kaspar-Zeuss prize from the Lucas-Cranach town Kronach. After graduating with honors, he rejoined the Laboratory of Macromolecular and Organic Chemistry at the Eindhoven University to start a PhD project under the supervision of prof. dr. E.W. Meijer and prof. dr. Anja R.A. Palmans. During his PhD studies, Andreas synthesized and investigated novel organic charge transfer materials for spintronic and surface patterning applications. The most important results are presented in this dissertation.

List of Publications

Stepwise formation of charge transfer complexes at the 1 phenyloctane/HOPG interface, [A.T. Rösch](#), R. Reynaerts, K.S. Mali, S. De Feyter, A.R.A. Palmans, and E.W. Meijer, *in preparation*, **2021**.

Spin-controlled water splitting facilitated by novel electrode coatings prepared from chiral, nitrogen-rich supramolecular building blocks, [A.T. Rösch](#), H. Su, N.C. Jansen, Q. Zhu, Q. Song, M.C. Figueiredo, R. Naaman and E.W. Meijer, *in preparation*, **2021**.

Tuning the pitch of *N,N'*-bis(*n*-alkyl)-naphthalenediimide double lamellae in 2D and 3D, [A.T. Rösch](#), R. Reynaerts, B.A.G. Lamers, K.S. Mali, S. De Feyter, A.R.A. Palmans, and E.W. Meijer, *in preparation*, **2021**.

Rotational isomerism of an amide substituted squaraine dye – a combined spectroscopic and computational study, [A.T. Rösch](#), S.H.M. Söntjens, J. Robben, A.R.A. Palmans, and T. Schnitzer, *submitted*, **2021**.

Helicity control in the aggregation of achiral squaraine dyes in solution and thin films, [A.T. Rösch](#), Q. Zhu, J. Robben, F. Tassinari, S.C.J. Meskers, R. Naaman, A.R.A. Palmans, and E.W. Meijer, *Chem. Eur. J.*, *27*, 298, **2021**.

Chiral aggregates of triphenylamine-based dyes for depleting the production of hydrogen peroxide in the photochemical water-splitting process, B. Adelizzi, [A.T. Rösch](#), D.J. van Rijen, R.S. Martire, S. Esiner, M. Lutz, A.R.A. Palmans, and E.W. Meijer, *Helv. Chim. Acta*, *102*, e1900065, **2019**.

Acknowledgements

It is my pleasure to thank those who supported me during the last four years while I have been working on this thesis.

First of all, I want to thank my promotor Bert very much for the great guidance during this incredible period of time. At this point I want to note that I was always most intrigued by your incredible speed and care for detail when analyzing the chemical structure of any given molecule. Out of everything that I learnt from you during the PhD, I appreciate most the quality that you bring both to science and science communication.

I am also very grateful to Anja, my co-promotor, for always having time for a discussion on day-to-day operations, during the preparation sessions of the MOC module and many more matters. I value your input and support very much and I am very glad and grateful for everything that I learnt from you. I hope that when Corona is finally over you can resume exploring the world again!

I want to thank the members of the committee for the critical review of this thesis. Prof. dr. Steven De Feyter, I want to thank you especially for inviting me to come to Leuven, our collaboration and the many fruitful discussions that we had. I want to thank prof. dr. Hans-Werner Schmidt very much for his guidance during my master thesis which has brought me in contact with the *s*-heptazine chemistry for the first time. Prof. dr. Željko Tomović, I want to thank you very much for your suggestions that helped improving the thesis. I want to thank dr. Ghislaine Vantomme and dr. Stefan Meskers for many fruitful discussions during the last years which gave me vital input for many of the presented experiments.

I want to thank prof. dr. Ron Naaman for our collaboration on spin-filtering materials. Thank you very much, Qirong, for measuring mc-AFM and sharing your results with me. Francesco, Bea and Chidambar, I thank you for our discussions on the CISS effect. At this point, I also want to thank all other people who were at some point involved in unravelling the properties of the amide functionalized squaraine dyes presented in this thesis. I want to thank Jorn who supported me during his graduation project with the synthesis and Koen, Nicolas and Serkan for many discussions on electrochemical measurements. I thank Mengmeng for demonstrating that the compounds are semiconductors and Haijun that we can also use them as donor materials in solar cells. Tobias and Serge, it was astounding to see how fast we were able to make a story out of the rotational isomerism. I am still impressed with all the shapes that a research study can take when multiple experts are involved in a project revolving around novel molecules.

I want to extend my gratitude to the remaining people involved in the collaboration with KU Leuven. First of all, Christiaan, I thank you very much for driving me to Leuven and doing experiments together. I thank Robby and Kunal very much for the many fruitful discussions that we had. Robby, I thank you especially for recording all the STM images and Brigitte, I thank you very much for measuring SAXS for all of my compounds.

I express my gratitude to the research support at the department. Thank you, Bas, Carla, Hans, Henk, Jolanda, Joost, Lou, Margot, Martina and Ralf for organizing everything and allowing me to focus fully on research and education. I also want to Marcel for organizing everything so well that giving the werkcollege for the BMT students went very smoothly.

I want to continue the acknowledgements by thanking my paranymphs. Elisabeth and Hao, I want to thank you very much for your friendship and our time together. Elisabeth, I am particular grateful that I could use your kitchen a couple of times when mine was not working yet and want to thank you again for providing me with bread when you returned from your trips to Germany. Hao, it was really great working together with you. I value especially your reliability when we were working in shifts to get the nitrogen rich molecules done. Of course, I want to extend my gratitude to the rest of the former and present members of the group and department. At first, I want to thank Andreas H. for introducing me to the group. I thank my office mates Gijs (I want to thank especially you for helping me set up all the software in the beginning), Sjors, Hao and Linlin in STO 4.81 and later Bart and Stef in Lab 4. In Lab 4, I also want to thank Brigitte (incredible how much time we spend together making all kinds of different molecules!). Mathijs, I always enjoyed our time together on conferences, parties and of course also when you were living in my place, I wish you the best in Switzerland. It was very nice to have Diederik, Huiyi, Patricia, Soumabrata and Yunfei as coworkers in Lab 4, you all helped to create a safe and enjoyable work environment. Anjana, Bas, Christiaan, Fabian, Giulia, Hirotooshi, Jesus, Joost, Julian, Lafayette, Lu, Marcin, Marco, Marle, Martin, Mischa, Nate, Peter-Paul, Pongphak, René, Sandra, Silvia, Simone, Stefan, Takuya, I want to thank you all for your kindness. It was nice getting to know you and discussing with you, attending conferences together or simply enjoying the lunch breaks. I wish you all the best for your future.

I thank all the people who were working in close collaboration with me as part of their studies. Felix, Gianfabio, Joep, Jorn, Nils and Weiling. You were very different personality types that were all interested in conducting chemical research. It was very intriguing for me to see how each of you was tackling the different challenging research questions in your own way. I am very happy that that I could guide you all to a successful graduation/ research stay.

I want to thank my family for all the support that they gave me and without whom completing this thesis would have been very much more difficult.

Andreas